EXPLOITING ADDITIVELY MANUFACTURED LATTICES TO CONTROL MECHANICAL PROPERTIES AND DRUG DELIVERY IN BONE IMPLANTS

by

SOPHIE ELIZABETH THOMPSON LOUTH

A thesis submitted to
The University of Birmingham
for the degree of
ENGINEERING DOCTORATE

School of Chemical Engineering
College of Engineering and Physical Sciences
The University of Birmingham
August 2023

Abstract

Metal bone implants are used extensively to provide mechanical support, fixation or to fill defects due to disease, aging or trauma. Examples of implant include joint replacement, fracture plates, and fusion cages. These are very successful surgeries; however, failures do occur. The most common causes of bone implant failure are infection and aseptic loosening which can be caused by stress shielding or poor fixation.

Additive manufacturing enables the creation of implants with complex geometries such as lattices which cannot be easily made with conventional manufacturing techniques. Despite lattices being used in medical devices for fixation, and extensively researched for stress shielding their potential to be exploited as drug delivery vehicles has not been fully explored. In this work the novel technique of manipulating lattice geometry to control drug release is proposed.

The mechanical properties of lattices manufactured from Ti-6Al-4V by laser powder bed fusion was investigated. Four lattice designs provided sufficient compressive strength to be weight bearing while having sufficient void volume to fill with a drug loaded biomaterial. For example BCCZ lattices with a 350 μm strut thickness had an offset stress of 365 $\pm$ 7 MPa with a volume fraction of 0.583 $\pm$ 0.001. Additionally the effects of strut and wall thickness, lattice rotations during building, loading and a combination of the two, and unit cell size were investigated; to understand which factors were important when designing additively manufactured medical devices.

Secondly, BCCZ and gyroid lattices with volume fractions of 0.2, 0.4 and 0.6 were filled with brushite cement containing 2.5% w/w gentamicin sulphate. The drug release fitted the Korsmeyer-Peppas model with R^2 values of at least 0.98 and could be controlled by changing the lattice geometry. There were also statistical differences in the size of inhibition zones of *Staphylococcus aureus* and *Pseudomonas aeruginosa*. The presence of brushite cement in the lattice structure did not reduce the compressive strength.

Finally, a coating was developed to immobilise therapeutics to the surface of implants. Albumin was used as a model therapeutic, it was covalently attached via amide bond coupling to PCL which was dip coated onto Ti-6Al-4V coupons. This process was optimised and albumin continued to intrinsically fluoresce on coupon surfaces after immersion for four months in phosphate buffered saline at 37°C.

This thesis focuses on the exploitation of lattices manufactured by laser powder bed fusion to control drug delivery while manipulating the mechanical properties, with a view to using them in hip replacements to treat infection, and spinal interbody fusion cages to improve bone ingrowth.

ACKNOWLEDGEMENTS

I am deeply indebted to my supervisors Dr Sophie Cox, Dr Luke Carter, Professor Liam Grover and Dr Kenneth Nai. Their insight and thoughtful comments have guided me throughout my research, and made for a richer experience. To Dr Thomas Hall, and Dr Victor Villapún for teaching me bacteriological techniques and Dr Lucy Arkinstall for all your chemistry support. Special thanks go to Dr Luke Carter, Dr Thomas Robinson, and Dr Lucy Arkinstall for their editorial support. I am extremely grateful to the Formulation Engineering CDT (EPSRC grant no. EP/L015153/1) and Renishaw PLC for funding this Engineering Doctorate.

The support of the staff at this University is unparalleled. Thanks to Daniel Wilmot for keeping the Centre for Custom Medical Devices running. Emma Lardner for being the glue that stops the Healthcare Technologies Institute splintering. Thanks to David Price for his support in using the analogue compression testers. Special thanks to Professor Vikki Burns without whom I would not have overcome my barriers to actually write this thesis.

The support of my peers has been invaluable, particularly Morgan, Matt and Emily. Additionally to Mr Fannon for starting me on this journey 14 years ago, and encouraging me to do a doctorate. This endeavour would not have been possible without the patience and support of my partner, Marty.

CONTENTS

LIST OF FIGURES

LIST OF TABLES

CHAPTER 1

INTRODUCTION

1.1 Bone Implants

Metal bone implants are used extensively in the body predominantly to provide weight bearing support where it has been lost due to disease, trauma or aging (figure 1.1). This can include providing mechanical fixation of bones after trauma such as bone plates, wires, nails and screws [1]. Joint replacements are used to replace damaged joints generally due to arthritis [2]. Fusion cages are used in complex bones including vertebrae and ankles to provide stability by fusing bones together [3]. Dental implants replace teeth after decay or trauma [4]. Osseointegrated percutaneous implants are used to attach prostheses for missing limbs [5, 6].

Despite the greater number of hospital admissions for fractures than joint replacements [8, 9], joint replacements are the most common surgical procedure involving bone implants in both the USA and UK [10, 11]. With around 200 hip replacements per 100,000 population and 150 knee replacement per 100,000 inhabitants in Europe [7]. With a population increasing in number, age and weight, the demand for joint replacements is increasing [7]. Along with a demand for new design approaches to overcome some of the challenges posed by current implant designs.

The metals most commonly used for bone implants are stainless steel, cobalt chrome and titanium alloys [1], all of which provide strength an order of magnitude above that

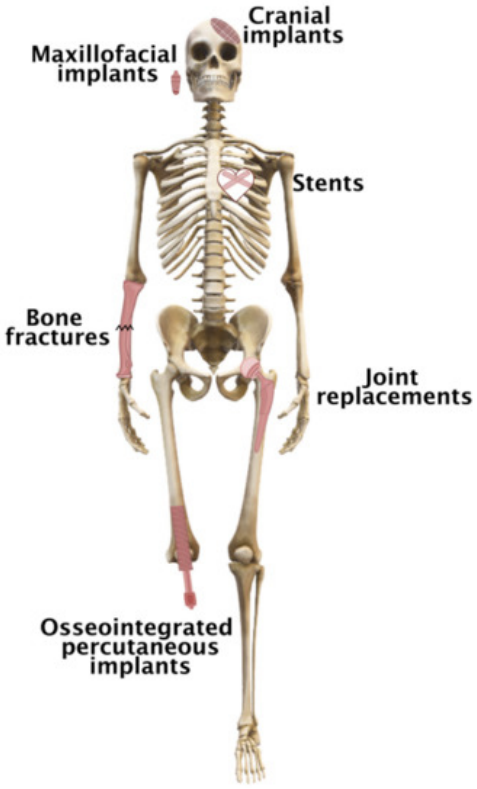

Figure 1.1: Some examples of metal-based implants used in the human body. Adapted from [7]

of cortical bone ($\sim$ 200 MPa) [4]. These metals are also predominantly bioinert due to the formation of oxide layers on their surfaces which controls the ion release and provides corrosion resistance [12]. Despite the extensive use of these metals for bone implant applications they have some challenges.

Although the high mechanical strength of metals used in implants enables them to provide sufficient strength for weight bearing applications, this comes with a high stiffness that can lead to stress shielding. This is where the loading occurs through the implant rather than the bone leading to bone loss near the implant [13]. This in turn can lead to implant loosening and failure [14]. Methods proposed to reduce stress shielding have included the use of alternative materials with lower modulus of elasticity [15], or altering the geometry of the implants including the use of porous structures to reduce the stiffness [14, 16]. The wide variety of porous structures available enables a greater tunability of the stiffness compared to altering the material and so will be investigated in this work.

The use of porous structures can also enable fixation through osseointegration where the bone grows into the implant which provides mechanical fixation [17].

Implant movement both intentional in joint replacements and not, for example due to implant loosening, can create wear particles. Additionally corrosion can lead to metal particles in the surrounding tissues, due to fretting and also galvanic corrosion between dissimilar metals, which have different electrode potentials. This is more prevalent in stainless steel than titanium alloys [12]. The presence of these particles can lead to inflammation, osteolysis and pseudotumors, which can result in implant failure [7, 18]. Changing the wear surfaces in joint replacements to ceramics or polymers reduces the presence of metal wear particles. However, polymer wear particles bring their own challenges, such as biological reactions including osteolysis, the degradation of bone tissue [19]. Corrosion can be reduced by changing the metals used in implants, as well as avoiding mixing metals to remove the risk of galvanic corrosion [1]. In this work the titanium alloy Ti-6Al-4V will be used to reduce the risk of corrosion compared to other metals, while the use of a porous structure to promote osseointegration will help to reduce implant movement due to loosening.

Another mechanism of implant failure is infection, which has a generally low rate in bone implant applications of below 5%, compared to 10% for bowel surgeries [20]. However these infections can be challenging to treat, resulting in a cost that is in the region of three times the original surgery cost [21]. The presence of a foreign body increases the risk of infection due to bacterial colonisation of the implant surface [22]. Often the only successful treatment is removal of the implant [23]. New technologies to prevent and treat infection in implants are wide ranging, including the use of antibiotic loaded bone cement for implant fixation [24], implant coating with antibiotics, antimicrobial metals or nanosurfaces [25]. More recently implants with drug eluting reservoirs have been explored [26]. This will be further discussed in section 1.8.

1.1.1 Case Studies

In this work technologies to improve bone implants will be explored. Specifically, the use of additively manufactured lattices to control drug delivery of antibiotics and growth factors. Additionally the use of lattices may improve the mechanical properties including reducing stress shielding. Two bone implant applications will be discussed in more detail as potential implants to exploit these technologies. These are hip implants to treat infection and spinal fusion cages.

Hip Implants to Treat Infection

Hip replacements are one of the most common surgeries performed in the UK with 241,000 performed between 2019 and 2021 [9]. They are predominantly performed to treat osteoarthritis (91.2%), although other causes include fractures or abnormal anatomy [27]. Failure rates are low with 70% survival at 15 years, and 5 revisions for every 1000 years of implantation [9]. Aseptic loosening (loosening not cause by infection) makes up 48% of the revisions while infection leads to 10% [9]. Additional causes include fracture, dislocation and wear. Due to the high prevalence of the surgery the cost is low for a primary implantation (€ 7490 ± 1030) although revision surgeries are more expensive (€ 9240 ± 1210), especially if they are for a septic revision (€ 23,800 ± 8240) [21].

There is a sliding scale of treatment options for infected hip replacements from the conservative administration of systemic antibiotics which are the least invasive and the least successful [28]. At the other extreme, two stage revision involves the removal of the infected implant and tissues, and implantation of an antibiotic loaded hip spacer. This spacer is left in for six to eight weeks, followed by a second surgery to remove the hip spacer and implant a new permanent prosthetic [29]. This process is more successful at treating the infection but the burden of the two surgeries and prolonged hospital stay can lead to poorer patient outcomes overall [28].

Hip spacers are temporary devices which provide local antibiotics directly to the site of the infection. They hold open the cavity from the hip replacements and provide some

mechanical support which enables some patients to partially bear weight [30]. Spacers are made of poly(methyl methacrylate) bone cement (PMMA), loaded with one or two antibiotics [31]. They can be made freehand or in a mould by the surgeon in which case the drug loading can be controlled, or they can be bought prefabricated [32]. Some spacers articulate generally with a metallic support, or are fixed in position confining many patients to bed [33]. The use of handmade and non articulating spacers can lead to dislocation [29], while the limited mechanical strength of PMMA can lead to fracture [29]. Further challenges with PMMA as a material are discussed later in section 1.9.1.

Given the challenges with the two stage revision in terms of multiple surgeries and limited weight bearing properties, there is a clinical need for a new hip implant that can clear the infection while providing sufficient mechanical support to be used as a permanent implant to remove the need for a second surgery and the bed rest while the spacer is present. This implant would control the antibiotic release to provide the optimal release profile for the antibiotics chosen.

Spinal Fusion Cages to Promote Bone Ingrowth

Spinal fusion cages are used to provide mechanical support between vertebrae in the spine and prevent non union when two or more vertebrae are being fused together [34, 35]. Fusion is generally performed due to degradation of the cartilage between vertebrae, often caused by degenerative disc disease [36] leading to pain which is the main presenting symptom [37]. Other causes include fracture of the spine and scoliosis [35]. In the USA 4-500,000 spinal fusion procedures are performed each year [34, 38]. However success is not consistent and failures including non union can present in up to 45% of cases [34].

Spinal cages generally consist of a hard structure with an internal void which can be packed with bone graft material. The structure provides mechanical support and stability while osseointegration occurs [39], while the bone graft promotes bony fusion [39]. Prior to the widespread introduction of cages, bone grafts were used without support which often led to the collapse or fragmentation of the bone grafts resulting in the need for

reoperation [35]. The material used for bone grafts can be autographs from the patient's own body, however this requires a second surgery site and limits the quantity of bone available [35]. Alternatively allografts from cadavers can be used which provide larger quantities of material without the need for additional surgery sites. These materials do require sterilisation, which can damage the tissues and carry a risk of disease transmission [38].

Alternatives to bone grafts include scaffolds, ceramics or demineralised bone matrices which can all be loaded into spinal cages. Scaffold can be used to deliver growth factors to promote bone formation, while being osteoconductive themselves. Examples of materials include collagen, ceramics and polymers [34, 39]. Demineralised bone matrices are organic scaffolds of proteins and growth factors. They are derived from bone that is demineralised using acid. This process reduces the mechanical properties, which can lead to collapse, and there is a risk of disease transfer due to the allogenic bone source [40].

Bone graft substitutes can be used with osteoinductive supplements to optimise fusion rates. Growth factors such as transforming growth factor-beta (TGF-β), and vascular endothelial growth factor (VEGF) activate osteoblasts and fibroblasts [34, 39]. While bone morphogenetic proteins enhance osteogenesis and osteoinduction [34, 40, 41]. Mesenchymal stem cells can differentiate into osteoblasts and chodrocytes in order to promote fusion [35, 38]. Alternatively, synthetic peptides rather than natural proteins can be used [38]. Finally, instead of releasing growth factors from the implant, the body's cells can be targeted to produce more growth factors using gene therapy however this can be difficult to measure *in vivo* [34].

The use of spinal cages is not without challenges, some of which overlap with those of hip replacements such as stress shielding [39] and infection [41, 42]. Other challenges are more specific to fusion surgery, such as radiographical artefacts [39] and loss of motion in the spine [36]. Rates of infection are higher in spinal surgery at around 5% [43] than in hip replacements ($\sim$ 1%) [9]. This leads to a greater need for imaging of the implant site which can be challenging as metallic cages give artefacts on X-ray, CT and MRI

radiographs [39].

Despite continuous improvements in spinal cage design over the last 30 years, failures occur in more than 10% of cases [39]. New research is working to overcome some of the challenges discussed above. The use of additively manufactured lattice structures has enabled the mechanical properties of the cage to be manipulated to reduce the risks of stress shielding [39]. This effect has also been achieved by switching from titanium to polyetheretherketone (PEEK) a polymer which is radiolucent and with a lower elastic modulus than titanium [35, 38]. However no statistical differences in clinical outcomes between PEEK and titanium cages were found [38], and PEEK cages have been found to suffer from migration, subsidence and lack of fusion in some cases [38]. Coatings have been explored to provide local drug delivery including antibiotics to reduce the infection risk and growth factors to increase osteogenesis [35, 39]. Expandable devices have been explored to improve primary fixation and have been shown to reduce subsidence [44].

Spinal cage failure due to non union is a common problem, the use of lattices as a large surface area for the immobilisation of a bone ingrowth promoting coating would enable prolonged ossification. Meanwhile the lattice could provide mechanical support, tailored stiffness to reduce stress shielding, and a reduced volume to minimise radiographical artefacts.

1.2 Infection in Bone Implants

Infection is a leading cause of failure in bone implants for fracture repair, where it is listed as the cause in 20% of failures [45], however this can rise to as high as 33% in open fractures [46]. The infection rate for spinal surgery is around 4% [47, 48], however the use of hardware such as spinal fusion cages leads to a higher incidence of infection [49, 50]. The infection rate for cranial surgery is around 16% [51]. For cancer survivors there is a 5-13% infection rate after reconstruction which can lead to amputation [52], rising to 43% if a revision is required [53]. As previously noted, for spinal surgery the presence of

implants increases the infection rate, however the use of an implant can rarely be avoided [46].

The most commonly found bacteria in bone implant infections are from the *Staphylococcus genus* which are gram positive bacteria and are found in around 60% of infection [20, 54]. Other gram positive bacteria found in these infections include *Enterococcus* ($\sim$ 7%), and bacteria from the *Streptococcus genus* ($\sim$ 6%) [20, 54]. *Enterobacteriaceae* is the most commonly found gram negative bacteria, while *Escherichia coli* and bacteria from the *Pseudomonas genus* are also found [20, 55, 56].

Infections are classified into early infections which occur during the first three months, and where the microorganisms enter during the surgery or wound, or late infections where the infection enters the body through an alternative route such as a dental procedure or new wound [57]. Early infections often lead to complications with wound healing, and are predominately caused by highly virulent bacteria [58]. Between 3 and 24 months low virulent bacteria can lead to delayed low grade infections which can be hard to identify due to the non specific symptoms of implant loosening and joint pain [58]. Late infections after 24 months can have almost any microorganism present as these enter by an alternative route [57].

The implantation of hardware during surgery leads to an increased risk of infection [46]. This is in part because the implant interferes with the local tissues leading to local inflammation and immunosuppression [59]. Once bacteria are present on the implant surface they colonise, forming biofilms surrounded by extra polysaccharide substances (EPS) which enables colony binding, nutrient and waste movement, protection and signalling [60]. The presence of the biofilm reduces the potency of antibiotics due to the biofilm preventing the antibiotics penetrating into the colony, substances within the biofilm inhibiting the antibiotic activity and slower rates of growth of bacteria within the biofilm [61]. Additional challenges with the presence of biofilms include chronic inflammation caused by repeated attempts to treat the infection, and the presence of a large quantity of bacteria which can shed bacteria into the body [62].

In early stage infections the pathogens are already on the surface of the implant during implantation, or move from the patients skin to the implant through the wound [59, 60]. However for late stage infections opportunistic pathogens migrate to the implant surface where they transform into virulent forms [59]. How and why the bacteria migrate is not fully understood. It is known that bacteria prefer to grow on surfaces than in solution and they may be attracted to the implant surface by chemotaxis or haptotaxis (concentration gradients of chemoattractants) [63]. Alternatively, they may migrate using blood cells as vectors, especially immune cells [64].

1.3 Antibiotics

Antibiotics are used to treat bacterial infections. Different antibiotics have different pharmacokinetic properties which can be categorised as time-dependent where more virulent strains require a longer time to kill, concentration-dependent where a higher drug concentration is required, or those which experience persistent effects where bacteria growth is suppressed after antibiotic exposure [65]. Antibiotics are then classified into three categories, type I antibiotics are concentration dependent and experience prolonged persistent effects [66]. Aminoglycosides such as gentamicin sulphate are type I, the best loading regime maximises concentration to hasten bacteria death [67]. A peak concentration 8-10 times higher than the minimum inhibitory concentration (MIC) is beneficial to reduce the risk of antibiotic resistance [67]. Type II antibiotics such as penicillin have time-dependent pharmacokinetics with little persistent effects [68], so maximising the time that the drug concentration is above the MIC with a continuous release is ideal [68]. Vancomycin is a type III antibiotic which means it has time-dependent killing and moderate persistent effects [69]. Maximising the amount of antibiotic eluted leads to ideal bacterial kill [70]. As it can be seen it is important to control the release profile to maximise the bacteria killed and to prevent antibiotic resistance, and different antibiotics suit different approaches to release.

Antibiotic resistance occurs when bacteria are resistant to the effects of one or more antibiotics. Resistance can be divided into natural resistance which occurs inherently in some bacteria without the presence of an antibiotic, and acquired resistance which is induced by the selection pressure of the presence of low levels of antibiotics [71]. Bacteria can also develop resistance from horizontal gene transfer from other bacteria [72].

The over use of antibiotics in healthcare and farming practices has led to high levels of subtherapeutic doses which create these selection pressures, and have been linked to new antibiotic resistance cases [73]. In order to reduce the risk of a future where routine surgery is fatal due to a lack of antibiotics, more antibiotics need to be developed, and over prescription of antibiotics for viral infection must stop. The practice of using antibiotics to prevent livestock infections, and promote faster growth must cease. Additionally where antibiotics are added to implants it is important to control the kinetic profile in order to achieve the optimum dosing strategy and prevent subtherapeutic levels in the surrounding tissues.

Not all antibiotics are suitable for use in infection treating implants. The ideal antibiotic is broad ranging, working against gram positive and negative bacteria, as the microorganisms present in an infection site are generally not known until surgical incision at the implant site, at which point immediate antibiotic delivery is desired rather than waiting for bacteria culture to occur [74]. Last resort antibiotics should be avoided to reduce the risk of resistance occurring.

The most commonly used antibiotic in hip replacements in the United States and the Netherlands is gentamicin which is sometimes used in combination with another antibiotic such as clindamycin or vancomycin [75, 76], elsewhere in Europe cefazoline is most commonly used [77, 78]. These are chosen due to their broad spectra of activity and synergistic properties [76, 79]. Gentamicin and vancomycin are thermally stable and so are regularly used in PMMA spacers which set exothermically [76].

Gentamicin sulphate is an aminoglycoside that works against gram negative, and aerobic bacteria [80]. It was first approved for use in 1969 which means that it is now out

of patent and generics can be made at low costs [81, 82]. Gentamicin sulphate works by inhibiting bacterial protein synthesis [83]. This makes gentamicin sulphate an appropriate antibiotic to use in this research.

1.4 Bone Growth

Cementless implant fixation and spinal fusion both rely on bone growth for long term stability. Osteogenesis, the process of bone formation, occurs through a cascade. This starts with inflammation triggered by blood reaching the implant surface, then signalling molecules such as growth factors are released [84]. The formation of a hematoma follows [15] which then turns into a callus [85] which subsequently hardens by ossification [15].

Osteoinduction follows ossification, which is the chemotaxis and mitosis of mesenchymal cells [86], which differentiate into osteoblasts [85].Angiogenesis is the formation of vasculature [87], which is followed by osteoconduction, ingrowth into host bone [38, 87]. Finally the callus remodels into bone under mechanical load [15].

1.5 Growth Factors

Growth factors are proteins for signalling and regulation of cells [86]. They are heavily involved in bone growth [88], however they are not specific, therefore affecting multiple cells and eliciting different responses from each [86]. This has some disadvantages, for example systemic delivery of growth factors can lead to cells in a different region of the body being affected, such as proteolytic degradation in the gastrointestinal tract [89]. An additional challenge with oral delivery of systemic growth factors is bolus release reaching toxic levels, and tends to come with a burst release [89]. Growth factors signal cells by binding to the cell's receptors, which induces a ligand receptor response and then signals the nucleus [86]. Some cells require multiple growth factors before they will respond, for example the process of osteoinduction [86].

It is important to get the release of growth factors right because some such as bone

morphogenic protein (BMP) can induce osteoclasts, which cause bone degradation [90]. Some growth factors are only present early in the bone growth cascade while others have a prolonged presence [89]. Appropriate release for each growth factor, and the correct combinations are necessary, however not all growth factors have approval for implant loading applications [85].

The incorporation of growth factors in polymer coatings, for example by electrospinning, often leads to rapid release within a couple of days [89]. This is acceptable for growth factors present at early stages of the bone growth cascade but unsuitable for those with a more prolonged presence. Immobilization of growth factors onto polymer (or alternative) surfaces enables prolonged bioactivity [91]. Growth factors are not impaired by immobilisation [92] and it prevents their internalisation [93]. Some immobilisation techniques enable control of the orientation of the growth factor which can improve its effects [94]. However immobilisation is only appropriate if the growth factor effect is needed in the local vicinity of the implant and not in the surrounding tissues [95].

1.6 Additive Manufacturing of Medical Devices

The majority of metal bone implants are manufactured by casting and machining, however additive manufacturing (AM) is increasingly being introduced as a manufacturing method [1]. This process starts with computer aided design (CAD) modelling of the implant design, this is then exported into a format that can be interpreted by the printer, often in a sliced format. This is then loaded onto the printer where the print is produced before part removal and post processing are performed [96, 97].

A number of different AM techniques are available to manufacture metal parts, these include binder jetting, powder bed fusion, direct energy deposition and sheet lamination [96, 98]. Most of these processes use metal powder as the feedstock, while sheet lamination uses metallic sheets. The power sources used are laser beams, electron beams or thermal energy [98]. For medical device applications powder bed fusion is most commonly used

[99, 100], which includes laser powder bed fusion (L-PBF) and electron beam melting (EBM) [98]. These methods use a powder bed built up in layers which is melted in specific locations using a laser or electron beam in an inert atmosphere in order to build up the part (figure 1.2) [96, 98].

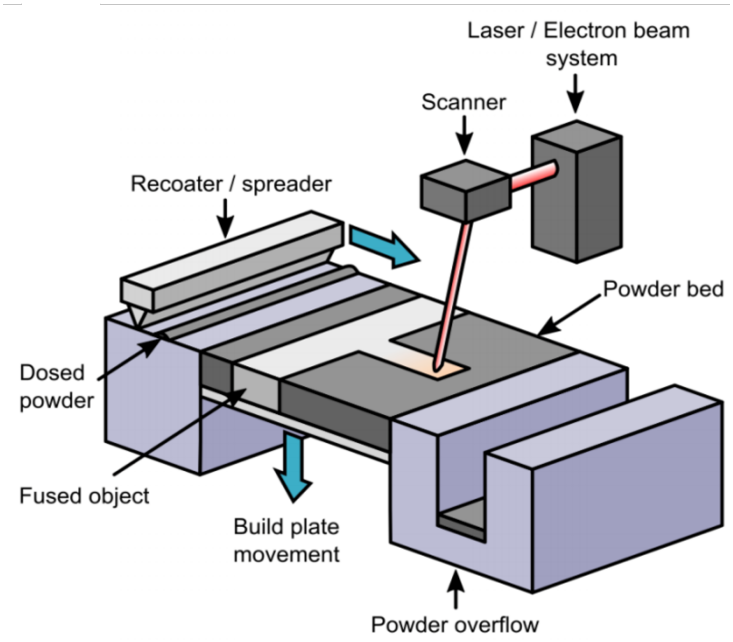

Figure 1.2: Schematic showing the principles of powder bed fusion additive manufacturing. Dosed powder is spread across the build substrate and the part is fused by a laser or electron beam. The build plate then lowers, and another layer of powder is spread, followed by scanning of the next layer which fuses both within the layer and to the layers below. Adapted from [101]

Although L-PBF and EBM are similar processes there are some differences between them. EBM must be carried out in a vacuum as a gaseous atmosphere attenuates the electron beam, decreasing power, beam control and accuracy, while L-PBF is carried out in an inert atmosphere to prevent oxidation which is less energy intensive [100]. For both processes the powder bed is heated to reduce residual stresses, however in EBM it is heated sufficiently that partial powder adhesion occurs which forms a cake with the part inside it. This makes part removal more challenging and does not allow immediate powder recycling, which is possible with some L-PBF systems [102]. This cake does provide some support, reducing the quantity of support structures needed for EBM parts. However the longer cooling time necessary for these parts results in larger crystals and therefore

a coarser microstructure and rougher surface finish [100]. Additionally the larger layer height, beam width and powder diameters can add to the increased surface roughness of EBM parts. The choice of metals which can be manufactured using EBM is limited to those that are conductive [102], while highly reflective metals such as silver are challenging to manufacture by L-PBF [103].

Despite being a relative new technology, devices manufactured using AM have been approved by regulators and are available for implantation. These include acetabular cups and femoral stems of hip replacements, tibial plates of knee replacements, and fusion cages for ankles, hips and spines [104]. All of these use additive manufacturing to create a porous surface to improve fixation and enable osseointegration. In addition for the fusion devices the reduced density enables a reduction in radiographic artefacts [104].

Laser powder bed fusion brings a number of benefits over conventional manufacturing techniques. These are customisation, including the ability to create patient specific implants [105], shorter lead times [106], and the ability to produce low volumes at no extra cost [107]. The material wastage is often lower as the excess powder can be recycled, although robust quality control is needed to reduce risks associated with reuse [106, 108]. The design flexibility is substantially larger than conventional techniques, which enables the manufacture of complex shapes such as lattices, as well as designs with solid and porous features [4, 109, 110].

However L-PBF is not without challenges. Some of these are to do with the build process which can introduce porosity into the parts [96], as well as thermal stresses [111], and a rough surface due to semi sintered particles [112, 113]. Additionally, work is still ongoing to check the repeatability [98], cleaning and sterilisation processes necessary for complex parts [114].

Currently AM parts have reduced wear properties and fatigue life compared to implants manufactured by conventional techniques [115, 116, 117]. Although L-PBF offers a lot of design freedom, there are still some limitations on what can be built. These include overhanging angles, which are machine and feature size dependent but in the range of

15 to 45° [118, 119], as well as resolution and minimum feature sizes, which tend to be around 150 μm [120, 121, 122].

Stainless steel, cobalt chrome and Ti-6Al-4V are the most commonly used metals for additively manufactured bone implants [111]. Stainless steel is regularly used for bone implants including those manufactured using AM. It has a high corrosion resistance, good mechanical properties and is biocompatible; however, it can release chromium and nickel [123]. Cobalt chrome has been regularly used for dentistry and wear surfaces in joint replacements as it is hard and wear resistant. However if it is subject to ion release due to corrosion or wear, then the ions can lead to adverse reactions in the body [12].

Titanium alloys, specifically Ti-6Al-4V have been extensively investigated in L-PBF, due to their use in aerospace applications [124]. Ti-6Al-4V is a titanium alloy containing 6% aluminium and 4% vanadium, the material is biocompatible and corrosion resistant [123]. The presence of aluminium and vanadium in the alloy allow the α and β phases of the crystal structure to be stabilised and manipulated to change the mechanical properties [124]. However these metals are not desirable if they leach into the body so some alternative alloys with different α and β stabilisers have been researched including niobium, zirconium and tin [123]. Due to the abundant research on Ti-6Al-4V it was used for this work to enable comparison with the existing literature. The development of a novel material was beyond the scope of this research.

The Regulation of Additively Manufactured Medical Devices

Medical devices require approval from regulators before they can be sold. Different markets have different regulators for example the regulator for the USA is the Food and Drug Administration (FDA) [125], while in the European Union the European Medicines Agency [126] is involved in the regulatory process as well as individual country regulators. The UK regulator is the Medicines and Healthcare Products Regulatory Agency [127], while in China medical devices are regulated by the National Medical Product Administration [128].

Each agency has a different process, and approval is only for a specific market, although many regulatory bodies have a lower threshold for authorisation in their country if a medical device has already been authorised elsewhere. Medical devices are generally classified based on risk, examples of low risk devices include wheelchairs and glasses, while high risk devices include pacemakers and heart valves. Higher risk devices are subject to more stringent regulatory controls [129].

The regulations lay out a number of requirement that must be met such as the performance of the device, labelling, packaging and information provided with the device, and post market surveillance. The medical device company must also specify how the device will be manufactured and sterilised, as well as providing clinical data including reporting side effects [129].

The International Organization for Standardization (ISO) and ASTM International provide standards in order to standardise processes across the industry. There are standards for testing for example ISO 13314:2011 'Compression test for porous and cellular metals'. For loading requirements ISO 7206-6:13 specifies the loading requirements for partial and total hip joint prostheses, while ISO 12189:2008 specifies these for implantable spinal devices. There are also standards for materials, such as Ti-6Al-4V for additive manufacturing ASTM F3001-14. Lots of medical devices have their own standards such as hip replacements: ISO 21535:2023 and spinal fusion cages ASTM F2077-22. Additive manufacturing has standards including for vocabulary ISO/ASTM 52900:2021, and for validation of the production process ASTM F3604-23, as well as for validating the cleaning of medical devices ASTM F3127-22. It is important to understand which standards are regulations are relevant to the medical device being developed and follow them, or document why a deviation from the standard has occurred.

1.7 The Use of Lattices in Medical Devices

One of the ways metal additive manufacturing can be used to add value is through the use of porous lattice structures that are hard to manufacture through conventional implant manufacturing techniques. A lattice is a cellular structure made of solid material interspersed with pores. This can have either an open (figure 1.3a) or closed cell structure (figure 1.3b) depending on whether the pores are interconnected with the outside of the structure [130]. Open cell lattices are predominantly used for medical applications, as there are no internal voids to trap powder when manufactured by powder bed fusion techniques [131]. They also result in a less rigid structure which is favourable for osseointegration, vascularisation, and reducing the effects of stress shielding [132].

If the structure has a repeating design then it can be called reticulated (figure 1.3a), while those with a random design are stochastic (figure 1.3c) [109]. Stochastic structures are often heterogeneous which makes predicting the mechanical behaviour challenging, and do not necessarily meet the design limitations of the printing process, so reticulating lattices are more commonly used for implants [133, 134]. Reticulated lattices can be based on a surface (figure 1.3d) or strut (figure 1.3a) based repeating unit called a unit cell [135]. Examples of strut based lattices include those based on crystal structures such as body centre cubic (BCC) and diamond, while surface lattices include gyroid and Neovius sheet [136]. Strut based lattices can be divided into bend and stretch dominated structures based on Maxwell's stability criterion, which provides some insight into the expected failure mechanisms [137].

By changing the lattice parameters the mechanical properties of the structures can be manipulated. Lattice parameters include strut thickness, the diameter of the struts; wall thickness, the thickness of the walls of surface based lattices; volume fraction, the percentage of the overall shape that is occupied by the lattice; porosity, the percentage occupied by the voids, the volume fraction and porosity should sum to 100%; relative density has the same value as volume fraction but is calculated by dividing the density of the lattice by the density of the reference material the lattice is made of; unit cell length,

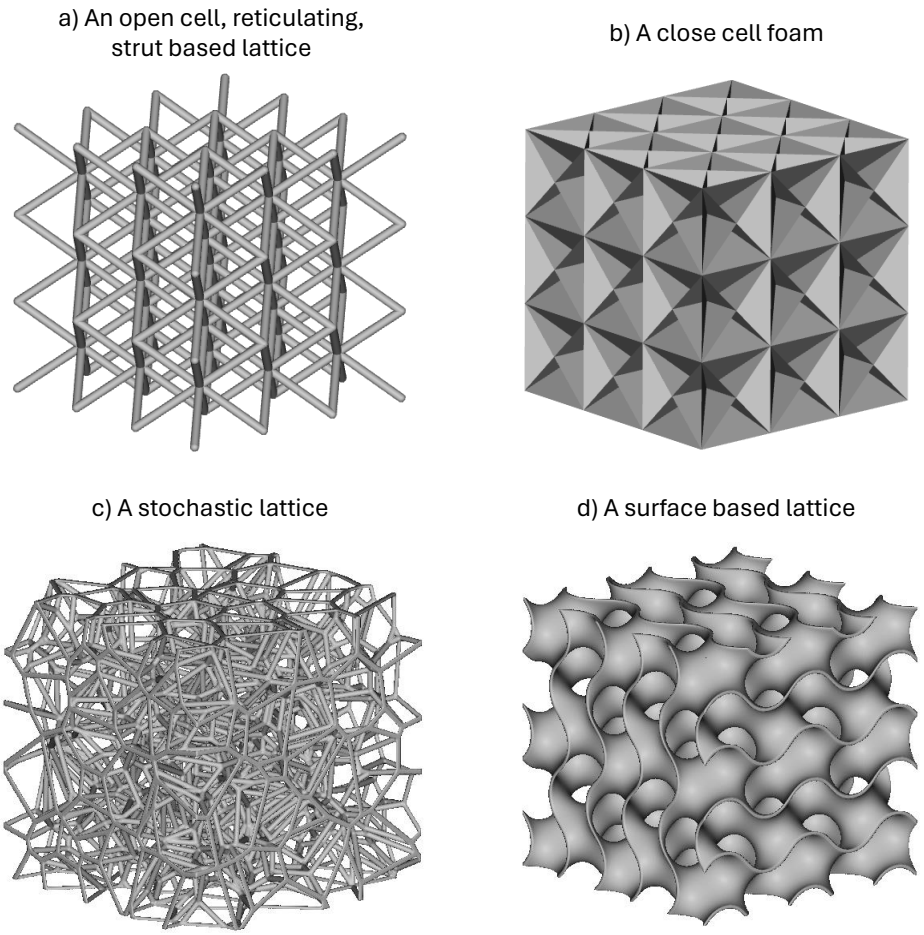

Figure 1.3: Examples of lattices to show comparison between a) open and b) closed cell structures, a) reticulated and c) stochastic lattices, and a) strut based and d) surface based lattices

this is the side length of the unit cell if it is cubic.

Different unit cell designs offer distinct mechanical properties, for example the surface based lattices have more isotropic compression behaviour than some of the strut based lattices including the BCCZ lattice which is modelled on the body centred cubic crystal structure with additional vertical struts [138, 139]. Increasing the strut or wall thickness of lattices increases the strength and stiffness [140, 141]. While increasing the volume fraction has the same effect [142, 143]. Decreasing the unit cell size increases the strength when the strut thickness is kept the same [144, 145], or when the volume fraction is kept constant [146, 147]. Volume fraction, unit cell size and strut or wall thickness are not independent. If two are changed then the other is defined from those. Processing

parameters such as laser power and dwell time can influence the mechanical properties and change the build quality, for example by reducing the porosity within the struts [148, 149].

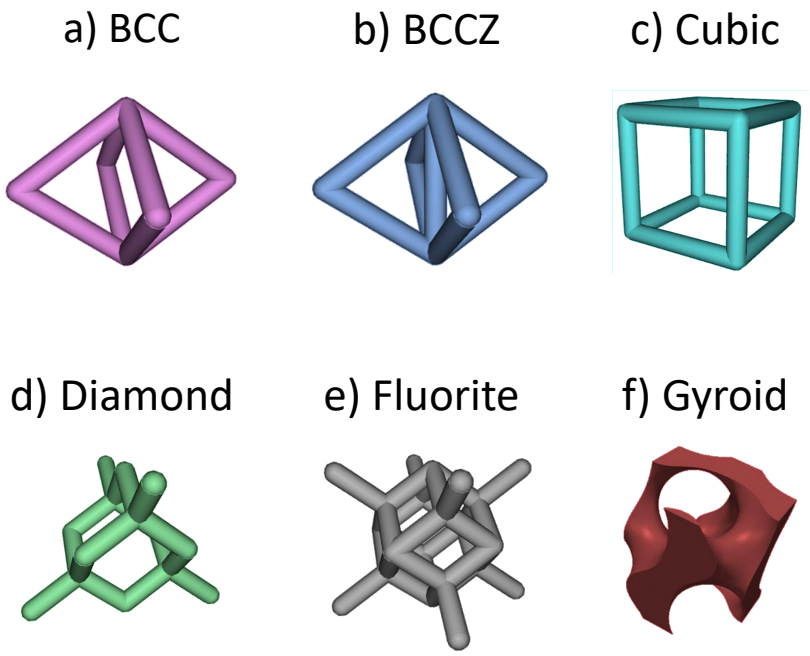

Figure 1.4: CAD of the unit cells used in this work. a) BCC, b) BCCZ, c) cubic, d) diamond, e) fluorite, f) gyroid

The unit cells used in this work were BCC, BCCZ, cubic, diamond, fluorite and gyroid these can be seen in figure 1.4. BCC lattices are based off the body centred cubic crystal structure which is a form of crystal packing where nine atoms are packed in a cube with eight atoms at the corners and one in the centre, this is the form iron takes at room temperature. This can be used as a lattice structure with struts joining the central atom (node in the lattice) to each of the atoms on the cube corners (figure 1.4a). It is shown here transposed 50% higher with the nodes that form the central atom in the crystal structure at the top and bottom rather than in the centre.

BCCZ lattices are BCC lattices with an additional vertical strut (figure 1.4b). Cubic lattices have struts joining the corners of a cube orthogonally (figure 1.4c). Figure 1.4d shows a diamond unit cell, which is constructed of 16 struts, and based on the diamond cubic crystal structure which was first discovered in carbon. If this unit cell is formed of

two mirrored diamond unit cells, and forms a rhombic dodecahedron (figure 1.4e).

The last unit cell used in this work is the surface based gyroid (figure 1.4f). This is a triply periodic minimal surfaces which was discovered by NASA in the 1970s [150]. Gyroid structures have two forms, in the sheet gyroid form the structure has two domains (intertwined regions that do not intersect), while in the skeletal form one of the domains is solid [151]. The skeletal form is used in this work as it allows the wall thickness to be manipulated.

Lattice Applications

Some of the main reasons for using lattices for bone implants include osseointegration for fixation, drug release, decreased radiographic artefacts and alleviating stress shielding. Lattices have been explored as drug delivery vehicles with the therapeutic loaded into either a coating or in a delivery vehicle in the lattice voids. For delivery from coatings the lattice provides a larger surface area than solid implants, providing the possibility of greater drug loading, and faster delivery [152, 153, 154]. While for bulk delivery the lattice provides mechanical support with space for the drug loaded biomaterial [155, 156, 157].

Metallic implants can produce signal artefacts in MRI, CT and X-ray images. In CT and X-ray images this is mainly due to the X-rays becoming attenuated by the metal in the beam path [158]. While in MRI imaging the artefacts are introduced by interference with the magnetic field [159]. Replacing solid implants with lattices reduces the overall volume of metal which reduces the artefacts in both cases. Stress shielding occurs when a bone is insufficiently loaded, generally due to the loading being bypassed by a stiff implant. This can lead to bone resorption followed by implant loosening [14]. Lattices can be used to alleviate stress shielding by reducing the stiffness of the implant [160].

There has been a decline in cemented hip replacements over the last twenty years, replaced by designs using push fit with osseintegration [9]. Spinal fusion cages are cementless with mechanical fixation and osseointegration, while cement is only used as a

spacer when a vertebrae requires removal [161]. Implant loosening is the largest cause of failure in hip replacements (cemented and uncemented) in the UK [9], while implant migration in spinal fusion surgery reduces the chances of a successful fusion [162], so designs which improve implant fixation are needed.

Osseointegration (or osteointegration) is said to have occurred when there is direct contact between the bone and the implant, that is mechanically stable and forms a structural and functional connection [84]. A number of factors related to implant geometry influence osseointegration. These include the size of the pores within the structure although there is little consensus as to what the best size is with anything from 100 to 1000 μm quoted [163, 164, 165, 166]. The interconnectedness of the pores influences the availability of vascularisation, gas exchange, and movement of nutrients and waste [166, 167, 168]. While pores with a structured arrangement such as in a reticulating lattice design provide better osseointegration than those which are tortuous, while tight pores tend to end up occluded [163, 169, 170]. Some degree of roughness is beneficial [84, 171], while the implant must not be too far from the bone initially with the limit around 2 mm [172, 173, 174]. Implant motion disrupts osseointegration although below 150 μm bone growth can still occur [175, 176]. The implant material needs to be biocompatible or coated in a material that is biocompatible [84], additionally it can be coated in pharmacological agents such as growth factors to increase the likelihood of successful osseointegration [84].

1.7.1 Manufacturing Limitations and Defects

Build Limitations of Lattices

One of the limitations of printing lattices is the minimum strut or wall thickness. This is influenced by the powder size and processing parameters which both influence the melt pool size [118]. Generally the limit of Ti-6Al-4V specimens printed using L-PBF is 150 μm [118, 120, 121]. However Van Bael et al were able to print struts with a 112 μm diameter using a custom printer [177]. Although design guides for L-PBF suggest not building struts closer to horizontal than 45° [119] a number of researchers have successfully built

horizontal struts [178, 179]. Changing the build angle of struts leads to differences in strut thickness. Struts closer to horizontal overbuild due to a lack of strut below for heat to dissipate into, so the heat radiates into the surrounding powder causing additional powder to melt increasing the strut size. While struts closer to vertical have sections of strut below which the heat can be transferred into [118, 180, 181].

Dimensional Inaccuracies of Printed Lattices

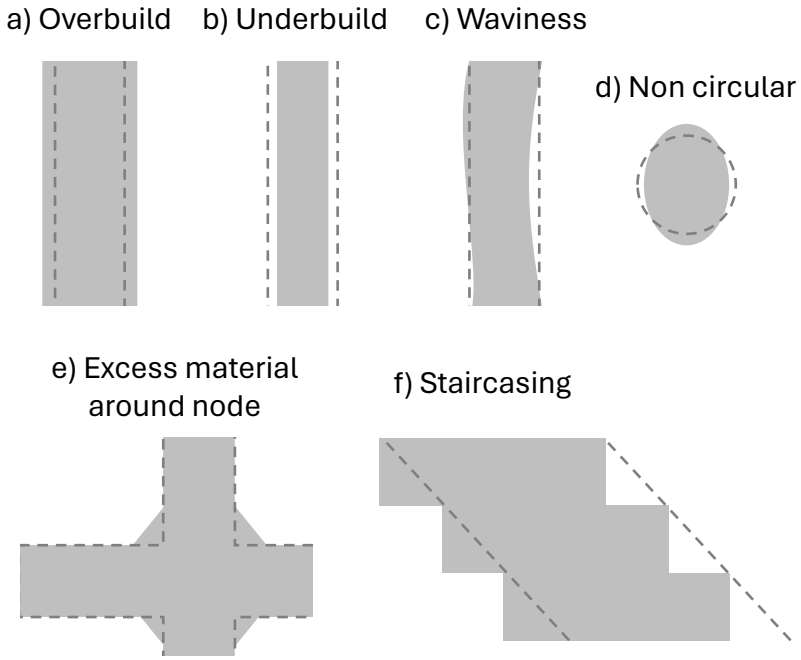

Figure 1.5: Illustration of types of dimensional inaccuracy in lattices, where the grey shading shows the as built part and the dashed line indicates the design. a) overbuilt strut, b) underbuilt strut, c) strut exhibiting waviness, d) strut with a non circular cross section, e) strut with an inconsistent thickness along its length, specifically with excess material around the node, f) the staircasing effect

Although it would be ideal if the specimens printed as designed in CAD that is not the case. One of the ways that geometric inaccuracies can occur is with strut or wall thickness, these could be overbuilt or underbuilt. Processing parameters can lead to these changes as they influence the melt pool size, however this generally occurs in a repeatable way so can be designed around [118, 177, 182]. The variations in thickness can also be influenced by the angles of the struts, and this can influence the failure mechanisms [118,

177, 183].

Not all struts build in a circular cross section as designed, this can be referred to as cross section eccentricity or strut thickness variation although that can also include variation in thickness with length [183]. This most often takes the form of elliptical struts with the elongation in the vertical direction [184]. This effect has been attributed to staircasing [184], heat transfer [180, 184], and large unsupported overhangs, leading to a large melt pool size causing additional particle adhesion and gravitational effect [122]. The effect is more pronounced for struts closer to horizontal with no effect seen in vertical struts [184]. Non circular struts contributed to lattices with lower strength and stiffness [183, 185]. This is thought to be due to local heterogeneities leading to stress concentrations [177, 186].

The strut thickness may not be uniform along the length of struts, this most commonly appears as excess material at the end of struts around the nodes [180, 187]. This can be caused by additional scan paths at nodes which can lead to excess energy which radiates into the surrounding powder, resulting in additional powder melting onto the lattice in that region [188]. When struts are at angles the additional material will not be evenly distributed around the nodes due to the layer by layer nature of the build process and gravitational effects, this can lead to offset junction centres which introduce bending loads altering the failure mechanisms [185].

Strut waviness is where the centre axis of the built strut differs from the design, it can also be referred to as a misaligned strut or with a centre offset [183]. This is thought to be caused by heat transfer and gravitational effects [189] or staircasing in 45° struts [177]. Dallago et al found strut waviness caused a drop in stiffness and strength, probably due to the introduction of bending loads [185]. Computational modelling by Lozanovski et al showed different deformation behaviour of face centre cubic lattices when strut waviness was present [186]. L-PBF printed ASi10Mg lattices showed greater waviness on horizontal than diagonal struts [183]. It was found that strut waviness had a larger impact on stiffness than non circular struts but the opposite was true for strength.

Material accumulations called protrusions can be found at apparently random locations on parts [190, 191]. These are solidified material that is larger than powder particles, and is thought to be caused by splashes or balling [189], or by liquid metal failing to adhere to the previous layer and peeling away [192]. It is more common on horizontal and overhanging surfaces due to the lack of a previous layer to attach to [185, 193].

Lattice Surface Quality

The quality of the surfaces of as built lattices can be influenced by powder adhesion, this is not uniform across the surfaces, nor within the build chamber. Powder particles used in AM are not a uniform size, with diameters spread over a size range, and the recoater arm moves more coarse particles to the front of the chamber [194]. There is also an air flow across the chamber which moves spatter material [194, 195, 196, 197]. Additionally in some machines the distance to the laser may influence the roughness [193]. All these effects are machine specific and so must be understood prior to printing. Additionally care must be taken to position parts in the optimal locations in the build chamber to reduce the effects of these potential sources of defects.

The geometry of the parts can influence the particle adhesion with upward facing surfaces displaying less particle adhesion than downward facing surfaces due to the presence of previous powder layers on downward facing surfaces, and the lack of previous build layers to dissipate the laser energy [198]. The angle of downward faces also influences powder adhesion with shallow angles experiencing increased roughness due to staircasing [120]. Thicker struts also lead to increased particle adhesion due to a build up of laser energy required to build them [120].

Surface cracks can also reduce the lattice surface quality, these form during the cycles of rapid melting and cooling that AM parts undergo. These thermal cycles cause residual stresses which initiate cracks from the edge of the parts [111, 199]. The staircase effect is caused by lattice builds progressing in discrete layers, this causes ridges of one layer thickness to develop in angled faces or struts [149, 200, 201]. This can lead to additional

powder adhesion when parts are built at a low angle as there is only a small contact area between each layer for heat to dissipate to the previous layer, so heat radiates to the surrounding particles causing partial melting and attachment of these particles [120].

Types of Lattice Porosity

Unintentional porosity in the parts comes from three main sources, pores which originate in the feedstock powder, lack of fusion and keyholing. The powder feedstock may contain pores due to the gas atomisation process often used to generate the powder, these holes are generally in the size range of the powder particles [104, 136, 202]. If the processing parameters are not correct, for example the laser power is too low, the scan speed is too high or the layer height is too large, then insufficient laser power is provided to the particles to fully melt them resulting in a lack of fusion [136]. This can lead to unmelted powder and pores within the structure, this leads to poor fatigue life and can often be seen on the surfaces of fatigue cracks [104]. If, however, too much laser energy is provided then vapourisation of the metal powder can occur, which forms an unstable vapour cavity which collapses, leaving a pore called a keyhole [136]. Keyholing is characterised by an vertical elongated pore in a V-shape, which contains a different microstructure [104].

1.7.2 Post Processing of Lattices

Given the multitude of potential flaws in lattices produced by L-PBF, methods are needed to non destructively detect and repair these defects. Additionally L-PBF leads to a rough surface finish and a mixture of loose and semi sintered particles within the structure. It is important that all loose particles and those that may become loose are removed during post processing to prevent loose particles entering the body upon implantation.

The powder removal process can be performed using a number of different techniques including sand blasting, chemical or ultrasonic baths, and plasma boiling [203]. Grit blasting is a commonly used technique but the success of this approach is dependent on the size of the voids in the structure, with larger voids more readily cleared [203].

As well as powder removal, medical devices must be cleaned to remove residues [204]. Ultrasonic cleaning is most commonly performed, this can be in conjunction with solvents to remove surface contaminants that are solvent in the particular solvent used, for example alcohols [205].

All implanted medical devices must be sterile. A number of techniques are used to sterilise metal implants these generally fall into three categories; heat for example using an autoclave, chemical such as ozone, and radiation such as gamma irradiation [206]. Care must be taken to choose a method that is appropriate for the implant used, for example direct methods such as UV light cannot be used on lattice structures with hidden faces. Additionally chemical methods may not reach all surfaces in a lattice structure if air become entrapped in the structure.

Removal of powder, cleaning and sterilisation must be validated to ensure consistent results and to prevent adverse effects due to contaminants [204, 207]. Visual inspection can be used if lattice structures allow full thickness light penetration, the occlusion area can be used to semi quantitatively measure the degree of contamination [204]. X-ray fluorescence (XRF) and micro-computed tomography (microCT) are spectroscopy tools that enable a non-destructive visualisation of the internal structures to be viewed, however there is a trade off between the size of the part, the size of the defects detectable (resolution) and the speed of the process. With larger parts at higher resolution taking longer to scan [208].

Additional post processing can be performed to change the surface roughness for example by acid etching, or to change the geometry such as through machining [209]. Thermal stresses within the structures caused by the rapid cooling of the structures during printing can be alleviated by heat treatment however this process can semi sinter further loose powder to the surface making removal more challenging so the order of post processing must be considered [203]. Alternatively hot isostatic pressing can be performed which can alleviate thermal stresses and has also been shown to reduce the size or remove entirely defects in L-PBF parts [210].

As it can be seen there are a large number of post processing techniques that can be used to change the properties of additively manufactured parts. Each of these techniques requires optimisation and validation prior to use. For this work loose powder was removed with water jetting, and the samples were cut from the build plate using an electron discharge machine, but no further post processing was undertaken.

1.7.3 Compression Testing of Lattices

Given hip replacements and spinal fusion cages are weight bearing implants it is important to determine the compressive strength of lattices used for these functions. As these lattices will provide void space for therapeutics the strength will be compared against the volume fraction of the lattices. Additionally it is known that stress shielding can lead to implant loosening, which is the largest cause of failure in hip replacements [9], and a substantial cause of lack of fusion in spinal cages [162], so determining the stiffness of the lattices could be used to reduce the stress shielding of future implants. Compression testing is routinely performed on lattices to check whether they provide sufficient strength to enable patients to weight bear, while having a modulus of elasticity in the range of bone [211, 212].

Researchers have successfully manufactured Ti-6Al-4V lattices using L-PBF, which have greater strength than cortical bone ($\sim$ 200 MPa [213, 214, 215]), and stiffness in the region of that of cortical bone ($\sim$ 17 GPa [213, 214]). For example, cubic lattices with a unit cell length of 3 mm and strut thickness of 1.1 mm had a strength of 203 $\pm$ 50 MPa and a stiffness of 7.2 $\pm$ 0.5 GPa [145]. BCC lattices with a unit cell length of 2 mm, strut thickness of 0.22 mm and volume fraction of 35% had a strength of 216 $\pm$ 5.1 MPa and stiffness of 4.7 $\pm$ 0.1 GPa [216]. Gyroid lattices at the same volume fraction had a larger wall thickness of 0.6 mm and higher strength (392 $\pm$ 3.9 MPa) and stiffness (7.6 $\pm$ 0.6 GPa) [216].

Comparison can be made between the strength and stiffness of lattices with the same unit cell size and volume fraction but different unit cell designs (table 1.1). For example

Table 1.1: Comparing compressive strength and stiffness from the literature of lattice with the same unit cell length and volume fraction but different unit cell designs manufactured in Ti-6Al-4V using L-PBF

Unit Cell	UC Length /mm	Strut Thick-ness /mm	Volume Fraction	Strength /MPa	Stiffness /GPa	Citation
Diamond	1.2	0.28	0.11	6.8 ± 2.3		[217]
Diamond	1.2	0.45	0.20	28.9 ± 6.2		[217]
Diamond	1.2	0.52	0.26	31.7 ± 13.0		[217]
Diamond	1.2	0.60	0.34	70.6 ± 7.0		[217]
Cubic	1.8	0.35	0.11	29.9 ± 0.9		[217]
Cubic	1.8	0.54	0.21	63.3 ± 2.2		[217]
Cubic	1.8	0.61	0.26	65.6 ± 12.3		[217]
Cubic	1.8	0.72	0.34	112.6 ± 7.2		[217]
BCCZ	5.0	1.23		115.6 ± 2.3	3.4 ± 0.3	[218]
Diamond	5.0	1.28		63.9 ± 2.2	1.9 ± 0.1	[218]
Fluorite	5.0	1.21		180.6 ± 4.9	4.4 ± 0.1	[218]
BCC	2.0	0.22	0.35	216.0 ± 5.1	4.7 ± 0.1	[216]
Gyroid	2.0	0.60	0.35	392.1 ± 3.9	7.6 ± 0.6	[216]
Cubic	1.3	0.79	0.58	464.7 ± 11.3	12.8 ± 0.6	[143]
Cubic	1.3	0.71	0.49	348.7 ± 7.5	8.3 ± 0.8	[143]
Cubic	1.3	0.61	0.40	227.0 ± 4.6	4.3 ± 0.6	[143]
Gyroid	1.3	1.00	0.58	762.7 ± 9.7	21.7 ± 0.5	[143]
Gyroid	1.3	0.82	0.49	608.0 ± 9.5	15.3 ± 1.0	[143]
Gyroid	1.3	0.45	0.39	476.3 ± 7.4	8.8 ± 0.6	[143]

it was found that cubic lattices with a 1.25 mm length, 0.6 mm strut thickness and a volume fraction of 0.395 had a strength of 227 ± 4.6 MPa and a stiffness of 4.3 ± 0.6 GPa. Whereas gyroid lattices with the same unit cell length and volume fraction, were stronger and stiffer, reqiring a wall thickness of 0.45 mm to achieve the same volume fraction, the strength was found to be 476 ± 7.4 MPa and the stiffness was 8.8 ± 0.6 GPa [143].

Lattices generally fail through one or more of three failure modes, which are successive cell collapse, crack propagation and diagonal shear. Cell collapse can be buckling of vertical struts, or crushing failure. Crack propagation generally starts at an existing defect, while diagonal shear tends to follow a plane of struts and results in a 50% drop in strength followed by densification [149].

Lattices can be classified as bend or stretch dominated based on their deformation behaviour. Maxwell's stability criterion was adapted for lattices as it applies to pin jointed frames, whereas lattices have rigid joints [219]. This has the equation $M = b - 3j + 6$, where the value of M indicates whether it is a mechanism, b is the number of struts and j is the number of joints. If M is less than 0 then the structure is assumed to exhibit bend dominated behaviour. If $M = 0$ then the lattice shows stretch dominated behaviour and if $M > 0$ then the structure is over defined and can end up with internal stresses [137].

Stretch dominated lattices tend to be stronger and stiffer than bend dominated lattices with the same volume fraction as they tend to fail due to tensile and compressive loads rather than undergoing bending failure [220]. Stretch dominated structures exhibit buckling while bend dominated structures tend to barrel. Buckling is not limited to a single plane so after the initial yield subsequent planes undergo collapse leading to a stress strain curve with an oscillating region [136]. Both bend and stretch dominated lattices have a linear elastic region which ends with the initial yield, this is followed by a plateau region and then densification (figure 1.6). For the stretch dominated lattices there is a larger drop to the plateau region than in bend dominated lattices, and the plateau region oscillates [136, 221, 222].

Gibson and Ashby created equations to predict the strength of metal foams based on the relative density which is the ratio of the densities of the lattices and the bulk materials [132, 149].

$$\frac{\sigma^*}{\sigma_s} = C\left(\frac{\rho^*}{\rho_s}\right)^m \tag{1.1}$$

$$\frac{E^*}{E_s} = C\left(\frac{\rho^*}{\rho_s}\right)^n \tag{1.2}$$

Equation 1.1 equates the yield strength ratio (lattice denoted by * over the bulk material s) to the relative density, with C which is the Gibson Ashby constant which relates to the geometry and is derived from experimental results. Equation 1.2 equates

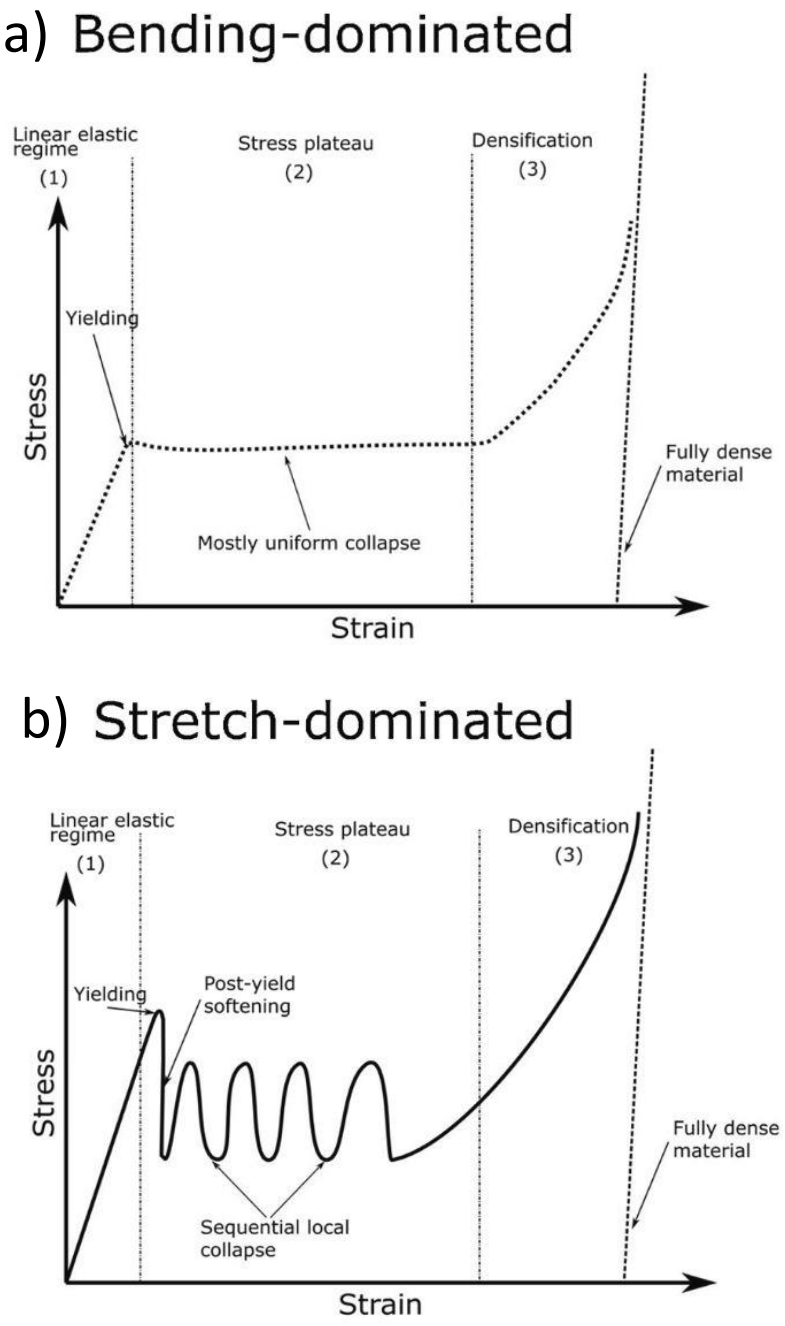

Figure 1.6: Typical compressive stress strain curves for bend and stretch dominated lattices with same relative density. a) typical bend dominated curve showing linear elastic region (1) which ends with yielding, flat plateau region (2), densification (3), b) typical stretch dominated structure with linear elastic region (1) ending in yielding, followed by a drop which is larger than that seen in bend dominated structures, then a stress plateau with oscillations due to planes collapsing (2), followed by a densification region. Adapted from [136]

the ratio of the elastic moduli to the relative density with another constant. For bend dominated lattices $m = 3/2$ and $n = 2$, while for stretch dominated lattices m and n are one [132].

Influence of Lattice Geometry on Compressive Strength

Lattices with thicker struts have increased strength and stiffness (assuming the same unit cell size, unit cell design and angles), as seen in table 1.2. This is because a thicker strut is able to support greater bending and buckling loads.

Volume fraction is dependent on strut thickness, so it unsurprising that increasing the volume fraction but keeping the unit cell size the same results in increased strength and stiffness as this is the same as increasing the strut thickness (table 1.2). This also follows from the Gibson Ashby Model which predicts stronger and stiffer lattices when the volume fraction increases [132].

Generally struts built closer to vertical are stronger than those built horizontally due to better build quality as previously discussed [184, 226, 227]. However Buttmann et al found vertical struts printed from stainless steel by L-PBF failed under tensile testing more readily than those are lower angles due to poor bonding between layers [228, 229].

Given the build angle of a strut influences the strength and stiffness, and different unit cell designs have different mechanical properties it follows that changing lattice angle will also change the mechanical properties. However there are a number of different ways of rotating a lattice that are not always clearly differentiated. Three parameters can be rotated to change the lattice angle; the orientation of the sample during building, the orientation of the sample during compression, and the orientation of the unit cell within the sample. In this work when a sample is rotated during building and the principle unit cell direction (e.g. the Z strut in a BCCZ lattice) is in the same direction as the sample direction and the compression direction then this is referred to as a rotation of the build angle (figure 1.7b). If the sample is rotated during building but the principle unit cell direction is aligned with the build direction, then the it is referred to as a rotation of the

Table 1.2: Comparing compressive strength and stiffness values from the literature, of lattice with different strut thicknesses and volume fractions manufactured in Ti-6Al-4V using L-PBF

Unit Cell	UC Length /mm	Strut Thickness /mm	Volume Fraction	Strength /MPa	Stiffness /GPa	Citation
BCC	5.0	0.60	0.14	8.0	0.2	[140]
BCC	5.0	0.80	0.15	16.0	0.4	[140]
BCC	5.0	1.00	0.24	34.0	0.7	[140]
BCC	2.0	0.30	0.11	8.6	1.7	[144]
BCC	2.0	0.50	0.26	49.3	1.0	[144]
Cubic	4.0	2.20		510.7 ± 67.8	18.9 ± 1.2	[145]
Cubic	4.0	1.80		369.7 ± 40.3	10.9 ± 1.0	[145]
Cubic	3.0	1.80		761.1 ± 108.6	21.6 ± 1.9	[145]
Cubic	3.0	1.10		203.1 ± 50.4	7.2 ± 0.5	[145]
Cubic	1.3	0.79	0.58	464.7 ± 11.3	12.8 ± 0.6	[143]
Cubic	1.3	0.71	0.49	348.7 ± 7.5	8.3 ± 0.8	[143]
Cubic	1.3	0.61	0.40	227.0 ± 4.6	4.3 ± 0.6	[143]
Diamond	2.5	1.08	0.10	16.7 ± 1.0	1.2 ± 0.1	[141]
Diamond	2.5	1.59	0.20	69.6 ± 3.9	3.6 ± 0.1	[141]
Diamond	2.5	1.98	0.30	127.1 ± 8.4	5.7 ± 0.2	[141]
Diamond	2.5	2.37	0.40	156.5 ± 11.3	7.9 ± 0.4	[141]
Diamond	1.0	0.39	0.36	99.6 ± 9.0	4.2 ± 0.1	[223]
Diamond	1.0	0.33	0.27	62.9 ± 5.0	2.6 ± 0.0	[223]
Diamond	1.0	0.26	0.18	25.6 ± 2.6	1.2 ± 0.1	[223]
Diamond	1.0	0.13	0.11	8.2 ± 0.4	0.4 ± 0.0	[223]
Fluorite	1.0	0.12	0.12	14.3 ± 1.7	0.4 ± 0.0	[224]
Fluorite	1.0	0.23	0.32	77.7 ± 12.8	1.6 ± 0.2	[224]
Fluorite	1.0	0.14	0.16	19.4 ± 0.3	0.6 ± 0.1	[225]
Fluorite	1.0	0.22	0.29	78.7 ± 2.2	2.6 ± 0.0	[225]
Fluorite	1.0	0.25	0.34	117.2 ± 1.1	3.5 ± 0.0	[225]
Gyroid	1.3	1.00	0.58	762.7 ± 9.7	21.7 ± 0.5	[143]
Gyroid	1.3	0.82	0.49	608.0 ± 9.5	15.3 ± 1.0	[143]
Gyroid	1.3	0.45	0.39	476.3 ± 7.4	8.8 ± 0.6	[143]

load angle (figure 1.7c). Whereas if the sample is not rotated but the principle unit cell direction is rotated within the lattice this is referred to as a combined rotation, because the unit cells are built at an angle and compressed at an angle. In the literature this is sometimes referred to as a unit cell rotation (figure 1.7d).

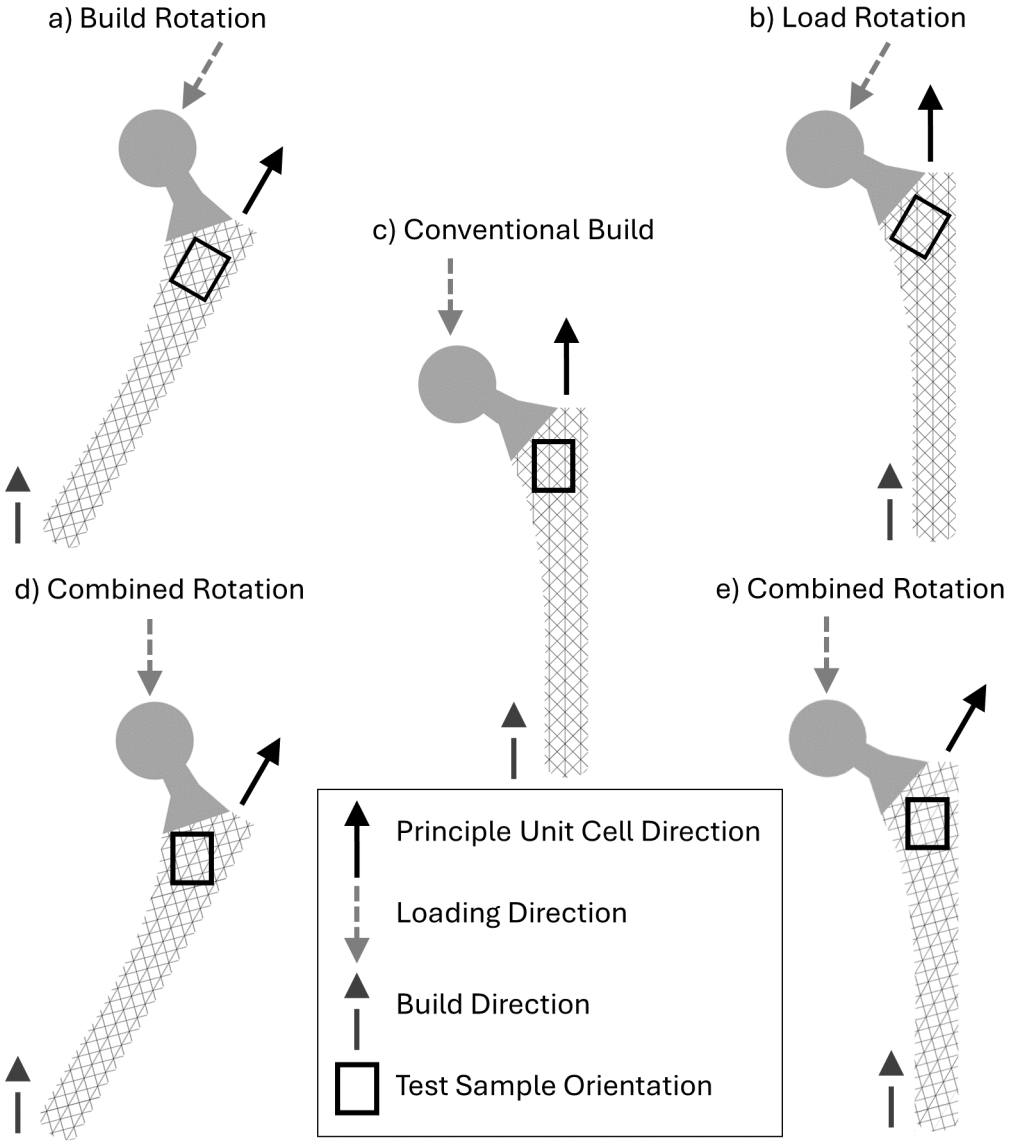

Figure 1.7: Diagram to explain different ways of rotating the building and loading of lattices within medical devices. a) rotation of the build angle, b) conventional build, c) rotation of the load angle, d& e) two ways of combining rotation of building and loading directions

A build rotation enables the influence of building struts at different angles to be compared, and mimics if the implant was built at an angle within the build chamber. This

rotation has been shown to influence the build quality as expected from previous observations about the effect of different strut angles on build quality [185, 230]. Weißmann et al found no statistical difference in strength or stiffness when rotating vertical struts to 45° [231]. While Wauthle et al found diamond lattices had lower strength and stiffness when rotated 45° [232], but both the lattice designs had struts which built poorly and were oriented horizontally during the build. However for the rotated lattice, this was then at 45° during compression where it was subjected to a higher percentage of the load so had a greater influence on the strength and stiffness resulting in a reduction in those parameters [232].

By looking at the effects of load orientation the influence of offset implant loading can be seen. This is influenced by which orientations of the unit cell are stronger and stiffer, so an isotropic lattice would not show any differences under this rotation. Hossain found that BCC lattices rotated such that the direction of compression was aligned with the long axis of a strut had strength and stiffness values which were significantly higher than if this alignment was not there [233]. When diamond lattices were rotated 45° there was a 35% reduction in strength and stiffness which corresponds with struts rotating from vertical during compression (where they are stronger due to buckling) to angled (where they are weaker due to bending). Whereas when the rotation was 90° which is the same shape (just mirrored) due to the rotational symmetry of the diamond lattice shape, there was no statistical difference in strength or stiffness [232].

Combined rotation is the most common rotation found in the literature and the hardest to work out what is causing the effects, because the struts are built at different angles and the unit cells are loaded in different directions between rotations. The strongest rotations are consistently those with vertical struts [226, 234, 235, 236]. This is not surprising given vertical struts have the highest build quality, and they fail under buckling rather than bending.

Lattice compressive strength decreases with increasing unit cell size (table 1.3). This is true whether strut thickness or volume fraction is kept constant [144, 146, 147, 222, 237].

Table 1.3: Comparing compressive strength and stiffness values from the literature, of lattice with different unit cell sizes manufactured in Ti-6Al-4V using L-PBF

Unit Cell	UC Length /mm	Strut Thick-ness /mm	Volume Fraction	Strength /MPa	Stiffness /GPa	Citation
BCC	3.0	0.30	0.04	4.0	0.1	[238]
BCC	2.0	0.30	0.08	18.0	0.4	[238]
BCC	2.5	0.50	0.18	20.9	0.5	[144]
BCC	2.0	0.50	0.26	49.3	1.0	[144]
Cubic	4.0	1.80		369.7 ± 40.3	10.9 ± 1.0	[145]
Cubic	3.0	1.80		761.1 ± 108.6	21.6 ± 1.9	[145]
Fluorite	0.8	0.19	0.22		1.4 ± 0.1	[239]
Fluorite	0.7	0.19	0.30		2.6 ± 0.1	[239]

For samples where the strut thickness is kept the same, the volume fraction decreases with increasing unit cell size which leads to the reduction in strength and stiffness [238]. While the differences in strength for samples with the same volume fraction were attributed to differences in sample pores. Samples with smaller unit cell sizes had a smaller cross section so the scan vectors are shorter resulting in a more rapid return of the laser. The energy in the strut had less time to dissipate, resulting in a reduction in pores within the struts [146].

1.8 Drug Delivery from Bone Implants

Bone implants can be loaded with drugs as a secondary function. There are three main reasons why drugs are incorporated, to treat or prevent infection, to promote bone growth for fixation or bone fusion, and to treat cancer [240]. The drugs are either loaded onto the surface of the implant or bulk loaded into a void [241].

A number of coatings have been developed for additively manufactured metal implants, these are generally polymeric or ceramic [242]. Some examples of polymers include natural polymers such as chitosan, gelatin and cellulose [152, 153, 243], and synthetic polymers such as poly(lactic-co-glycolic acid) (PLGA) and polycaprolactone (PCL) [244, 245].

These are predominantly explored for preventing and treating infection and are generally loaded with antibiotics such as vancomycin or gentamicin sulphate [152, 153], or with alternative antimicrobials such as silver nanoparticles or silver ions [152, 246].

Ceramics are more often loaded with therapeutics to promote bone growth as the biomaterials are inherently bioactive, i.e. having an effect on living tissue. Calcium phosphate cements such as hydroxyapatite have been loaded with drugs or autograph bone material to promote bone growth [247, 248].

Alternatively drugs can be attached to surfaces without the use of a secondary phase. Approaches include adsorption of biologics [240, 249], addition of an oxide layer containing antimicrobial metal ions [246], or the use of nanotubes with therapeutics adsorbed inside [240, 250, 251]. Lattices can be used to increase the surface area for coating, which enables greater drug loading [240, 249].

Instead of coating therapeutics onto the surface of implants they can be bulk loaded, this could be in a reservoir with channels to the surface [101, 252], or with a porous membrane [253]. Alternatively, lattices can be used to provide both mechanical support and void space for therapeutics [155, 224, 254], these lattices could be within a reservoir [157]. Polymers, especially as hydrogels, are a common way of loading therapeutics into these void spaces as they have good rheological properties [155, 255]. Alternatively, cements such as calcium sulfate hemihydrate, or magnesium oxychloride are explored because they can be injected into voids prior to setting [101, 256, 257].

1.8.1 Geometric Control of Drug Release

Additive manufacturing enables significant design freedoms, which as well as being utilised to manipulate the mechanical properties of implants, can also be used to control the drug release. The void volume filled with drug loaded biomaterial, the length of the release path, and the surface area of the biomaterial have all been investigated as potential parameters which can influence release [157]. The drug loading concentration has also been used to control the drug release [250].

Changing Void Volume to Control Release

Increasing the reservoir volume increased the rate and mass of gentamicin sulphate released from calcium sulphate hemihydrate [157]. An increased reservoir volume of tetracycline in solution was also found to lead to an increased drug concentration in the saline solution after elution through microchannels [258].

Altering the Release Path Length

Increasing the length of channels from a reservoir led to slower release of gentamicin sulphate for Allen et al, however this may be due to the hydrophobic nature of the the polymer used for the reservoir [256]. Cox et al designed reservoirs with different channel positions to look at the influence of the placement on release. Channels with a longer release path had a faster release rate in contrast to the results found by Allen et al, however there were some challenges with completely filling the reservoirs which may have influenced the release [257].

Influence of the Biomaterial Surface Area on Release

Increasing the exposed surface area of the drug loaded biomaterial increased the rate of release in bulk loaded devices [101, 253, 256]. Bezuidenhout et al used a porous membrane rather than channels to enable release from the reservoir and found for a porosity below 0.25 that the release was controlled by the porosity, while above this threshold vancomycin was able to diffuse freely [253].

Release of adsorbed icariin from Ti-6Al-4V lattices varied with surface area but not in order of surface area. This may have been influenced by uneven drug loading onto the surfaces of the lattices [240]. Nune et al did not measure the release of adsorbed BMP-2 directly from fluorite lattices, but instead investigated the cell seeding efficiency, it was found that specimens with a lower porosity and therefore higher surface area had a higher cell seeding efficiency. It was noted that only the cells on the external surface were counted, and cells are more likely to fall through large holes when the porosity is higher

[249].

Cell seeding efficiency was also compared on lattices coated in bioactive calcium phosphate cements but not therapeutics, and Man et al found that higher porosity with a lower surface area had a higher cell seeding efficiency [259], while Vlad et al found new bone area was proportional to the implant area, but not volume [260].

Varying the Concentration of the Therapeutic

In addition to geometric control of release, the concentration of drug loaded into the biomaterial can be varied. Increasing silver ion concentration on the surface of titanium lattices led to an increased rate of release and concentration of silver ions in the solution [250]. This also equated to reduction in colony forming units of *Staphylococcus aureus* at one and seven days of incubation, but not 14 days [250]. Increasing vancomycin concentration in PCL coated titanium lattices lead to an increased rate of release, and increased absolute mass released [244].

Increasing the concentration of simvastin bulk loaded into a hydrogel in a Ti-6Al-4V lattice, increased the absolute rate and amount of release, while the percentage rate of release decreased. Both concentrations had total release within 11 days [261]. Around the lattice, increased drug concentration led to increased bone volume and density, and vascularisation at both four and eight weeks. Inside the lattice the lower concentration had increased levels at four weeks while the higher concentration performed better at eight weeks [261].

1.9 Biomaterials for Drug Delivery

As has previously been discussed metal implants can be used as a scaffold to hold biomaterials loaded with therapeutics for drug delivery. Biomatrial carriers tend to either be polymers or ceramics as these provide biocompatible materials with tunable properties [241]. These materials can either be degradable, for example to enable bone to subse-

quently fill the space, or permanent which enables them to be used for fixation or as a surface for immobilisation of drugs [241].

Polymeric biomaterials can be used as a coating or turned into a hydrogel for bulk or surface loading. Natural polymers come from biological sources such as collagen and alginate, while synthetic polymers are chemically derived. Natural polymers have the advantage of being more readily biocompatible and resorbable, while synthetic polymers have a higher strength and durability, they are also more reproducible [262]. Drug loading methods for polymers include covalent attachment, adsorption and entanglement within the polymer chains [263], while for ceramic materials the drug tends to be mixed into the cement during setting [264].

Some biomaterials are intrinsically antimicrobial or osteoconductive and do not require drug loading [265]. Biomaterials can also be manipulated to promote cell attachment, for example by altering the hydrophobicity [266]. Choosing a biomaterial with an appropriate drug release profile for the drug and function is key.

Different materials offer different release profiles. The main mechanisms of drug release are bulk degradation, surface erosion and diffusion. Bulk degradation occurs throughout the material and occurs when water ingress is faster than the degradation rate [267]. Surface erosion occurs when the sample erodes from the surface releasing the drug [268], the erosion can be driven by enzymes or water [269]. Degradation and erosion tend to involve the hydrolysis of the polymer chain while drugs attached to the chain either release more rapidly than they permeate through the structure, at which point the release rate is diffusion limited, otherwise it is limited by the break down of the linkage [265, 270]. Diffusion is most common from hydrogels, ceramics, matrices or reservoirs, with rapidly soluble drugs [268].

A number of models have been proposed to describe drug diffusion through a matrix. Two that are particularly relevant to this work are the Higuchi and Korsmeyer Peppas models [271, 272].

Higuchi proposed a series of equations for the diffusion of a drug from a thin film

which culminated in the most famous equation where the amount of drug released in proportional to the square root of time (equation 1.3). Despite how it is often applied, this model was developed for thin films and assumes the diffusion is unidirectional with negligible edge effects [273]. In order for the model to fit the initial drug concentration needs to be much higher than the solubility of the drug, with constant diffusivity and perfect sink conditions [272]. The matrix must be significantly larger than the drug molecules and not swell or dissolve [273].

$$M = k * t^{0.5} \tag{1.3}$$

If a swellable matrix is used then the Korsmeyer Peppas model is more relevant, although this has also been used for degrading matrices [271]. This is a semi empirical adaptation of the Higuchi model with equation 1.4. Where M is the drug release, a is a coefficient related to the geometry, and b is an exponent related to the release kinetics [271]. The values of the exponent b indicate whether the release is Fickian, anomalous, case I or case II transport, but the matrix geometry must be taken into account. For example the cut off for anomalous transport into case I is 0.85 for spherical matrices but 1.00 for thin films [274, 275]. The model only holds for the first 60% of release [276].

$$M = a * t^{b} \tag{1.4}$$

1.9.1 Poly(methyl methacrylate) Bone Cement

Poly(methyl methacrylate) (PMMA) bone cement is a non-degradable polymeric cement which is currently licensed for use in a number of bone implant applications, especially joint replacements where it is used for implant fixation [277]. Commercial PMMA is mixed from a powder and liquid component during surgery. PMMA sets in five to ten minutes by free radical polymerisation to form polymer chains [278]. The powder consists of polymethyl methacrylate polymer particles, benzoyl peroxide which initiates the

reaction and a radiopaque agent to make the cement visible on x-rays which can either be barium sulphate or zirconium dioxide. The liquid component mainly consists of the monomer methyl methacrylate (MMA) stabilised with hydroquinone, plus the activator N,N-Dimethyl-p-Toluidine [279, 280].

The cement can be loaded with an antibiotic to treat or prevent infection, which can be added into the liquid or powder component. Most antibiotics are unsuitable for this due to the exothermic polymerisation reaction which can reach temperatures of 87°C [**Kluin2013**]. Gentamicin is most commonly used in PMMA due to its thermal stability and broad range of bactericidal activity [75, 281]. The release mechanisms of antibiotics from the cement is not fully understood with both surface release and partial bulk release from cracks and pores being proposed as potential mechanisms [282, 283], These mechanisms only enable a small (5 - 18%) and unpredictable proportion of the antibiotic to be released leading to drug wastage and patients receiving an unknown dose [284, 285].

There are differences between the ratios of the component in PMMA in different commercial cements. However in each case the PMMA is in excess so that all the MMA monomer reacts. This is to prevent excess MMA leaching out of the cement which can lead to chemical necrosis of the surrounding bone [285]. The exothermic setting reaction can also lead to thermal necrosis, so different reactant ratios can be used to slow the reaction, causing a reduction in temperature [286]. If the cement is left to set outside the body then tissue damage does not need to be considered and faster polymerisation can be used as it enables better mechanical properties [287]. However this has the potential to introduce bubbles which can act as stress risers [288]. These can be air bubbles from hand mixing, which can be reduced by vacuum mixing, or from monomeric boiling which are not alleviated by vacuum mixing [285]. PMMA shrinks during setting up to 20% which can lead to internal stresses and introduce cracks further reducing the mechanical strength [285, 289].

1.9.2 Calcium Phosphate Cements

Given the challenges of using PMMA cement for bone implant applications some alternatives have been considered including calcium phosphate cements (CPCs) which have been approved for bone fixation, cavity filling and reinforcement [264, 290]. These cements form by dissolution and precipitation reactions from an aqueous phase made predominantly of water, and calcium phosphate powders [264]. The powder dissolves in the liquid phase into calcium and phosphate ions which become supersaturate in solution, leading to crystal nucleation and growth. The entanglement of the crystals leads to hardening of the cement [290, 291]. Apatite cements generally form at pH > 4.2 while brushite cements are most stable at pH < 4.2 [264]. Antibiotics can be added to CPCs in either the powder or liquid phase and the lower setting temperature than PMMA enables a greater range of antibiotics to be viable. The presence of the drugs influences the setting reaction causing changes in the rheology and microstructure which influence the mechanical properties, degradation process and drug release kinetics [290].

CPCs have a number of advantages over PMMA cement including a much lower setting temperature of around 37°C [264], excellent biocompatibility [292, 293], and repeatable and complete drug release [291, 293]. Additionally these cements are resorbable, which enables them to be used for temporary fixation or defect filling which can then be replaced by the native bone [294, 295]. Among the CPCs, brushite cements have the advantages of faster bone conversion than apatite cements [296], with a suitable resorption rate, whereas calcium sulphate dihydrate is too soluble, dissolving prior to bone infiltration, and apatite cements are insufficiently soluble at physiological pH to enable bone conversion [297].

1.9.3 Brushite Cement

Brushite cement is dicalcium phosphate dihydrate, $CaHPO_4 \cdot 2H_2O$, manufactured from an alkaline calcium component, generally β-tricalcium phosphate (β-TCP) which is used here, or α tricalcium phosphate, hydroxyapatite, tetracalcium phosphate, calcium oxide or calcium hydroxide. β-TCP is more commonly used as its production is less energy inten-

sive [298]. This is combined with an acidic phosphate component such as phosphoric acid, monocalcium phosphate anhydrous or monocalcium phosphate monohydrate (MCPM), the latter is often used (including in this work) because it contains water molecules that can be donated to the precipitate reaction to form brushite [298]. Additionally, additives can be added to alter the setting time, injectability and mechanical properties [298].

The setting reaction of brushite cement (figure 1.8) is initiated with the dissolution of MCPM into calcium ions and phosphoric acid (equation 1.5). This reduces the pH of the solution to around 2.5 [299], enabling the β-TCP to dissolve (equation 1.6). These two dissolution reactions cause calcium and phosphate ions to be in solution and when they reach supersaturation brushite nucleation occurs (equation 1.7) followed by crystal growth [290, 298, 300].

Dissolution of MCPM

$$Ca(H_2PO_4)_2 \cdot H_2O \rightarrow Ca^{2+} + 2H_2PO_4^- + H_2O \tag{1.5}$$

Dissolution of β-TCP

$$\beta{-}Ca_3(PO_4)_2 + 4H^+ \rightarrow 3Ca^{2+} + 2H_2PO_4^- \tag{1.6}$$

Precipitation of brushite

$$Ca^{2+} + H_2PO_4^- + 2H_2O \rightarrow CaHPO_4 \cdot 2H_2O + H^+ \tag{1.7}$$

Brushite Additives

Brushite crystals consist of parallel calcium phosphate chains with water molecules in between [302]. When sulphate ions are present, for example if the antibiotic gentamicin sulphate is used, then calcium sulphate dihydrate (CSD) nucleation occurs rather than brushite nucleation. This has the same structure, just with a sulphur atom in the center of the negative ion rather than a phosphorus atom [297]. At sulphate ion concentra-

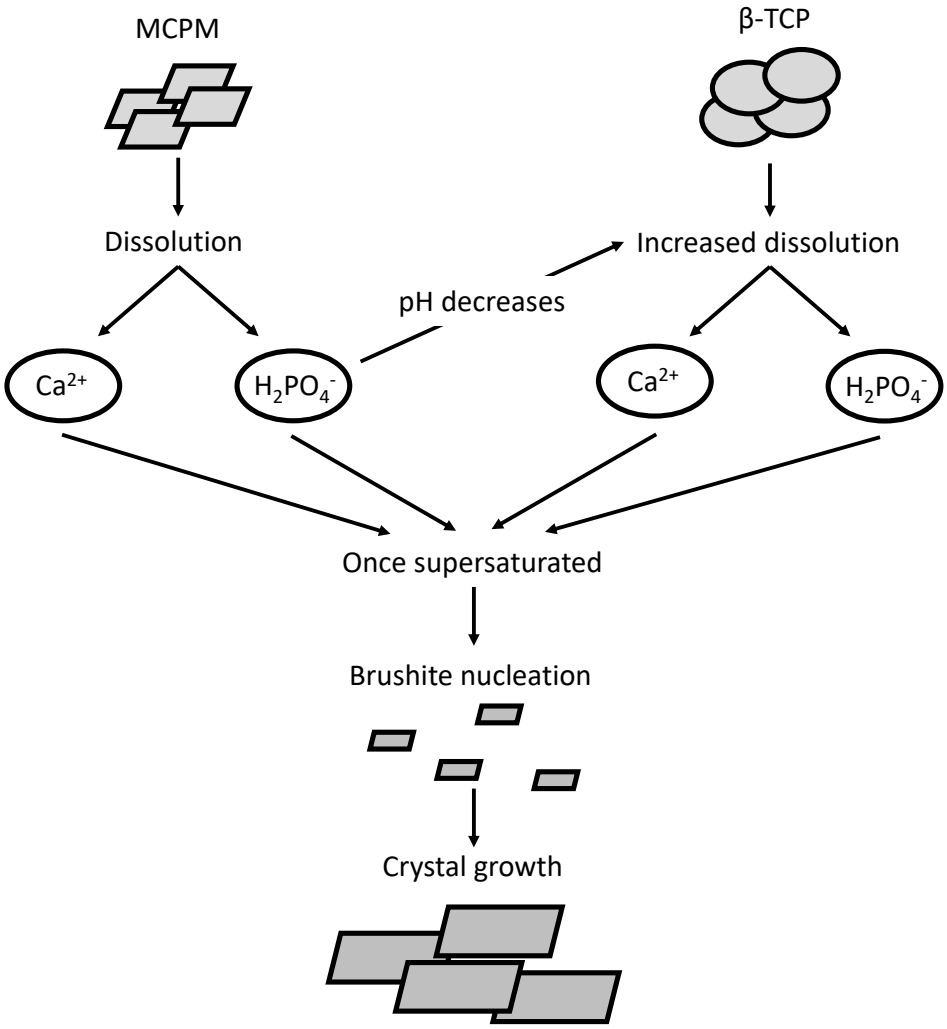

Figure 1.8: Schematic of brushite cement formulation showing dissolution of MCPM into calcium ions and phosphoric acid which increases the pH enabling decreased β-TCP dissolution, allowing supersaturation of calcium and phosphate ions leading to brushite nucleation and crystal growth. Adapted from [301]

tions below 0.1 M CSD does not form, instead the sulphate ions lead to a longer setting time [303] as the sulphate ions interfere with the precipitation and crystal growth of the brushite crystals [298]. When sulphate ion concentrations are above 0.1 M CSD nucleation is preferential to brushite nucleation, due to the lower solubility of CSD so supersaturation occurs first, and the crystals are smaller [297]. At concentrations between 0.1 and 0.9 M CSD crystal nuclei act as nucleation sites for brushite crystals, leading to faster brushite crystal formation and therefore smaller crystals. Additionally the formation of CSD reduces the sulphate ions in solution so they cannot interfere with the precipitation

reaction further increasing the rate of brushite formation [303]. Once the sulphur concentration exceeds 0.9 M so much CSD is formed that the phosphoric acid concentration is insufficient to drop the pH to enable the β-TCP to dissolve, therefore brushite does not form [303]. Although the gentamicin base does not covalently attach to the brushite cement during setting, it is positively charged and can interact with the crystals reducing the release rate [302, 304].

Another additive that can be used to alter the setting kinetics is citric acid, which slows the setting reaction by limiting the dissolution of β-TCP by chelating calcium ions [298, 305, 306]. It is not incorporated into the crystal structure but causes a higher nucleation barrier [307]. This means it does not influence the porosity or strength of the cement [297], but it can extend the shelf life of the cement [308] and improve injectability [298].

Brushite Physical Properties

One method of filling voids with cement is via injection, however there are some challenges with the injectability of brushite cement. The biggest challenge is liquid phase separation where the liquid phase of the unset cement travels faster than the solid phase resulting in a higher liquid concentration in the extrudate than desired [298]. This effect can be reduced by modifying the syringe geometry as well as the cement composition [309]. Increasing the viscosity of the aqueous phase, such as through the use of gelling agents, reduces the flow rate which leads to reduced separation [305]. Reducing the powder to liquid ratio gives better injectability but a weaker cement due to a high porosity [298, 309]. The addition of citric acid can reduce the viscosity which is counter to the previous point, however the reduction in viscosity is combined with an increase in the zeta potential (surface charge) of the particles which reduces agglomeration and has been found to reduce separation when injecting the cement [305].

Brushite cement is often chosen for applications where the space will be later filled with bone due to its resorption properties. Brushite is resorbed by a mixture of dissolution

and cellular activity [310]. Early resorption is regulated by macrophages rather than demineralisation by osteoclasts [311]. The initial degradation can be faster than the bone regeneration which can lead to gaps between the cement and native bone if used for fixation, so care must be taken in load bearing applications [312]. Over time the brushite converts to apatite which is less soluble than brushite so the resorption rate reduces [313]. The conversion to apatite can be slowed with the addition of additives including magnesium ions and pyrophosphate [314, 315].

Brushite cement is a brittle material with higher strength under compression than tensile loading. The mechanical strength is strongly dependent on the porosity of the cement with a higher porosity leading to a lower strength [316]. However the presence of pores enables bone ingrowth and the impregnation of fluid for resorption [317], so a balance between short term mechanical properties and long term functionality must be achieved. Porosity can be manipulated by changing the powder to liquid ratio (PLR), with excess liquid leading to a higher porosity. The precipitation reaction of brushite consumes water (equation 1.7), so in combination with a high PLR a very low porosity can be achieved. However mixing can be challenging with a high PLR, so the use of additives, such as citric acid can improve the mixing and therefore the strength [298].

Compact crystals lead to a stronger cement, which can be achieved by using retardants to reduce the crystal size, starting with a finer powder, or slowing the setting reaction [318]. Crystal organisation can also lead to more compact cement. Efforts to improve the arrangement of crystals have included freezing cement during mixing, where the ice crystals arranged the cement in a structure that was four times stronger than without the freezing step [319]. The addition of sulphate ions to the brushite cement leading to CSD nucleation did seed brushite crystals but did not improve the mechanical properties [297, 320]. Compaction has previously been used to increase the compressive strength of brushite cements although this would not be possible if the cement was being injected into a bone defect [321].

1.9.4 Polycaprolactone

Polycaprolactone (PCL) is a synthetic polymer with chemical formula $(C_6H_{10}O_2)_n$. It is most commonly synthesised by catalysed ring-opening polymerisation of ϵ-caprolactone (figure 1.9), however it can also be formed by polycondensation of 6-hydroxyhexanoic acid but this tends to lead to a poor quality product and higher chain lengths are not possible. However ring-opening polymerisation is not without challenges as the catalysts tend to be toxic metals which can be difficult to remove [322].

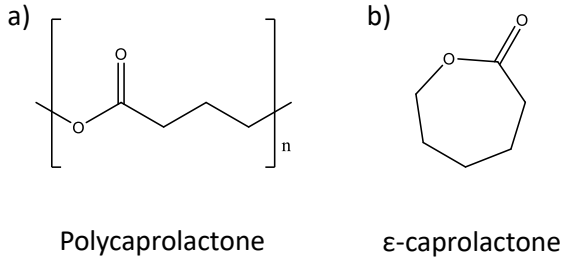

Figure 1.9: Chemical structures of a) PCL and b) ϵ-caprolactone

PCL is biocompatible, non toxic and degradable [323]. It is soluble in polar, aromatic and chlorinated hydrocarbons while it is insoluble in alcohols, glycols and aliphatic hydrocarbons [323]. The chain length can be altered to alter the mechanical properties, for example PCL with a molecular weight of 15,000 $gmol^{-1}$ is brittle, while PCL at 40,000 $gmol^{-1}$ is soft and semi crystalline [323]. PCL can also be blended with other polymers or materials to form composites with different materials properties [324].

PCL degrades under physiological conditions by the hydrolysis of ester linkages [325]. Degradation can be by bulk degradation if the specimen is more than 13 mm thick [326] or surface erosion if it is thinner [327]. PCL can be broken down by microorganisms including fungi and bacteria [324]. However in physiological environments the degradation is driven by enzymatic, oxidative or pH catalysis [322]. Small polymer fractions are metabolised by cells so there is no toxic effects [327]. Temperature increases lead to faster degradation rates as do pH values above 11 or below 3, while variations around physiological pHs have not been shown to have any effect [322].

The property that has been shown to have a large effect of PCL degradation is what groups are present on the ends of the PCL chains. Ester groups were stable end groups, while hydroxy groups are stable at physiological temperatures as long as a catalyst is not present, however they undergo degradation by oxidation and chain scission at higher temperatures or in the presence of a catalyst. Acetylation of the hydroxy end groups can prevent degradation [322].

PCL can be mixed with drugs where its high permeability enables rapid drug release [323]. The use of PCL to encapsulate drugs enables greater control of the release and can be used for targeted delivery [325]. Alternatively drugs can be immobilised onto the surface of PCL using covalent bonding to take advantage of its slow degradation rates [323].

PCL is often used as a drug delivery vehicle due to its cost [328], the fact that it has FDA approval [329], and that unlike similar polymers it can withstand high energy irradiation so can be sterilised [92]. However PCL is hydrophobic which results in poor cell attachment, this can be overcome by changing the surface properties of the PCL for example through chemical or plasma treatment, or through the attachment of proteins by coating, blending or covalent bonding [327].

1.10 Aims and Overview of this Research

Additive manufacturing techniques, such as laser powder bed fusion have opened up the possibilities for developing new medical devices through the use of complex geometries such as lattices. Lattices are currently approved for use in joint replacements and fusion cages for fixation. They are also being researched for the reduction of radiographic artefacts, stress shielding and as platforms for drug delivery, and cell scaffolding. This work aims to expand these applications by exploiting lattices for tailored drug delivery applications. This would include the use of lattices to control the release of therapeutics to optimise the release profile to the pharmokinetic properties of the therapeutic, or through

immobilisation of a therapeutic to the lattice surface. These approaches will support the creation of novel hip implants in the future which will be able to treat infection with a permanent implant rather than the use of a hip spacer, and eliminating the need for a costly two stage procedure, an example of what this might look like can be seen in figure 1.10b. Additionally these technologies may lead to new spinal fusion cage designs which do not require bone graphs to promote bone growth, such as in figure 1.10a.

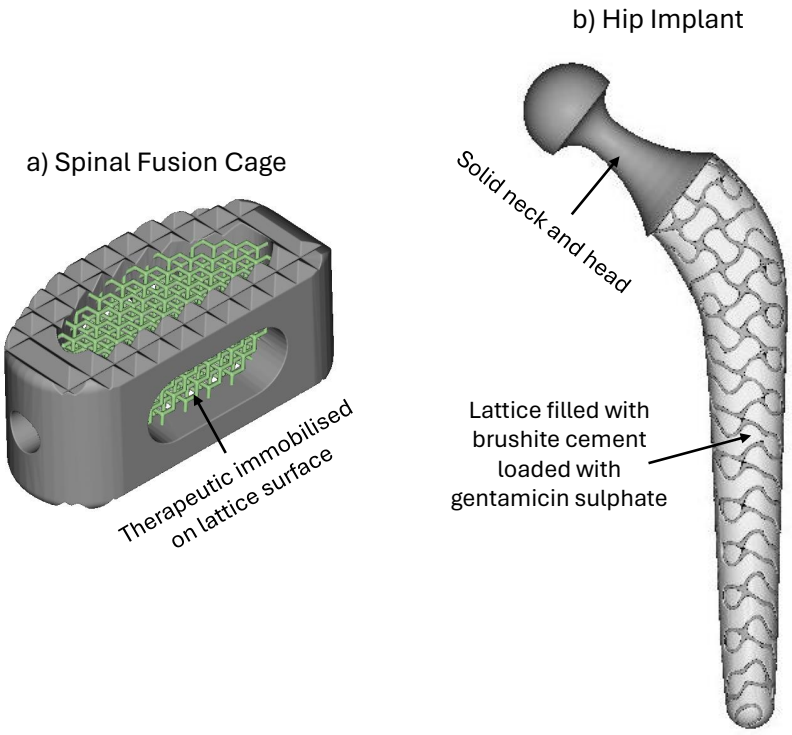

Figure 1.10: Examples of potential future implants using this technology include a) spinal fusion cages with a therapeutic immobilised on the surface of a lattice, and b) a hip implant with a lattice structure filled with a secondary phase such as brushite cement loaded with an antibiotic such as gentamicin sulphate

The aim of this research is to find out if it is possible to make medical devices with additional functionality by using lattices to control the release or availability of therapeutics to treat infection and improve fixation. In order to achieve this aim lattices must be found with sufficient mechanical strength and void volume for bulk loading of a therapeutic. The release of a therapeutic from different lattice designs must be compared to investigate whether different designs can influence the release kinetics. Finally a method for immobilisation of a therapeutic to an implant surface should be developed.

The mechanical performance of lattices for medical devices will be investigated through compression testing of cylindrical samples. Six different unit cell designs will be investigated (BCC, BCCZ, cubic, diamond, fluorite, and gyroid) in order to compare lattices with different characteristics such as bend and stretch dominated, more or less anisotropic, and strut and surface based designs. Lattices will be compared on offset strength and stiffness, which are measured from the stress strain curves as well as the shape of the curves and the visual deformation of the lattices after compression. Scanning electron microscopy will be used to image individual lattice struts, which gives an indication of the strut thickness and density of semi sintered particles. Lattices with different unit cell designs, strut thickness, and unit cell sizes will be compared, as well as lattices with unit cells rotated during building, loading and in the combination of the two.

The use of lattices for the geometric control of the elution of gentamicin sulphate from brushite cement will be investigated. The release mechanisms of gentamicin sulphate from PMMA and brushite cements will be explored. After that a fundamental study will be performed to understand how different geometric factors influence release. Following that will be a comparison of different lattice designs for geometric control. The control of antimicrobial efficacy will be explored, and then the compressive properties of the cement and lattice composites will be compared.

The development of a method to immobilise therapeutic agents to PCL will be investigated. Albumin will be used as a model therapeutic to simulate growth factors or antibiotic attachment. Dip coating will be used to layer PCL on Ti-6Al-4V coupons, and then EDC/NHS coupling will be used to attach albumin to the PCL layer. Methods will be developed to quantify the albumin attachment, then an optimisation of the coupling process will be carried out. Finally the samples will be placed in PBS to check the immobilisation.

CHAPTER 2

COMPRESSION TESTING OF LATTICES

2.1 Introduction

The use of additively manufactured lattices to reduce stress shielding while providing sufficient mechanical strength for weight bearing requires an understanding of the mechanical properties of the lattices. It is important to understand the appropriate mechanical properties in order to compare the potential designs against them.

Smart technology has enabled adapted implants to measure loading in metal implants such as hip replacements and interbody fusion cages [330]. Maximum loading in healthy spines has been found to be in the range of 2000-3000 N [331, 332], while loading in interbody fusion cages has been found to be an order of magnitude lower at 400-600 N [333, 334, 335]. ISO 12189:2008 specifies the use of 2000 N for fatigue testing of implantable spinal devices for the lumbar spine [336].

ISO 7206-6 specifies the use of 5340 N for fatigue testing of femoral components of total hip joint prostheses [337]. However large loads have been measured in hip joints, for example during stumbling when 11,000 N was measured [338]. This force equates to stresses of 97 MPa and 35 MPa over the 12 and 20 mm diameter cylinders used in this work.

Alternatively the strength of bone can be used for comparison, where the compressive strength of the femur has been measured in the range 167-215 MPa [213, 214, 215].

While the modulus of elasticity in compression of femurs was measured in the range 14.7-19.7 GPa [213, 214]. This gives an indication of the appropriate stiffness of the implants to enable stiffness matching to reduce stress shielding.

As the lattices will also be used for drug delivery, sufficient void volume for loading the carrier biomaterial is needed. For bulk loading previous work has used lattices up to 30% volume fraction [155, 156, 254, 255]. While for surface loading of lattice the volume fractions used have been from a much wider range from 9.8% [339] to 86% [246], although 20 to 40% is more common [247, 250, 340, 341]. Successful loading will also be dependent upon the carrier material properties and pore sizes of the lattices.

Volume fraction is the percentage of the overall shape that is occupied by the lattice, while porosity is the percentage occupied by the voids, the two should sum to 100%. Relative density has the same value as volume fraction but is calculated by dividing the density of the lattice by the density of the reference material the lattice is made of.

Six different unit cell designs were used in this work, BCC, BCCZ, cubic, diamond, fluorite and gyroid (figure 2.1). BCC lattices are based on the body centred cubic crystal structure with struts where the bonds are, and nodes in place of atoms in the crystal structure. Maxwell's stability criterion [219] predicts BCC lattices would be mechanisms if they were pin jointed, and Ashby predicts these lattices will fail with bend dominated behaviour [137]. However when BCC lattice built from Ti-6Al-4V by L-PBF were compression tested they failed due to shear collapse of planes of unit cells, and the stress strain curves displayed behaviour associated with stretch dominated failure, specifically oscillation in the plateau region and a drop after the yield point [140, 144, 238, 342].

BCC lattices can be adapted with the addition of a vertical strut in the centre, at which point they are referred to as BCCZ. These lattices also have a strut to node ratio that falls under the bend dominated structure by Ashby's prediction. However these lattices have been found to fail via shear plane collapse [139, 343]. Additionally the stress strain curves exhibit typically stretch dominated shapes including oscillating plateau regions and a large drop in stress after yielding [139, 343].

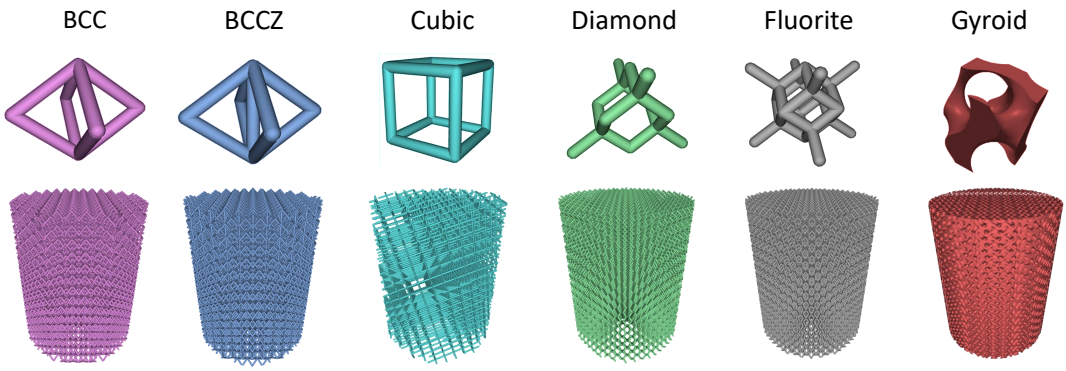

Figure 2.1: CAD designs of single unit cells and cylinders of the six unit cells

Cubic lattices have struts on all the edges of a cube, this makes them a bend dominated structure under Ashby's prediction. However they exhibit stretch dominated behaviours with an oscillating plateau region on the stress strain curve and a drop after the yield point. The failure mechanism depends on the orientation of the unit cells, when these are composed of vertical and horizontal strut buckling occurs in the vertical struts leading to planar collapse, whereas when the unit cells are rotated 45° the planes collapse under shear [143, 344, 345].

The diamond crystal structure can be used as a basis for lattices. The diamond crystal structure contains 14 atoms which make up the nodes of the lattice unit cell, while the lattice struts connect these nodes where the bonds are in the crystal structure. Despite the large numbers of nodes which suggest a bend dominated structure, the lattices demonstrate shear failure in 45° bands. This is accompanied by oscillations in the stress strain curve [141, 142, 218, 223].

The fluorite crystal structure can be used as a unit cell design, this is a rhombic dodecahedron, and is made of two mirrored diamond unit cells. It has been shown to fail under compressive loading by shearing in 45° bands. The plateau region of its stress strain curve has oscillations and is below that of the yield point [218, 344].

Gyroid lattices are triply periodic minimal surfaces which were discovered by NASA in the 1970s [150], they arise in nature, and are often exploited due to their large surface area. In contrast to the other lattices explored here they are a surface rather than strut based

lattice. Gyroid structures have two forms; in the sheet gyroid form the structure has two domains (intertwined regions that do not intersect), while in the skeletal form one of the domains is solid [151]. The skeletal form is used in this work as it allows the wall thickness to be manipulated. As gyroid lattices do not have struts Ashby's predictions based on the Maxwell's stability criterion do not apply. However Khaderi et al tried approximating gyroid lattices as strut based and concluded that they were bend dominated structures [221]. Gyroid lattices have been found to fail by either shear fracture or barreling [143, 216, 346]. With stress strain curves that either show oscillations in the plateau regions or not, however these oscillations have been less substantial than with the strut based lattices [143, 216, 346].

Changing the lattice parameters influences the strength, stiffness and build quality of the structure. For example, lattices built closer to vertical are stronger and have a better build quality than those built horizontally [184, 226, 227]. This means that lattices built with more of their struts vertically are stronger, so lattice strength is dependent on build angle. Lattices with a smaller unit cell size are stronger as they have a larger volume fraction [238], or if the volume fraction is kept the same, the struts are smaller but with a better build quality [146].

The aim of this chapter is to identify if there are lattice designs with sufficient compressive strength to enable patients to weight bear while providing sufficient void volume for drug loading. This aim will be achieved by firstly identifying lattice designs which can be manufactured by L-PBF. Some limitations of this method will also be sought including understanding the print quality, minimum strut thickness and variability in strut thickness from design. Strut based lattices (BCC, BCCZ, cubic, diamond and fluorite) with strut thicknesses of 150 μm (thinnest consistently achieved in literature), 250 μm and 350 μm, and gyroid with nominal wall thicknesses of 60, 100, 150, 200, 250 μm will be printed and compression tested to find a lattice design with strength above 200 MPa and a void volume of at least 0.4.

Additionally lattices with different rotations and different unit cell lengths (1.0, 1.5

and 2.0 mm) will be built and tested under compression to understand which parameters must be considered during design. The lattices used for these additional studies will be BCCZ 250 because it is strongly anisotropic, Diamond 250 as it is less anisotropic, and Gyroid 150 which is a surface based lattice. The use of 250 μm thick struts for the BCCZ and diamond lattices enables these to be compressed on the Universal tester due to challenges with access to the ESH tester. The experimental results will be compared with the Gibson Ashby Model. The stiffness of all lattices will also be measured to see if the use of lattices could provide an additional benefit by reducing stress shielding.

2.2 Methods

2.2.1 General Methods

Material Feedstock

Gas atomised spherical Ti-6Al-4V grade 23 powder was used as the feedstock (LPW Technology Ltd, UK). Three powder batches were used during this work, and the new powder was blended with all previous powder in the machine silo. The powder composition values from the three batches were provided by the manufacturer and conformed with ASTM F3001. They are listed here as ranges based on the test certificates: Aluminium 6.3-6.4 % w/w, Vanadium 3.9-4.0% w/w, Oxygen 0.07-0.12% w/w, Iron 0.19-0.21% w/w, and Titanium was not measured but assumed to be the balance of around 89% w/w. Sieve analysis found 2-3% w/w of the powder was above 45 μm per ASTM B214. Laser size diffraction per ASTM B822 found 0.4-1.1 volume percentage of the powder was less than 16 μm.

Lattice Manufacture and Processing

Digital models of samples were produced using Element nTop Platform (nTopology, Inc, USA), and exported in .stl format. These were then sliced for manufacture using QuantAM vs. 4 (Renishaw, PLC, UK), which separates contour scans that follow the

edge of the part with an offset (50 μm) and hatching which infills the structure (figure 2.2). Sample manufacture was performed using an L-PBF system, specifically a RenAM 500M (Renishaw, PLC, UK), from Ti-6Al-4V powder described above, using a continuous wave 1070 nm Ytterbium fibre laser with a maximum power of 500 W. All samples were produced under argon atmosphere with O_2 below 1000 ppm, using a preheated Ti-6Al-4V substrate at 170°C, onto which powder is laid down in 30 μm thick layers.

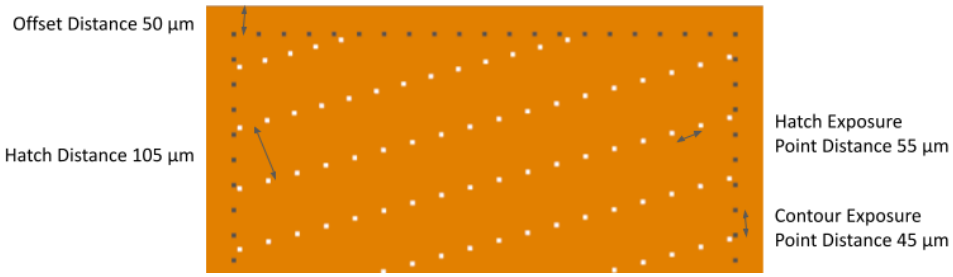

Figure 2.2: Diagram of slice of lattice CAD to show the hatch spacing, offset distance and exposure point distance

The RenAM 500M uses a modulated series of laser exposures where energy is delivered at a fixed point for a set time and then moves rapidly while turned off between points. For contour scans the exposure time was 40 μs and the point distance was 45 μm and speed is distance over time so this gives an effective scan speed of 1125 mms^{-1}, while for hatching scans the exposure time was 50 μs and the point distance was 55 μm giving an effective scan speed of 1100 mms^{-1}.

The contour lines are set 50 μm from the edge of the CAD, while the rows of hatch lines are set 105 μm apart, these rotate 67° between each slice. The laser uses a 75 μm spot diameter, and provides 100 W of power onto the contour lines and 200 W for the hatching points. Key processing parameter are provided in table 2.1. Excess powder was removed from the parts using water jetting (Quill Vogue powder wash, Quill International Group Ltd, UK). The samples were removed from the substrate using wire electrodischarge machining, Cut 20 (Beijing Agie Charmilles Ltd, China).

Table 2.1: L-PBF parameters used in this work

Parameter	Contour	Hatching	Description
Spot diameter	75 μm		Diameter of laser exposure point
Laser power	100 W	200 W	
Slice thickness	30 μm		Thickness of powder layers
Layer angle	67°		Rotation of hatch lines with respect to hatch lines in previous layer
Substrate temperature	170°C		Temperature substrate heated to before printing
Offset distance	50 μm		Distance between edge of CAD and contour line
Hatch distance		105 μm	Perpendicular distance between hatch lines
Exposure point distance	45 μm	55 μm	Distance between exposure points
Exposure point time	40 μs	50 μs	Dwell time of laser at each exposure point
Effective scanning speed	1125 mms^{-1}	1100 mms^{-1}	Equivalent speed if continuous laser path was used

2.2.2 Sample Methods

Samples were designed to investigate the effect of: unit cell type, lattice rotation, and unit cell size on mechanical properties. The samples were built in a L-PBF system where the powder is spread from back to front and the gas flow is from right to left (figure 2.3).

Samples to Compare Unit Cell Designs and Strut Thicknesses

The parameters used for samples generated to compare different unit cell designs and strut thicknesses are shown in table A1 in the Appendix. The samples were cylindrical with a height of 15 mm and diameter of 12 mm. The unit cells were cubic with a side length fixed at 1 mm in order to meet the criteria for ISO 13314-2011, specifically the diameter should be at least 10 times the average pore size and the height should be between one and two times the diameter. The unit cells used were BCC, BCCZ, cubic, diamond, fluorite and gyroid. While the strut thicknesses were 150, 250 and 350 μm for the strut based lattices

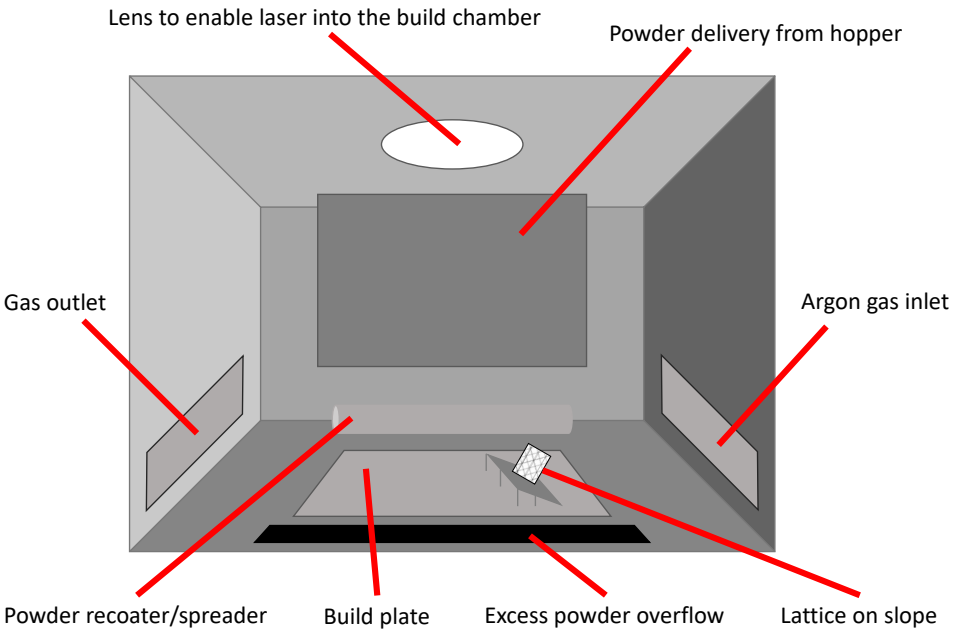

Figure 2.3: Diagram of the build chamber showing the powder is spread from back to front and the gas flow is from right to left. Parts built on slopes were angled towards the right hand side of the chamber

and the wall thickness were 60, 100, 150, 200 and 250 μm for the gyroid lattices. Cubic lattices were rotated 15° so that horizontal struts were not present.

Influence of Rotations on Compressive Strength

Lattices were rotated in three different ways in order to understand how these rotations influence their compressive properties. These were build, load and combined rotations (figure 2.4). The samples were all cylindrical with a height of 15 mm and a diameter of 12 mm, with 1 mm^3 unit cells. The lattices were BCCZ, diamond and gyroid, with strut thicknesses of 250 μm for BCCZ and diamond lattices, and a wall thickness of 150 μm for the gyroid lattices.

For the build rotation samples the same lattice designs as those used in the unit cell comparison study were placed on ramps at 0, 10, 20 and 30°, to investigate the influence of different build orientations of additively manufactured lattices. This replicates the influence of rotating parts within the build chamber. The sample parameters are in table A2 in the Appendix, this rotation causes the struts to be built at different angles to the

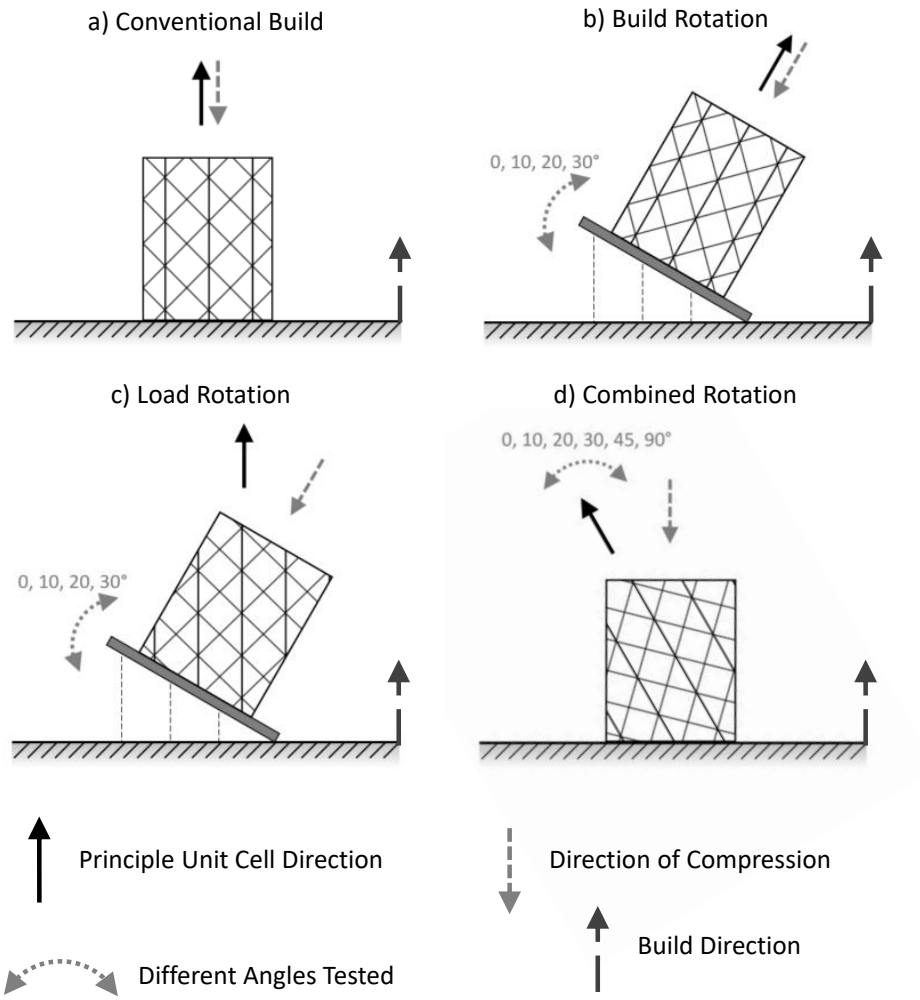

Figure 2.4: Diagram to explain the different ways the lattices were rotated during building. a) Conventional Build, b) Rotation of the Build Angle, c) Rotation of the Load Angle, d) Combined Rotation

0° case. Visualisations of the rotated unit cells can be seen in figures 2.5 and 2.6, with the angles listed in table 2.2.

Alternatively samples can be built on slopes but with the unit cells in the same orientations throughout, in which case this mimics the influence of varying the angle at which parts are loaded. Samples were rotated at 0, 10, 20 and 30°. The final type of rotation combines these two modes, in this situation the lattices are built directly onto the build substrate, and the unit cells are rotated within the sample.

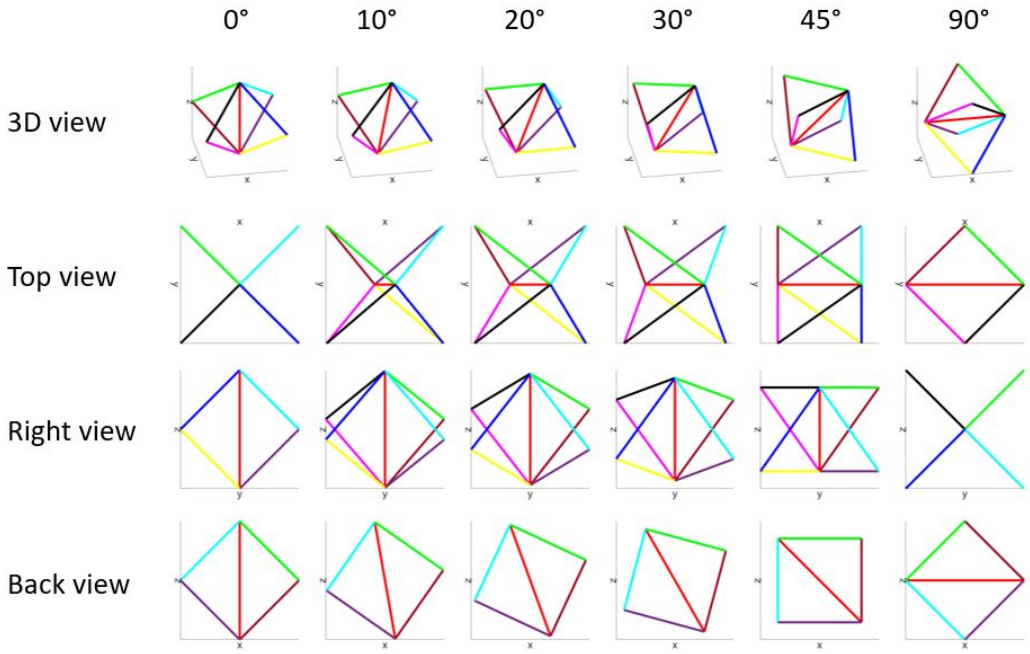

Figure 2.5: Diagram of the rotations of BCCZ unit cells from 0 to 90°. These were the orientations of the unit cells during build for build rotation, compression for load rotation, and build and compression for the combined rotation experiment

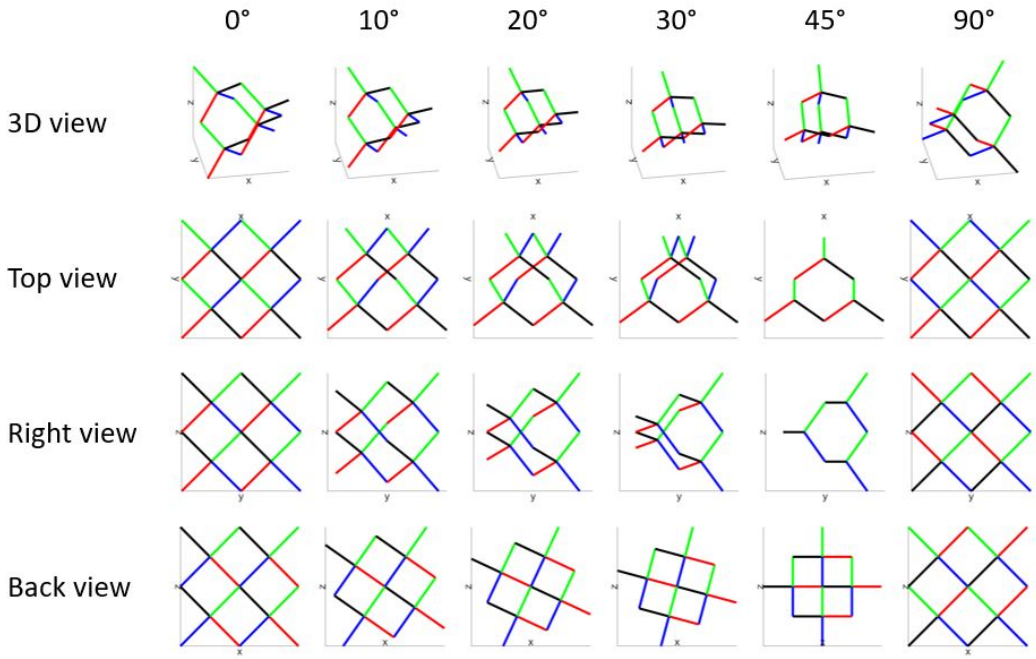

Figure 2.6: Diagram of the rotations of diamond unit cells from 0 to 90°. These were the orientations of the unit cells during build for build rotation, compression for load rotation, and build and compression for the combined rotation experiment

Table 2.2: Angle of struts during rotations. These were the strut angles during build for build rotation, compression for load rotation, and build and compression for combined rotation experiment

	Miller Index	0	10	20	30	45	90
				BCCZ			
Red	[001]	0.0	10.0	20.0	30.0	45.0	90.0
Blue	<111>	54.7	48.0	42.3	37.9	35.3	54.7
Black	<111>	54.7	62.1	69.8	77.8	90.0	54.7
Cyan	<111>	54.7	48.0	42.3	37.9	35.3	54.7
Green	<111>	54.7	62.1	69.8	77.8	90.0	54.7
Yellow	<111>	54.7	62.1	69.8	77.8	90.0	54.7
Magenta	<111>	54.7	48.0	42.3	37.9	35.3	54.7
Purple	<111>	54.7	62.1	69.8	77.8	90.0	54.7
Brown	<111>	54.7	48.0	42.3	37.9	35.3	54.7
				Diamond			
Red	<111>	54.7	62.1	69.8	77.8	90.0	54.7
Green	<111>	54.7	48.0	42.3	37.9	35.3	54.7
Blue	<111>	54.7	48.0	42.3	37.9	35.3	54.7
Black	<111>	54.7	62.1	69.8	77.8	90.0	54.7

Unit Cell Size

In order to test the effect of unit cell size on the mechanical properties of lattices, samples with unit cell lengths of 1.0, 1.5 and 2.0 mm were produced. The samples were cylindrical with a height and diameter of 20 mm to allow 10 unit cells in each direction in order to comply with ISO 13314-2011. The lattices were BCCZ with 250 μm thick struts and diamond with a 150 μm strut thickness. Gyroid lattices were designed with the same volume fraction of 49%. The 1.0 mm unit cells had wall thicknesses of 150 μ, the 1.5 mm unit cells had wall thicknesses of $\sim$ 200 μm, and the 2.0 mm unit cells had wall thicknesses of $\sim$ 250 μm. The sample parameters are in the appendix, table A5.

2.2.3 Analysis

Scanning Electron Microscopy and Analysis

Back scattered electron SEM micro-graphs were taken at three locations on the top, back and right side of each sample, with respect to the build chamber (figure 2.3) (TM3000, Hitachi High-Technologies Corporation, Japan). To analyse the thickness of the struts, the micro-graphs were imported as an array of grayscale values into Matlab (MathWorks Inc, USA). Five lines were manually identified perpendicular to each strut including some of the void (figure 2.7a), the intensity profile of the line was then created (figure 2.7b). The median value within the image was used as a threshold, with the first and last intersections used to identify the width of the strut in number of pixels. The angle of the line and the scale bar are then used to convert this measurement into millimeters.

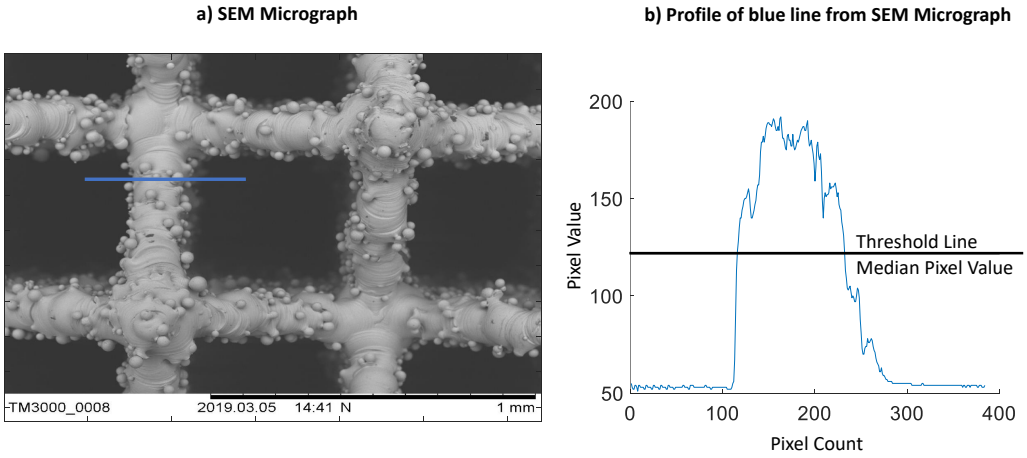

Figure 2.7: Diagram to explain how strut thickness is measured, a) SEM of lattice showing perpendicular line in blue, b) intensity profile of the line

Measuring the Lattice Volumes

One method used to measure the volume of the lattice samples was an Archimedes balance (Adventurer Analytical balance with density determination kit, Ohaus Corp, USA) where the samples were weighed in air (figure 2.8) and ethanol (Fisher Scientific Ltd, UK) in order to calculate the density and volume of the part according to equation 2.2.1. Where

V is the lattice volume (ml), α is the balance correction factor (0.99985), A is the mass of the lattice in air (g), and B in ethanol, ρ_o is the density of ethanol and ρ_l is the density of air (g cm^{-3}).

$$V = \alpha \frac{(A - B)}{(\rho_o - \rho_l)} \tag{2.2.1}$$

Alternatively the mass of the lattices can be measured in air and divided by the density of Ti-6Al-4V to give the volume. The volume fraction was the fraction of the cylinder taken up by the lattice, while the overbuild was the measured volume of the lattice with the design volume subtracted. The percentage overbuild was the overbuild divided by the design build multiplied by 100.

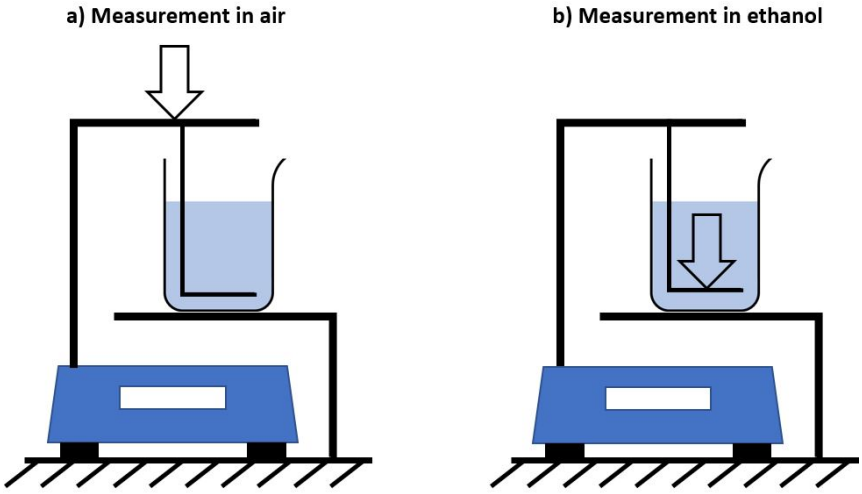

Figure 2.8: Diagram of Archimedes method for calculating volume, a) measuring mass in air, b) measuring mass in ethanol

Compression Testing

Prior to compression testing the diameter and height of the cylindrical samples was measured in triplicate using calipers. Compression testing was performed in accordance with ISO 13314:2011. Samples were placed in the centre of the platens of the Z030 universal testing machine (Zwick, UK) with a 500 kN load cell unless the max strength is above 200 kN at which point tested on ESH servo-hydraulic fatigue testing machine (ESH limited,

UK). Testing was performed under displacement control at a rate of 4.5 mm min^{-1} until the first of either 50% total strain or a maximum load of 200 kN was reached (max load for samples tested on the Universal tester due to loading constraints of the frame).

Force displacement data was imported into Matlab (MathWorks Inc, USA) where it was combined with the diameter and height of the cylindrical samples to generate stress strain data (equations 2.2.2 & 2.2.3), which was then plotted. The elastic region of the stress strain curve forms a straight line, the gradient of which is the Young's Modulus. The ends of the elastic region were manually identified, and then the data in this region was fitted to a straight line using the inbuilt function polyfit which uses the least-squares regression method. The Young's Modulus was taken as the gradient of this line. A 0.2 % strain offset from the linear fit region was plotted to provide the 0.2 % proof stress where it met the stress strain curve. This is typically recognized as an approximation to yield stress.

$$\text{Stress} = \frac{4 * \text{Force}}{\pi * \text{Diameter}^2} \tag{2.2.2}$$

$$\text{Strain} = \frac{\text{Displacement}}{\text{Original Height}} \tag{2.2.3}$$

Gibson Ashby Analysis

The 0.2% offset stress and Young's Modulus values were plotted against measured volume fraction for all the samples. The Matlab function fit power1 was fitted to all the data together, and to all for each unit cell, with the R^2 value used to determine goodness of fit. This function takes the form in equation 2.2.4, where C is the coefficient and n is the exponent.

$$\text{Offset stress or Young's Modulus} = C * \text{volume fraction}^n \tag{2.2.4}$$

Statistical Analysis

For all experiments three independent samples were generated for each variable. Statistical analysis was performed using Matlab (MathWorks Corp, USA). Initially a one way ANOVA test was performed to see whether all the data has an equal mean, if they did not then Tukey post hoc testing was performed to identify which means were statistically different.

2.3 Results

2.3.1 Geometric Accuracy of Manufactured Lattices

Volume Fraction

All samples built with no visual evidence of missing struts. To compare the lattice design with the manufactured geometry, both mass and Archimedes balance measurements were used to estimate the volume fraction of the unit cell comparison lattices. Both mass and Archimedes balance measurement were found to be highly repeatable processes with standard deviations of the volume fraction measurements of less than 2% except for Fluorite 150 and 250. For these the standard deviation was 2.82 and 3.49% of the volume fractions respectively for the measurements using the Archimedes method. The standard deviation for the mass in air method was below 2% for all measurements. For most samples there was no statistical difference between the volume fraction estimates produced by the two methods, however differences were seen for Fluorite 250 and 350, and Gyroid 200 and 250 which had some of the highest design volume fractions of all the lattices at 0.44, 0.92, 0.66 and 0.84 respectively (figure 2.9a).

The designed volume fractions fell below the measured values for all samples except Fluorite 350 (figure 2.9b). With the absolute overbuild volume by mass measurement ranging from 59.6 $\pm$ 0.3 mm^3 for Cubic 150 to 247.0 $\pm$ 1.1 mm^3 for Gyroid 60. For strut based lattices within a unit cell the 150 μm lattice had lower absolute overbuild

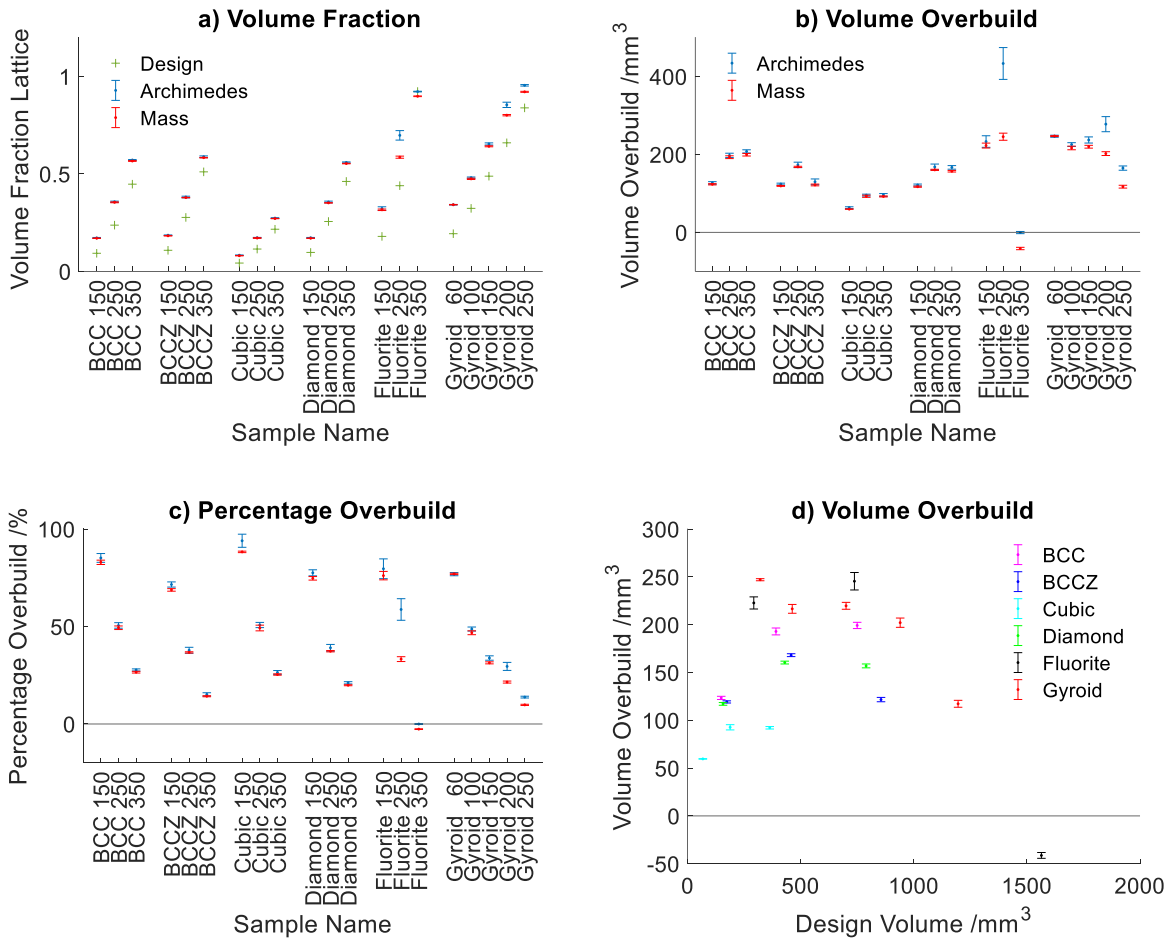

Figure 2.9: Comparing mass in air and Archimedes Balance as methods of estimating volume fraction of built lattices, a) volume fraction measurements, b) absolute volume overbuild, c) percentage overbuild above design volume, d) comparing measured lattice volume by mass with the design volume. Error bars are one standard deviation, n=3

than the 250 and 350 μm samples (figure 2.9b), while percentage overbuild decreased with increasing strut thickness (figure 2.9c). For the gyroid lattices the absolute and percentage overbuild decreased with increasing wall thickness (figure 2.9b&c). For the Fluorite 350 samples the Archimedes method gave a predicted volume fraction range that included the design volume. In contrast the mass measurements predicted a volume $41.3 \pm 3.0\ mm^3$ below the design volume. For fifteen of the twenty lattice designs the volume predicted by the Archimedes Balance was within 2% of that predicted by the mass measurements, this includes five designs which were within 1%. For the rest the Archimedes method provided a higher estimate of volume ranging from 3.03% for Cubic

150 to 19.1% for Fluorite 250. When all the mass estimates for volume are plotted against the design volume in figure 2.9d there are no clear trends across all the unit cells.

Given the smaller variability and ease of use of using mass in air to calculate volume fraction, as well as the fact that for most samples there was no statistical difference between the methods, mass in air measurement will be used in the rest of this work to calculate volume fraction.

Strut Diameter

Scanning electron microscope (SEM) micrographs of the top of the unit cell comparison samples were taken to compare how the built strut thicknesses differed from the design. For the Fluorite 350 lattices the struts were thicker than the distance between struts such that they conjoined (figure A.1a), thus measurements could not be taken. Additionally the gyroid lattices are surface based not strut based so are not part of this analysis. Although strut based lattices have a nominal wall thickness this is not consistent throughout the unit cell and so the precise location of a measurement is needed in order to compare with the design value which was not practical in this analysis (figure A.1b). For the samples with a designed strut thickness of 150 μm the BCC lattice had the highest measured thickness of 183 $\pm$ 20 μm while the lowest was cubic with 157 $\pm$ 25 μm. All the samples' means were greater than the designed thickness (figure 2.10a).

The ranges of measured values for all the 250 μm lattices include the design thickness (figure 2.10b). The thinnest was cubic at 230 $\pm$ 28 μm, while the highest thickness was for BCC at 254 $\pm$ 29 μm, although there was no statistical difference between the cubic, diamond and fluorite measurements. Among the 350 μm strut lattices the thickest and thinnest struts came from the BCC and cubic again, with thicknesses of 362 $\pm$ 33 and 324 $\pm$ 47 μm respectively. Post hoc testing showed the cubic lattice struts were statistically different for the other lattice designs (figure 2.10c).

When strut thickness is calculated as a percentage of the design thickness it can be seen that the 150 μm lattice are proportionally thicker. While for a given unit cell the

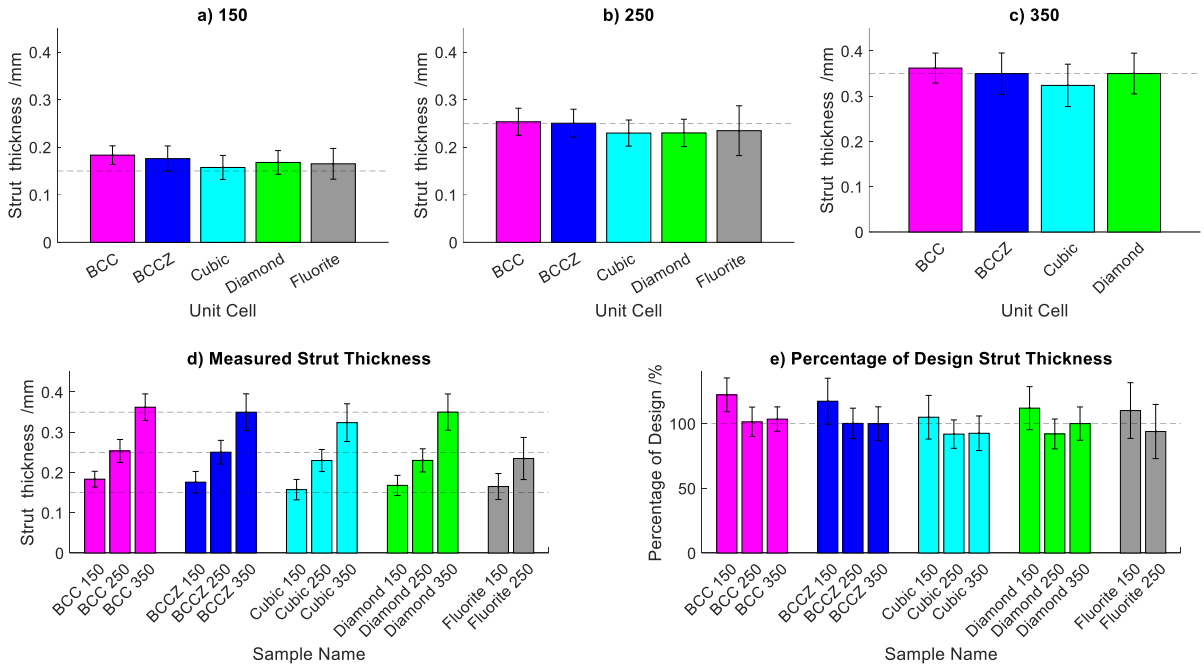

Figure 2.10: Measured values of strut thickness taken from the top view of the lattices used for the unit cell comparison study. Fluorite 350 was not measured as the struts combined, and gyroid was not measured as it is a wall based lattice. a,b,c) 150, 250 and 350 μm designed thickness lattice, d) all lattice measured thicknesses, e) percentage overbuild compared with design. Error bars are one standard deviation, n=3

250 and 350 μm struts tend to be either both thicker or both thinner than the design (figure 2.10e). For the diamond lattices the 250 μm struts are thinner than the design value while the 350 μm struts had a mean of 350 μm. Six sets of lattices have means within 5% of the design thickness - specifically BCC 250 and 350, BCCZ 250 and 350, Cubic 150 and Diamond 350.

Observations of Strut Morphology

SEM micrographs (figure 2.11) show differences in particle adhesion density between the sides of the lattice with the right (figure 2.11d) having a lot of particles and the top being sparse (figure 2.11a). On the front, back and left views greater particle adhesion can be seen on the lower edge of the strut compared to the upper edge. It can also be seen that the struts are not a uniform width. For example on the left view the vertical [001] strut (circle arrow) appears thinner than the angled <111> struts (square arrow) and on the

front and back views the struts which were built closer to horizontal (star arrows) appear thicker than those which were built at a more vertical angle (pentagon arrows). The top view struts appear thinner than some side view struts.

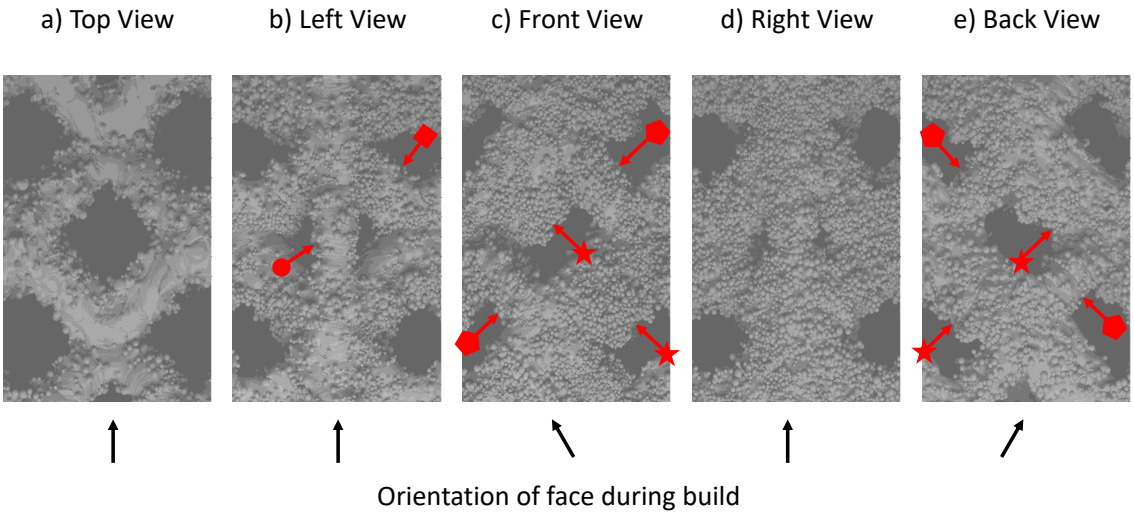

Figure 2.11: SEM micrographs of a BCCZ lattice with 250 μm struts built at 30°. a) the top view of the lattice showing minimal particle adhesion, b) viewed from the left of the build chamber with the [001] strut labelled with circle arrow thinner than the <111> struts labelled with the square arrow, c) lattice viewed from the front of the build chamber with struts which were built closer to horizontal visibly thicker (star arrows) than those built closer to vertical (pentagon arrows), d) the lattice viewed from the right showing extensive particle adhesion, e) the lattice viewed from the back showing mismatched strut thicknesses

The Influence of Angle on Strut Thickness

It was found that struts successfully built at all the designed angles which included horizontal. The struts were designed to be 250 μm thick which fell within the the range of measurement values from the top view (figure 2.12a), whereas 250 μm fell outside the measurement ranges for most of the strut angles for both the right and back views (figure 2.12b&c), this indicates that the struts are not entirely cylindrical (as cylindrical struts would give the same measurement values from all views). Within the BCCZ unit cell there are struts that form parts of the original BCC unit cell which have the Miller index <111> and then the addition Z struts with Miller index [001].

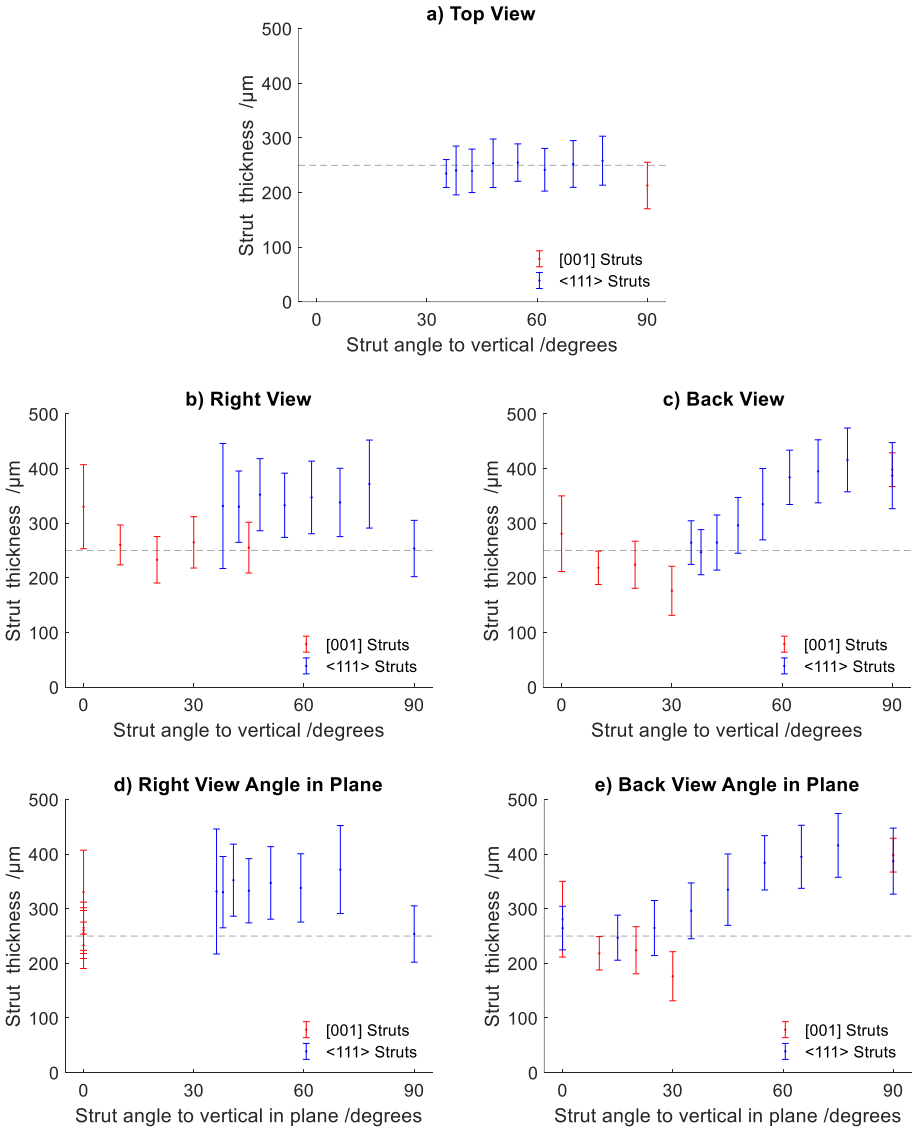

Figure 2.12: Strut thicknesses of individual struts by angle built from vertical, i.e. 0° is vertical and 90° is horizontal. a) Strut thicknesses from the top view showing no statistical differences between the <111> struts, while the [001] struts at 90° to vertical are statistically thinner. b) strut thicknesses from the right view showing no clear trend in strut thickness with angle c) strut thicknesses when measured from the back of the lattices increased with angle for <111> struts except at 90°, while [001] struts decreased in thickness with angle. d) when the strut thicknesses were compared with the in plane strut angle from the right view all the [001] struts were vertical, while the <111> struts had no trend except that the 90° struts were thinner, while from the back view e) the <111> struts increased in thickness with angle with 0 and 90° struts breaking the trend, while [001] struts decreased in thickness with angle. No graph is shown of in plane strut angles from top view because all angles would be the same. Struts are from BCCZ lattices with designed strut thicknesses of 250 μm, horizontal line at 250 μm is the design thickness. Error bars are one standard deviation

For the top views of the lattices the [001] struts are not visible except in the combined rotation experiment when the unit cells are rotated 90° within the lattice. In this instance the [001] appear at 90° to the vertical and are therefore visible from the top view (figure 2.5). The <111> struts had thicknesses around the design thickness of 250 μm when measured from the top view. There was no statistical difference between the thicknesses by ANOVA testing, however there was a statistical difference between the thicknesses of the [001] and <111> struts which were thinner.

For the right view (figure 2.12b) two trends are seen, the [001] struts decrease in thickness from 330 $\pm$ 77 μm at 0° to 254 $\pm$ 52 μm at 90°. The <111> struts show no clear directional trend. However there were statistical differences in the strut thickness, for example those at 77.0° and 90.0° were thinner than the rest by post hoc testing.

The <111> struts show an upward trend in thickness with angle from vertical for the back view (figure 2.12c), with the thickness increasing from the minima of 247 $\pm$ 41 μm at 37.9° to 416 $\pm$ 58 μm at 77.8°. The [001] struts decreased in thickness from 281 $\pm$ 69 μm at 0° to 176 $\pm$ 45 μm at 30°, while at 90° the thickness measure was 393 $\pm$ 48 μm. There was no statistical difference in the horizontal struts from the back view regardless of their location within the unit cell.

The strut thicknesses were also compared with the in plane strut angles, although not for the top view as the plane is at 90° to the vertical so there is not point of reference. For the right view samples all the [001] struts are vertical in this plane (figure 2.12d), while the <111> struts have similar angles, so the trends are the same.

For the struts viewed from the back the [001] struts are at the same angles, while the <111> struts are spread over the whole range of angles (figure 2.12e). Thus it can be seen that the [001] struts are thinner than the <111> struts at similar angles, except at 0 and 90° where there is no statistical differences in the strut thicknesses.

2.3.2 Comparing the Mechanical Performance of Six Unit Cell Designs

An example stress-strain compression curve of each lattice unit cell type (250 μm for strut based and 150 μm for gyroid) is shown in figure 2.13. The general trend is for an elastic region followed by yielding, a plateau region and then densification. The BCC and BCCZ lattice exhibit plateau regions with general downward trends in stress with an uneven profile.

The cubic and diamond lattices have plateau regions with periodic oscillations, a frequency of 1 peak per 0.06 strain for the cubic lattice and a frequency of 1 peak per 0.03 strain for the diamond lattice. During these oscillations the stress reaches values similar to the yield stress before dropping to below a quarter of the yield stress for the cubic lattice and below a third of the yield stress for the diamond lattice.

The stress strain profile of the fluorite lattice has a vertical drop in stress after the yield point to just above a quarter of the yield stress. This is followed by a plateau region where the stress climbs back to the yield stress in an uneven manner. For the gyroid lattice the stress climbs over the whole profile, first in the elastic region and then at a reduced rate during plastic deformation.

0.2% Offset stress line was used to approximate the yield stress to give an indication of the strength of the lattices. For all lattice designs increasing the strut or wall thickness increased the offset stress (figure 2.15a). Increasing thickness also led to stiffer lattices, with the exception of the gyroid with 60 μm thick walls which was slightly stiffer than Gyroid 100 (figure 2.15b). The cubic lattices were the weakest, with the strongest cubic lattice with a strut thickness of 350 μm having an offset strength of 59.4 $\pm$ 1.4 MPa which is weaker than all of the fluorite and gyroid lattices, and weaker than the 250 μm lattices of BCC, BCCZ and diamond.

Fluorite was the strongest strut based lattice design used here, with the 350 μm strut design having a strength of 934 $\pm$ 20 MPa. The gyroid lattices were the strongest overall with the Gyroid 250 lattice having a 0.2% offset stress of 995 $\pm$ 18 MPa. Young's Modulus

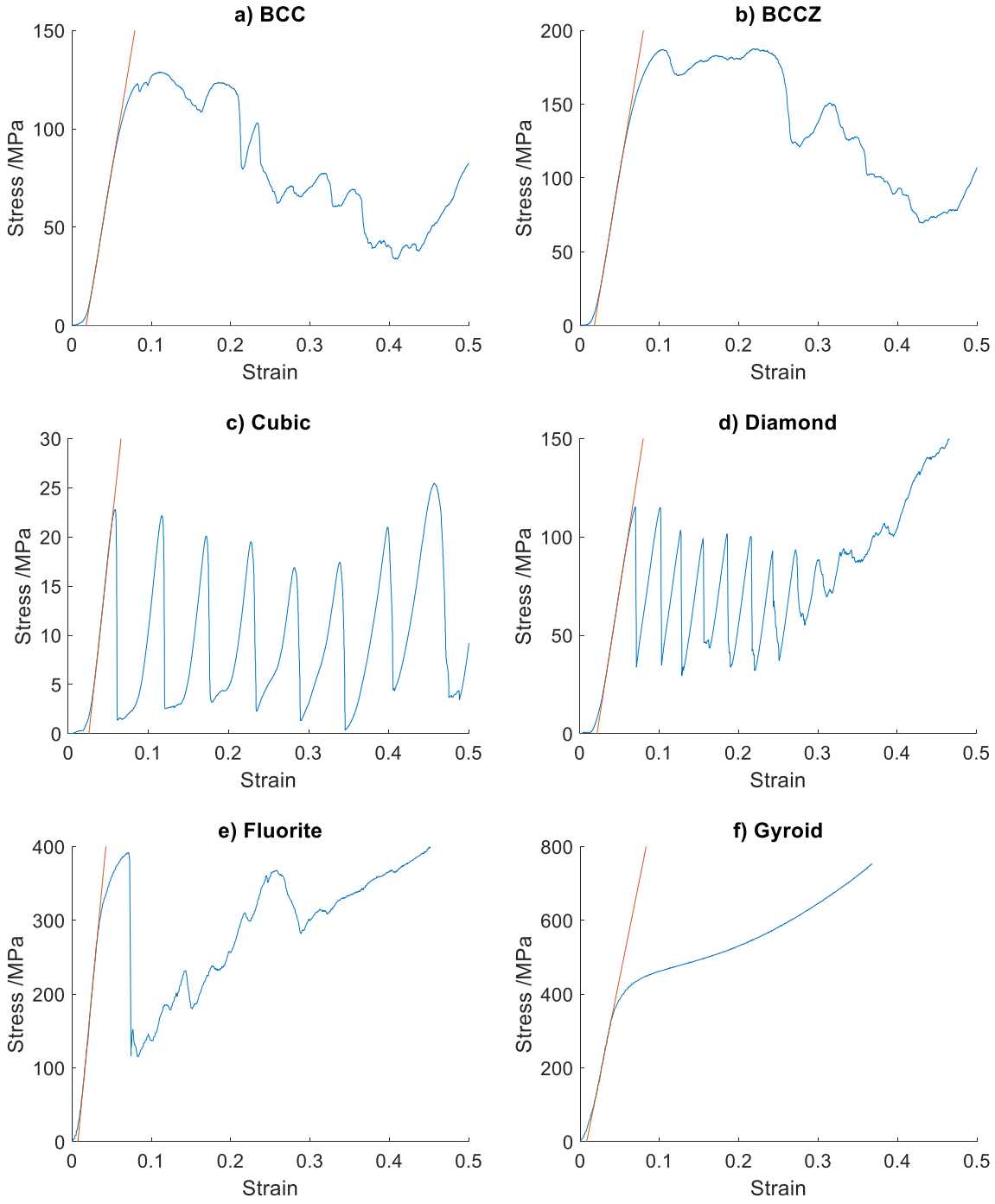

Figure 2.13: Example compression curves for BCC, BCCZ, cubic, diamond and fluorite lattices with 250 μm thick struts and gyroid lattice with 150 μm wall thickness. The Young's Modulus is shown in red

results followed much the same pattern with the stiffest lattice at 19.0 $\pm$ 0.4 GPa being the Gyroid 250 and the least stiff design coming from Cubic 150 at 0.09 $\pm$ 0.00 GPa.

By plotting the strength and Young's Modulus against volume fraction the correlation

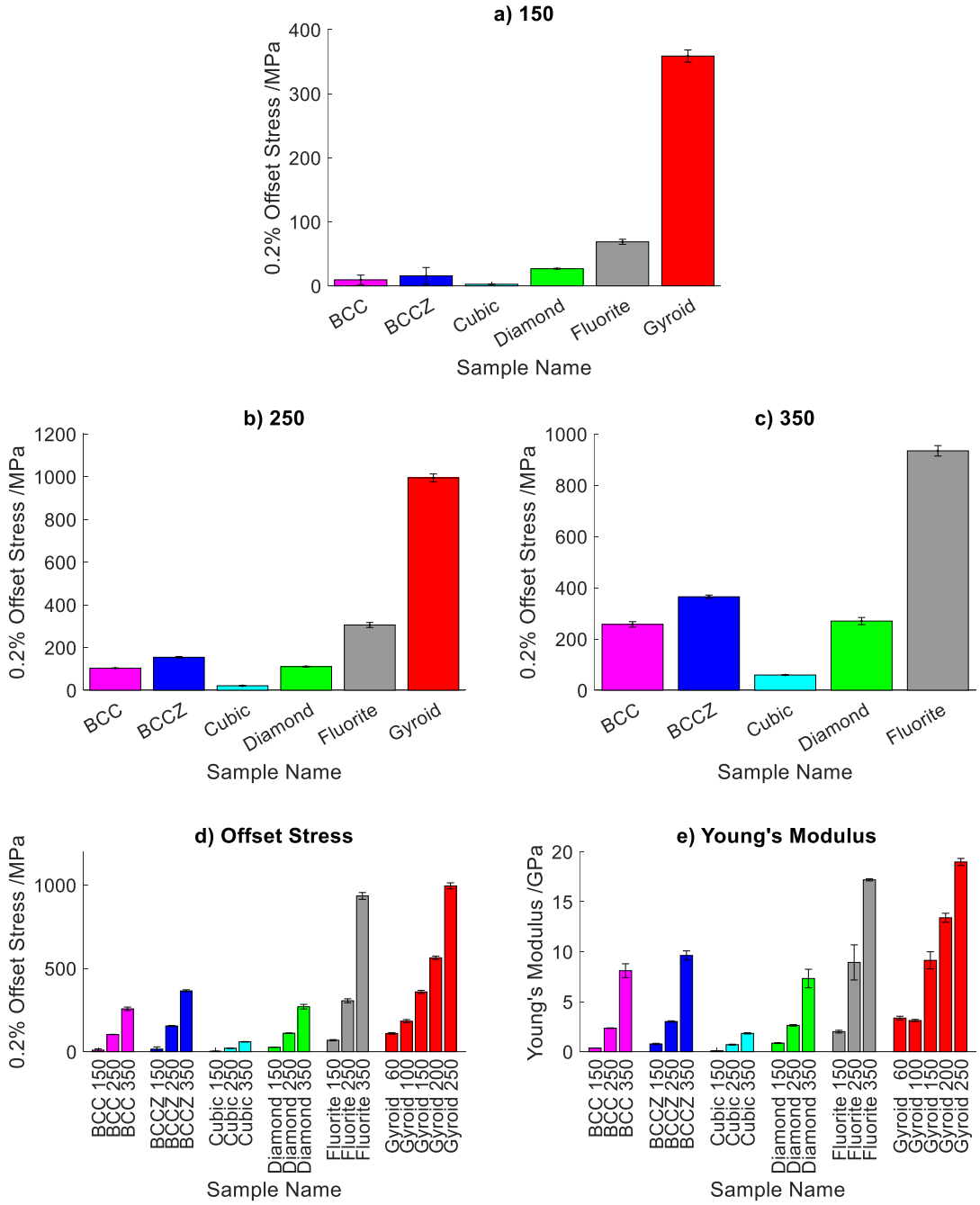

Figure 2.14: 0.2% offset stress and Young's Modulus values for unit cell comparison samples. Offset strength by designed strut thickness a) 150, b) 250, c) 350 showing gyroid had the highest strength and cubic the lowest for all strut thicknesses. d) Offset stress for all data showing the stress increases with strut thickness for all unit cell designs, e) Young's Modulus for all designs showing stiffness increases with strut thickness, and the the gyroid lattices were the stiffest and cubic the least stiff. Error bars are one standard deviation, n=3

between the two can be seen, with larger volume fractions leading to higher strength and stiffer lattices (figure 2.14a&b). A power law curve was fitted to both the strength and Young's Modulus data with equations 2.3.1 and 2.3.2 respectively.

$$\text{Offset stress} = 1170 * \text{volume fraction}^{2.48} \tag{2.3.1}$$

$$\text{Young's Modulus} = 21.7 * \text{volume fraction}^{1.90} \tag{2.3.2}$$

Generally there appears to be good correlation between volume fraction and mechanical strength, however there are notable influences of unit cell design when comparing similar fraction samples. The BCCZ 350 is 40% stronger than BCC 350 but with only 3% more volume fraction. Additionally the BCCZ 250 and 350 lattice sit above the curve while the Gyroid 200 sits below the curve.

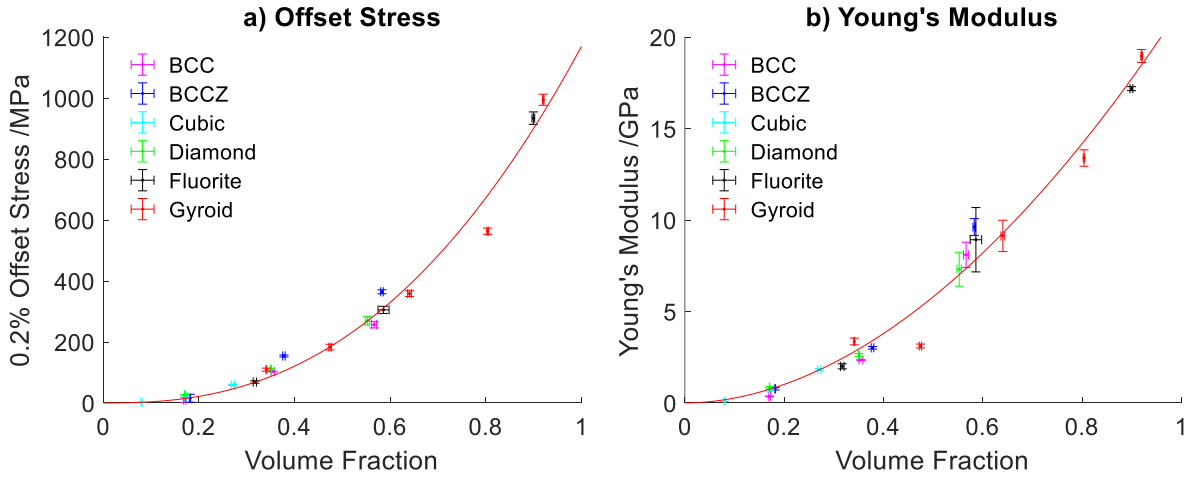

Figure 2.15: a) 0.2% offset stress and b) Young's Modulus values for all unit cell comparison samples, with power law curves fitted with equations Offset stress $= 1170 *$ volume fraction$^{2.48}$ and Young's Modulus $= 21.7 *$ volume fraction$^{1.90}$

For the stiffness curve BCCZ 350 sits the furthest above the curve while Gyroid 100 is furthest below the curve. There are a number of samples above the strength of bone ($\sim$ 200 MPa [215]) but with a volume fraction below that aimed for in this work (0.6). With the aim of having sufficient void volume for a secondary phase, namely BCC 350, BCCZ 350, Diamond 350, and Fluorite 250. These also have stiffnesses below that of bone ($\sim$ 17 GPa [213, 214]) with the aim that they do not contribute to stress shielding.

SEM micrographs of the lattice prior to compression (figure 2.16) show differences between the top and side views of the lattices, for example reduced particles adhesion on the top view. Additionally, thicker struts can be seen on the side view especially for the cubic lattices where the nearly horizontal strut is thicker than those that are closer to vertical. This is consistent with results shown in section 2.3.1.

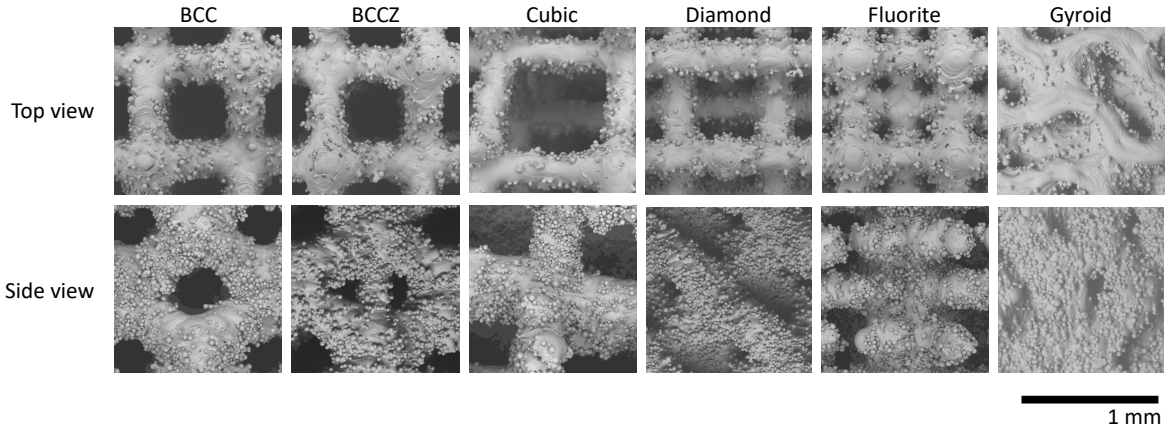

Figure 2.16: SEM micrographs of lattices used to compare unit cells. Strut based lattices shown with 250 μm struts and gyroid shown with 150 μm thick walls

Photographs were taken of the lattices after compression to compare the failure modes (figure 2.17). Shear bands were generally seen in the strut based lattices along lattice planes. The BCC lattices exhibited shear failure along planes at 45° to vertical, some bending, collapse and barrelling was also seen. Although shear failure at 45° was seen in the BCCZ lattices the continued loading led to further collapse in a more adhoc way, including at other angles.

The cubic lattices show shear failure in plane, these lattices are rotated at 15° so that horizontal struts were not present. Bending and buckling are also seen. The diamond lattice shows evidence of both crush failure and shear bands at 45°. Fluorite lattice have planes at 45° and shear band failure through this plane can be seen here in addition to crush failure for the 150 μm lattices. All the gyroid lattices show barrelling, with the 200 and 250 μm lattice also exhibiting shear failure but not in flat planes, and the Gyroid 60 lattice experiencing crushing in the 45° plane.

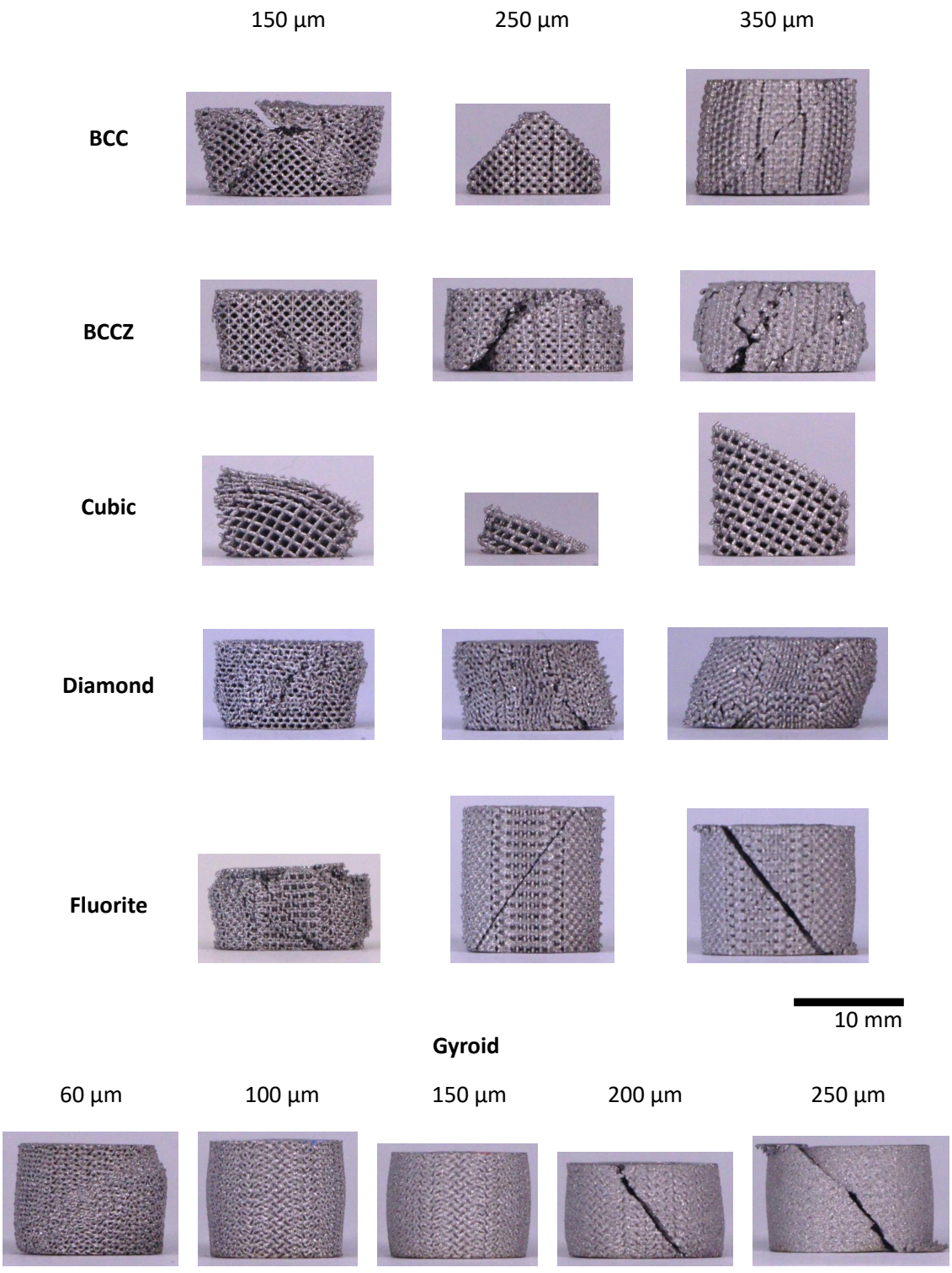

Figure 2.17: Photos of lattices after compression so failure modes can be seen

2.3.3 Lattice Rotations

Across the three unit cell designs it can be seen that the build rotate samples have the lowest strength and the load rotate lattices have the highest strength for any given angle. The build rotate lattices are weaker at angles greater than 0° for all the different unit cells.

For the BCCZ lattices all the angled lattices had a lower strength than those at 0°. For the load and combined rotate lattices there is a downward trend in strength with angle, which is more pronounced for the combined angle. For the build angle rotation there is a drop in strength between 0 and 10° and then no statistical difference in strength between the other angles.

The build rotation diamond lattices show a statistically significant decrease in strength with increasing angle. The load rotate lattices decrease in strength from a maxima at 10° of 126 ± 2 MPa, while the lowest strength of 111 ± 2 MPa was at 0°. The combined rotate lattices increase in strength with angle from a minima at 10° of 102 ± 7 MPa to 128 ± 4 MPa at 90°.

The gyroid lattices have a drop in strength under build rotation from 0° to 10° and then no statistical difference in strength with angle. While the strength increases with load angle up to a maxima of 393 ± 12 MPa at 30°. For the combined rotate the angle does not statistically influence the strength.

The trends of rotation with stiffness are less clear. The gyroid lattices are stiffer than the BCCZ and diamond lattice. The stiffness of the BCCZ lattices was lower at 45 and 90° than the lower angles. The combined rotate lattices were less stiff than the build and load rotate lattices when they had diamond or gyroid unit cells. For all the unit cells the load rotate lattices had lower stiffness at 0 and 20° than 10 and 30°.

Deformation photographs offer clues as to the causes of these changes in strength and stiffness (figure 2.19). For the BCCZ lattices where the build angle was rotated, all angles exhibited shear fracture along the 45° plane through the thinner plane of struts (which were closer to vertical during build). The load rotated BCCZ lattices showed some

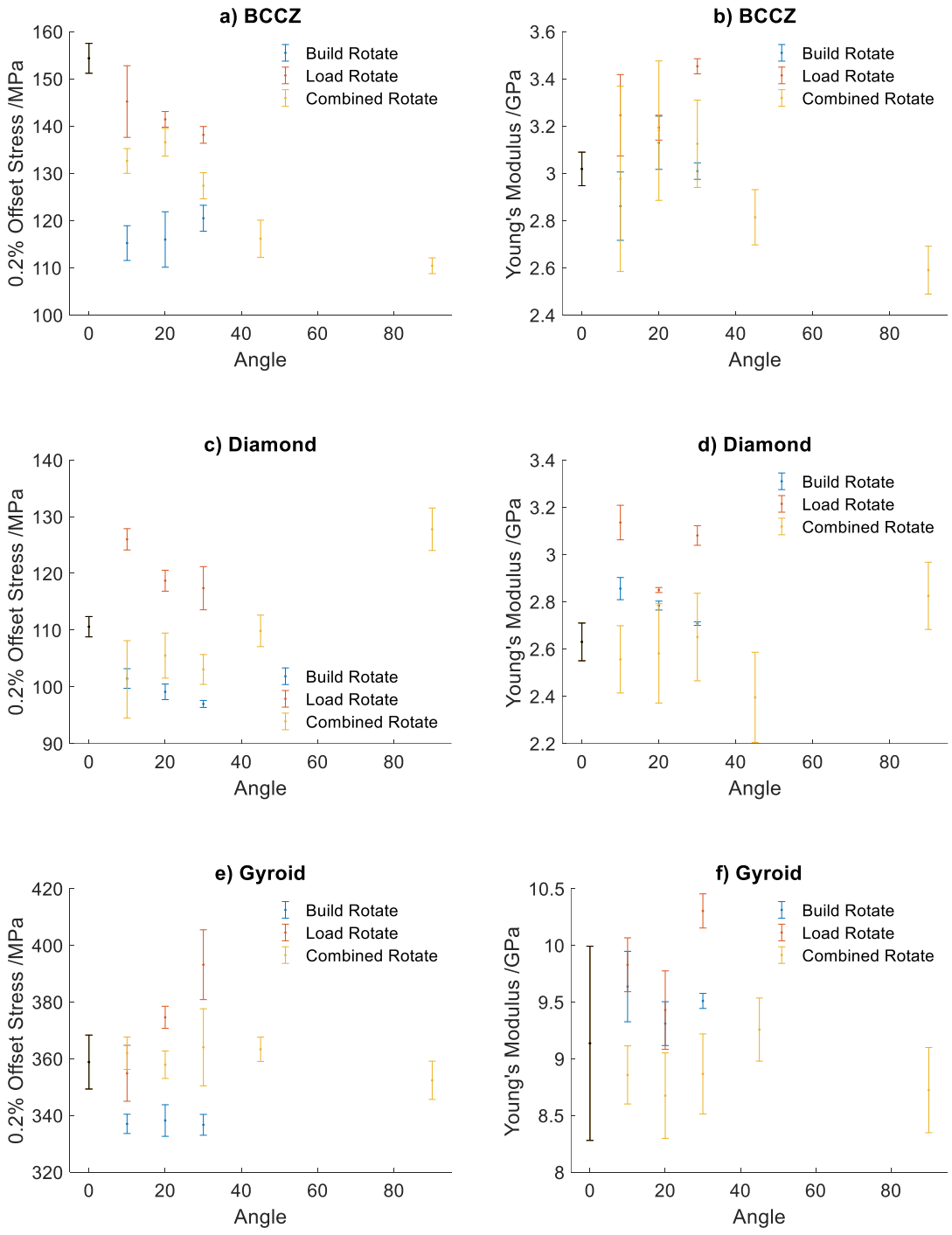

Figure 2.18: 0.2% offset stress and Young's Modulus values for BCCZ, diamond and gyroid lattices at different rotations. Error bars are one standard deviation, n=3

cracking. For the 20 and 30° samples these may be shear planes at 65 and 75° to vertical respectively. For the combined rotate lattices, banded crush failure can be seen for the 10, 20, 30 and 45° lattices. The 90° lattice displays a shear plane at 45°. The diamond

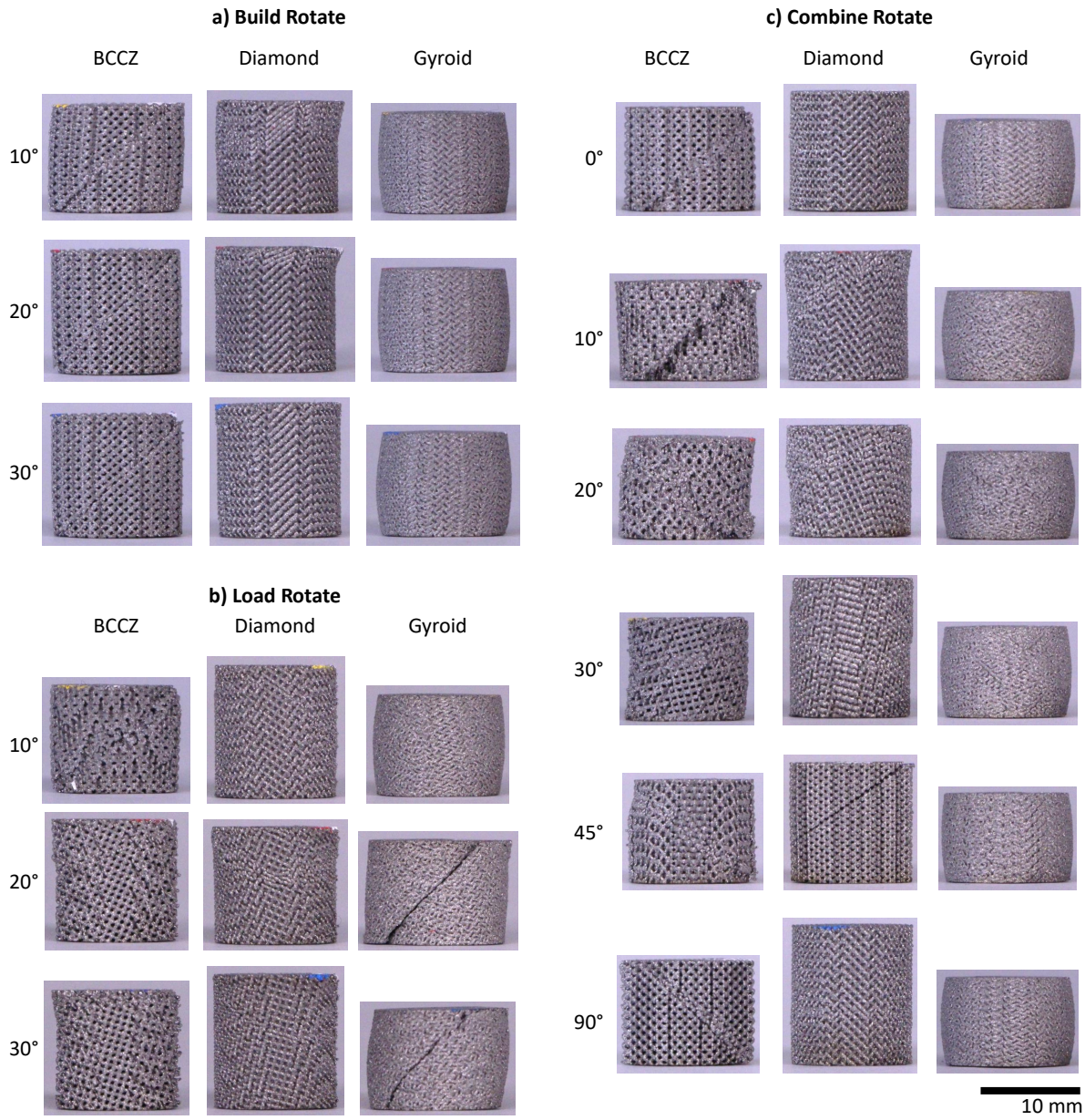

Figure 2.19: Photographs of lattices after compression to show the deformation behaviour. The same 0° samples were used for all rotations so only shown once in the combined rotate column

lattices crushed when built rotated. The load rotated diamond lattice cracked, but not in single planes. While the combine rotated diamond lattices showed shear failure in the 30 and 45° cases, angled cracking at 10 and 20°, with horizontal crush failure at 0 and 90°. Gyroid lattices experienced barrelling in all cases, with load rotate 20 and 30° samples also shearing.

2.3.4 Unit Cell Size

By increasing the unit cell size the effects of longer struts can be seen on the strength, stiffness and failure mechanisms of the lattices. Increasing the unit cell size decreased the strength of BCCZ and diamond lattices (figure 2.20a), while there was not statistical difference in the strength of the gyroid lattices. BCCZ had a 13 fold reduction in strength from a unit cell size of 1.0 mm to 2.0 mm from 149 ± 3 MPa to 11.0 ± 0.2 MPa. While the reduction in strength for diamond was 11 fold.

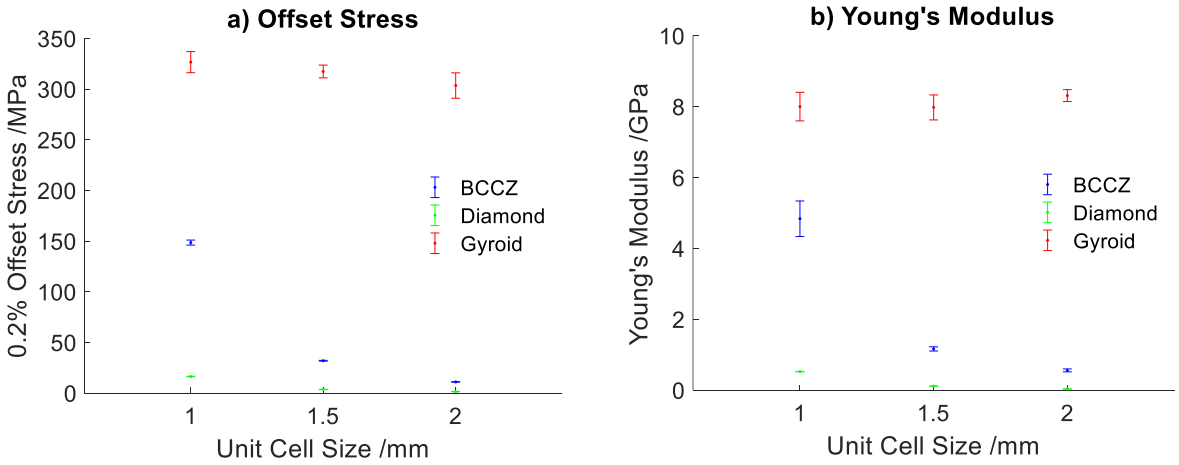

Figure 2.20: 0.2% offset stress and Young's Modulus values for lattice built at different unit cell sizes. Error bars are one standard deviation, n=3

The Young's Modulus was also not statistically different with different unit cell sizes for the gyroid lattices. The BCCZ and diamond on the other hand saw a reduction in stiffness with increasing unit cell size. For BCCZ this was an eight fold reduction from 4.83 ± 0.50 GPa to 0.56 ± 0.04 GPa and for diamond this was a 17 fold decrease from 0.52 ± 0.00 GPa to 0.03 ± 0.00 GPa from 1.0 to 2.0 mm. Photos of the deformation (figure 2.21) show BCCZ lattices with shear planes at 45°, the diamond lattices with horizontal crushing and the gyroid lattices barrelling. The gyroid lattice with 2.0 mm unit cells also has a crack at approximately 45°. The 2.0 mm BCCZ shows angled struts in the failure plane rotating at the nodes, while the vertical struts are buckling.

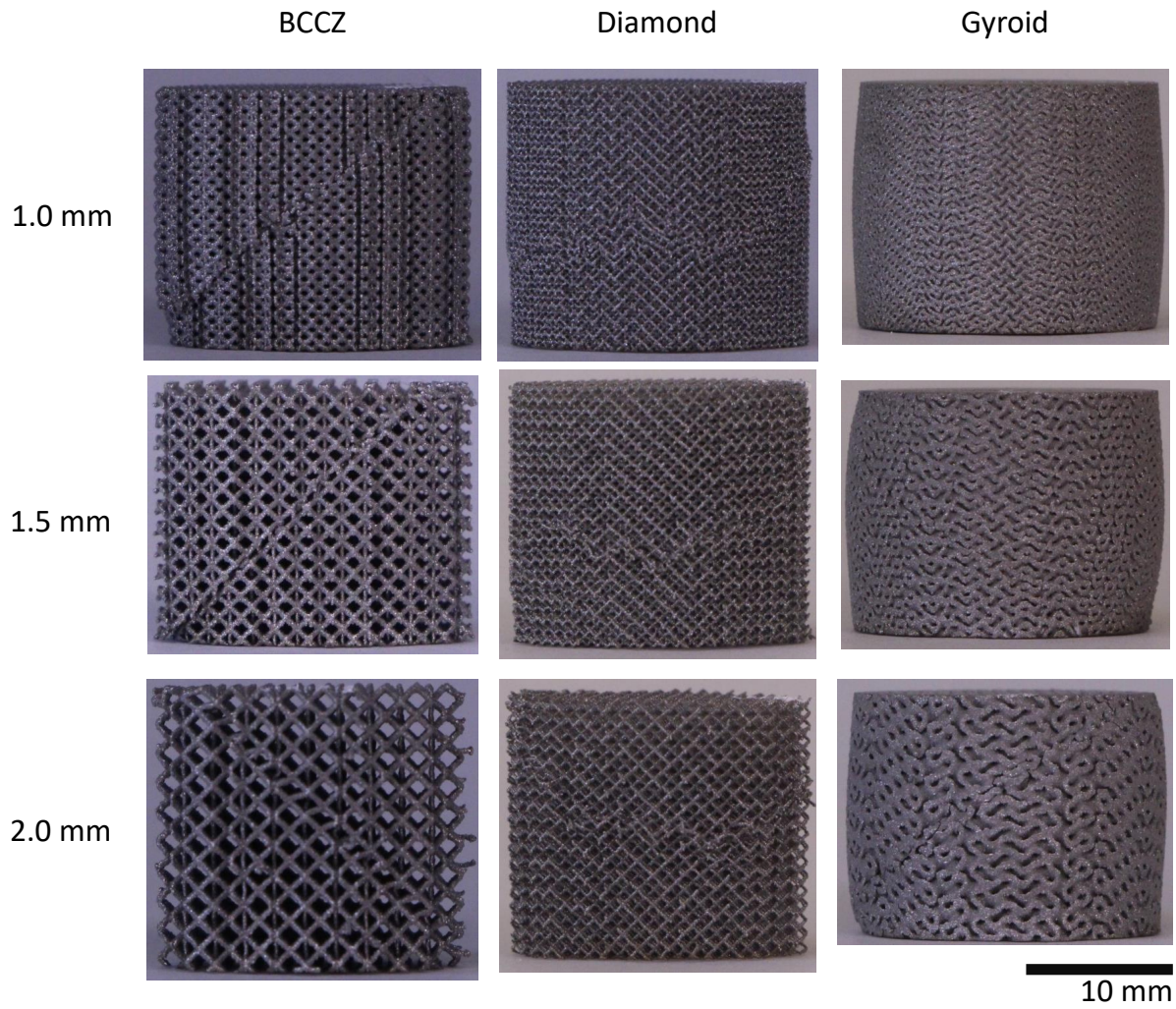

Figure 2.21: Photographs of lattices at different unit cell sizes showing deformation behaviour

2.3.5 Comparing All Compression Data with the Gibson Ashby Model

By plotting all the data against the volume fractions it can be seen whether the data fits one trend with volume fraction or whether different experiments lead to different trends. When all the data was considered together (figure 2.22), the data showed an increase in strength and stiffness with increased volume fraction. Both data sets fitted power law curves with R^2 values of 0.97 for strength and 0.98 for stiffness. The exponent was 2.40 for strength which does not correlate with either bend or stretch dominated lattices according to the Gibson Ashby model [347], while the exponent for the stiffness was 1.99

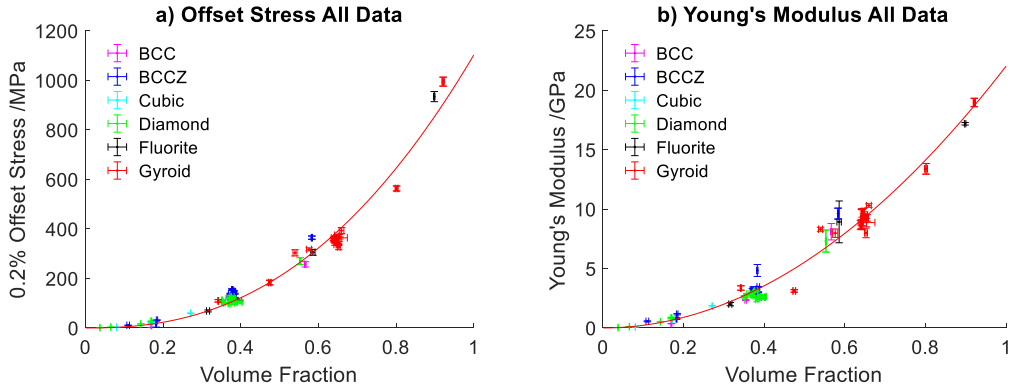

Figure 2.22: Compiled graphs of a) 0.2% offset stress and b) Young's Modulus against volume fraction for all data. Power law curves were fitted with equations: Offset stress $= 1102 * \text{volume fraction}^{2.40}$ and Young's Modulus $= 22.0 * \text{volume fraction}^{1.99}$

Table 2.3: Regression analysis of all compression data, compared with Gibson Ashby model values for bend and stretch dominated lattices

	Strength /MPa			Stiffness /GPa		
Unit Cell Topology	Coefficient (C)	Exponent (n)	Correlation (R^2)	Coefficient (C)	Exponent (n)	Correlation (R^2)
All data	1102	2.40	0.97	22.0	1.99	0.98
BCC	848	2.09	0.99	36.1	2.63	1.00
BCCZ	1253	2.30	0.95	37.3	2.54	0.93
Cubic	1237	2.33	1.00	30.6	2.15	1.00
Diamond	942	2.16	0.95	28.8	2.37	0.96
Fluorite	1233	2.59	1.00	20.9	1.74	0.99
Gyroid	1167	2.68	0.95	21.8	1.97	0.93
Theoretical Values from Gibson Ashby Model						
Bend Dominated		1.5			2	
Stretch Dominated		1			1	

which correlates with the value expected for bend dominated lattices.

Power law curves were also fitted to the data for each unit cell design separately according to equation 2.2.4. This included data from three lattice configurations for each of BCC, cubic and fluorite, 17 configurations for BCCZ and diamond, and 19 configurations for gyroid. For the strength curves the data had a correlation of at least 0.95 for all unit cells, while for stiffness it was a minimum of 0.93. The exponent values ranged from 2.09 for BCC to 2.68 for gyroid, with all the values outside the range proposed by Gibson Ashby. The power law curves fitted to the stiffness data had exponents between 1.74

for fluorite and 2.63 for BCC, with gyroid (1.97) being the closest to the Gibson Ashby model prediction of 2 for a bend dominated structure. No values were close to 1 which is proposed for a stretch dominated structure.

2.4 Discussion

The key finding from this chapter was that it is possible to build lattices with compressive strengths in the range of cortical bone ($\sim$ 200 MPa) [213, 214, 215], and elastic moduli in the range of cortical bone ($\sim$ 17 GPa) [213, 214] while providing void volume for a secondary phase. However care must be taken to optimise build angle as this influences strength and stiffness. While the loading angles must be considered as different designs behave differently when the angle at which they are loaded changes.

Volume Fraction

Comparing mass in air with an Archimedes Balance as methods to determine volume fraction showed no statistical difference in readings for the majority of samples. Both Archimedes Balance [14, 348, 349] and mass measurements [350, 351] have previously been used to calculate the volume fraction of lattices. The Archimedes Balance has the advantage that the strut porosity can be estimated for the lattices by comparing the measured density with the standard density. However the Archimedes method is more cumbersome with an increased error due to two mass readings per measurement. Additionally there is potential for errors to be introduced due to trapped air during the ethanol weighing or trapped ethanol from a previous repeat during the air weighing. Larger variations in the standard deviation in the Archimedes results were seen for Fluorite 250 and 350 and Gyroid 200 and 250 which all have volume fractions above 0.5 leading to more potential for residual air or ethanol.

Where the Archimedes method and mass measurements have previously been compared as methods for measuring the volume of lattices, mass has been found to give a

lower estimate of volume [225, 344, 348, 352], this was in agreement with the results found here. This suggests that similar sources of over estimation in the Archimedes method are present in both.

When the porosity measurements were converted to volume fraction (by subtracting porosity from 1) to directly compare with this work, it was found that the Archimedes measurements of volume fraction were between 0.55 and 9.09% higher than the mass measurements of volume fraction [225, 344, 348, 352]. The largest difference was found in cubic lattices with small volume fractions (0.1), where the absolute difference in magnified by the small starting volume fraction, which was also seen in this work. None of the lattices in these papers had volume fractions above 0.5 so comparison could not be made with those lattice in this work and the effects of these high volume fractions on the reliability of the methods.

The repeatability limit and reproducibility limit of the Archimedes method for Sintered Powder Metallurgy are listed by ASTM B962-23 as 0.05 and 0.6 gcm^{-3} respectively. So for Ti-6Al-4V this equates to approximately 1% i.e. the difference between mass and Archimedes methods for measuring volume approaches this limit for five lattice designs in this work. Where there were greater percentage differences between the mass and Archimedes methods for measuring volume fraction it was lattices with either a smaller design volume fraction, or where the volume fraction was above 0.5 i.e. the larger gyroid and fluorite lattices.

The Fluorite 350 lattices did not overbuild in contrast to the other lattice designs. With the mass measurement indicating an underbuild. The samples were nearly fully dense with closed porosity - i.e. the internal voids were not accessible to the outside. This meant the ethanol could not penetrate these voids, so the lattice is treated as a part with a lower density by the Archimedes Balance leading to a higher estimate of volume. Whereas the mass measurement works the same for open or closed porosity, thus giving a lower volume estimate. Given that the design volume for the Fluorite 350 is 1530 mm^3 while the volume for a dense cylinder of the same size is 1700 mm^3, it is not surprising it

was unable to achieve the 12-25% overbuild seen in other 350 μm lattices as this would have been impossible within the fixed cylinder size.

Larger absolute overbuild was seen in the 250 μm and 350 μm than 150 μm lattices, while percentage overbuild was larger for 150 μm lattices. This could be caused by an increase in strut diameter. If diameters are increased by a fixed distance, a thicker initial strut will gain more absolute volume but less percentage volume than a thick volume as it is thicker to start with.

The future use of gas pycnometry to measure the volume fraction of lattices would eliminate the challenges caused by trapped air or ethanol caused by the Archimedes Balance, as the second fluid is gas rather than ethanol, and so does not encounter the effects of surface tension. However, the gas would still not be able to penetrate regions of closed porosity such as in the Fluorite 350 lattices, nor any internal defects in the lattice struts or walls.

Strut Thickness

Given that one cause of overbuild is an increased strut thickness SEM micrographs of the struts were taken, initially from the top. Strut thickness measurements were generally in agreement with the designed thickness indicating the processing parameters were appropriate. The fluorite with 350 μm struts was unable to be measured due to the struts merging as they overbuilt. The BCC lattices exhibited the largest struts for all design thicknesses, however these were not significantly different from the BCCZ lattices in each thickness. This is not surprising as these are based on the same design but with the addition of vertical [001] struts that cannot be seen from the top view.

Strut thickness can be influenced by processing parameters [118, 182], strut angle [233] as well as the designed strut thickness [183] and strut length [144]. The processing parameters were the same for all designs. The designed strut thickness were the same so length and angle of struts should be considered. BCC, BCCZ, diamond and fluorite have struts at 54.74° to the vertical with cubic at 15 and 75°.

Cubic had the thinnest struts which were the closest to horizontal, this in contrast to literature which shows that horizontal struts and those at low angles are thicker than those close to the vertical, due to a lack of layers of strut below to dissipate the laser energy it radiates into the surrounding powder causing additional powder to attach to the strut [180, 181]. The strut thicknesses were measured from micrographs taken from the top view of the lattices, where it has been previously shown in this work that changing the angle a strut is built at has no statistical difference on the measured strut thickness (figure 2.12a). However struts built closer to horizontal had thicker profiles when measured from the back view (figure 2.12c), so the theory about overbuilding does hold it is just not uniform in direction.

The length of struts has also been found to influence the strut thickness, Crupi et al designed BCC lattices with unit cell length of 2.50 and 3.75 mm with a designed strut diameter of 400 μm and found the struts of the 3.75 mm unit cells built to design, but the other struts underbuilt by 6% [144]. In contrast the longest struts in this study belonged to the cubic lattices which also had the thinnest struts. The measured variation in strut thickness between unit cell designs (from the top view) was 10%, while the variation seen between struts at different angles from the back view was 66%, so the effect of strut angle led to larger changes in volume than any effect of strut length on the top view.

When comparing the error between design and build we can see that the thicker lattices have less absolute and percentage error, this agrees with Melancon et al who found the error increased with decreasing feature size [179].

The thinnest lattice built in this study Cubic 150 had a measured strut thickness of 157 $\pm$ 25 μm. 150 μm was chosen as it is believed to be the thinnest strut thickness possible on this machine [119]. This thickness has been achieved previously on this machine with a measured thickness of 155 μm for a diamond unit cell [121]. Ghouse et al were able to print struts at 0.142 $\pm$ 0.014mm on an earlier design (Ren AM250, Renishaw PLC, UK) [118]. While Van Bael et al printed 112 μm struts using a 100 μm design using a custom printer [177].

Strut thickness measurements taken from the top are within 5% of the design for most of the lattice designs while the volume fraction measurements indicate an overbuild greater than 5% for all the strut based lattices except Fluorite 350 which is a special case. Variations in strut profile i.e. non circular struts would account for these differences.

Observations of Strut Morphology

Two main observations were made from the SEM micrographs of a BCCZ lattice with 250 μm struts built on a 30° slope shown in figure 2.11: uneven powder adhesion and unequal strut thickness. The top view SEM showed noticeably thinner struts than the side views suggesting a non-circular strut profile. Likewise struts appeared thicker as they approached a horizontal build angle. This suggests an elliptical, or 'teardrop' profile where the major axis is proportional to build angle. This behaviour has been previously observed in L-PBF with a variety of metals including Ti-6Al-4V and is more pronounced the closer the struts are to horizontal [180, 184]. The effect is thought to be caused by thermal effects where heat from the laser cannot dissipate into previous layers due to a small overlap so additional powder melts into the strut causing the increase in size [122, 184]. This can negatively influence the mechanical properties as discussed later.

Additionally, differences in powder adhesion are seen between the different faces. The top view shows the least particle adhesion due to the top face not being in contact with the loose powder during the laser scanning. However the struts were not horizontal during printing, as the lattice was built on a 30° slope, so more particles are present on the top view than for a lattice printed flat, as seen in figure 2.16, due to the build angle [350]. On the front and back views more particles can be seen on the lower edge than the upper edge of the struts. The struts are intended to be cylindrical so during the bottom half of the printing the strut is slightly larger each layer so the melt pool is in contact with the powder from the previous layer at the edges increasing the probability of particle adhesion. Whereas for the upper portion of the strut the melt pool is narrower than the previous layer bringing it into less contact with the unmelted powder and with a greater

mass of strut below it to dissipate heat into, reducing the chances of melting additional unwanted particles. The right hand side of the lattice is overhanging the build plate and shows greater particle adhesion than the others. It has previously been shown that down facing struts exhibit greater particle adhesion [350]. Murchio et al found that the strut angle influenced the surface roughness with struts close to the horizontal more rough (Ra = 73.7 ± 32.8 μm) due to an inability to dissipate the heat into the strut due to a small area of overlap, while vertical struts were less rough (Ra = 17.3 ± 8.5 μm) (figure 2.23) [184].

Strut Thickness of Struts at Different Angles

During the experimental work all lattices built successfully, including those showing horizontal struts with unsupported lengths up to 1 mm. This is contrary to some literature which suggests that such elements may not print correctly [238]. However the Renishaw design guide includes overhangs up to 1 mm [119], and Melancon et al and Simonelli et al have successfully built Ti-6Al-4V horizontal struts on the Ren AM 250 (Renishaw PLC, UK) the precursor to the Ren AM 500M (Renishaw PLC, UK) used in this work [178, 179].

As was previously seen in the strut thickness analysis of the defects in unit cells, the top view did not show an overbuild for the angled struts. However overbuilds were seen in the right and back views indicating that the struts had non circular cross sections. This effect was more pronounced as the strut angle increases from vertical struts at 0° to horizontal struts at 90° particularly from the back view. This is inline with observations made by Hossain et al and Murchio et al [184, 233]. This is thought to be because struts closer to horizontal have less overlap between layers to dissipate the laser energy so more energy is radiated into the surrounding powder resulting in an overbuild (figure 2.23) [122, 184].

The [001] struts exhibit lower thicknesses than the <111> trends would suggest. This could be because the [001] struts are rotating in plane, while the <111> struts are rotating

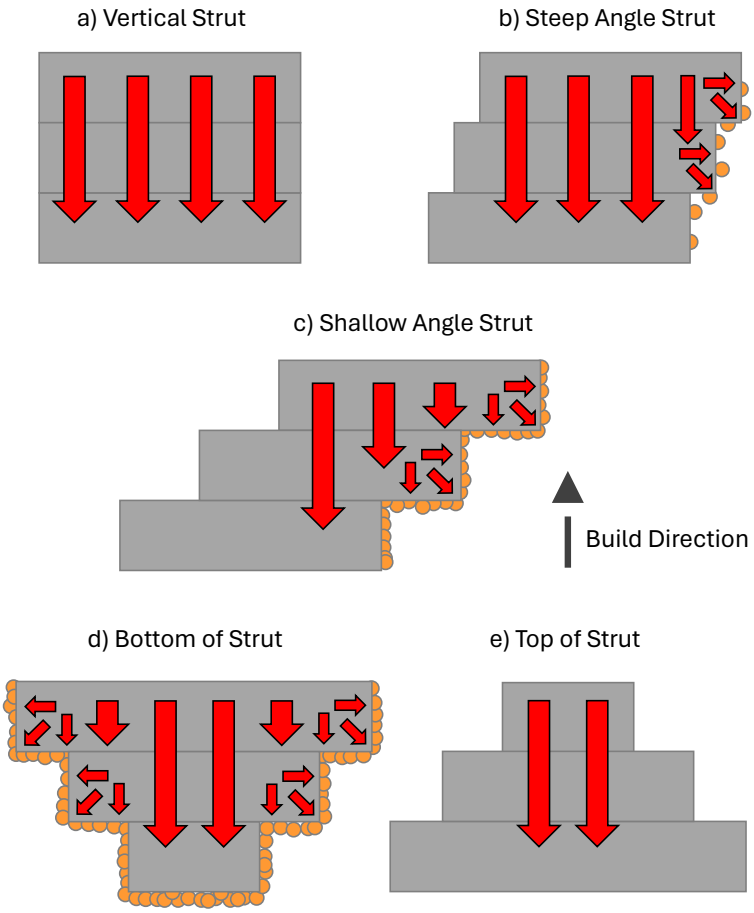

Figure 2.23: An idealised visual illustration of heat flow causing additional powder adhesion in struts built at different angles, and between the top and bottom surfaces of struts. heat energy is shown with the red arrows shown flowing into lower layers where available, otherwise flowing into the surrounding powder leading to attached particles (orange circles). a) vertical strut where the additional heat is able to transfer into the previous layers leading to minimal additional particle adhesion, b) steep angled strut where most of the additional energy can transfer but there is some particle adhesion, c) shallow angled strut where a lot of heat energy is radiated into the surrounding powder leading to high levels of particle adhesion, d) at the bottom of the strut there are few layers below to act as a heat sink so many particles adhere, e) at the top of the strut where almost all the excess energy is absorbed by the previous layers so minimal particle adhesion

out of plane. Or it could be that the [001] struts are longer than the <111> struts. However neither Crupi et al nor Campanelli et al found a trend in strut thickness with length [144, 353], while Alghami et al found longer struts were more eccentric [354].

A smaller standard deviation in strut thickness was found from the back view than the right view. It has previously been seen (figure 2.11) that the right view struts exhibit

greater particle adhesion than the back view. This is because the gas flow enters the chamber from the right which leads to greater particle adhesion than other sides of the samples. Some of the lattices used for this analysis were from the combined rotation samples, while the rest were from the build rotate lattices. The combined rotation lattices were all built vertically so the faces were all vertical during building. The build rotate lattices are rotated towards the right. Therefore the right view face is tilted towards the build plate and has additional particle adhesion due to this orientation. So there will be a difference in particle adhesion between the right view of the combined and build rotated lattices due to this rotation. While both the build rotation and combined rotation lattices are vertical in the back view so there will be no difference in particle adhesion due to tilting.

The particle adhesions is likely to lead to over estimates and greater variability of strut thickness. As just discussed there is greater adhesion and greater variability in particle adhesion in the right view leading to the greater standard deviations in strut thickness seen in the strut thickness measurements from the right view. This could explain why there is a trend in strut thickness with angle from the back view but not the right view as it could be being obscured by the large variation in strut thickness measurement. The trend is in line with the literature [180, 181].

Comparing Different Unit Cells - Example Compression Curves

All the example compression curves (figure 2.13) for strut based lattices have a 250 μm designed strut thickness and the gyroid lattice shown has a 150 μm wall thickness. They all demonstrate a toe in the region where the plattens and sample settle to parallel, followed by an linear elastic region followed by plastic deformation. The cubic, diamond and fluorite demonstrated collapse characterised by a vertical drop in the graph after the initial yield point to below half of the yield stress. This behaviour was also seen in the literature [141, 142, 143, 223, 344]. However some literature saw a smoother transition into collapse for diamond and fluorite lattices, with fluorite not dropping as far as the

cubic and diamond lattices, which is also seen here [344].

The cubic and diamond lattices then exhibit a plateau region characterised by sharp oscillations which reached similar stresses to the yield stress, and dropping below 50% of the yield strength. Wang et al and Ahmadi et al saw a similar shape in their plateau regions although for Wang et al there was an overall downward trend in stress [143, 344]. The cubic lattice curve oscillated at 1 peak per 0.06 strain, which corresponds to 1 peak per 1 mm distance, which suggests that each drop in stress corresponds to a single unit cell layer collapsing. The diamond lattice curve oscillates at 1 peak per 0.03 strain, suggesting that a layer of unit cells is collapsing to 50% of its original height at each drop in stress. This is probably due to the shape of the unit cell which includes four nodes at half the height, with eight struts above and eight below. These structures that make up half the unit cell are reflections rotated 90° (figure 2.1). So the collapsed section is probably one of these half unit cell structures.

For the diamond lattices in the literature similar shapes were seen, sometimes not as high as yield stress and some had an upward trend while others were flatter as seen here [141, 142, 218, 223, 344]. Denisification is seen after the plateau region. The gyroid lattice has a plastic yield after the elastic region but no collapse with associated drop in stress. This shape matches Gümrük et al's idealised bend curve [222]. However in the literature some drops in stress are seen and the plateau region includes some oscillations in some papers [143, 216, 346, 355]. All of these papers used unit cell sizes larger than in this work with the thicker wall, which may contribute to the differences seen. When larger unit cell sizes were used in this work compression curves had some reductions in stress and oscillations in agreement with the literature.

Gyroid lattices can be approximated as strut based with bend dominated deformation under Maxwell's criterion [221]. FEA analysis also indicated bend dominated deformation [356]. However experimental analysis has not been as clear cut with sheet gyroid lattices as used in this work attributed to stretch dominated failure by Wang et al and Al-Ketan et al [143, 350]. This behaviour indicates that these lattices are demonstrating stretch

dominated behaviour with key features, including an initial collapse below 50% of the yield stress and oscillations in the plateau region followed by a densification region. This is in contrast to the Maxwell stability criterion that predicts these lattice designs to be bend dominated. However these lattices have consistently shown stretch dominated behaviour [143, 218]. Reasons that the Maxwell criterion fails to predict compressive behaviour include the fact that it was developed for pin jointed frames but lattices have fixed joints. The model also assumes that either bending or stretching are the only failure mechanisms, which is too simplistic with shearing, torsion and nodal interactions also seen [357].

For the fluorite lattices after the initial collapse the plateau region climbs with some bumps but not repetitive oscillations, this behaviour mirrors that seen in the literature [218, 344]. There is no clear transition into a densification region. The behaviour is classified as bending dominated deformation behaviour by Li et al [218]. This does not agree with the Maxwell criterion, which classifies fluorite as stretch dominated. The shape of the curve aligns with Benedetti et al's example curves for bend dominated lattices [136] but not with Gümrük et al, whose example curve does not include initial collapse [222]. It is known that defects can introduce bending moments into otherwise stretch dominated structures idealised to be under pure compression and tension [185]. These bending moments can cause the failure mode to shift to bend dominated leading to a reduction in mechanical properties [221].

The BCC and BCCZ lattices have similar compression curves with the BCCZ lattices exhibiting higher stresses. After the initial elastic region there is an elongated region at high stress prior to the first collapse. This behaviour was seen by some papers [144, 218, 238] while other papers had early collapse [140]. In this work the collapse was approximately a third of the yield stress, while for most papers it was more than half the yield stress [139, 140, 216, 218, 238, 342]. Crupi et al found reducing the ratio of strut thickness to strut length led to a reduction in collapse stress [144], including into the range seen in this work. After the initial collapse the stress gradually reduces in a bumpy manner without clear pattern. This non structured shape is seen in the literature but with

an upwards trend [139, 140, 216, 218, 238, 342]. This is followed by a densification region. Maxwell's stability criterion labels both BCC and BCCZ as bend dominated lattices. However the compression curves do not entirely match either of the model shapes which leads to some conflict in the literature with similar curves being attributed to opposite modes. Crupi et al and Li et al described BCC and BCCZ as stretch [144, 218] while Mazur et al described BCC as bend and their data fit with the Gibson Ashby bend criterion too [238]. Alomar et al did not classify BCC lattices despite classifying other lattices in the same paper [140].

Comparing Different Unit Cells - Strength and Stiffness

Young's Modulus and 0.2% offset stress are calculated from the stress strain curves. Within a unit cell type both strength and stiffness increase with strut thickness. This result has previously been seen in Ti-6Al-4V L-PBF lattices with BCC [140, 144], BCCZ [120], cubic [143, 236, 344], diamond [141, 142, 223, 344], fluorite [224, 225, 239] and gyroid [143]. These effects are mainly attributed to the increase in volume fraction. In addition, defects which reduce the mechanical performance are more common as the geometry reaches the limits of printability i.e. the smallest strut thicknesses at 150 μm [183] and roughness makes up more of the overall thickness. When comparing lattices at the same strut thicknesses the strongest is the gyroid followed by the fluorite, BCCZ, diamond, BCC then cubic as the weakest. Stiffness follows a similar pattern. Li et al compared BCCZ, diamond and fluorite lattices with the same unit cell size and similar strut thicknesses (within 3%) [218]. Fluorite was 3 times as strong as diamond, while BCCZ was nearly twice as strong as diamond. Fluorite was twice as stiff as diamond while BCCZ was 1.8 times as stiff as diamond.

In comparison in this study, fluorite is three times stronger than diamond for 350 and 250 μm, but less than three times for 150 μm. However BCCZ is weaker than diamond for 150 and about 1.4 times for 250 and 350. Fluorite is 2.5 to 3 times stiffer than diamond and BCCZ is in the range of the stiffness of diamond in this study. He et al compared

BCCZ and diamond and found BCCZ 3.4 times stronger and 7 times stiffer than diamond whereas they are far more similar in this study [139]. Wang et al compared cubic and gyroid lattices with the same volume fraction and the strut thicknesses are different [143]. Comparisons can still be made, for example when the cubic strut thickness was twice the wall thickness of the gyroid, the gyroid strength was higher and within the same range as the cubic even though the cubic lattices were 1.45 times as stiff and with a higher volume fraction. The cubic lattices in this work were rotated at 15° to avoid horizontal struts in contrast to most in the literature. When Choy et al compared cubic lattices in two orientations either with horizontal and vertical struts or with 45° struts they found those at 45° to be half as strong due to the lack of vertical struts [345].

Photos of the samples after compression testing show the failure mechanisms. The BCC lattices show shear failure at 45° through single planes for 150 and 250, while for 350 some rows are skipped. The 150 lattice also has some evidence of bending, and the 350 exhibits barrelling. In the literature the majority of BCC lattices undergo cell collapse by buckling or crushing [226, 227, 237, 358, 359, 360] while a few experience shear failure as seen here [140, 361].

The BCCZ lattices demonstrate shear failure at 45° through places as well as other angles for the 350 lattices, some crush is also evident. This behaviour mirrors that seen in the literature [237, 358, 361, 362]. The failure modes seen for BCC and BCCZ match with the stress strain curves where the initial collapse is likely due to be the 45° shear, but then crushing and other shear collapse would explain the bumpy but not oscillating plateau region.

The cubic lattices in this study are rotated at 15° to remove horizontal struts, the photos show shear failure in the lattice planes, followed by bending and buckling. In the literature most cubic lattices are not rotated with failure occurring in flat planes by crushing or buckling [145, 363], however Choy et al tested both parallel and 45° rotated cubic lattices and found that the 45° lattices experience in plane shear as seen in this work [345]. Subsequent shear failure in additional planes leads to the oscillating stress strain

curve in figure 2.17. As these are likely to be parallel to the original shear plane due to the cubic lattice being rotated in an unequal way, this means each shear band is likely to be the same length and therefore require similar force to shear leading to similar height peaks on the compression curve.

Diamond lattices exhibited shear failure in 45° planes in agreement with previous studies [142, 218, 223]. This resulted in a stress strain curve with an oscillating plateau region where the oscillations returned to a similar height to the yield stress. This is in contrast to previous research which has found plateau regions at lower stresses than the yield stress, and with an upward trend [142, 218, 223, 344]. Given the stress is able to reach the yield stress value after initial shear failure it suggests that only the single plane was effected in the initial loading and collapse, and that after collapse the collapsed plane was able to support the load.

Fluorite lattices underwent shear failure in a 45° plane, this resulted in a drop in the stress strain curve to a quarter of the yield stress. This was followed by the stress climbing with the strain with irregular fluctuations, indicating densification of the lattices providing an increase in strength, but the failure plane was unable to support as much load as prior to the collapse. This failure mechanism has been previously seen especially with lattices with thicker struts [218, 344].

All the gyroid lattices exhibited some barreling, while the Gyroid 60, Gyroid 200 and Gyroid 250 displayed shear failure, for Gyroid 60 this included collapse in multiple parallel planes. The stress strain curves for gyroid lattices show a linear elastic region followed by a yield point which is the onset of barrelling, then the stress continues to climb as the lattice densifies. If shear failure occurred then a vertical drop in stress is seen as the failure planes cannot support much load. In previous research where the only failure observed is barreling then the stress strain curves match those seen in this study [364], this is more often seen with heat treated lattices [216, 365]. However when shear failure occurs this has previously been found to not lead to total lattice failure and the structures have been able to continue to support load leading to stress strain curves more similar to the one

seen for fluorite lattices in this research (figure 2.13e) [143, 216, 346, 355].

2.4.1 Rotation of Lattices

By rotating the lattices in different ways the effects of building devices at different orientations, or if the loading is not entirely vertical or a combination of the two, can be explored. When the lattices are built at different angles the unit cell is kept parallel with the sample, so it is rotated during building and then vertical again during compression (figure 2.4a), this means that individual struts will be at different angles during building but the unit cell will be loaded in the same direction as the 0° case so the mechanical properties will be influenced by the angles the struts are during build.

Build Angle Rotations

The effects of building struts at different angles include: strut waviness, inconsistent thickness, non circular struts, variations in powder adhesion, and changes in strut thickness. Generally building struts closer to horizontal leads to an increase in deviation from design in all of these factors [183]. Non cylindrical struts and changes in strut thickness were the only defects measured in this work, however they were in agreement with the literature with strut thickness and non cylindricity increasing with angle from vertical.

For both BCCZ and diamond lattice the struts are at 54.7° from vertical in the 0° case, plus the vertical struts in the BCCZ lattice, so it would be expected that the different unit cells would be influenced by the build rotation in the same way. However the failure mechanisms are different so the influence of the changes in strut thickness might be different. For the BCCZ lattices the samples fail by shear failure at 45°, this is through a plane of the unit cells. During building one plane of struts rotate closer to vertical so they build thinner, while another plane becomes thicker. During shear failure only struts in one plane plus the [001] struts fail, so the thinner struts fail preferentially, so as strut get thinner at increased build angle the lattice gets weaker.

By using the known strut thicknesses at angles from figure 2.12, combined with the

known angles of the struts during compression from table 2.2 a new figure can be created to compare the strut thicknesses at the angles of the lattices (figure 2.24). The compression data shows a step down in strength between 0 and 10°, 20 and 30°, which matched the trend seen in the strut thickness of the thin struts, especially from the right view (figure 2.24a).

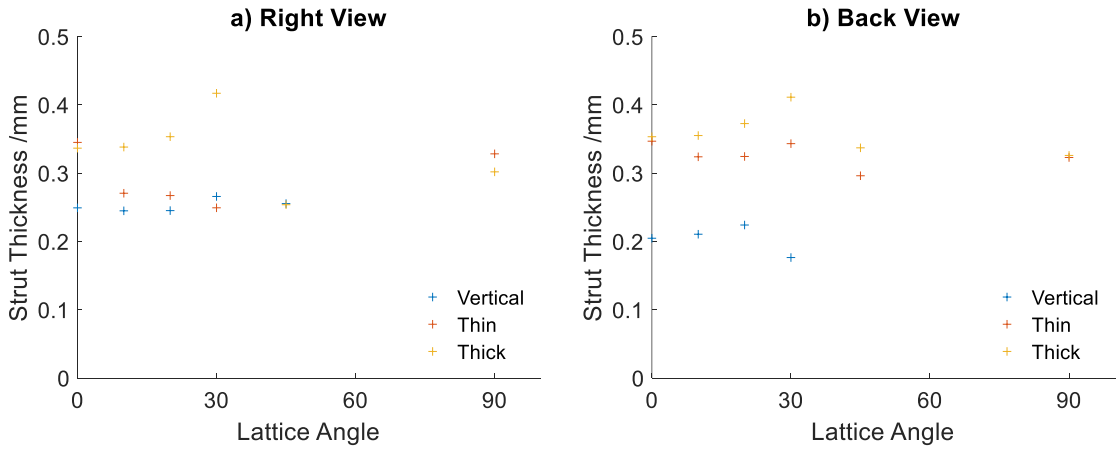

Figure 2.24: Thickness of struts from a) right and b) back views, at the orientations of the lattice rotations, for build and combined rotate (load rotate is the same as 0° case). The standard deviations are not included to make the trends clearer

For the diamond unit cell the mechanism of failure is crush bands, so it is less clear whether the strength will be influenced by only the thick or thin struts, or whether both are involved in the lattice failure. The continuous downward trend in strength with build angle seen in the diamond lattices is not clearly seen in the strut thickness data, however this strength reduction could be caused by another of the defects influenced by the angle of the struts. Wauthle et al built diamond lattices out of Ti-6Al-4V using L-PBF in a number of configurations of angles that enable a comparison with the build angle used here. Lattices were built at 0 and 45° and the lattice built at an angle was 35% lower in strength and stiffness. This was attributed to the fact that both angles had struts built horizontally which resulted in poor quality struts, but in the rotated case these were then in an angled position where they were subjected to more force than in the 0° case where these struts remained horizontal [348]. Both of these lattice designs were rotated at 45° to those used in this work so the struts were loaded at 90 and 35.3° to the vertical (see table

2.2 to compare the strut angles).

Weißmann et al used L-PBF to make Ti-6Al-4V samples with just vertical struts, built at either 0 or 45° and found no statistical difference between the angles in strength or stiffness [231]. Additional papers have looked at build quality when rotating L-PBF metallic lattices of BCC and cubic designs. Kabbur et al attempted to build BCC lattice at 45° and found that a number of struts did not build when horizontal [230]. While Dallago et al found variation in thickness along the struts with extra material around overhanging nodes [185].

Although the gyroid unit cell is a surface based design it does have some strut like features and so the build angle can influence the quality of build in certain areas too, however the curved shape enables more support between layers so the reduction in quality is less severe than in strut based lattices [234]. This may explain why the drop in strength from 0 to 10° for the BCCZ lattices is 30% while for gyroid it was only 6%.

Load Angle Rotations

When rotation the BCCZ lattices to enable the influence of rotating the loading direction to be studied it is seen that the mechanism of failure changes from the shear failure at 45° seen in the 0° case, to cracking and potential shear failure at 65 and 75° for the 20 and 30° rotated lattices. It is known that vertical struts increase the strength of lattices (which is why the vertical strut was added to BCC lattices in the first place [226]). Hossain rotated L-PBF printed Ti-6Al-4V BCC lattices at a number of different build angles and found that the one with struts aligned vertically was approximately six times stronger than the other angles, while there was not much difference in strength between other rotations [233]. So it follows that a BCCZ lattice at 0° would be stronger than at other angles. As the lattice angle changes the planes of unit cells shift from being at 45° to 35 and 55°, 25 and 65°, and 15 and 75°. It requires less force to shear a material at an angle closer to horizontal [366], which would explain why the stress is lower for the sample with increasing angles.

Diamond lattices do not have a vertical strut, and the failure mechanism appears similar between all the angles during load rotation. So without modelling the stress in individual struts it is hard to understand why the 10° lattices are stronger than the other angles. Wauthle et al did compare lattices by changing the load rotation, and found those at 45° to be about 35% weaker and less stiff than those at 0° however, the cause of this was attributed to struts built horizontally being at different angles during compression [348], but in this work all the struts are built at 54.7° so there should be no difference between the quality of the struts.

The gyroid lattices increase in strength with load rotation, while the failure mechanism changes from barrelling at 0 and 10° to shear fracture at 20 and 30°. Although the gyroid lattice is often thought of as isotropic [221, 356], it has been shown to have different mechanical properties when rotated. For example Yan et al rotated L-PBF stainless steel gyroid lattices at 0 and 45° and found that those at 45° were 20% stiffer and 8% stronger than those at 0° due to wall regions approximating struts which were vertical [234]. One thing to note is that the gyroid lattices in this paper were all built on the flat so in addition to the influence of the unit cells being at an angle during compression, they were also rotated during printing.

Combined Angle Rotations

Combining build and load rotation led to BCCZ lattices which decreased in strength with increasing angle, but at a rate slower than load rotate and faster than build rotate. The deformation behaviour was different from both the build and load rotate, with angled crushing seen, apart from 0 and 90° where 45° shear failure was seen. This difference may be due to the different unit cell size of 2.5 mm compared to 1 mm used in this study, for similar strut thicknesses.

The diamond lattices had similar strengths at 0 and 45° which was also seen by Wauthle et al, but a higher strength at 90°, which Wauthle et al found to be a similar strength to 0 and 45° [348]. The failure mode at 45° was 45° shear and at 90° was horizontal crushing,

while 0, 10, 20 and 30° exhibited angled cracking. There was no statistical difference between the strength of the gyroid lattices at any of the combined rotate angles, and all the lattices exhibited barrelling.

Combined rotation of lattices was also investigated by Choy et al [345]. Choy et al investigated Ti-6Al-4V cubic lattice manufactured by L-PBF with either horizontal and vertical struts, or struts at 45° and found that those with vertical struts were stronger due to the vertical struts and rigidity. Weißmann et al investigated L-PBF Ti-6Al-4V lattices with a unit cell design called twisted and found the strongest was at 0° and the weakest rotated both 45 and 90° in different axes [236]. This was attributed to the presence of columnar grains which grow vertically, with longer grains giving greater strength as the cracks do not cross the grains but run along them, so designs with more vertical struts have longer grains and therefore increased strength. This could help to explain the BCCZ results but is in contrast to the results seen in the diamond lattices.

Unit Cell Size

Increasing the unit cell size led to decreased strength and stiffness for BCCZ and diamond lattices, but no changes in the gyroid lattices. Large differences in strength and stiffness as seen here, were also found by McKown et al who used L-PBF to create stainless steel BCCZ lattices with unit cell sizes of 1.5 and 2.5 mm at 250 μm strut thickness [237]. With the smaller unit cell resulting in a 4.6 times increase in strength and six times increase in stiffness. Crupi et al investigated Ti-6Al-4V BCC lattices manufactured by L-PBF with unit cell sizes of 2 and 2.5 mm both at 500 μm and found a 2.4 times increase in strength and 2.2 time increase in stiffness for the small size [144].

These effects were attributed to the smaller unit cells having a higher density which has previously been shown to lead to increased strength and stiffness [238, 367], and also to changes in build quality with smaller unit cells having shorter scan vectors so each strut is returned to more quickly so more energy in each strut leading to better wetting conditions [146]. However this will depend on the specific scan strategy of the L-PBF

machine and slicing software used.

Bending moment is proportional to the stress times the span length squared, so for the same loading the stress will be less for longer struts. So the offset stress for the lattice with 1 mm unit cell length should be four times stronger than for the lattices with 2 mm unit cell length, in fact it was 13.5 times stronger for BCCZ, and 11.6 times stronger for diamond, while it was only 1.08 times stronger for the gyroid lattice.

The gyroid lattices were designed with the same volume fraction, and did not exhibit statistically different strength or stiffness. Some previous research has found no statistical difference in strength when the unit cell size has been increased but the volume fraction maintained [147, 368]. In both cases this was only true for small increases in unit cell size. While others have found strength decreased with increasing unit cell size, these findings were for larger changes in unit cell size beyond those explored here [146, 147]. So larger unit cell sizes should be explored to further understand the influence of unit cell size on the mechanical properties.

2.5 Conclusions

This work demonstrated that it is possible to manufacture lattices using laser powder bed fusion of Ti-6Al-4V which are stronger than the loads experienced in hip replacements and spinal fusion cages, and with sufficient void volume for a secondary drug delivery phase. Four lattice designs were found that met this criteria, specifically BCC 350, BCCZ 350, Diamond 350 and Fluorite 250. These all had a volume fraction between 0.5 and 0.6 and a strength between 200 and 400 MPa.

All struts including horizontal struts built successfully, however there was some variability in build quality. The lattices overbuilt in the vertical direction leading to non circular struts, with struts built closer to horizontal having larger disparities in thickness. The sides of struts facing towards the gas inlet on the right hand side of the build chamber experienced the most powder adhesion. The thinnest struts measured from the top view

were designed at 150 μm and measured at 157.4 $\pm$ 25.3 μm.

Six different unit cell designs were compared, specifically BCC, BCCZ, cubic, diamond, fluorite and gyroid. It was found that lattices with thicker struts were stronger. When lattices with the same strut thickness were compared it was found that gyroid was stronger than the strut based lattices, and fluorite was the strongest of those. Lattices exhibited shear failure (strut based, and some gyroid) and barrelling (gyroid) under compression.

Rotating the lattices during building to mimic the effects of building implants in different orientations led to decreased strength in all three lattice designs (BCCZ, diamond and gyroid), due to differences in strut thicknesses of struts built at different angles.

Rotating the lattices to mimic the effects of loading implants from varying angles led to decreasing strength for BCCZ lattices, increasing strength for gyroid lattices, and a maxima at 10° for diamond lattices. Suggesting that the diamond and gyroid unit cells have optimum loading directions that are not the 0° direction. Computer modelling would enable the effects of rotating unit cells under loading to be better understood.

Combining the building and loading rotations by rotating the unit cells within the cylindrical samples on the build plate led to lattices which were not as strong as the load rotate lattices, but stronger than the build rotate lattices.

In each lattice the strength at each angle was higher for the load rotate than the combined rotate suggesting that although for diamond and gyroid having an offset loading direction might give higher strengths, the 0° building direction is better. So if an implant was to be loaded predominantly vertically but wanted to take advantage of the 30° load angle maxima then the unit cell could not just be rotated within the implant, the implant would need to also be rotated within the build chamber in order to take advantage of the optimum build angle too. So care must be taken to optimise both the loading direction and the build direction to maximise the loading capacity of the implants. While studies combining the two rotations do not give the full information as to the effects of rotations on mechanical properties.

Increasing the unit cell size led to a reduction in strength and stiffness for the strut

based lattices (BCCZ and diamond), which had decreasing volume fractions. While there was no statistical difference in strength or stiffness of the gyroid lattices. These had the same volume fractions. BCCZ lattice failed with shear planes at 45° with <111> struts bending at the nodes, and [001] struts buckling. The diamond lattices exhibited horizontal crushing and the gyroid lattices barrelling.

All the data was plotted as offset strength against volume fraction or Young's Modulus against volume fraction. Power law curves were fitted to the data and it was found that all data fit these curves with R^2 values of at least 0.93. The strength exponent varied between 2.09 for BCC, and 2.68 for gyroid lattices, neither of which fitted the Gibson Ashby predictions of 1.5 for bend dominated structures or 1 for stretch dominated structures. The stiffness exponent ranged between 1.74 for fluorite lattices and 2.63 for BCC lattices. With the gyroid and all data combined values being within 10% of the Gibson Ashby bend dominated prediction of 2.

Additionally two lattice designs were found to be stronger than bone and with a stiffness in the range of cortical bone. This could be investigated further to understand whether this would enable a reduction in stress shielding. The lattice designs were Fluorite 350 with a strength of 934 $\pm$ 20 MPa and a stiffness of 17.2 $\pm$ 0.1 GPa, and Gyroid 250 with a strength of 995 $\pm$ 18 MPa and a stiffness of 19.0 $\pm$ 0.4 GPa.

It was found that all the lattice parameters considered (unit cell design, strut thickness, volume fraction, rotations and unit cell size) had an influence on the mechanical properties of the lattices, so all must be considered when designing implants involving lattices. Given a number of lattice designs were found that had sufficient compressive strength to support weight bearing while providing sufficient void volume for a secondary drug delivery phase, the use of lattices to control drug release can now be investigated.

CHAPTER 3

BULK LOADING OF LATTICES

3.1 Introduction

The previous chapter has shown that it is possible to generate lattices which have a greater strength than bone and the loading in hip replacements and spinal cages. These lattices also have volume fractions in the range of previous lattices used to deliver therapeutics, and below the desired volume fraction of 0.6. Given there was a strong correlation between volume fraction and offset strength for each of the unit cell designs, the unit cell size can be increased to enable easier entry of a drug loaded biomaterial.

The focus of this chapter is to investigate whether it is possible to control the release of a drug from a carrier material bulk loaded into a lattice by changing the lattice geometry. For example, the release of an antibiotic from a hip implant to treat infection. It is therefore necessary to understand the ideal release quantity and profile of the antibiotic.

Antibiotics generally fall into three categories of pharmacodyamic properties based on time-dependent or concentration-dependent release and whether they experience persistent effects [65]. These lead to three regimes that give ideal release characteristics, the first maximises concentration which is used for the aminoglycosides such as gentamicin sulphate. The second maximises the time that the drug concentration is above the MIC, and a continuous release is ideal, penicillin performs best under these conditions. While vancomycin works best when the amount of drug is maximised as it has time-dependent

killing with persistent effects [66]. Given that each type of antibiotic has a different desired release profile if lattices can be used to control the release then the ideal lattice design for the specific antibiotic can be chosen in order to maximise the amount of bacteria killed and minimise antibiotic resistance.

The desired quantity of antibiotic released will depend on the infection conditions, however for treating infection in hip replacements the current release from PMMA hip spacers gives an indication. When PMMA containing gentamicin sulphate was implanted into humans and the release measured, between 5 and 8% of the drug was released [284, 369, 370, 371]. Hip spacers generally contain between 1 and 3 g of gentamicin sulphate so it would be expected that between 60 and 240 mg of gentamicin sulphate would be released into the body.

As it can be seen not all the gentamicin sulphate releases from PMMA cement. Additionally, the release mechanism is not fully understood, with both surface release and partial bulk release from cracks and pores being proposed as potential mechanisms [282, 283]. So understanding the release mechanisms of the PMMA and the brushite used in this work will enable a better understanding of how device geometry could be used to control release.

Implant geometry has been explored to control the release of drugs in carrier biomaterials. Biomaterial volume, release path length, surface area and positioning of channels from reservoirs have all been explored, as has the drug loading concentration as potential mechanisms to control the drug release [157, 253, 257].

Reservoirs have been explored for drug storage with channels or membranes for drug release [256, 258]. However more relevant to this work, lattices have been bulk loaded with therapeutics including antibiotics such as gentamicin sulphate and vancomycin, and growth factors such as BMP-2 and VEGF [156, 157, 372, 373]. There is therefore scope to manipulate the lattice geometry to add functionality to implants by controlling the drug release.

Gentamicin sulphate can be quantified using the fluorogen ortho-phthalaldehyde (OPA),

this is performed in the presence of propan-2-ol to avoid precipitation [374], and 2-mercaptoethanol as a reducing agent [375]. OPA reacts with primary amines on the gentamicin, and the thiol group of 2-mercaptoethanol to form a fluorescent isoindole derivative (figure 3.1).

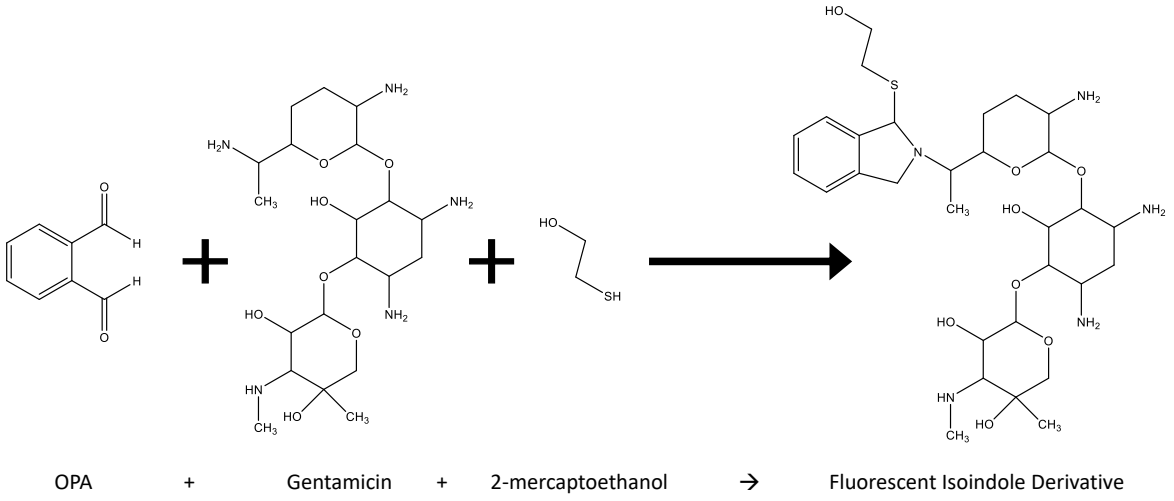

Figure 3.1: Schematic of OPA and gentamicin sulphate chemistry showing one possible reaction of OPA with a primary amine on gentamicin. the thiol group of the 2-mercaptoethanol also reacts with the OPA. The propan-2-ol, sulphate ion and reaction byproducts of water are not shown

The aim of this chapter is to investigate whether varying lattice geometry can be used to control drug release. Gentamicin sulphate was chosen as the drug as it is the most commonly used antibiotic in hip replacements in the USA, and is thermally stable enabling its use in PMMA. This will be bulk loaded into brushite cement as it has a low enough viscosity to flow into the lattices, it is also degradable and approved for use in spinal surgery. This will be compared against controls made of PMMA cement as this is currently used in hip replacements.

Initially the use of OPA as a fluorogen to detect gentamicin sulphate in solution will be validated. Then two new methods are proposed to improve the understanding of the mechanism of release of gentamicin sulphate from PMMA cement, these will also be performed for brushite cement for comparison.

Four factors will be assessed to understand which influence the release of gentamicin

sulphate from brushite cement, in order to control the release of drugs from implants to best suit the ideal release profiles of the therapeutic used. These factors are volume, path length, surface area and drug loading concentration.

Comparisons of the release of gentamicin sulphate from different lattices, specifically BCCZ and gyroid lattices with 0.2, 0.4 and 0.6 volume fraction will be observed. These will also be compared to controls of brushite and PMMA without lattices. Kinetic models will be fitted to these curves.

The chapter will undertake an assessment of antimicrobial efficacy with *Staphylococcus aureus* and *Pseudomonas aeruginosa* to investigate whether changing the lattice geometry influences the bacterial inhibition. These bacteria were chosen as they are gram positive and negative respectively, and are both commonly found in the hip cavity of infected hip replacements. Finally compression testing of the cement lattice composites will be performed to confirm the presence of the cement does not lead to a reduction in strength.

3.2 Methods

3.2.1 Materials, Equipment and Reagents

The reagents used to make brushite cement were citric acid powder (Fisher Scientific, UK), gentamicin sulphate powder (G - Biosciences, USA), β - tricalcium phosphate ($\beta - Ca_3(PO_4)_2$) (β-TCP) (Sigma – Aldrich, USA), and monocalcium phosphate monohydrate ($Ca(H_2PO_4)_2 \cdot H_2O$) (MCPM) (Sigma - Aldrich, USA). For PMMA the reagents were Methyl Methacrylate stabilised with Hydroquinone (Scientific Laboratory Supplies, Ltd, UK) (MMA), N-N Dimethyl-p-Toluidine (Merck, KGaG, Germany), Polymethyl Methacrylate (Alfa Aesar, Thermo Fisher, Inc, USA) (PMMA), Gentamicin Sulphate powder (G - Biosciences, USA), Barium Sulphate (Scientific Laboratory Supplies, Ltd, UK), and Benzoyl Peroxide (Scientific Laboratory Supplies, Ltd, UK).

Fluorescence readings used Phthaldialdehyde Reagent Complete Solution, containing phthaldialdehyde (1 $mgml^{-1}$), Brij 35, methanol, 2-mercaptoethanol, potassium hydrox-

ide, and boric acid (Sigma, Merck, KGaG, Germany) (OPA), and Propan-2-ol (Fisher, Thermo Fischer Scientific, Inc, USA). The antibacterial assay used LB broth (Lennox, Sigma, Merck, KGaG, Germany), LB agar (Lennox, Sigma, Merck, KGaG, Germany), the bacteria used were *Staphylococcus aureus* and *Pseudomonas aeruginosa*. The feed-stock for the polymer printing was poly lactic acid (PLA), while the laser powder bed fusion machine uses gas atomised spherical Ti-6Al-4V grade 23 powder in the size range 15-53 μm (LPW Technology Ltd, UK). Spectroscopy was performed on a plate reader which was a Spark Multimode Microplate Reader (Tecan Trading AG, Switzerland), using UV transparent 96 well plates.

3.2.2 General Methods

Brushite Formulation

Dicalcium phosphate dihydrate cement ($CaHPO_4 \cdot 2H_2O$), known as brushite was manufactured from a powder and liquid phase in a powder to liquid ratio of 2. The liquid phase was formed by dissolving citric acid at 5.5% w/w and gentamicin sulphate powder at 2.5% w/w in deionised water. β-TCP at 35% w/w (7% excess) and MCPM at 28% w/w were hand ground and mixed together. The mixed powders were then combined with the liquid phase in a 2:1 ratio by mass and hand mixed for 30 seconds to form a paste. The paste was cast into moulds by pouring from the top and shaking on a vortexer at 100rpm for one minute to remove air bubbles. Cement was allowed to set in the mould for 24 hours at room temperature.

$$\beta{-}Ca_3(PO_4)_2 + Ca(H_2PO_4)_2 \cdot H_2O + 7H_2O \rightarrow 4CaHPO_4 \cdot 2H_2O \tag{3.2.1}$$

PMMA Formulation

Poly(methyl methacrylate) (PMMA) was manufactured from a powder and liquid phase at a ratio of 2.36 following the protocol previously developed to mimic commercially available

cements [376]. Briefly the powder components of PMMA at 60.5% w/w, barium sulphate at 6.8% w/w, benzoyl peroxide at 1.2% w/w and gentamicin sulphate at 2.5% w/w if present were mixed, and separately the liquid components were combined specifically MMA at 28.6% w/w and N-N Dimethyl-p-Toluidine at 0.4% w/w. The liquid and powder components were then combined and hand mixed for a minute prior to mould filling. Cement was allowed to set in the mould for 24 hours.

Manufacture of Metal Parts by L-PBF

Laser Powder Bed Fusion (L-PBF) was used to manufacture the metal samples used in this chapter as previously described in chapter 2, section 2.2.1. Briefly a RenAM 500M (Renishaw, PLC, UK) L-PBF system was used to print the samples from gas atomised spherical Ti-6Al-4V grade 23 powder in the size range 15-53 μm (LPW Technology Ltd, UK), using optimised parameters (table 2.1). Water jetting, Quill Vogue powder wash (Quill International Group Ltd, UK) was used to remove excess powder before part removal from the substrate using wire electrodischarge machining, Cut 20 (Beijing Agie Charmilles Ltd, China).

Manufacture of Polymer Parts by Extrusion Printing

Parts for polymer printing were generated on nTopology Platform (nTopology, Inc, USA), and sliced on PrusaSlicer-2.2.0 (Prusa Research a.s., Czech Republic) to generate gcode. which was then loaded into the Original Prusa i3 MK3+ (Prusa Research a.s., Czech Republic) extrusion printer, which prints the parts from PLA.

3.2.3 General Procedure for Measuring Gentamicin Sulphate Elution from Brushite Cement

The samples were placed in PBS and at each time point all the solution was removed and replaced. 33 μl of the solution was mixed with 33 μl of propan-2-ol and 33 μl of OPA reagent. This solution was placed in the well of a UV transparent 96 well plate, and

scanned with the fluorescence intensity scan top reading function of the plate reader with an excitation wavelength of 340 mm and emission wavelength of 430 mm. The fluorescence readings were converted to the mass of gentamicin sulphate in solution using a calibration curve (discussed later in section 3.2.4).

Cumulative release curves were generated for the elution data in Matlab (MathWorks Inc, USA) with the cumulative standard deviation calculated by the variance sum law equation 3.2.2. The curve was deemed to have reached its plateau region when the fluorescence value was lower than 20,000, which equates to 0.5 mgml^{-1}.

$$Var(x+y) = Var(x) + Var(y) + 2Cov(x,y) \tag{3.2.2}$$

Korsmeyer Peppas curves with equation 3.2.3 [271] were fitted to the data using Matlab function fit, power1. Where M is the drug release, a is a coefficient related to the geometry, and b is an exponent related to the release kinetics.

$$M = a * t^b \tag{3.2.3}$$

3.2.4 Experiments

Gentamicin Sulphate Calibration and Validation

Brushite samples were generated to validate the gentamicin sulphate measurement techniques following the protocol 'Brushite Formulation' in section 3.2.2. PLA moulds with cylindrical voids 6 mm in diameter and 14 mm in height were 3D printed following the protocol 'Manufacture of Polymer Parts by Extrusion Printing' in section 3.2.2, and filled with brushite cement. Additionally solutions were made up containing the individual components of brushite with or without gentamicin sulphate in 5 ml of PBS at the same ratios as in the brushite cement. Gentamicin sulphate was mixed at 3.5 mgml^{-1}, MCPM at 45 mgml^{-1}, β-TCP at 52 mgml^{-1}, and citric acid at 8.2 mgml^{-1}.

Two methods were used to detect gentamicin sulphate, the first was UV-Vis absorption

spectroscopy. In order to find the optimum absorbance wavelength gentamicin sulphate was dissolved in PBS at 30 $mgml^{-1}$. 100 µl of solution were placed in a well of a UV transparent 96 well plate, and an absorbance scan was performed between 220 and 340 nm using the absorbance function of the plate reader (Spark Multimode Microplate Reader, Tecan Trading AG, Switzerland), the maxiumum adbsorbance was found at 248 nm. Three dilution series were created starting at 30 $mgml^{-1}$, then using 50:50 mixtures with PBS to create a series, The absorbance of the solutions in these series at 248 nm were then measured and used to create a calibration curve. This wavelength was also used to measure the absorbance of 100 µl of each of the validation solutions.

Fluorescence was also used as a method to detect gentamicin sulphate. The samples were mixed with OPA and propan-2-ol in order to create a fluorescence signal. Initially 20 $mgml^{-1}$ gentamicin sulphate in PBS was used to determine the optimum excitation and emission wavelengths, these were found to be 340 nm and 430 nm respectively. 33 µl of solution, 33 µl of propan-2-ol, and 33 µl of OPA were aliquoted into a well of the 96 well plate, and scanned with the fluorescence intensity scan top reading function of the plate reader (Spark Multimode Microplate Reader, Tecan Trading AG, Switzerland). Three dilution series were generated starting at 125 $mgml^{-1}$ gentamicin sulphate in PBS and using 50% dilution per step. These were measured with an excitation wavelength of 340 nm and an emission wavelength of 430 nm. These wavelengths were also used to measure the fluorescence of each of the validation solutions.

Determining the Permeability of the Materials

To understand whether the polymers used in the elution studies were impermeable to gentamicin sulphate the following samples were made. Polypropylene tubes 200 mm in length and 4.8 mm in diameter were filled with brushite containing gentamicin sulphate in the middle 50 mm, and then placed in PBS with the end outside of the solution for four months. Additionally 10x10x10 mm cubes with one face missing were 3D printed in PLA and filled with brushite cement containing gentamicin sulphate. The exposed face

of the cement was then coated with ethylene-vinyl acetate (EVA) to test the permeability of the PLA print and the EVA coating. These specimens were then placed in PBS for four months.

Understanding the Rate of Release of Gentamicin Sulphate from PMMA and Brushite Cement

Polymer tubes 4.8 mm in diameter made of polypropylene were filled with brushite or PMMA cement containing gentamicin sulphate and cut to 100 mm of cement length. These tubes were placed in 40 ml PBS with the cut end exposed to the cement for one, three or five weeks. The media was refreshed at one, three and five weeks. The media was measured for gentamicin sulphate concentration following the protocol 'Fluorescence Quantification of Gentamicin Sulphate' in section 3.2.2. After the samples were removed from the initial elution they were dried for 24 hours prior to cutting into ten 10 mm long pieces (figure 3.2). These pieces were then placed in 2 ml of PBS for two months with regular removal and replacement of the media.

60 mm long, 4.8 mm diameter polymer tubes made of polypropylene were filled with brushite or PMMA cement in one of three configurations. In the first all the cement contained gentamicin sulphate, in the second the central third (20 mm) length-ways contained gentamicin sulphate while the outer thirds did not, named NGN. While in the third configuration none of the cement contained gentamicin sulphate figure 3.3). The samples were placed in 20 ml of PBS for two months with regular removal and replacement of the PBS.

Factors Influencing Elution

Samples with different cement volumes were manufactured by filling polypropylene tubes of 4.8 mm diameter with brushite cement following the protocol 'Brushite Formulation' in section 3.2.2 and cutting to 20 mm (V360), 40 mm (V720) or 60 mm (V1060) lengths (figure 3.4a). These samples were placed in 20 ml PBS for 8 weeks with regular removal

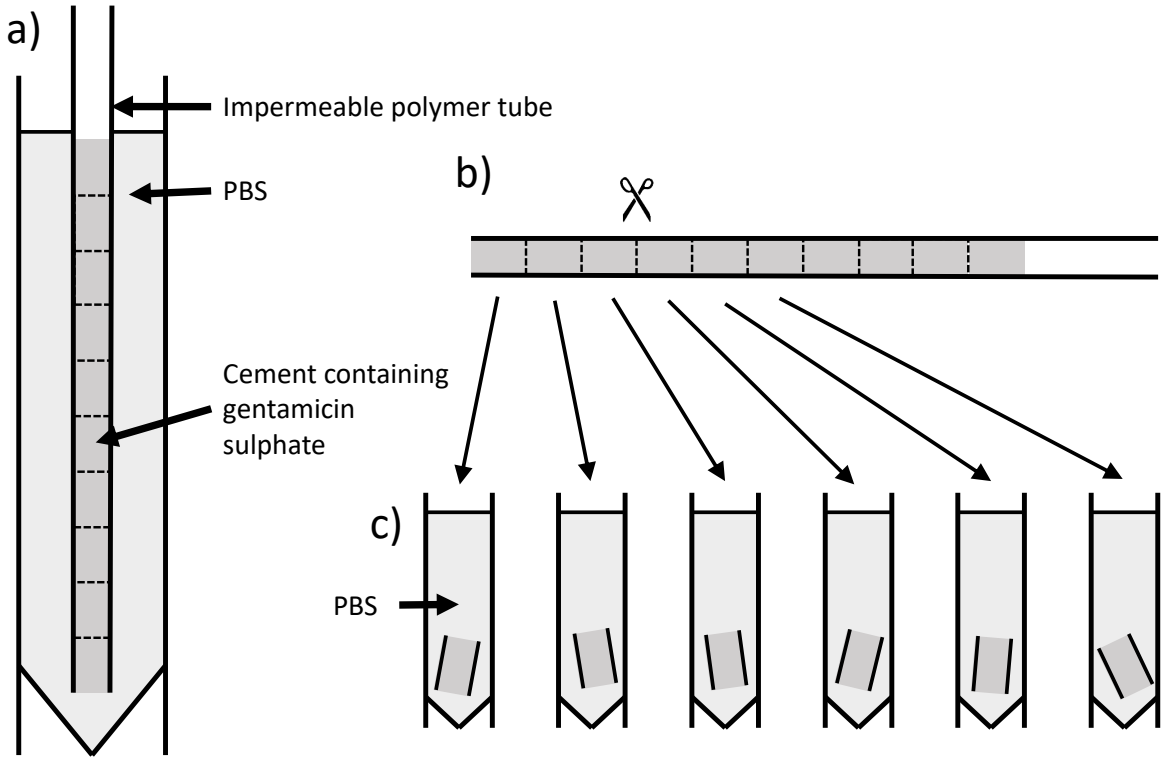

Figure 3.2: Schematic of experiment to investigate whether gentamicin sulphate elution is concentration driven, a) cement containing gentamicin sulphate in an impermeable polymer tube submerged with one end in PBS for 1, 3 or 5 weeks in triplicate, b) the polymer tube removed from initial elution, cut up into 10mm lengths, c) each section placed in fresh PBS

and replacement of the PBS. The solutions were analysed following the protocol 'General Procedure for Measuring Gentamicin Sulphate Elution from Brushite Cement' in section 3.2.3.

In order to investigate the influence of changing the gentamicin sulphate diffusion path length samples were manufactured following the protocol 'Manufacture of Polymer Parts by Extrusion Printing' in section 3.2.2. The parts had a void 10,000 mm^3 (50x20x10 mm), and interior baffles with total volume of 1350 mm^3 were placed inside the internal void as in figure 3.1b. The baffles for L50 were along the whole length of the void 50x2.7x10 mm, for L90 one baffle 45x3x10 in the centre of the void, for L130 two baffles 45x1.5x10 mm, and for L170 three baffles 45x1x10 mm. So the total cement volume was 8650 mm^3 for all samples. The top surface was coated in EVA leaving an opening on the vertical face

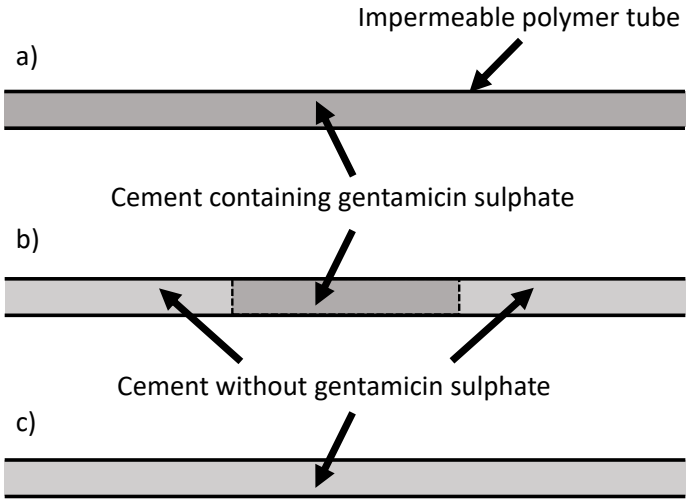

Figure 3.3: Schematic of experiment to investigate whether gentamicin sulphate can permeate the cement, a) impermeable polymer tube containing cement with gentamicin sulphate b) impermeable polymer tube containing cement with gentamicin sulphate in the centre section, capped with cement without gentamicin sulphate, referred to as NGN c) polymer tube containing cement without gentamicin sulphate

4.5x10 mm resulting in an exposed cement surface area of 45 mm^2. The samples were placed in 20 ml PBS for 8 weeks with regular removal and replacement of the PBS.

The samples generated to compare different surface areas were cubes with a side length of 10 mm. Five sided PLA cubes with an internal void 10x10x10 mm were generated following protocol 'Manufacture of Polymer Parts by Extrusion Printing' in section 3.2.2, these were filled with brushite cement containing 2.5% w/w gentamicin sulphate in accordance with protocol 'Brushite Formulation' in section 3.2.2. After setting, the sides were removed to leave cubes with 1, 3 or 5 sides exposed (figure 3.4c). The samples were placed in 5 ml PBS for 8 weeks with regular removal and replacement of the PBS.

In order to generate samples with different gentamicin sulphate concentrations polypropylene tubes of 4.8 mm diameter were filled with brushite cement containing 2.5, 5.0 or 7.5% w/w gentamicin sulphate, these were left to set for 24 hours and then cut to 31 mm in length. The samples were placed in 10 ml PBS for 8 weeks with regular removal and replacement of the PBS.

The parameters of all the samples are listed in table 3.1.

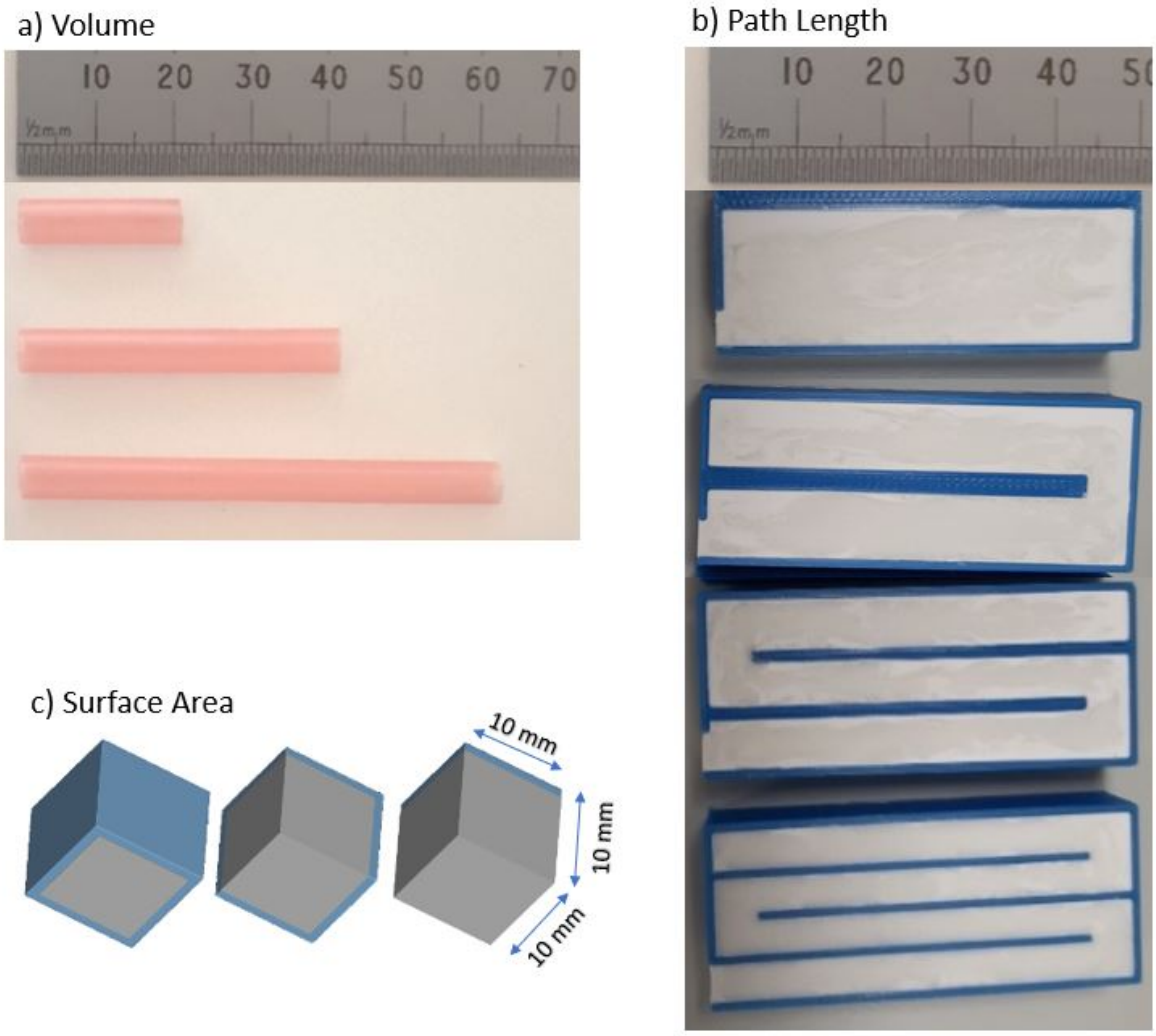

Figure 3.4: Photographs of samples to understand factors influencing release. A) Polymer tubes 20, 40, 60 mm in length with mean diameter of 4.8 mm. The samples with different gentamicin sulphate concentration were of the same design 31 mm in length. B) Samples to study path length (distance from the furthest point of the cement to the media) with internal void volume dimensions, 50 x 20 x 10 mm, opening 4.5 by 10 mm. C) Samples to compare different exposed cement surface area. 10 x 10 x 10 mm cubes with one, three and five faces exposed.

Lattice Elution

Lattice samples were generated following protocol 'Manufacture of Metal Parts by L-PBF' in section 3.2.2. Specifically BCCZ and gyroid lattices with 0.2, 0.4 and 0.6 volume fractions, 3 mm unit cell length in cylinders with 20 mm diameter and 20 mm height (figure 3.5). PLA split moulds were manufactured following protocol 'Manufacture of

Factor changing	Variable Names	Volume / mm^3	GS Concentration /% w/w	Path Length / mm	Surface Area / mm^2
Cement Volume	V360	362	2.5	10.0	36.2
	V720	724	2.5	20.0	36.2
	V1080	1080	2.5	30.0	36.2
Path length	L50	8650	2.5	52.9	45.0
	L90	8650	2.5	91.6	45.0
	L130	8650	2.5	131.0	45.0
	L170	8650	2.5	171.0	45.0
Exposed Cement Surface Area	A100	1000	2.5	5.0	100.0
	A300	1000	2.5	5.0	300.0
	A500	1000	2.5	5.0	500.0
Gentamicin Sulphate Concentration	C2.5	561	2.5	15.5	36.2
	C5.0	561	5.0	15.5	36.2
	C7.5	561	7.5	15.5	36.2

Table 3.1: Parameters of samples for fundamental studies, showing cement volume, gentamicin sulphate concentration, diffusion path length from the furthest distance in the cement to the exposed surface, and surface area of the exposed cement, GS is gentamicin sulphate

Polymer Parts by Extrusion Printing' in section 3.2.2. Lattice samples were placed in the moulds and filled with brushite cement containing 2.5% w/w gentamicin sulphate following protocol 'Brushite Formulation' in section 3.2.2. Additionally moulds were filled with brushite cement with and without gentamicin sulphate as controls. Finally moulds were lined with aluminium foil and filled with PMMA cement with and without gentamicin sulphate following protocol 'PMMA Formulation' in section 3.2.2. Sample parameters can be found in table 3.2). The samples were placed in 10 ml PBS for eight weeks with regular removal and replacement of the PBS.

In Vitro Assessment of Antimicrobial Efficacy

Two sets of samples that matched those used in the lattice elution were generated in the same way. 140 mm diameter plates were filled with 68 ml of LB agar and left to set overnight. Spread plates of *Staphylococcus aureus* (Newman's) and *Pseudomonas aeruginosa* (PA01) were generated and left overnight, then one colony of each bacteria

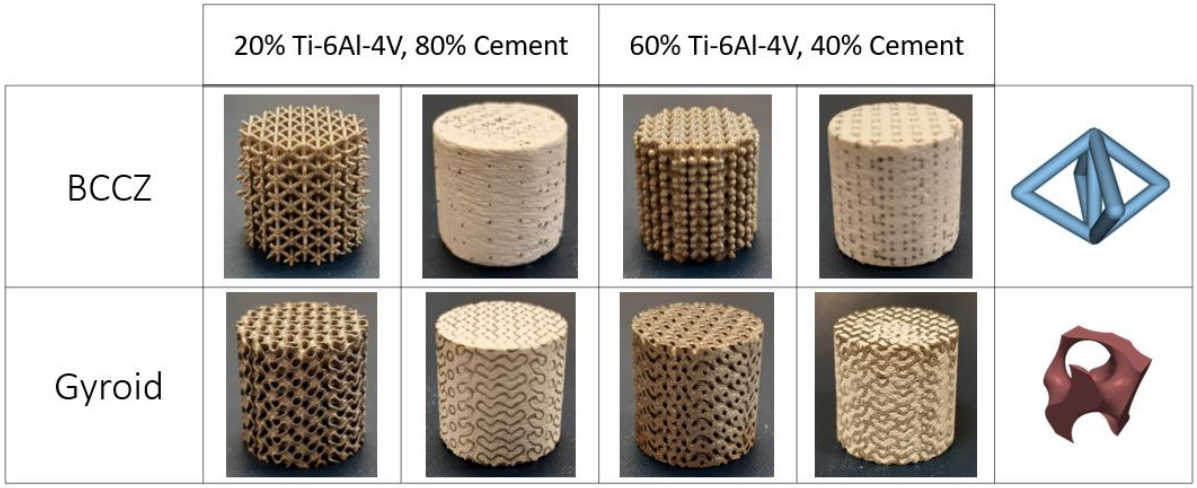

Figure 3.5: Photographs of empty and brushite cement filled lattices showing the shape and giving an indication of the exposed surface areas. Single unit cells of the BCCZ and Gyroid lattices are shown on the right

was added to LB broth and cultured overnight. These overnight broth cultures were then diluted until the optical density was 0.06 at 600 nm, measured on CE 7500 UV–Vis spectrophotometer (Cecil Instruments, UK). 540 μl of broth culture was then spread onto each agar plate. A hole of 20 mm diameter was bored into the centre of each plate and a sample inserted. These were then incubated overnight at 37°C, to enable a confluent lawn to grow. After incubation the diameters of each zone of inhibition was measured five times.

Compression Testing of Brushite Filled Lattices

Three sets of samples were used for compression testing of lattices. The first set were samples which had been used for the lattice elution experiments, these were referred to as aged. A second set of samples were made in the same way and referred to as new, and finally a set of lattices with the same characteristics were used but not filled with cement.

Compression testing was performed on ESH servo-hydraulic fatigue testing machine (ESH limited, UK) following the protocol 'Compression Testing' from chapter 2 section 2.2.3. Briefly, compression testing was performed under displacement control at a rate of 4.5 mm min^{-1}. Force displacement data was imported into Matlab (MathWorks Inc,

Variable Names	Volume Lattice / %	Volume Cement / %	Lattice Volume / mm^3	Cement Volume / mm^3	GS Concentration / % w/w	Surface Area / mm^2	Strut Thickness / mm
Brushite with GS	0	100	0	6280	2.5	1890	N/A
Brushite no GS	0	100	0	6280	2.5	1890	N/A
PMMA with GS	0	100	0	6280	2.5	1890	N/A
PMMA no GS	0	100	0	6280	2.5	1890	N/A
BCCZ20	20	80	1250	5030	2.5	1500	0.597
BCCZ40	40	60	2510	3770	2.5	1100	0.904
BCCZ60	60	40	3770	2510	2.5	739	1.192
Gyroid20	20	80	1260	5030	2.5	1530	0.309
Gyroid40	40	60	2510	3770	2.5	1130	0.615
Gyroid60	60	40	3770	2510	2.5	734	0.913

Table 3.2: CAD dimensions of lattice samples, showing the percentage and absolute volumes of the Ti-6Al-4V lattices and cement, the gentamicin sulphate concentration in the cement, the surface area of the cement exposed to the solution, and the strut or wall thickness of the lattice design. GS - gentamicin sulphate

USA) where it was converted to stress strain data. The Young's Modulus and 0.2% offset stress were then calculated from the curve.

Statistics

For all experiments three independent samples were generated for each variable. Statistical analysis was performed using Matlab (MathWorks Corp, USA), initially one way ANOVA testing was performed to see whether all the data had an equal mean. If there was not a common mean then Tukey post hoc testing was performed to identify which means were statistically different.

3.3 Results

3.3.1 Validation of Gentamicin Sulphate Detection Methods

Two spectrophotometric methods for quantifying gentamicin sulphate released from brushite cement were compared, specifically absorbance, and fluorescence with ortho-phthalaldehyde

(OPA) as a fluorogenic agent. An absorption spectra scan (not shown) was used to find the optimum wavelength for gentamicin sulphate, it was found to be 248 nm. The linearity, precision, range and detection limits were investigated using a calibration curve of gentamicin sulphate in PBS buffer (figure 3.6a). The data fitted a linear regression model well ($R^2 = 1.00$) with equation: $Absorbance = 0.0337 * Concentration + 0.0722$. The precision was at least 0.1 $mgml^{-1}$, with a range of 0.2 to 30 $mgml^{-1}$.

The selectivity of the method was investigated by comparing the absorbance of solutions containing different cement components with and without gentamicin sulphate with reference solutions containing gentamicin sulphate (figure 3.6b). The reference absorbance for 3.5 $mgml^{-1}$ gentamicin sulphate in PBS was 0.195 ± 0.031, this was not statistically different from the absorbance of the solutions containing gentamicin sulphate and brushite components (MCPM, β-TCP, and citric acid). PBS without gentamicin sulphate has an absorbance reading of 0.0795 ± 0.0008 which was not statistically different from solutions containing β-TCP and citric acid without gentamicin sulphate. However solutions containing MCPM and brushite without gentamicin sulphate had absorbances of 0.142 ± 0.001 and 0.199 ± 0.018 respectively, which were both statistically higher than PBS alone. Additionally, a solution containing brushite and gentamicin sulphate had an absorbance reading of 0.346 ± 0.015 which is 75% higher than the standard of gentamicin sulphate in PBS (0.195 ± 0.031). The absorbance assay is unsuitable to quantify the gentamicin sulphate concentration in solution because the presence of other cement components in solution increased the absorbance measurements, and brushite had an absorbance reading in the range of the gentamicin sulphate.

As an alternative OPA was used as a fluorogen for gentamicin sulphate, and the fluorescence was measured. Fluorescence excitation and emission scans were used to find the optimal wavelengths (not shown), and an excitation wavelength of 340 nm and an emission wavelength of 430 nm were found to give the maximum fluorescence values. A calibration curve of fluorescence and gentamicin sulphate concentration did not fit a linear regression model (figure 3.6c), but a power law fitted with an R^2 value of 1.00, and

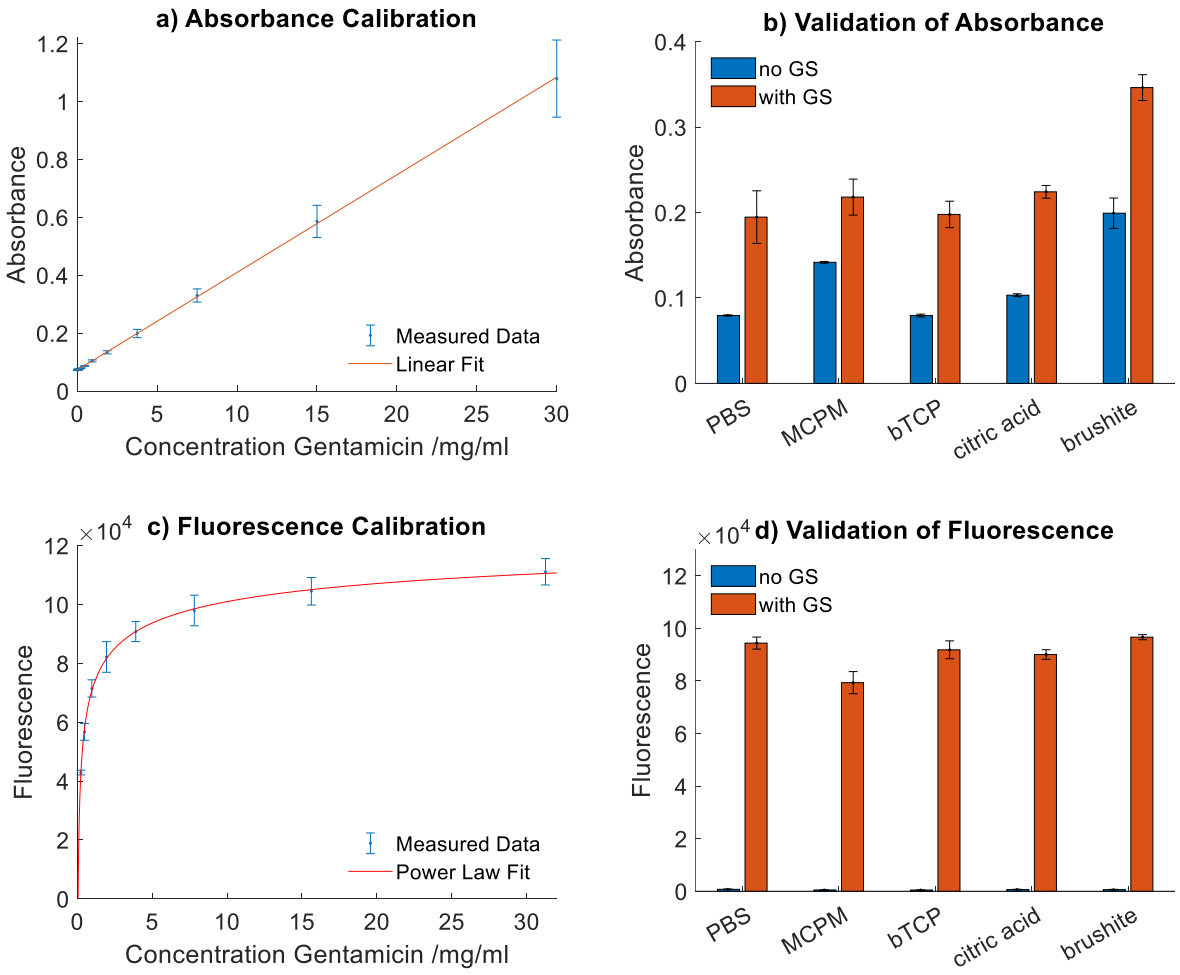

Figure 3.6: Validation of spectrophotometric methods for quantifying gentamicin sulphate released from brushite cement. a) Calibration curve for absorbance vs concentration of gentamicin sulphate with a linear regression line with equation $Absorbance = 0.0337 * Concentration + 0.0722$ fitted to the data, b) validation of absorbance selectivity to gentamicin sulphate compared with components of brushite cement, c) calibration curve for fluorescence vs gentamicin sulphate concentration with a power law regression line with equation $Fluorescence = -69100 * Concentration^{-0.245} + 140000$ fitted to the data, d) validation of fluorescence selectivity to gentamicin sulphate compared with components of brushite cement. Error bars are one standard deviation, GS - gentamicin sulphate

equation $Fluorescence = -69100 * Concentration^{-0.245} + 140000$. The precision was at least 0.01 mgml^{-1}, over the range 0.01 to 30 mgml^{-1}.

Comparing the fluorescence of solutions containing the components of brushite enabled the selectivity of the method to be investigated. The fluorescence values for solutions without gentamicin sulphate were below 1000 for all variations (figure 3.6d), which was at least 80 times lower than the solutions containing gentamicin sulphate. The reference solutions

of 3.5 $mgml^{-1}$ gentamicin sulphate in PBS had a fluorescence of 94400 $\pm$ 2290, the only other solution containing gentamicin sulphate which was statistically different from this was the solution containing MCPM and gentamicin sulphate which had a fluorescence measurement of 79300 $\pm$ 4220.

3.3.2 Determining the Permeability of the Materials

Prior to their use during elution experiments the permeability of the polymer tubes, 3D printed polymer parts and the EVA polymer coating were checked. No gentamicin was found in solution from the sealed parts after four months. Indicating that these materials were impermeable to gentamicin sulphate over this time frame.

3.3.3 Gentamicin Sulphate Release Mechanism

In order to understand how gentamicin sulphate was released from brushite and PMMA cement two experiments were devised. The first involved a two step elution to understand how the gentamicin sulphate moved through the cement during the initial elution, by looking at how much was left in each section during the second elution.

During the first elution there was a positive trend in mass of gentamicin sulphate released with time for both cement types (figure 3.7a&b). The mass of gentamicin sulphate released was higher for the PMMA cement than brushite at each time point, however it was only statistically significant at five weeks. The mass of gentamicin sulphate released from PMMA was 14.00 $\pm$ 5.35 mg (31%) at five weeks, while from the brushite it was 9.72 $\pm$ 1.37 mg (11.6%). There was no statistical difference between the gentamicin sulphate released from each cement at each time point although there was a greater variability within the PMMA samples than the brushite samples.

After the initial elution the samples were cut up into ten pieces and placed in PBS in order to ascertain how much gentamicin sulphate was left in each section along the length of the tubes (figure 3.2). Unfortunately the OPA reagent had degraded when the brushite samples with 5 weeks of initial elution were measured so no gentamicin sulphate

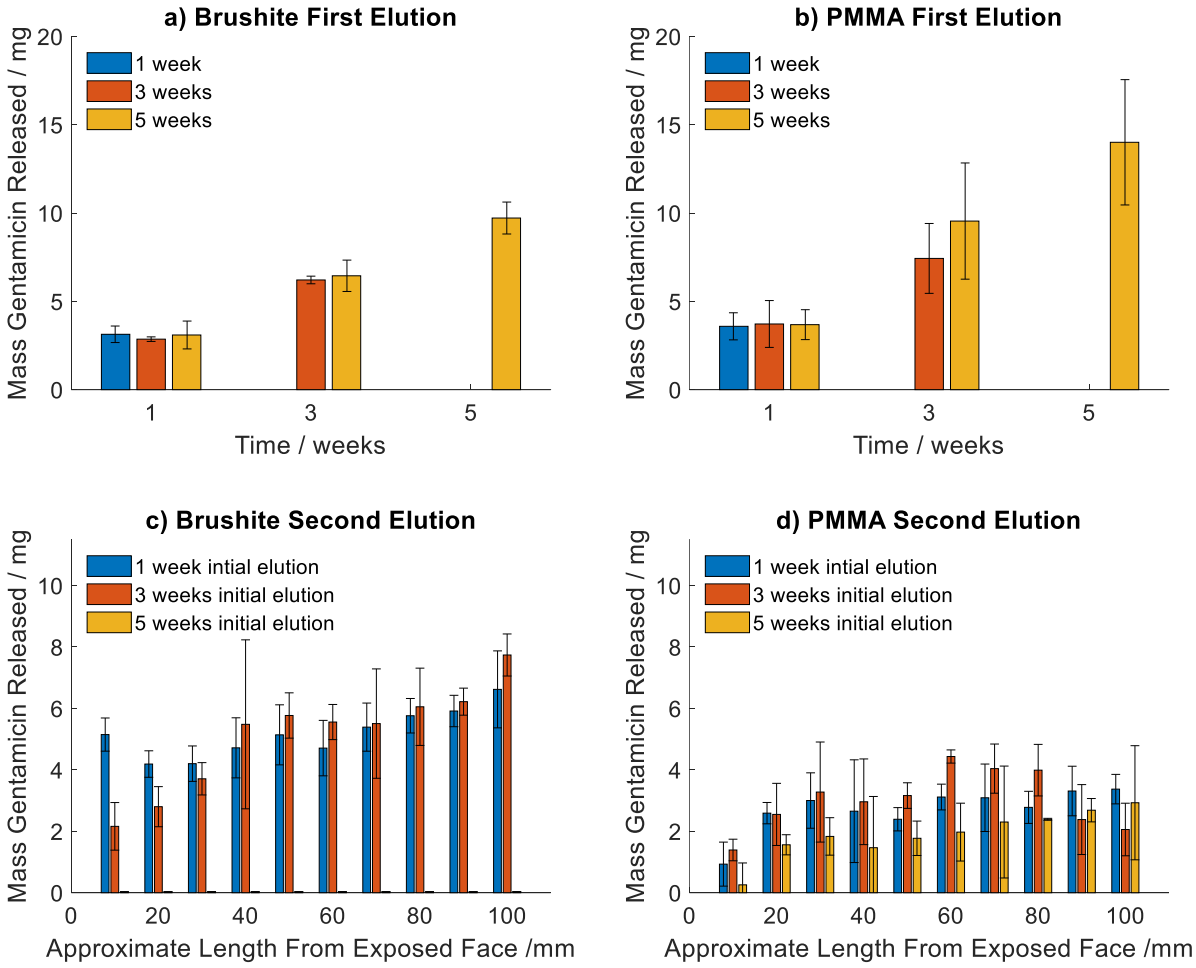

Figure 3.7: Mass of gentamicin sulphate released from two part elution experiment, which was used to investigate whether elution of gentamicin sulphate from brushite and PMMA cement was a surface effect or driven by a concentration gradient. The initial elution was for one, three of five weeks shown in a) for brushite and b) for PMMA. Followed by splitting the samples into ten pieces and a second elution of each piece shown in c) for brushite and d) for PMMA. Error bars show one standard deviation (n=3)

was detected. More gentamicin sulphate was released from the brushite cement than the PMMA cement during the second elution (figure 3.7c&d). For the brushite cement samples a positive correlation was found between the length of the tube (from the face exposed to PBS in the first elution) and the mass of gentamicin sulphate released in the second elution. This was clearer after a three week initial elution than a one week initial elution. After one week initial elution the mass eluted from the piece closest to the open end was 5.15 $\pm$ 0.54 mg while at the far end it was 6.62 $\pm$ 1.25 mg only 30% higher,

while for the three week initial elution the near end mass was 2.16 ± 0.78 mg compared the far end of 7.74 ± 0.68 mg, an increase of 360%.

The second elution of the PMMA did not have a correlation between the mass of gentamicin sulphate eluted and the length (figure 3.7d), instead the mass was independent of length with the exception of the first piece which had a lower mass. After one week of initial elution the first piece gentamicin sulphate mass was 0.93 ± 0.72 mg while the mean mass of the other lengths together was 2.92 ± 0.34 mg, for three weeks initial elution these values were 1.39 ± 1.01 mg and 3.21 ± 0.82 mg, and after five weeks of initial elution they were 0.26 ± 0.71 mg and 2.10 ± 0.51 mg. In each case the eluted gentamicin sulphate from the pieces nearest the exposed face were less than half the average from the rest of the pieces.

The second experiment investigated the permeability of brushite and PMMA cement with respect to gentamicin sulphate dissolved in PBS. This experiment explored whether the drug could travel through the cement or was only released from the surface by using cement without gentamicin sulphate as buffers to the drug loaded cement in the centre of the sample, these samples were referred to as NGN. Samples loaded with gentamicin sulphate throughout, and those with no drug were used for comparison (figure 3.3). For the brushite cement the samples containing gentamicin sulphate throughout had the fastest rate of gentamicin sulphate release reaching a plateau within ten days (figure 3.8a). They also had the highest mass of gentamicin sulphate released amongst the brushite samples at 2.21 ± 0.18 mg which equates to 4.93 ± 0.36% of the gentamicin sulphate in the samples. The NGN samples reached a plateau later at 24 days at a mass of 0.97 ± 0.04 mg which was 4.04 ± 0.17% of the gentamicin sulphate in the cement.

For the PMMA cement samples, those with gentamicin sulphate throughout exhibited release from day zero and although the rate of increase slowed the mass of gentamicin sulphate released did not plateau even after 150 days (figure 3.8c). At 49 days the mass of gentamicin sulphate released was 9.58 ± 6.73 mg which equated to 35.0 ± 25.6% of the gentamicin sulphate loaded into these samples. These values have a high standard

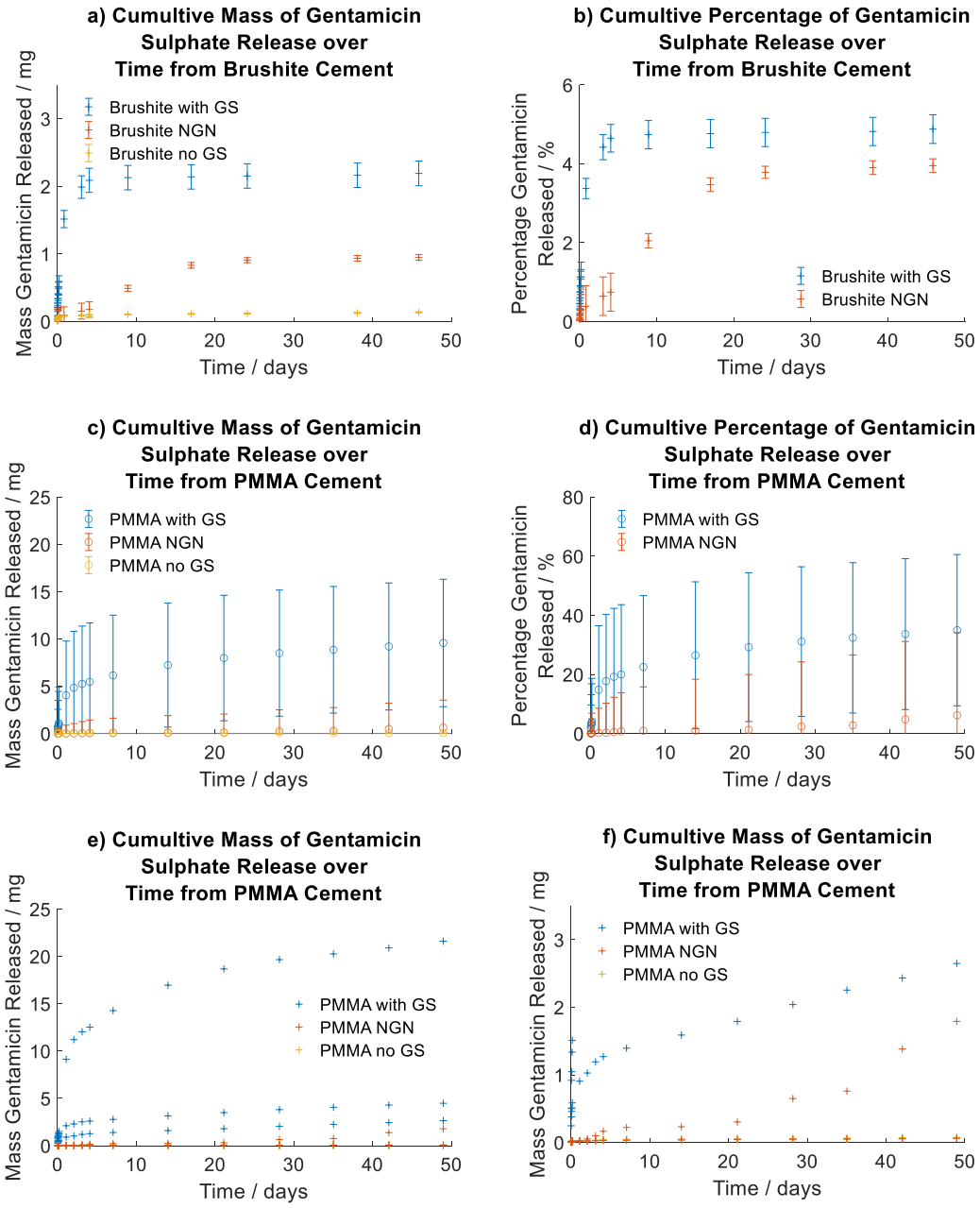

Figure 3.8: Elution of gentamicin sulphate from polymer tubes containing brushite and PMMA cement incorporating gentamicin sulphate to investigate gentamicin sulphate permeability, a) mass of gentamicin sulphate released from brushite cements b) percentage released, c) mass of gentamicin sulphate released form PMMA, d) percentage released, e) individual readings of mass of gentamicin sulphate released for PMMA cement, f) scaled view of e showing one of the NGN samples had a non zero release with a delayed starting point compared to the samples with GS throughout. GS - gentamicin sulphate, NGN - samples with cement containing gentamicin sulphate in the middle capped with cement without gentamicin sulphate. Error bars show one standard deviation (n=3)

deviation so each sample was plotted separately (figure 3.8e). It can be seen that one of the samples has a release four times higher than the other 'PMMA with GS' samples. The mass of gentamicin sulphate released from these two samples were in the range of the 'Brushite with GS' samples.

Two of the PMMA NGN samples had releases of gentamicin sulphate which could not be distinguished from those without gentamicin sulphate (figure 3.8f), while one sample had a delayed release compared to the 'PMMA with GS' samples, with no release until two days and then not reaching 1 mg of released gentamicin sulphate until 42 days, where it was measured at 1.38 mg. This equated to 13.4% of the loaded gentamicin sulphate.

3.3.4 Factors Influencing Elution

To understand the influence of volume on gentamicin sulphate release, samples with constant surface area and gentamicin sulphate concentration, but different volumes were produced. The mass of gentamicin sulphate released into solution over time showed the mass release for three volumes plateaued at different time points (figure 3.9a). V360 with the smallest volume (362 mm^3) plateaued at eight days while V1080 (1080 mm^3) did not reach a plateau until 47 days. The mass of gentamicin sulphate released once the release had plateaued was statistically different between the three designs (table 3.3). The largest mass released was for V1080 at 24.2 $\pm$ 2.9 mg, while the smallest was for V360 at 6.2 $\pm$ 1.1 mg, Tukey post hoc testing showed that all three release masses were statistically different from each other (table 3.4).

The Korsmeyer Peppas model was fitted to the three curves in order to compare the rate and shape of release. A good fit was found between the model and all three curves with R^2 values of at least 0.98. The Peppas a value was around 1.5 for all three curves with Peppas b values of approximately 0.7 (table 3.3). The Peppas a and b values were not statistically different between the three designs, $p = 0.17$ for Peppas a, and $p = 0.05$ for Peppas b by ANOVA (table 3.4). This indicates that the curves had the same shape and rate of release.

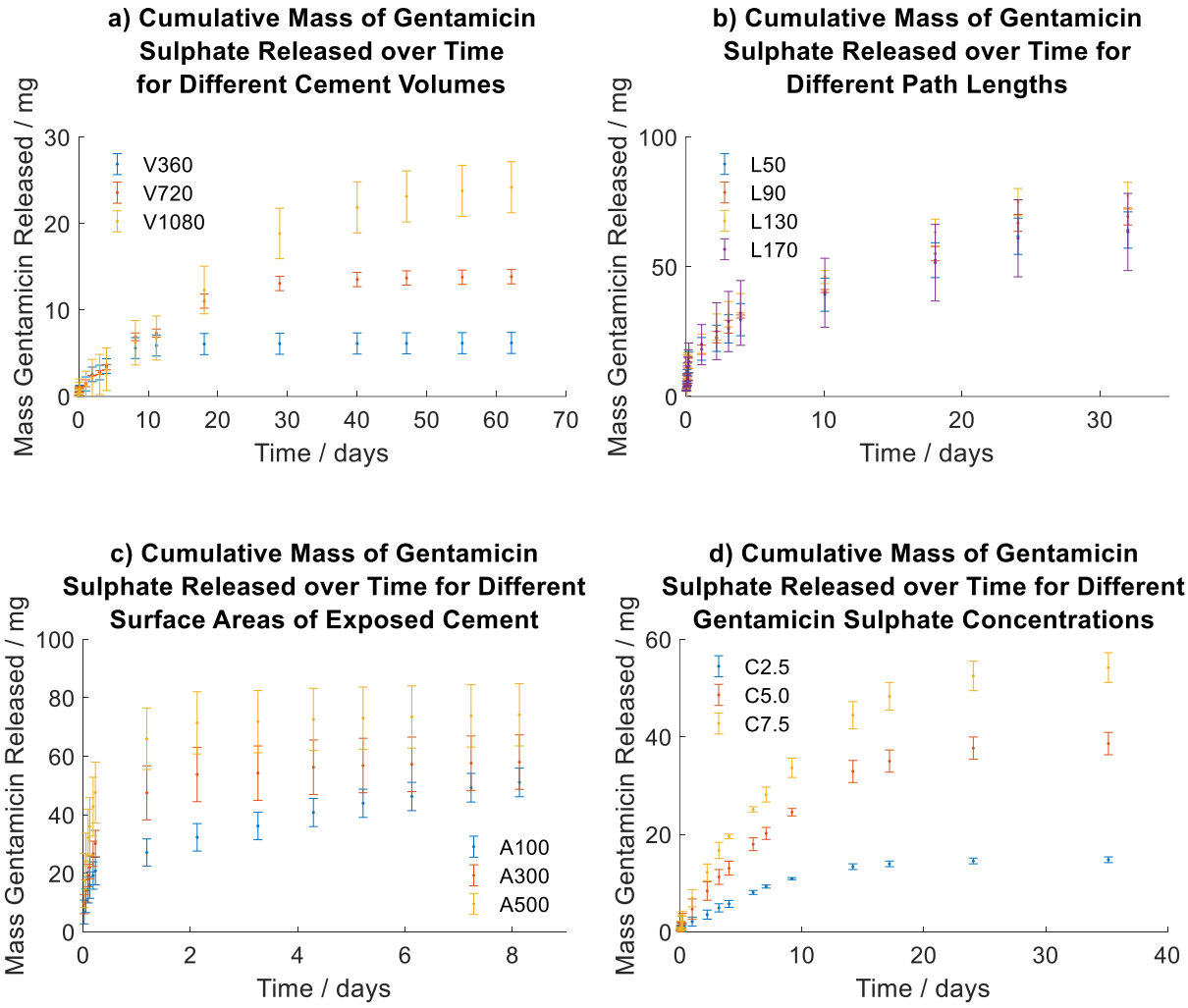

Figure 3.9: Absolute cumulative release of gentamicin sulphate over time, to understand factors influencing release. a) Samples with increasing volume showing increased mass of gentamicin sulphate released, b) samples with varying path length from furthest cement to the media showing no statistical difference in release over this range, c) release profiles showing increasing rate of release with increasing surface area but the same mass of gentamicin sulphate released, d) increasing gentamicin sulphate concentration led to increased rate of release and increased mass of gentamicin sulphate released. Error bars are one standard deviation, n=3

In the study varying volume the path length was also varied so a separate study was developed with samples varying path length but with consistent volume, surface area and gentamicin sulphate concentration. For all the samples the mass of gentamicin sulphate plateaued at 32 days with values of around 68 mg (specific values in table 3.3), there was no statistical difference between the mass of gentamicin sulphate released from each of the designs ($p = 0.33$). The Korsmeyer Peppas model was fitted to the curves and was

Table 3.3: Fit of the release curves to the Korsmeyer Peppas Model – M = a x t^b as well as the mass of gentamicin sulphate released when the graphs plateau, GS - gentamicin sulphate

Factor Changing	Variable Names	Peppas a value	Peppas b value	Peppas R^2 value	Mass of GS at plateau / mg
Cement Volume	V360	1.53 ± 0.17	0.59 ± 0.06	0.99	6.19 ± 1.11
	V720	1.56 ± 0.41	0.66 ± 0.10	0.98	13.85 ± 0.93
	V1080	1.03 ± 0.37	0.85 ± 0.14	0.98	24.20 ± 2.94
Path Length	L50	17.96 ± 1.52	0.34 ± 0.02	0.98	64.17 ± 7.26
	L90	18.01 ± 0.69	0.36 ± 0.01	0.99	69.38 ± 3.34
	L130	20.07 ± 4.69	0.37 ± 0.05	0.98	77.35 ± 8.46
	L170	19.08 ± 1.60	0.34 ± 0.04	0.98	63.41 ± 15.20
Surface Area	A100	26.69 ± 9.38	0.28 ± 0.05	0.97	54.31 ± 9.17
	A300	45.86 ± 16.35	0.35 ± 0.03	0.97	58.40 ± 18.18
	A500	88.75 ± 27.21	0.44 ± 0.07	1.00	74.55 ± 19.82
GS Concentration	C2.5	2.06 ± 0.16	0.75 ± 0.11	1.00	14.78 ± 1.56
	C5.0	4.70 ± 0.67	0.75 ± 0.06	1.00	38.61 ± 1.65
	C7.5	7.17 ± 0.98	0.70 ± 0.06	1.00	54.19 ± 2.18

found to have a good fit with R^2 values of at least 0.98 for all the curves. There was no statistical difference (p = 0.73) between the Peppas a values of around 19 for all curves, nor between the Peppas b value of approximately 0.35 (p = 0.68).

Samples were generated to compare the cement surface area exposed to the release solution, with the same volume and gentamicin sulphate concentration. Samples with the largest surface area A500 reached a plateau in mass of gentamicin sulphate in solution first within five days, while those with the smallest surface area A100 took 16 days to reach a plateau. Despite the different times taken to reach a plateau there was no statistical difference (p = 0.47) in the mass of gentamicin sulphate at the plateau despite the graph showing a higher value of 74.6 ± 19.8 mg for A500 (figure 3.9c). The Korsmeyer Peppas model was a good fit for all the curves with R^2 values of at least 0.97 for all samples. The shape of the curves were different with higher exposed cement surface area equating to larger Peppas a and b values (table 3.3). There was a statistical difference between the A100 and A500 values for both Peppas a and b (p = 0.02 for both), however there was

Table 3.4: Significance values for ANOVA and Tukey post hoc testing to understand which pairs of samples within a factor were significantly different. Where Anova testing showed the data was not significantly different Tukey post hoc testing was not performed. Significantly different values are shown in bold, GS - gentamicin sulphate, error bars are one standard deviation, n=3

	Variables Compared		p value by ANOVA			p value by Tukey post hoc		
			Peppas *a*	Peppas *b*	GS plateau mass	Peppas *a*	Peppas *b*	GS plateau mass
Cement Volume	V360	V720	0.17	0.05	**0.00**	N/A	N/A	**0.01**
	V360	V1080						**0.00**
	V720	V1080						**0.00**
Path length	All		0.73	0.68	0.33	N/A	N/A	N/A
Surface Area	A100	A300	**0.02**	**0.02**	0.47	0.48	0.22	N/A
	A100	A500				**0.02**	**0.02**	
	A300	A500				0.07	0.15	
GS Concentration	C2.5	C5.0	**0.00**	0.70	**0.00**	**0.01**	N/A	**0.00**
	C2.5	C7.5				**0.00**		**0.00**
	C5.0	C7.5				**0.01**		**0.00**

no statistical difference between A100 or A500 with the A300 samples.

Instead of changing the geometry the gentamicin sulphate concentration can be changed. The mass of gentamicin sulphate released plateaued at 35 days but with statistically different masses for each concentration (p = 0.00). The highest concentration samples C7.5 released the greatest mass at 54.2 $\pm$ 2.2 mg while the lowest concentration released the lowest concentration of 14.7 $\pm$ 1.6 mg. The curves had a good fit to the Korsmeyer Peppas model with R^2 values of one for all curves. The Peppas *a* values were statistically different between the concentrations varying between 2.06 $\pm$ 0.16 for C2.5 to 7.17 $\pm$ 0.98 for C7.5 (p=0.00). The Peppas *b* values were not statistically different, p = 0.70, with values of around 0.73. This suggests that the different concentrations do not affect the mechanisms of release.

In summary, these studies have shown how rate of release can be controlled by the cement exposed surface area and gentamicin sulphate concentration. The shape of the release curves can be controlled by the exposed cement surface area. While total mass of

gentamicin sulphate released can be controlled by the cement volume and the gentamicin sulphate concentration in the cement. While path length was not found to influence total release or the release curve in the range 52.9 and 170.8 mm.

3.3.5 Lattice Elution

In order to investigate whether the results shown in section 3.3.4 also apply to more complex structures with real world applications lattice designs with two different unit cell designs (BCCZ and gyroid) and three different volume fractions (0.2, 0.4, and 0.6) were produced. BCCZ lattices with different volume fractions reached a plateau in mass of gentamicin sulphate released within 17 days (figure 3.10a). BCCZ20 had the highest mass released at 284 $\pm$ 17 mg, while BCCZ60 had the lowest at 84.8 $\pm$ 5.9 mg all of the masses were statistically different p = 0.00. A good fit was found between the data points and the Korsmeyer Peppas model with R^2 values of at least 0.99. Peppas a values ranged from 46.3 $\pm$ 3.7 for BCCZ60 to 163 $\pm$ 11 for BCCZ20, these were all statistically different (p = 0.00). While there was no statistical difference between the Peppas b values (p = 0.10 : 1.00), with values of around 0.46. Tables of significance values for post hoc testing can be found in the appendix, for Peppas a (table B1), for Peppas b (table B2, and for the total mass of gentamicin sulphate released (table B3).

When comparing gyroid lattices, similar trends are seen to BCCZ with a plateau region also being reached in 17 days (figure 3.10b). The lowest volume fraction also had the highest gentamicin sulphate mass released of 248 $\pm$ 17 mg (table 3.5). This is lower than that reached by BCCZ although not statistically different by Tukey post hoc testing, p = 1.00 (table B3). In fact all the pairs of lattice designs with the same volume fraction had masses of gentamicin sulphate released which were not statistically different, while the samples within a unit cell design but with different volume fractions were statistically different. The Korsmeyer Peppas model was fitted to the data with an R^2 value of at least 0.99. Peppas a values varied between 44.3 $\pm$ 5.5 for Gyroid60 and 147 $\pm$ 7 for Gyroid20 and all combinations were statistically different. However there

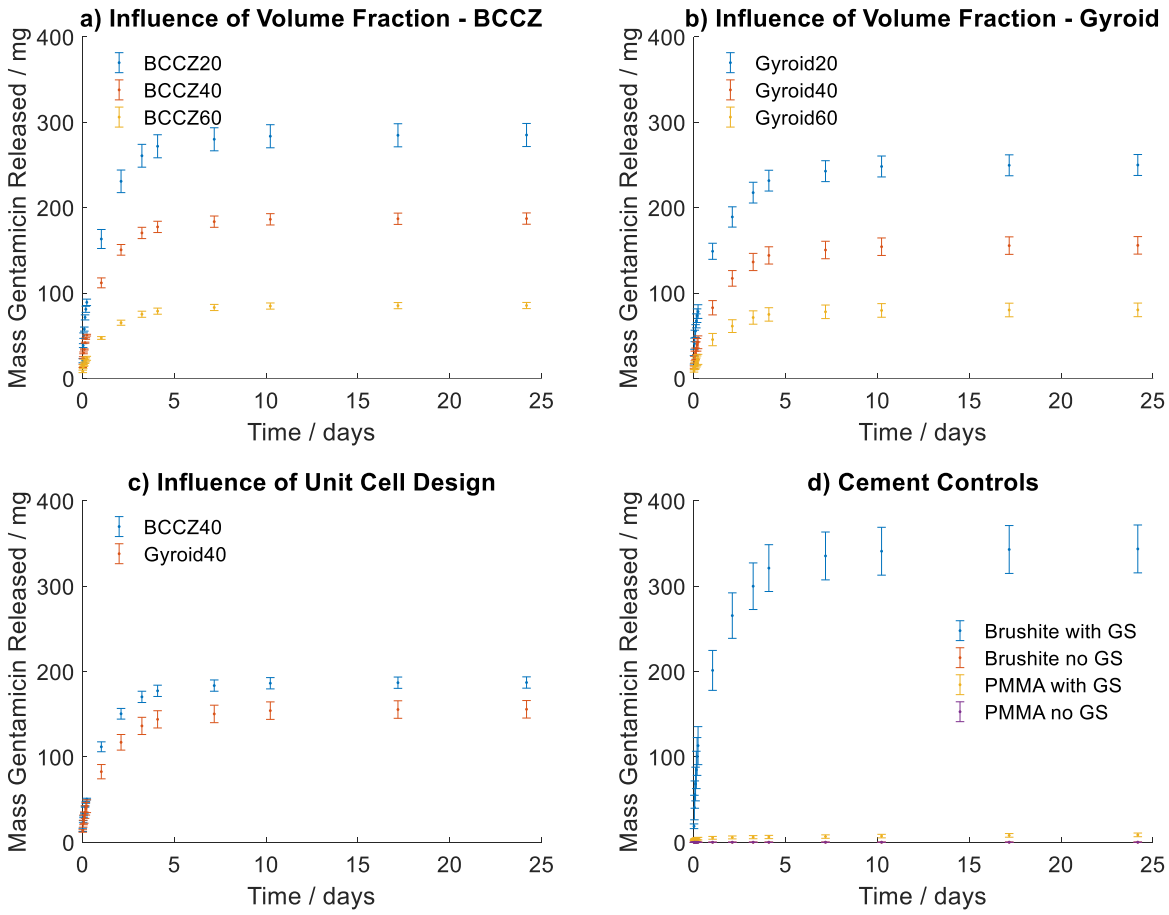

Figure 3.10: Absolute cumulative release of gentamicin sulphate over 25 days, showing how changing lattice geometry can be used to change the release profiles. a) BCCZ lattices with increasing cement volume and surface area leading to increased rate and volume of gentamicin released, b) gyroid lattices showing the same trends as the BCCZ lattices but with a lower mass released, c) comparing BCCZ and gyroid latticed samples with the same volume but different exposed surface area showing a difference in release rate and mass released, d) release of cement controls without metal lattices, showing brushite cement with gentamicin sulphate released a higher mass than the samples containing lattices. While the samples without gentamicin sulphate and those made of PMMA released a lower mass. GS - gentamicin sulphate, error bars are one standard deviation, n=3

were no statistical differences between the Peppas b values which were around 0.44 ($p = 1.00$).

Instead of comparing the influence of volume fraction within a unit cell design, the influence of unit cell design can be compared using the same volume fraction. An example with 0.4 volume fraction is shown in figure 3.10c, where it can be seen that both data sets follow very similar trends, there are in fact no statistical differences between the plateau

Table 3.5: Fit of the release curves to the Korsmeyer Peppas Model – M = a x t^b as well as the mass of gentamicin sulphate released when the graphs plateau, GS - gentamicin sulphate

Variable Names	Peppas a value	Peppas b value	Peppas R^2 value	Mass of GS at plateau / mg
Brushite with GS	203 ± 23	0.47 ± 0.04	0.98	341 ± 45
Brushite no GS	*N/A*	*N/A*	N/A	0.13 ± 0.03
PMMA with GS	6.41 ± 1.09	0.22 ± 0.02	0.94	7.34 ± 1.77
PMMA no GS	*N/A*	*N/A*	N/A	0.14 ± 0.02
BCCZ20	163 ± 11	0.45 ± 0.04	0.99	284 ± 17
BCCZ40	110 ± 3	0.50 ± 0.03	1.00	186 ± 3
BCCZ60	46.3 ± 3.7	0.44 ± 0.03	0.99	84.8 ± 5.9
Gyroid20	147 ± 7	0.42 ± 0.00	0.99	248 ± 17
Gyroid40	81.4 ± 8.1	0.44 ± 0.01	1.00	154 ± 16
Gyroid60	44.3 ± 5.5	0.44 ± 0.01	0.99	79.7 ± 10.4

mass of gentamicin sulphate released, nor the Peppas a or b values. This was also seen for the 0.2 and 0.6 volume fraction lattices.

Cement controls without metal lattices were used to compare the release (figure 3.10d). The 'Brushite with GS' samples released over 40 times the mass of gentamicin sulphate than the 'PMMA with GS' samples, and 20% more than the BCCZ20 samples (table 3.5). 'PMMA with GS' eluted 10 times less gentamicin sulphate than Gyroid60. The Korsmeyer Peppas model was fitted to the 'Brushite with GS' and 'PMMA with GS' samples, but not the controls without gentamicin sulphate, as the non zero gentamicin sulphate plateau mass for these is an artefact of the analysis. The R^2 value for 'Brushite with GS' was 0.98 whereas for 'PMMA with GS' it was 0.94. For 'Brushite with GS' the Peppas b value of 0.47 ± 0.04 was not statistically different from that of the other brushite samples with lattices. Whereas the Peppas b value for the 'PMMA with GS' samples was 0.22 ± 0.02 which was statistically different from the brushite samples (p = 0.00). The Peppas a value for 'Brushite with GS' was 203 ± 23 which was around 30% higher than for BCCZ20 and Gyroid20. While the Peppas a value for 'PMMA with GS' was 6.41 ± 1.09 which was 7 to 25 times less than the brushite with lattice samples.

3.3.6 *In Vitro* Assessment of Antimicrobial Efficacy

Two bacterial species were selected for *in-vitro* testing, both of which are widely reported to be associated with orthopaedic device infections (*Staphylococcus aureus* and *Pseudomonas aeruginosa*). This was performed to see whether the geometric control of gentamicin sulphate release translated into variation in bacterial kill. For *Staphylococcus aureus* the brushite control with gentamicin sulphate had the largest inhibition zone with a diameter of 50.7 $\pm$ 2.2 mm which was statistically larger than all the other brushite samples (figure 3.11b). Brushite without gentamicin sulphate had a zone of inhibition with a diameter of 36.1 $\pm$ 2.2 mm, which extends eight millimeters in each direction beyond the sample. 'PMMA with GS' also had zones larger than the brushite samples with lattices at 45.7 $\pm$ 2.7 mm. For the gyroid samples larger volume fractions had smaller zones of inhibition decreasing from 42.7 $\pm$ 0.8 mm for Gyroid20 to 33.1 $\pm$ 3.4 mm for Gyroid60. While no clear pattern in zone diameter with volume fraction was seen for the BCCZ samples.

There were very few differences in the diameters of the zone of inhibition with *Pseudomonas aeruginosa*. The largest diameter of inhibition was measured for 'Brushite with GS' samples at 49.7 $\pm$ 2.4 mm but this was not statistically different from 'PMMA with GS', BCCZ20, BCCZ40, Gyroid20, Gyroid40 and Gyroid60. 'Brushite no GS' samples again exhibited zones of inhibition which protruded beyond the sample despite the lack of gentamicin sulphate measured at 38.1 $\pm$ 4.9 mm. 'PMMA no GS' displayed no inhibition. Despite the visual decrease in diameter with increasing volume fraction for BCCZ there was no statistical difference in inhibition zone size (figure 3.11d). Gyroid lattices showed no correlation between volume fraction and the size of the zone of inhibition of *Pseudomonas aeruginosa*. Full Tukey post hoc test analysis is shown in the appendix tables B4 & B5.

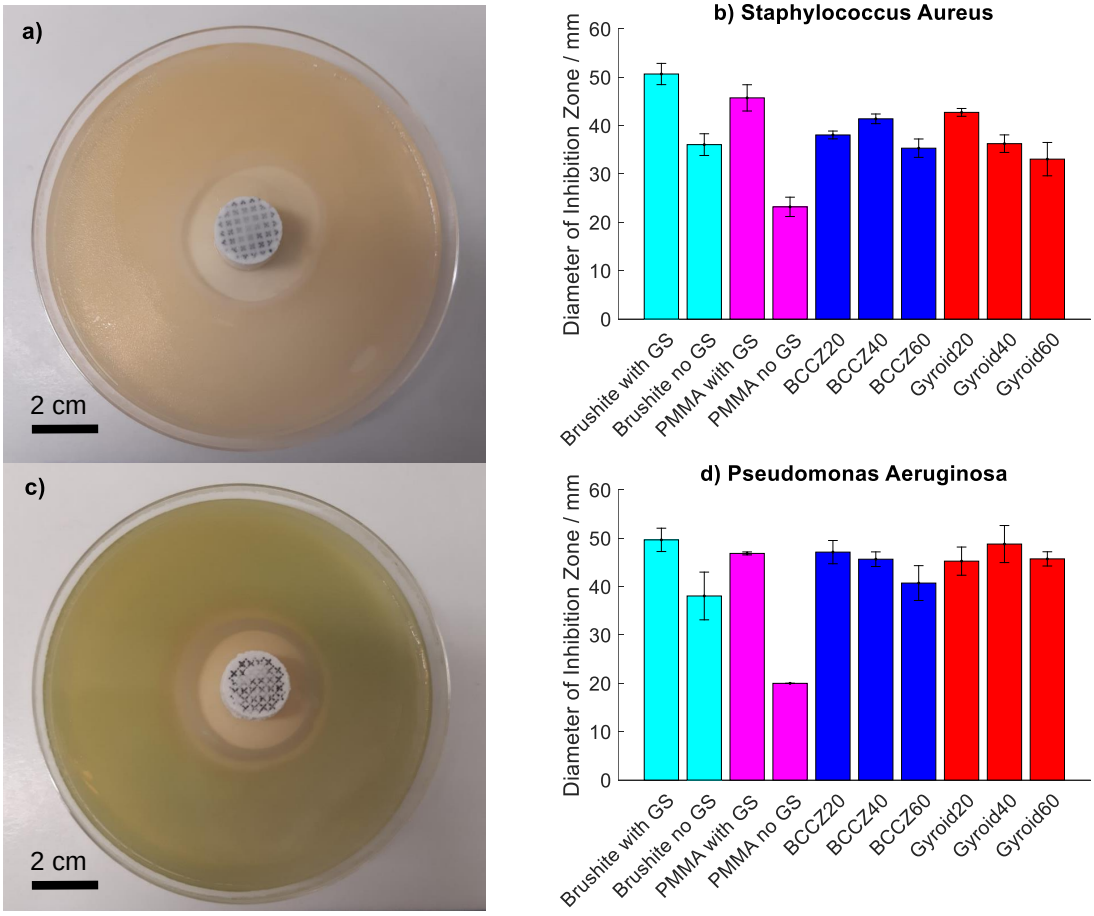

Figure 3.11: Zones of Inhibition. a) Example petri dish with cement filled lattice sample coated in *Staphylococcus aureus*, b) total diameters of zones of inhibition including the 20mm diameter samples showing variation in zone diameter with different lattice designs, c) example zone of inhibition for a lattice sample with *Pseudomonas aeruginosa*, d) graph of samples with *Pseudomonas aeruginosa* showing inhibition for samples with gentamicin sulphate above that of those without. GS - gentamicin sulphate, error bars are one standard deviation, n=3

3.3.7 Compression Testing of Brushite Filled Lattices

Compression testing was performed on lattices with and without brushite cement to understand whether the presence of the cement reduced the mechanical properties. This was not the case with all cement lattice composites providing more strength than the same sized empty lattice (figure 3.12a&b). The composite samples were also stronger than the cement samples with the strongest cement having an offset stress of 57.6 $\pm$ 1.6 MPa ('PMMA no GS' aged) while the weakest composite (BCCZ20 with aged brushite) had

an offset stress of 61.6 ± 1.8 MPa. Although the weakest empty lattice (BBCZ20) was slightly weaker than the strongest cement at 54.3 ± 1.9 MPa. Overall there was a positive correlation between offset stress and the lattice volume fraction for both BCCZ and gyroid lattices, this was true for empty lattices and composite samples.

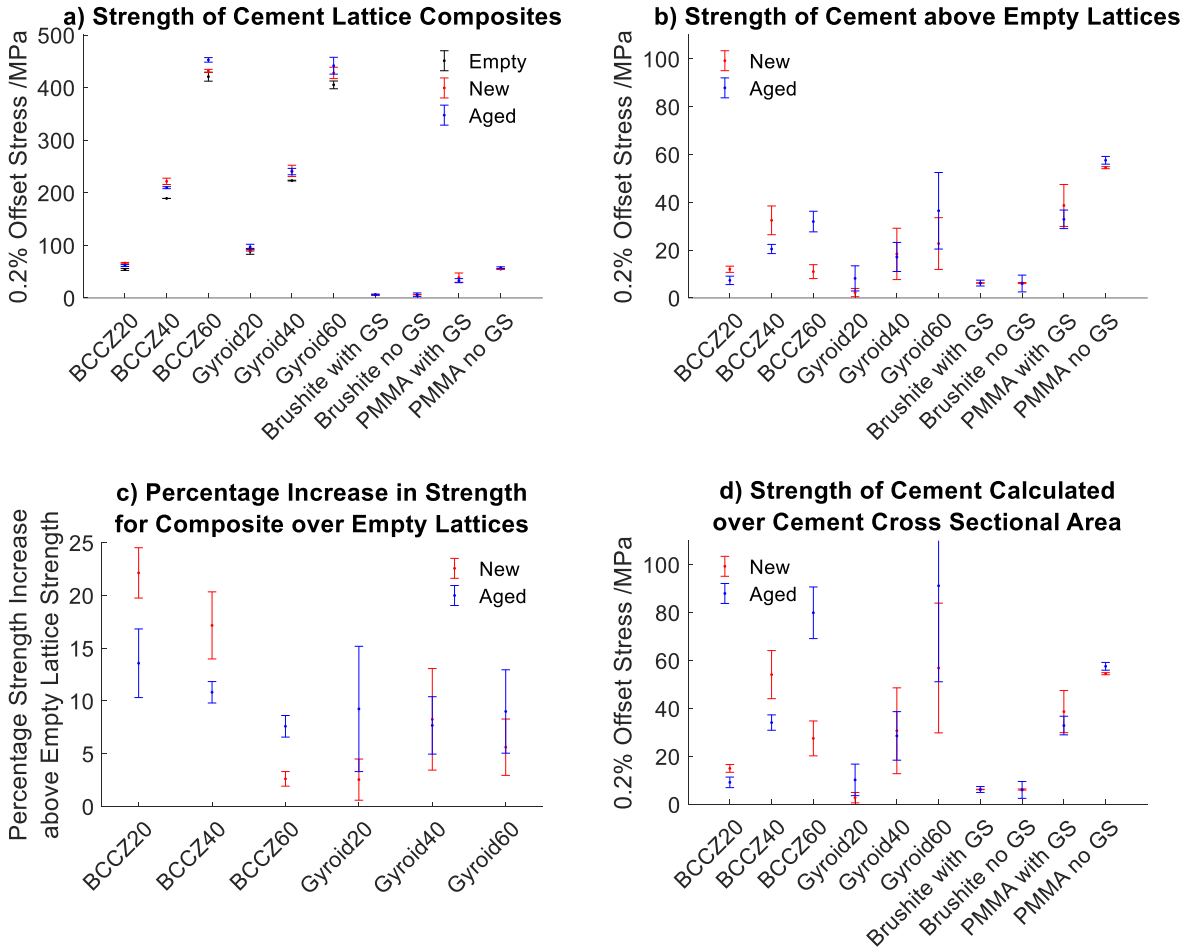

Figure 3.12: Compression of lattices either empty - without cement, new - with fresh brushite cement containing gentamicin sulphate, or aged - with brushite cement containing gentamicin sulphate which has been in PBS for eight weeks. a) shows the total strength of each sample, b) the absolute increase in strength of the cement over the empty lattices, c) the percentage increase in strength of the lattices containing brushite over empty lattices, d) the different in strength between the lattices and the composites but calculated using the cement cross sectional area. Error bars are one standard deviation, n=3

There was no statistical difference in strength between the brushite cement controls with and without gentamicin sulphate with offset stress of around 6 MPa for all samples. The PMMA cement samples were stronger than the brushite controls, with PMMA with-

out gentamicin sulphate giving the highest offset stress of 57.6 $\pm$ 1.6 MPa for the aged samples, while those with gentamicin sulphate had a mean of 32.9 $\pm$ 3.9 MPa for aged samples. There was no statistical difference between offset stress of the new and aged samples for both of the cement types in the controls.

By subtracting the offset strength of the empty lattices from the composites the strength of the cement can be seen (figure 3.12b). This shows that the general trend was cement strength increasing with lattice volume fraction (i.e. decreasing cement volume). The one exception to this was new cement in BCCZ lattices, where the BCCZ60 cement strength was lower than expected given the trends at 11.0 $\pm$ 2.9 MPa (432 $\pm$ 3 MPa for the composite). Most of the composite samples had cement strengths which are higher than those of brushite cement, the only exception to this was new cement in Gyroid20 where the cement offset strength was 2.3 $\pm$ 1.7 MPa (with a composite strength of 90.7 $\pm$ 1.7 MPa). No statistical differences were seen between the strength of the new and aged cement for each lattice volume fraction for the gyroid lattices. While there was no pattern with the BCCZ lattices as to whether the new or aged cement was stronger.

Figure 3.12c shows the percentage increase in strength of the composites compared to empty lattices. It can be seen that there was a decrease in percentage strength with increasing lattice volume fraction for the BCCZ lattices, i.e. there was a positive correlation between the percentage strength increase and the cement volume fraction. However for the gyroid lattices there was no correlation between the percentage change and the volume fraction, indicating that cement strength was proportional to the lattice strength.

In the previous calculations the stress of the cement was calculated over the whole cross sectional area of the sample, however the stress can be recalculated over the cross sectional area of the cement instead (figure 3.12d). This amplifies the increase of strength for samples with larger lattice volume fractions. The 0.6 volume fraction lattice have a strength nine times higher than the 0.2 lattices under this analysis compared to 4.5 times when absolute change in offset strength was used in figure 3.12b.

3.4 Discussion

Validation of Gentamicin Sulphate Detection Methods

In order to study the elution of gentamicin sulphate from cement a detection method is needed that has a number of characteristics. It needs to have a high enough resolution to allow different quantities of gentamicin sulphate released to be identified, specifically variations of 10 μgml^{-1}. The test must be specific, i.e. not giving readings for non gentamicin sulphate chemicals, and reproducible so that readings can be taken over the course of an elution study. Linearity is desirable but not essential. The range of concentrations that it should be able to detect is 100 μgml^{-1} to 30 mgml^{-1} [377].

UV-Vis absorption spectroscopy has previously been used to detect gentamicin sulphate release from brushite cement [257, 378]. This method has the advantages that it is quick, non destructive and does not require any additional reagents. There is a linear relationship between absorbance and gentamicin sulphate concentration over this range. However gentamicin sulphate only weakly absorbs UV light [374, 379], for example the gentamicin sulphate standard used here with 3.5 mgml^{-1} gentamicin sulphate in PBS had an absorbance of 0.195 $\pm$ 0.031 which was less than 2.5 times the reading of PBS without gentamicin sulphate (0.0795 $\pm$ 0.0008). This means that the addition of substances in solution with larger absorbances interfere with the signal from gentamicin sulphate, which was seen in the brushite signal. In order to avoid this challenge Cox et al used a control with brushite without gentamicin and subtracted that absorbance signal from the sample signals [257]. This relies on the assumption that brushite cement with gentamicin sulphate degrades at the same rate as cement without. If this was true it would be expected that the 'PBS with GS' signal minus the 'PBS no GS' signal would equal the 'Brushite with GS' signal minus the 'Brushite no GS' signal. However the first equals 0.115 while the second equals 0.147 suggesting that brushite with gentamicin sulphate dissolves faster than without. The presence of sulphate ions in the gentamicin sulphate during the brushite setting reaction results in smaller brushite crystals with different degradation profiles [303].

By using a fluorogen which only fluoresces when covalently bonded to the gentamicin sulphate no separation step was required. This makes the fluorescence spectroscopy a relatively quick method of detecting gentamicin sulphate. The calibration curve was non linear, however linearity is only a desirable but not essential characteristic. This short coming was offset by the high resolution and low detection limit of the method (0.01 $mgml^{-1}$). The non linearity was likely due to fluorescence quenching caused by aggregation of the gentamicin sulphate in solution or resorption of the emitted photons [380].

Fluorescence was found to have a high level of selectivity for gentamicin sulphate, due to the OPA preferentially reacting with amine groups which are not present on MPCM, β-TCP, citric acid nor brushite, but are present on gentamicin sulphate [381]. Fluorescence measurements are sensitive to pH and MCPM is acidic, so the reduction fluorescence measurement for 'MCPM with GS' was consistent with previous research [382]. This effect was not seen for the brushite samples, suggesting that the effects of MCPM are reduced when in the cement, with sufficiently little released to overcome the pH maintenance properties of the PBS buffer.

Understanding the Rate of Release of Gentamicin Sulphate from PMMA and Brushite Cement

The release of gentamicin sulphate from brushite cement is a predominantly diffusion controlled process [290, 383, 384]. Whereas the release mechanism of gentamicin sulphate from PMMA cement is a less well understood process [282, 283]. There is evidence to suggest that only the gentamicin sulphate present at the surface is released [283, 284], while other studies have shown that cracks and porogens enable release from inside the bone cement [286, 385].

By performing a two stage release of polymer tubes filled with cement containing gentamicin sulphate, the movement of the drug along the length can be compared and indicate the potential release mechanisms (figure 3.7). During the initial elution which

lasted up to five weeks the mass of gentamicin sulphate released increased over time, indicating that only partial release had occurred after one and three weeks of elution. There was greater variation in the mass of gentamicin sulphate released from PMMA than from brushite. This is consistent with previous research that saw a large spread in release data [386]. Torrado et al attributed the release of gentamicin sulphate from PMMA to an interconnecting series of voids and cracks in the cement, which form in a non repeatable way and leads to variation in the release profile [386, 387].

In order to establish the location of gentamicin sulphate along the length of the samples, they were cut into ten pieces and each placed in PBS for further elution. The total mass of gentamicin sulphate released from each piece was plotted in figures 3.7c&d. Unfortunately the OPA reagent had degraded when the brushite samples with 5 weeks of initial elution were measured so no gentamicin sulphate was detected. The 3 weeks of initial elution samples showed a positive correlation between mass of gentamicin sulphate released and approximate length from the exposed face, this was a concentration gradient which reflects the current hypothesis that the release was diffusion controlled [290, 383, 388].

The trend in the second elution data for the samples after 1 week of initial elution was less clear, this could be due to uneven gentamicin sulphate distribution along the length of the samples which had insufficient time to disperse during the first elution of one week. In order to test this hypothesis samples could be created and then cut up for the second elution process without any time in PBS for the first elution in order to investigate the distribution of gentamicin sulphate along the length. Due to the length of the polymer tubes in this work (100 mm) some of the challenges of brushite injectability may have caused an uneven distribution of gentamicin sulphate, specifically liquid phase separation [298], this is where the liquid phase travels faster than the solid phase during injection leading to gradients in cement properties [389].

The second elution of the PMMA samples produced a graph with a different shape to the brushite graph (figures 3.7c&d), indicating different distribution of gentamicin

sulphate along the length and therefore a different release mechanism. There was not a concentration gradient along the length, instead the mass of gentamicin sulphate did not change with length except for the first pieces, and there was no difference in the mass of drug released in these sections over the different inital elution time frames. This would suggest that only the end portion of each sample was involved in the first elution. This result supports the hypothesis that only the surface or surface cracks are involved in the release of gentamicin sulphate from PMMA [282, 283, 284].

If the release was from the surface without any cracks to enable gentamicin sulphate to be released from within the cement then the mass of gentamicin sulphate released from the first section would be greater than or equal to half of the subsequent sections. For example if the initial elution had removed all the drug from the surface of the sample, then during the second elution only the newly cut face would be able to elute, while for the subsequent section two faces would be able to elute releasing exactly twice the gentamicin sulphate of the first piece. When not all of the drug had released during the initial elution some additional gentamicin sulphate is available for subsequent release during the second elution, so the first section would have a higher release, while the other sections would have exactly the same release as in the previous hypothetical scenario. Instead, the first section released drug quantities which were less than half of those in the subsequent sections. This would indicated that the initial release includes more than just the gentamicin sulphate present on the cut face, therefore implying that cracks are part of the release mechanism. This result adds evidence to the surface cracks hypothesis [283, 284].

A second experiment was used to investigate the permeability of gentamicin sulphate release through PMMA and brushite cement. This used polymer tubes containing PMMA or brushite cement in one of three configurations, with or without gentamicin sulphate, or NGN where cement containing gentamicin sulphate was capped with cement without it. For the brushite cement, the samples with gentamicin sulphate had the fastest release and the greatest mass of drug released (figure 3.8a&b).

Brushite converts to apatite in aqueous solution as it is a thermodynamically more stable phase at physiological temperature, pressure and pH [390]. This can occur over 10 to 28 days, and occurs more slowly in PBS than serum or *in vivo* [313, 391, 392]. Apatite has smaller pores than brushite [391], which is likely to lead to a reduction in the release rate of the gentamicin sulphate. When gentamicin sulphate is incorporated into brushite cement it leads to smaller crystals due to the sulphate ions preferentially forming calcium sulphate dihydrate. The calcium sulphate dihydrate crystals then act as a nucleation point for the brushite crystals, reducing setting time which leads to smaller crystals [297, 320]. These smaller crystals are likely to have a closer packing density leading to a reduced pore size for the cement containing gentamicin sulphate than that without [300, 384]. This was unlikely to be the cause of the prolonged release from NGN compared to 'Brushite with GS'. However it would explain how the Brushite NGN samples did not have a delay in release, despite the lack of gentamicin sulphate in the cement at the surface initially. A non zero mass of gentamicin sulphate was measured for the 'Brushite no GS' samples, despite the lack of gentamicin sulphate in the cement, this was likely to be a zero error when converting the fluorescence to mass.

For the gentamicin sulphate released from PMMA there was a large variation between samples as previously seen in the two phase elution. During the two phase elution it appeared that cracks were only enabling the release of gentamicin sulphate from 10 mm of PMMA cement. In this study the NGN samples had 20 mm of PMMA without gentamicin sulphate at the ends so no drug was expected to be found in the solution. This was the case for two out of the three repeats (figure 3.8f), however for one of the samples release did occur, this would suggest that either the cracks are propagating at least 20 mm into the cement, or there was an alternative route for the gentamicin sulphate. One potential cause of this was shrinkage of the PMMA during setting causing gaps which the drug could travel down. PMMA can shrink as much as 20% during setting due to the presence of radiopacifiers [285]. The large variation in drug release from 'PMMA with GS' samples could also be due to shrinkage, given this variation was twice as large as with the two

phase study.

Factors Influencing Elution

In order to use geometry to manipulate drug release it was necessary to understand how geometry influences the release. When the volume of cement increased the time for the gentamicin sulphate mass released to plateau also increased. This finding reflects the results previously seen for release of gentamicin sulphate from calcium sulphate hemihydrate [157]. The total mass of gentamicin sulphate released increased with cement volume. This was in line with previous research which found the release of drugs from reservoirs with different internal volumes but fixed size of microchannels for drug elution resulted in increased drug release from larger volumes [157, 258]. The Peppas a and b values were not statistically different, indicating that the shapes of the curves are the same, but the curves for large volumes of cement extend further. This finding broadly supports the work of Allen who found no statistical difference in the shape of release curves although using a computational model rather than the Korsmeyer Peppas model was fitted to the data [157].

There was no statistical difference between the samples with different diffusion path lengths, nor time to plateau, mass of gentamicin sulphate released at the plateau, nor within the Peppas model values. This is in contrast to previous findings where increased path length led to slower release [256, 257]. However these differences in results may be influenced by contrasting experimental set up, Allen et al used photocured chemically cross linked RPU60, a polymer, for their reservoirs with 1.5 mm diameter pores which were hydrophobic, these two properties were attributed to the changes in release rate.

In this study each sample only had one opening for both solution entry and air escape, potentially reducing the ingress of solution into the samples, in contrast both Allen et al and Cox et al used reservoirs with multiple channels for fluid exchange [256, 257]. Another possible explanation for this is the complex, nanostructure of the cement material [317], which would mean that the drug dissolving from the matrix would have to take a

significantly more tortuous route than the macrostructures tested in these experiments.

Surface area was shown here to influence the rate of release, and the shape of the release curves (Peppas a and b values respectively), as well as the time taken for the mass of gentamicin sulphate to plateau (which is an indicator of rate of release). Rate of release has previously been shown to increase for samples with a larger surface area [101, 253, 256]. Lowther found that when mass was normalised by surface area there was no statistical difference in the release curves [101]. This was not seen here, where the release per surface area was higher for samples with smaller surface areas. Release characteristics are less sensitive to surface area than cement volume, or gentamicin sulphate concentration, requiring a five fold increase in surface area to create a statistically significant change in Peppas a or b value, where only a two fold change is sufficient for cement volume and gentamicin sulphate concentration.

Increasing the concentration of gentamicin sulphate in the brushite cement led to faster release (higher Peppas a value), and a larger mass of gentamicin sulphate released once the curve had plateaued. These values both increased more than the rate of concentration increased. While the shape of the curve was the same for all the samples with a Peppas b value of around 0.73 (table 3.3). These effects were also seen by Vorndran et al who found gentamicin sulphate concentration of 1.24 and 2.48 wt.% [393]had the same Peppas b values of 0.2, while the higher concentration released more cement by mass and percentage in line with the results found here. Meißner et al also found higher gentamicin sulphate concentration lead to fast release and more release, this was thought to be because the gentamicin sulphate reduced the production of apatite at the surface of the samples which slows down release due to lower porosity compared to other calcium phosphate cements [394].

Lattice Elution

To investigate whether the influence of geometry on gentamicin sulphate release also applies to more complex structures, BCCZ and gyroid lattices were used. When the

volume fraction was increased the mass of gentamicin sulphate released at the plateau increased, this agreed with both the earlier study here on varying cement volume (figure 3.9a), and the literature [157]. Additionally the Peppas a value increased with decreasing lattice volume fraction. This was unexpected because Peppas a values were only influenced by surface area and concentration in the earlier studies (table 3.3). Here the concentration was not changing, and while the surface area was changing it only doubles from BCCZ60 to BCCZ20, while a five fold increase was needed to see a statistical difference in the Peppas a value in the surface area study.

Also the same change in surface area led to a difference in Peppas b value, while no statistical difference was seen in Peppas b value between the lattice samples with varying volume fraction (table B2). This would suggest that either the difference was caused by a combination of changing volume and surface area together, or caused by the size of the pores for drug elution, rather than the total surface area which was not investigated here. Allen et al did investigate the size of channels for eluting gentamicin sulphate from calcium sulphate hemihydrate from RPU60 polymer reservoirs and found that channels below 1.5 mm in diameter had extended release. This was attributed to the hydrophobicity of the RPU60 polymer limiting solution transfer [256]. However, for larger channels they found no statistical difference in the release profiles from different channel diameters.

Another consideration was the different materials used for the reservoirs in these different experiments, with polypropylene (PP) used for the volume study, polylactic acid (PLA) used for the surface area study and Ti-6Al-4V used for the lattice study. PP and PLA are strongly hydrophobic while Ti-6Al-4V is hydrophilic. When the same geometry was made out of RPU60, which is hydrophobic, and cobalt chrome, which is hydrophilic, the release was quicker from the hydrophobic reservoirs. This was partly caused by the initial filling process where the hydrophilic structure enabled a more complete cement fill with fewer air bubbles, leading to a more densely packed cement which slowed the drug release [157].

Samples with the same volume fraction but different unit cell designs had no statistical

difference in release (figure 3.10c), despite differences in the surface area of the exposed cement (table 3.2). This is to be expected because the differences in surface area are less than 5% and a 500% increase was needed to create a statistical difference in the surface area study.

In Vitro Assessment of Antimicrobial Efficacy

It has been shown that geometry can be used to control release of gentamicin sulphate in solution, but this may not translate to variations in antimicrobial efficacy. Repeats of the samples used for elution were also placed in agar plates containing *Staphylococcus aureus* and *Pseudomonas aeruginosa* and the diameters of the inhibition zones measured. Changing the geometry did lead to differences in the bacteria killed, this was in agreement with the elution data for *Staphylococcus aureus* (figure 3.11b), while for *Pseudomonas aeruginosa* the differences were generally not statistically significant. For all lattice samples there was some bacterial kill, which demonstrates that these structures can be used to provide local delivery of therapeutics expanding their functionality beyond mechanical tailoring of implant properties.

The lattices were able to provide variation in the diameters of inhibition of *Staphylococcus aureus*, suggesting that changing geometry can provide control. For the gyroid lattices this was in agreement with the elution results, with the 'Brushite with GS' control also following the trend. Contrary to expectations, the zone of inhibition for the 'PMMA with GS' samples was not statistically different from that of 'Brushite with GS', despite an elution mass of nearly 50 times higher than from brushite. There are a few potential causes of this difference, firstly what was being measured in the elution study was the fluorescence of OPA conjugates with amine groups, it would be possible for the gentamicin sulphate to degrade such that it was no longer antimicrobial while still having amine groups providing a fluorescence value. It has been noted that the antimicrobial activity of gentamicin sulphate decreases with a reduction in pH, which the brushite would cause unlike the PMMA [300, 395]. In the future the solution from elution study could be used

for the agar diffusion tests in order to see whether the difference between the two studies was caused by the quantity released or the viability of the gentamicin sulphate [256, 396, 397].

Alternatively, this could have been caused by the conditions of the agar plate which differ to those in the PBS solution, and this could have resulted in different release profiles for gentamicin sulphate. In PBS the brushite cement will become saturated, since gentamicin sulphate dissolves readily [384], and so the gentamicin sulphate release rate was limited by diffusion whereas on the agar plate there was less moisture, so dissolution of gentamicin sulphate was likely to limit the gentamicin sulphate release rate. In contrast, PMMA has a release which was dominated by surface and surface crack effects, and so unaffected by the lower level of moisture in the antimicrobial assay.

Although the samples with gentamicin sulphate in *Pseudomonas aeruginosa* did not have statistically different diameters of inhibition zones, they did provide bacterial kill. This lack of difference could be due to the lack of sensitivity of the method, and a broth culture method could be used instead, which also has the advantage of being 3D which is a better model for *in vivo* conditions. In both *Staphylococcus aureus* and *Pseudomonas aeruginosa* the 'Brushite no GS' samples had non zero diameters of inhibition zone indicating bacterial kill. This was likely to be because brushite cement is acidic [398, 399], and the growth of both *Staphylococcus aureus* and *Pseudomonas aeruginosa* is mediated by acidic conditions [400, 401, 402].

Compression Testing of Brushite Filled Lattices

All samples with cement had a higher strength than the empty lattices of the same design. Thus lattices can be chosen for their mechanical strength without concern that the addition of cement will negatively impact the strength. Although PMMA was found to be stronger than brushite cement at 32.9 $\pm$ 3.9 MPa compared to around 6 MPa for brushite cement, this was below the compressive strength of cortical bone ($\sim$ 200 MPa) [213, 214, 215], however the cement-lattice composites were able to provide strength in

this range.

There was no statistical difference in the strength of the brushite controls, including aged and new, and with and without gentamicin sulphate. This is in contrast to previous research which has found the presence of gentamicin sulphate to increase the strength of the cement [257, 300]. This increase in strength was caused by the sulphate ions from the gentamicin sulphate forming calcium sulphate dihydrate (CSD) instead of brushite due to their smaller crystal size. The CSD crystals then act as nucleation points for the brushite crystals, causing those to form faster and therefore smaller crystals [297, 300]. However in this work citric acid was used to increase the setting time, which may have negated the effects of the sulphate ions, leading to the same strength between the brushite cement controls with and without gentamicin sulphate. In future, X-ray diffraction could be used to see whether CSD was present in the cement containing gentamicin sulphate.

Brushite aging was not found to change the strength of the controls, nor the cement in the gyroid lattices. For the BCCZ lattice at 20 and 40% volume fraction the aged samples were weaker, while at 60% volume fraction they were stronger than new cement. This may be due to the strength of the new cement being anomalous as it does not fit any of the trends. Aging of brushite cement containing gentamicin sulphate can lead to a reduction in strength due to CDS loss over time [320], however some experiments have found no difference in strength over time [403]. Additionally, the conversion of brushite cement to apatite cement can lead to an increase in strength over time [391]. Aging was performed in PBS, however brushite dissolves much more readily in serum than PBS. Grover et al found a six times increase of mass loss of brushite cement in foetal bovine serum than PBS due to serum proteins [391]. So in future, serum or *in vivo* studies should be performed to provide a more representative model of the *in vivo* environment.

PMMA cement without gentamicin sulphate was stronger than with it (figure 3.12b). This is in accordance with earlier observations, which showed that increasing gentamicin sulphate concentration decreased strength [404, 405, 406]. This was due to the drug forming discrete particles in the cement which act as additional defects [405]. Aging did

not lead to changes in mechanical strength either in this work or earlier work [404, 405, 406].

The strength of the cement in the composite structures can be compared by subtracting the strength of the empty lattices (figure 3.12b). This shows that the cement strength increased with lattice volume fraction, i.e. as the cement volume decreased the strength increased. This behaviour has been previously seen in civil engineering research where polymer lattices have been used to alter the mechanical properties of cements [407, 408, 409]. The addition of polymer lattices to cement specimens led to an increase in strength which was attributed to three things, crack propagation in the cements was disrupted by lattices which led to small cracks rather than the large cracks seen in cement only controls. The lattices held in the cement such that it did not separate from the sample so it could continue to provide some mechanical support even after the initial failure, and the lattices provided lateral constraint to cement movement which is the main mechanism of cement failure [408]. In this research it was found that lattices which provided greater residence to lateral movement resulted in stronger composites [408]. However this was not found when BCCZ and gyroid lattices were compared.

When cement strength was plotted as a percentage of the lattice strength the percentage strength of the BCCZ samples decreased with volume fraction, while the gyroid lattices showed no trend (figure 3.12c). This would suggest that the cement strength was proportional to the lattice strength for gyroid lattices. This could indicate that the additional strength of the composite was caused by the cement increasing the strength of the lattice rather than the lattice increasing the strength of the cement. Cement has been used to increase the impact resistance of steel pipes [410, 411, 412, 413], where the cement provides resistance to indentation due to its high compressive strength. BCCZ failure is dominated by buckling of the vertical strut (section 2.3.2), which requires lateral movement of the strut into the space where the cement is present. The lattice is constrained by the cement, so in order for the lattice to move into this space the compressive strength of the cement would have to be overcome. In contrast, gyroid lattices undergo barrelling

during compressive loading which causes lateral spread of the centre of the structure, this is a similar failure mechanism to cement structures which suggests that the cement would provide less resistance to lattice collapse.

Lattices are often thought of as a meta material rather than a truss with their bulk properties investigated, so in this study the lattice filled with brushite cement was considered a composite meta material too. This means that for compression analysis the cross sectional area used was that of the entire sample filled with a lattice rather than just the metallic cross sectional area. Equally the offset stress of the cement was calculated over the entire sample face. However the cement offset stress was also calculated over the cross sectional area of just the cement for figure 3.12d in order to understand whether this was influencing the differences in cement strength between different lattice designs. This change in calculation method amplifies the differences, suggesting that this was not the cause of the increase in cement strength with increased lattice volume.

3.5 Conclusions

This chapter investigated whether it was possible to control the release of a drug from a carrier material that was bulk loaded into a lattice by changing the lattice geometry. Gentamicin sulphate was used as the model drug and brushite cement as the carrier material. This was achieved with BCCZ20 releasing over three times the gentamicin sulphate as BCCZ60 over the same time frame of 17 days, and Gyroid20 also releasing over three times as much gentamicin sulphate as Gyroid60 over this time frame.

The use of ortho-phthalaldehyde (OPA) as a fluorogen to detect gentamicin sulphate in solution was validated. The method was highly selective with samples without gentamicin sulphate giving fluorescence values at least 80 times lower than those with the drug. The presence of brushite components in the gentamicin sulphate solutions did not lead to fluorescence readings that were statistically different from the reference solutions without these components. The exception of those contained unreacted MCPM which led to a

lower fluorescence, so excess β-TCP was used in the formation of brushite to prevent any unreacted MCPM being present.

Given the release mechanism of gentamicin sulphate from PMMA is not fully understood two new experiments were devised to gain a better understanding of the mechanism, and to compare it with the brushite mechanism. A two step elution was performed to understand how the gentamicin sulphate moved through the cements during elution. After initial elutions of one, three or five weeks, the cement samples were cut into ten pieces. Only the first section of PMMA cement showed a statistically significant different mass of gentamicin sulphate released which was lower than the other sections, suggesting that the majority of the initial elution had occured at the surface. In contrast the gentamicin sulphate released from the brushite cement in the second elution followed a positive trend of mass released and distance from the open end in the initial elution indicating a concentration gradient along the length of the cement that suggests that the release of gentamicin sulphate from brushite cement is diffusion controlled and in line with current literature.

The second release mechanism study assessed the permeability of the cements to the movement of gentamicin sulphate. It was found that the drug could travel through brushite cement in line with previous research. While for the PMMA, one of the three samples with drug-less cement caps did release gentamicin sulphate into solution, suggesting that the drug can penetrate the cement, or that there were cracks present that enabled the drug to bypass the cement.

The Korsmeyer Peppas model was fitted to the release curves from the studies investigating which factors influence release and also from the lattice release studies. It was found that all the release curves fit the model with an R^2 value of at least 0.95, except the PMMA controls. The Peppas a value corresponds to the rate of release, and the Peppas b value indicates the shape of release.

The factors which influenced the rate of release were surface area of the exposed cement or the drug concentration. The shape of the release curves could be controlled

by changing the exposed cement surface area, corresponding to different Peppas b values. While total mass of gentamicin sulphate released was controlled by the cement volume and the gentamicin sulphate concentration in the cement. Path length was not found to influence the release over the range 52.9 to 170.8 mm.

The release of gentamicin sulphate could be controlled by changing the lattice geometry. BCCZ and gyroid lattices with a smaller volume fraction released more gentamicin sulphate and at a faster rate. Changing the unit cell from BCCZ to gyroid did not lead to a statistically significant difference in the rate or quantity of drug released. All the lattice samples also had release curves which were the same shape, i.e. there was no statistical differences between the Peppas b values.

Differences in gentamicin sulphate release between lattice designs did not translate into statistical differences in the size of the zones of inhibition of *Staphylococcus aureus* and *Pseudomonas aeruginosa*. However bacteria diffusion assays are less sensitive than elution studies, so this is unsurprising.

Compression testing showed that these cement lattice composites were able to provide sufficient mechanical support to be used in bone implants, and that the presence of the cement did not reduce the mechanical properties.

It was found that lattice geometry can be used to control the release of gentamicin sulphate from brushite cement. Sufficient drug was released to inhibit the growth of *Staphylococcus aureus* and *Pseudomonas aeruginosa*. Additionally the presence of the brushite cement in the lattices did not lead to a reduction in compressive strength. This work will enable lattice geometry in future medical devices to be manipulated to tailor drug release in order to optimise the release profile to the pharmokinetic properties of different therapeutics.

CHAPTER 4

SURFACE LOADING OF IMPLANTS

4.1 Introduction

Previous chapters have shown lattices can be built with sufficient strength to be used as hip replacements or spinal cages. It has also been shown that lattices can be filled with brushite cement even at a volume fraction of 0.6. Lattices can be used to control the release of gentamicin sulphate and enable sufficient drug to be released to inhibit the growth of *Staphylococcus aureus* and *Pseudomonas aeruginosa*.

The focus of this chapter is the development of a coating that could be used to attach therapeutics to the surface of lattices. These could be antibiotics or other antimicrobials to prevent infection, or growth factors to enable bone attachment or fusion. Albumin will be used as a model therapeutic and will be immobilised on a polycaprolactone (PCL) layer by amide bond coupling using N-(3-Dimethylaminopropyl)-N'-ethylcarbodiimide hydrochloride (EDC) and N-Hydroxy-succinimide (NHS).

Albumin is a protein, which can be found in animal serum, including human serum and is used for transport. It can also be found in eggs where it is used for storage, this is a much cheaper source [414]. Albumin can be attached to PCL by adsorption, entanglement or covalent attachment [263]. Covalent attachment can be enduring, for example by amide bonding which immobilises the protein on the surface, or temporary such as cleavable linkages like hydrazone linkages which are pH responsive [415].

Albumin is an appropriate model therapeutic because it is cheap and has amine groups which enable amide bond coupling to PCL. All proteins, such as growth factors, have amine groups as they are made of amino acids. Many antibiotics also have amine groups which can be used to attach to PCL [416].

Immobilisation of growth factors, antibiotics and other therapeutics enables long term activity as they cannot be internalised by immune cells [93]. It can increase the efficiency of the therapeutics, for example by enabling fixation in a desirable orientation [94]. Although the effects are only local, some therapeutics electrostatically attract bacteria enabling a greater range [417]. Immobilisation prevents toxic therapeutics, for example biocides from interacting negatively with cells elsewhere in the body [265].

Amide bond coupling using EDC/NHS (figure 4.1) involves alkali hydrolysis of the PCL film to form carboxyl groups. It is then washed to remove the alkali so it does not neutralise the acid in the next step, which is acid protonation of the hydroxyl group. This makes it a good leaving group, a wash step then prevents acid hydrolysis occurring. EDC crosslinker bonds to the carboxyl groups to form O-acylisourea intermediate which is unstable. This is stabilised by NHS to form amine-reactive NHS ester, which is dry stable. The addition of the albumin results in the formation of an amide bond between an amine group on the albumin and the carboxyl group of the intermediate [329].

PCL is soluble in many solvents including chloroform which enables it to be dip coated onto metal surfaces such as Ti-6Al-4V lattices or coupons [323]. Surfaces generated using laser powder bed fusion have an inherent roughness due to semi sintered particles which enable bacterial colonisation [113]. So a PCL layer thickness which extends beyond these particles will reduce bacterial adhesion. As the PCL degrades these protrusions will become exposed and enable bone attachment. However in the short term this rough surface provides mechanical stability for the PCL.

The choice of PCL as the polymer for therapeutic immobilisation is due to its slow degradation rate and low cost [328]. It is also FDA approved [329] and can be sterilised by irradiation [92], so it is a practical choice for use in implants. The hydrophobic nature of

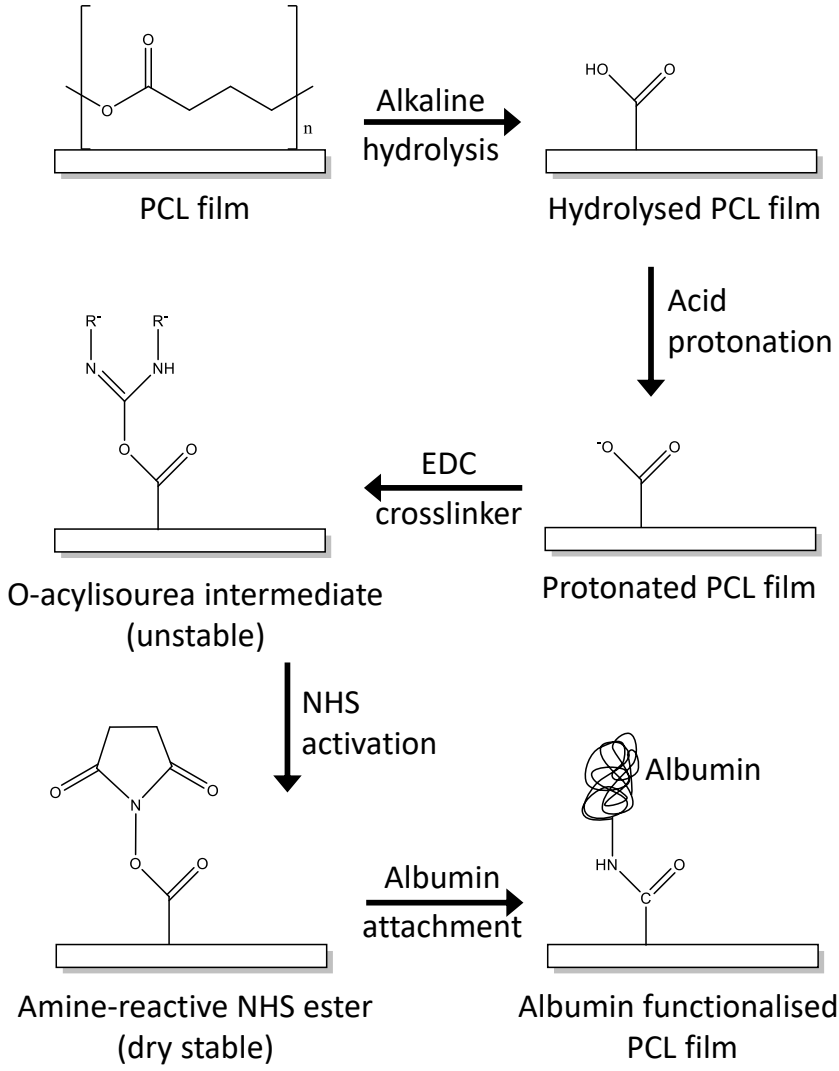

Figure 4.1: Schematic of chemical functionalisation of PCL films by amide bond coupling. Showing alkaline hydrolysis of ester bond on the PCL film, acid protonation of the hydroxyl group, activation with the EDC crosslinker to form O-acylisourea intermediate, followed by stabilisation with NHS to form amine-reactive NHS ester, which is replaced by the albumin

PCL is overcome by the therapeutic immobilisation, so challenges with poor cell adhesion do not prevent its use [327].

The aim of this chapter is to develop a coating to immobilise therapeutic agents on implant surfaces. The objectives include choosing a suitable polymer, model drug and immobilisation method. The coupons will be characterised by SEM to assess the surfaces prior to PCL coating. Dip coating will be optimised for PCL attachments and

the coating assessed by microscopy and weighing. A method for quantifying the albumin on the coupons will be developed and used to compare two albumin attachment methods, specifically adsorption and covalent attachment. Then this method will be calibrated by forcing the albumin into solution and comparing the fluorescence of the solution with standard solutions of known albumin concentration. Once the method for quantifying albumin on the coupons has been calibrated it can be used to inform the optimisation process for the immobilisation method.

The albumin will be attached to the PCL by amide bond coupling, the optimisation of this process will include the choice of buffers for the EDC/NHS step and the albumin step. The time spent in sodium hydroxide to hydrolyse the PCL as well as the time spent in EDC/NHS will be optimised, as will the time in albumin. The EDC/NHS and albumin steps can be performed as a one or two step process so these will be compared. The time the coupon spends soaking in water to remove the adsorbed albumin from the coupons will also be optimised. For all these studies the optimal process will be the one that has to most albumin attached. Finally, the immobilisation of the albumin will be tested over four months.

4.2 Methods

4.2.1 Materials, Equipment and Reagents

Gas atomised spherical Ti-6Al-4V grade 23 powder in the size range 15-53 μm (LPW Technology Ltd, UK) was used to manufacture the coupons. The polymer used to coat the coupons was polycaprolactone (PCL) with average Mn of 45,000 (Sigma-Aldrich, Merck KGaA, Germany), which was dissolved in chloroform (Sigma-Aldrich, Merck KGaA, Germany).

Sodium hydroxide solution was made from solid sodium hydroxide pellets (Fisher, Thermo Fisher Scientific, Inc, USA), and deionised water (Milli-Q, UK). Hydrochloric acid was diluted with deionised water from concentrated hydrochloric acid (Fisher, Thermo

Fisher Scientific, Inc, USA). N-(3-Dimethylaminopropyl)-N'-ethylcarbodiimide hydrochloride (EDC) (Merck KGaA, Germany) was mixed with buffers, as was N-Hydroxy-succinimide (NHS) (Sigma-Aldrich, Merck KGaA, Germany) and albumin (Purified albumin powder from egg, J.T.Baker, Avantor Inc, USA). The stirrer used was a RT2 Advanced Hotplate Stirrer (Thermo Fisher Scientific, Inc, USA).

Phosphate buffered saline solution (PBS) was created by dissolving a PBS tablet (Gibco, Thermo Fisher Scientific, Inc, USA) in 500 ml of deionised water. The process to generate 50 mM 2-(N-morpholino)ethanesulfonic acid buffer (MES) involves dissolving 4.88 g MES hydrate (Sigma-Aldrich, Merck KGaA, Germany) in 400 ml deionised water, adjusting the pH to 5.5 with sodium hydroxide, and then adding water until the volume was 500 ml.

Sodium phosphate buffer (Na-PB) was generated from 1.64 g sodium phosphate monobasic monohydrate (Sigma-Aldrich, Merck KGaA, Germany) and 0.16 g sodium phosphate dibasic (Sigma-Aldrich, Merck KGaA, Germany) in 400 ml deionised water, with hydrochloric acid used to adjust the pH to four, then the volume topped up to 500 ml with deionised water.

100 mM citrate buffer was made from 5.7 g citric acid powder (Fisher Scientific, Thermo Fisher Scientific, Inc, USA) and 20.7 g sodium citrate powder (Alfa Aesar, Thermo Fisher Scientific Corp, USA) in one litre of deionised water giving a pH of 5.18. Phthaldialdehyde Complete Solution (OPA) (Sigma-Aldrich, Merck KGaA, Germany) was used with propan-2-ol (Fisher Scientific, Thermo Fisher Scientific, Inc, USA) as a fluorogen to label albumin.

4.2.2 General Procedures

Coupon Manufacture

Ti-6Al-4V coupons, 5x20x20mm were manufactured in the same way as previously described (chapter 2, section 2.2.1). Briefly, a RenAM 500M (Renishaw, PLC, UK) L-PBF system was used to print the coupons from Ti-6Al-4V grade 23 powder using optimised

parameters (chapter 2, section 2.2.1 table 2.1). Water jetting, Quill Vogue powder wash (Quill International Group Ltd, UK) was used to remove excess powder before part removal from the substrate using wire electrodischarge machining (EDM), Cut 20 (Beijing Agie Charmilles Ltd, China). Coupons were built vertically with the large face perpendicular to the build substrate (section 4.3 figure 4.3a).

General Procedure for PCL Attachment

Polycaprolactone (PCL) was attached to the coupon surfaces by dip coating. PCL was dissolved in 20 ml chloroform at 0.04 gml^{-1}. Coupons were dipped in the solution vertically and removed slowly, before air drying. Between dips the coupons were rotated to mitigate potential imbalance of PCL thickness. This process was performed ten times per coupon.

General Procedures for Albumin Attachment

Two methods were investigated to attach albumin to the PCL, adsorption and covalent attachment. A flow chart of the methods can be found in figure 4.2.

Protocol for Attachment of Albumin by Adsorption

Albumin was adsorbed onto PCL by dissolving albumin powder in deionised water at a concentration of 0.2 gml^{-1}. Coupons were placed in the solution overnight.

Protocol for Covalent Attachment of Albumin

Albumin was covalently attached to the PCL using EDC/NHS coupling chemistry, a schematic of which can be seen in figure 4.1. Alkali hydrolysis was performed by placing the PCL coated coupons in 0.5 M sodium hydroxide for one hour, then rinsing in deionised water. The samples were then protonated in hydrochloric acid at 0.01 M for one minute before rinsing in deoinised water. The coupons were activated in a PBS buffer containing 0.12 M EDC and 0.1 M NHS for 30 minutes, before being left in a PBS buffer containing

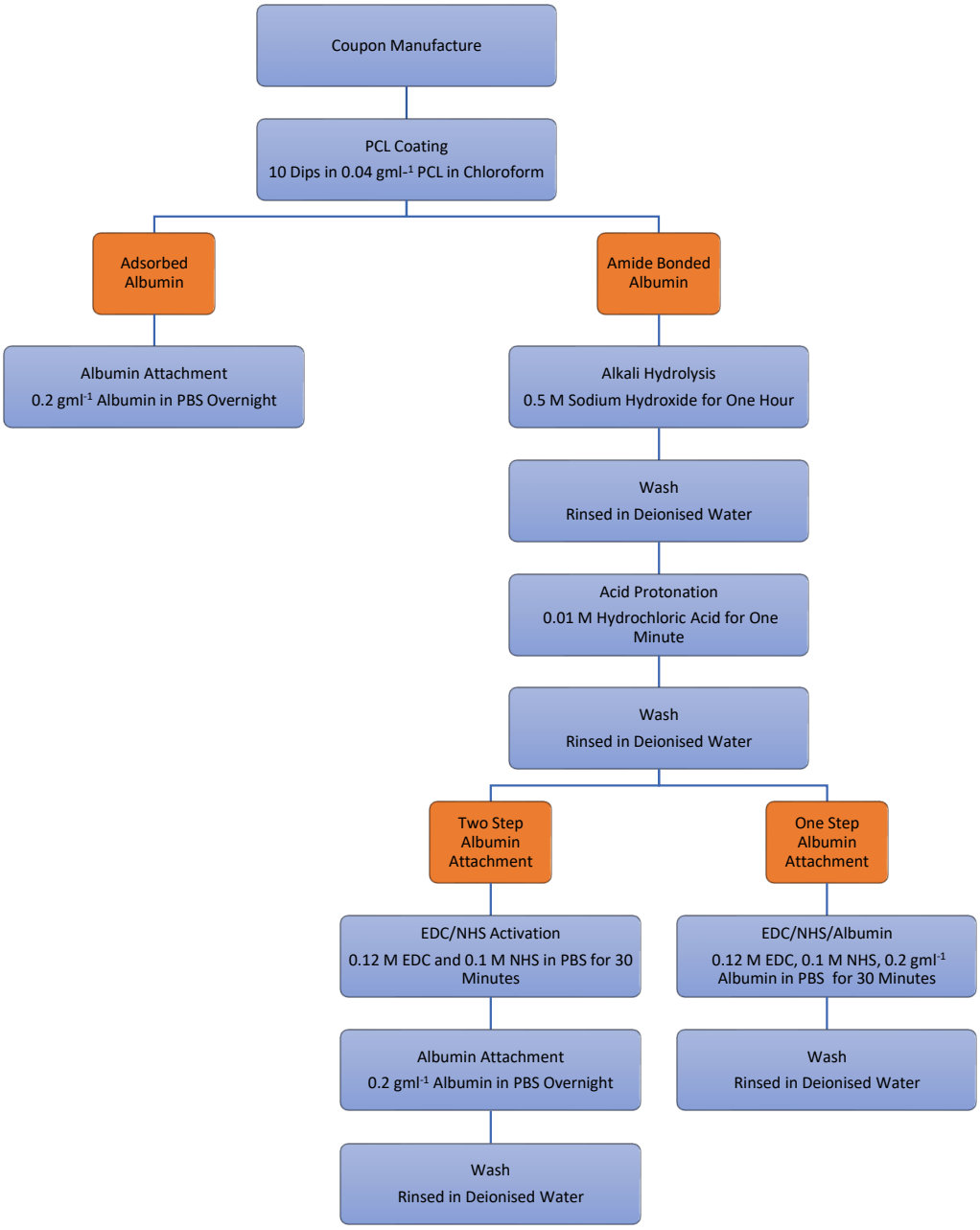

Figure 4.2: Flow chart of albumin attachment to PCL coated coupons. Showing the adsorption protocol, the standard two step covalent attachment, and the modified one step covalent attachment

0.2 gml^{-1} albumin overnight, then rinsing in deionised water. For some samples the coupons were then soaked in solution to remove adsorbed albumin.

4.2.3 Characterisation of PCL Attachment

Three coupons were dip coated in 0.04 gml^{-1} PCL in chloroform for ten dips. The mass of the coupons was measured prior to dip coating and after each dip on a Scout Pro balance (Ohaus Corp, USA).

In order to investigate the influence of the concentration of the PCL in the chloroform during dip coating on the quality of the polymer layer on the coupons, three concentrations were investigated, 0.02, 0.04, and 0.06 gml^{-1}. In each case the protocol 'General Procedure for PCL Attachment' from section 4.2.2 was followed. Coupons without PCL were also compared. Photographs were taken of the coupons. The coupons were cut in half parallel to the build direction (through the faces that the SEM micrographs were taken) on the ISOMet 5000 Linear Precision Saw (Buehler, USA). The cut face was then imaged on an optical microscope with incident lighting, (Brunel Microscopes Ltd, UK), to visualise the polymer layer thickness and attachment.

4.2.4 Characterisation of Albumin Attachment

Two methods for attaching albumin to the PCL coated coupons were investigated - adsorption and covalent attachment. The samples with covalently attached albumin followed the standard protocol 'Protocol for Covalent Attachment of Albumin' and no soak step was added after the final washing. For the samples with adsorbed albumin three samples had no soak step, and three had a ten minute soak in deionised water. Coupons with a PCL coating but no albumin were also compared.

4.2.5 Albumin Attachment Process Optimisation

Influence of Reaction Buffers

There is potential for the pH of the activation step or the albumin attachment step to influence the quantity of albumin attached, so two different buffers were investigated for each step. For the activation step involving EDC and NHS; PBS with a pH of 7.4 and

MES with a pH of 5.5 were compared. PBS (pH of 7.4) and sodium phosphate buffer with a pH of 4 were investigated for the albumin attachment step. The standard 'Protocol for Covalent Attachment of Albumin' was followed with the exception of the different buffers described above. A ten minute soak in deionised water was used after the final was step.

Influence of Sodium Hydroxide Hydrolysis Time on Albumin Attachment

Samples were generated using different hydrolysis time to see how this influences the quantity of albumin attached. The times used were 10, 20, 30, 60 and 120 minutes plus overnight. The standard protocol for covalent attachment of PCL was then followed, with a 60 minute citrate buffer soak.

Influence of Time in Buffer Containing EDC and NHS on Albumin Attachment

The length of the activation step may influence the amount of albumin covalently attached to the coupons so the time the coupons were in PBS buffer containing EDC and NHS was varied between 30, 60 and 120 minutes. The standard protocol for covalent attachment of PCL was otherwise used. The soak time was 60 minutes in citrate buffer.

Understanding the Influence of Time Spent in Albumin on Attachment

The standard protocol for covalent attachment of albumin to PCL was performed until the albumin attachment step. After activation the coupons are placed in albumin so that it can covalently attach to the PCL. The time for this step was altered to see whether shortening the albumin time decreased the quantity of albumin attached. Following the albumin attachment the samples were washed in deionised water and then soaked in citrate buffer for 60 minutes.

Investigating Whether a One Step Method for Activation and Attachment Improves Albumin Attachment

After hydrolysis and protonation a one step method was investigated where the samples were placed in a mixture of EDC, NHS and albumin, as an alternative to the two step method previously described. This provides albumin immediately after the amine-reactive NHS ester intermediate is created. The coupons were in the combined solution for 30, 60 or 120 minutes. The standard protocol for hydrolysis, protonation and washes was followed. After the samples had been removed for the EDC, NHS and albumin mixture they were washed in deionised water and soaked in citrate buffer for 60 minutes.

Understanding the Temporal Effects of Soaking in Deionised Water to Remove Adsorbed Albumin

The coupons which have covalently attached albumin also have adsorbed albumin due to the nature of the attachment process. So albumin was adsorbed onto PCL coated coupons to see how long it took to be removed. The samples were made with 0.04 gml^{-1} PCL concentration following the standard protocol for PCL attachment described in section 4.2.2. Then the samples were placed in 15 ml of 0.2 gml^{-1} albumin in PBS overnight, prior to a one minute wash in deionised water to remove the albumin solution.

Two time series were used to investigate how long coupons need to be in deionised water to remove adsorbed albumin. The first was every 60 minutes for six hours, and the second was every ten minutes for one hour. Coupons were scanned on the plate reader (Spark Multimode Microplate Reader, Tecan Trading AG, Switzerland), as described later (section 4.2.7), and then placed in deionised water for the first time interval. The coupons were then air dried prior to rescanning on the plate reader. They were then placed in fresh deionised water for the next time interval. The water used for each soak was also measured to find the albumin content, the method for which is described later.

4.2.6 Release Studies

Quantifying Albumin Detection on Coupons

Six samples were generated with covalently attached albumin, and six with adsorbed albumin following the standard protocols in section 4.2.2. The covalent samples were soaked in deionised water for 60 minutes after the final wash.

Albumin attachment was quantified by forced hydrolysis. The coupons were placed in 15 ml of 0.5 M sodium hydroxide (pH 13.7), or 100mM citrate buffer (pH 5.2). 1 ml samples were removed and replaced with fresh solution at each time point. The fluorescence of the albumin on the coupons before and after the forced hydrolysis was measured following the protocol 'Albumin Detection on Coupons' described in section 4.2.7. Additionally the solutions were measured for absorbance and natural fluorescence as is, then neutralised prior to OPA fluorescence measurement being taken.

Physiological Release

Samples with adsorbed or covalently attached albumin were made following the standard protocols. Three covalent samples and three adsorbed samples were then soaked in citrate buffer for 60 minutes, an additional three adsorbed samples were not soaked. The samples were placed in 15 ml of PBS and left in a OLS Aqua pro shaking water bath (Grant Instruments Ltd, UK), at 37°C, with shaking at 50 rpm for four months. Fluorescence scans of the coupons were taken before and after elution. While the absorbance, natural fluorescence and fluorogenic fluorescence of the solution was measured.

4.2.7 Analysis

Coupon Characterisation

Back scattered electron SEM micrographs (TM3000, Hitachi High-Technologies Corporation, Japan) were taken of coupons after printing to give an indication of the surface roughness and particle adhesion. These were taken of faces which were in the top, bottom

and vertical orientations during building (section 4.3 figure 4.3a).

Albumin Detection on Coupons

Dry samples were placed in black 6 well plates with the large 20x20 face upright, and the plates were placed in the plate reader (Spark Multimode Microplate Reader, Tecan Trading AG, Switzerland). Fluorescence Top Reading was used as albumin is naturally fluorescent, with excitation wavelength of 290 nm and emission wavelength of 335 nm, while the gain was 80. An area scan with a 15x15 grid of locations per well was used to ensure the coupon could be identified within the well and to provide sufficient data points on the coupon. Empty plates were scanned to identify the background fluorescence value of the plate, while coupons with just PCL were scanned to find the fluorescence value of the PCL. The coupons were scanned on both large faces. Fluorescence data was imported into Matlab (MathWorks Corp, USA). Fluorescence values below 1000 were considered to be background and removed while values above 1000 were assumed to be readings taken of the coupon. The mean and standard deviation of values for each coupon were recorded. However this gives a fluorescence value for each coupon not a quantity of albumin attached, so a calibration is needed.

Albumin Detection in Solution

Following the release of albumin from the coupons, the albumin concentration in solution was measured by absorbance, natural fluorescence or fluorescence with a fluorogen - here phthaldialdehyde (OPA) used in Chapter 3. Absorbance scans were performed between 250 and 300 nm on 5 $mgml^{-1}$ albumin in PBS. For fluorescence the sample was excited at 280, 285, 290 and 295 nm, with an emission range of 325 to 355 nm. For fluorogenic fluorescence with OPA the same excitation and emission wavelengths were used as per gentamicin sulphate in Chapter 3, i.e. 340 and 430 nm respectively.

In order to create a dilution series for the calibration, albumin was dissolved in PBS at a concentration of 20 $mgml^{-1}$ in triplicate. This was then mixed in 50:50 ratios with

PBS, repeatedly to create a series. For absorbance and natural fluorescence readings 100 μl was aliquoted into wells of the 96 well plate, these were measured at 280 nm for absorbance, and the natural fluorescence was measured with emission at 290 nm and an excitation wavelength of 335 nm. For the fluorogenic fluorescence 33 μl of solution, 33 μl of propan-2-ol, and 33 μl of OPA were aliquoted into a well of the 96 well plate, and fluorescence scanned. Three dilution series were generated in order to have triplicate readings. Calibration was also performed in deionised water so that the solution after the soak, for the soak time study, could be calibrated. This followed the same method as above but with deionised water as the solvent rather than PBS. The wavelength scans were not repeated.

In order to calibrate the albumin in the forced released solutions dilution series were also created for 0.5 M sodium hydroxide, and 100 mM citrate buffer. For absorbance and natural fluorescence the method is the same as above. However for the OPA fluorescence, the solutions were neutralised first. The sodium hydroxide solution was neutralised with 1 M HCL, while the citrate buffer solution was neutralised with 0.5 M sodium hydroxide. 33 μl of these neutralised solutions were then mixed with 33 μl of propan-2-ol, and 33 μl of OPA in wells and the fluorescence measured.

Solution samples were measured in the same way as calibration readings. In short, 100 μl of solution was placed in a 96 well plate and absorbance and fluorescence measurements taken. Then the solution was neutralised and 33 μl of neutralised solution, 33 μl of propan-2-ol, and 33 μl of OPA were aliquoted into a well and the fluorescence measured.

Statistical Analysis

For all experiments three independent samples were generated for each variable. Statistical analysis was performed using Matlab (MathWorks Corp, USA), initially one way ANOVA testing was performed to see whether all the data had an equal mean, if they did not then Tukey post hoc testing was performed to identify which means were statistically different.

4.3 Results

4.3.1 Characterisation of Uncoated Coupons

The coupons were built vertically with the large faces perpendicular to the build substrate (figure 4.3a). SEM micrographs of the faces show a rougher surface on the vertical faces (side view, figure 4.3c) than the top or bottom faces (figure 4.3b&d), as well as increased particle adhesion. The bottom face has greater roughness than the top surface, with evidence of pitting and cracks.

4.3.2 Characterisation of PCL Coating

To check whether 10 dips was an appropriate quantity, the mass of the coupon and PCL was measured after the drying stage of each dip. The mass of PCL on the coupons increased with each dip up to 0.0298 ± 0.0092 g after 10 dips (figure 4.4). When there were more dips there was greater variability between the mass measurements. Although this variability did not vary linearly with number of dips.

Different concentrations of PCL dissolved in chloroform were investigated for dip coating, with 0.02, 0.04 and 0.06 gml^{-1} used. The mass of the coupons before and after coating were compared, with the mass of PCL on the coupons dipped in 0.02 gml^{-1} was the lowest at 0.00108 ± 0.0013 g, while 0.06 gml^{-1} had the highest mass of PCL at 0.0658 ± 0.0035 g. The coupons dipped in 0.04 gml^{-1} PCL had a PCL mass of 0.0276 ± 0.0006 g, which was the lowest variation in mass.

Coupons were cut to visualise the PCL thickness by optical microscopy (figure 4.5). The striped light coloured section at the top on the left hand samples (a,c,e,g) and at the bottom on the right hand images (b,d,f,h) is the coupon, while the black region is air, the translucent substance in between is the PCL. No PCL is seen on the coupon only samples but the rough surface of the coupons can be seen. The coupons with PCL at 0.02 gml^{-1} have a PCL layer which is not as thick as the largest protrusions from the coupon (figure 4.5c), the layer cannot be seen on the blade exit side (figure 4.5d).

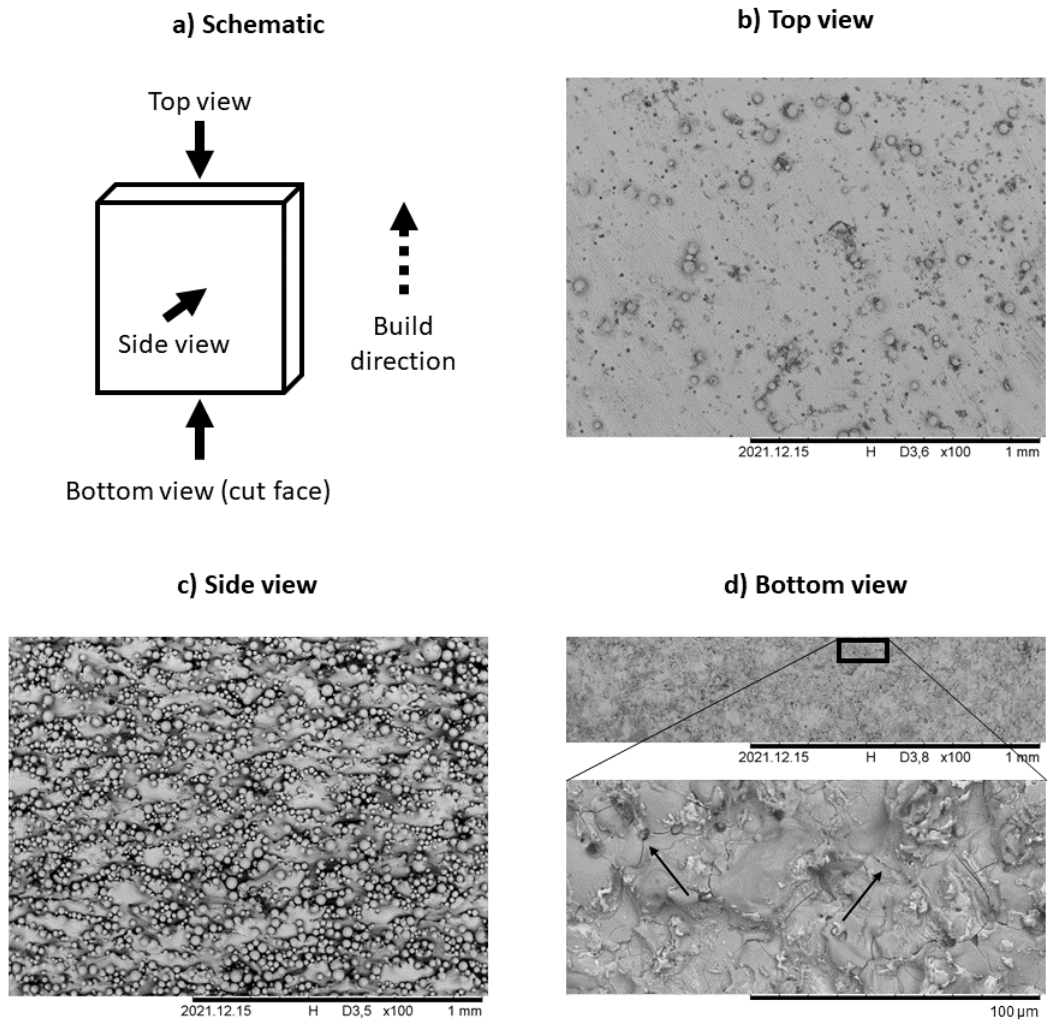

Figure 4.3: SEM micrographs of an as built coupon at 100x magnification, a) diagram of coupon orientation during build showing which faces SEM micrographs were taken of, b) top view showing minimal particle adhesion, c) side view showing extensive particle adhesion, d) bottom view (cut face) including view at 1000x magnification showing pitting and cracking

For the 0.04 gml^{-1} coupons the PCL layer can be seen on both the blade entry and exit edges (figure 4.5e&f), with some gap visible between the PCL and the coupon on the blade exit side (figure 4.5f). The PCL layer extends beyond the coupon protrusions, and has a similar thickness on the two images. The coupons which were dipped in PCL at 0.06 gml^{-1} have visible PCL layers in both images (figure 4.5g&h), with air visible between the coupon and the PCL on the blade exit side (figure 4.5h). The PCL layer is not the same thickness in the two images.

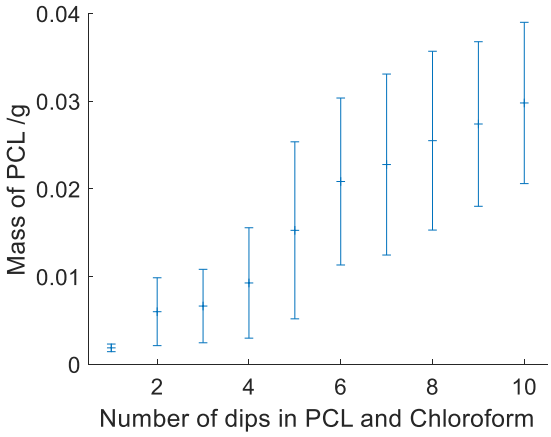

Figure 4.4: Mass of PCL after each dip of the coupons in 0.04 gml^{-1} PCL and chloroform after drying. Error bars show one standard deviation, n=3

By photographing the coupons with the PCL coating (figure 4.6 it can be seen that the 0.06 gml^{-1} coupons have an uneven coating of PCL. This is in agreement with the optical microscope images.

4.3.3 Characterisation of Albumin Attachment

Comparison of Adsorbed and Covalent Attachment of Albumin to PCL

The fluorescence scans of the coupons enable a heat map of each side of each coupon to be generated which shows the fluorescence signal at different points on the coupon surface. Two example heat maps can be seen in figure 4.7, one for a coupon without albumin (figure 4.7a), and one with albumin (figure 4.7b). It can be seen that the PCL gives a non zero value of fluorescence with some variation across the coupon. While the albumin coated coupon has areas with a larger fluorescence signal, but also some variation.

Relative frequency plots of the fluorescence signal can be used to compare the variation in signal within a coupon (figure 4.8). It can be seen that the fluorescence values for the coupon without albumin are over a narrow range, specifically 0 to 15,000 (figure 4.8a), whereas the ranges for the adsorbed without the wash and covalently attached albumin are larger from 0 to 60,000 (figures 4.8b&d). However the adsorbed albumin without the wash has a peak in relative frequency in the range 5,000 to 10,000, whereas the

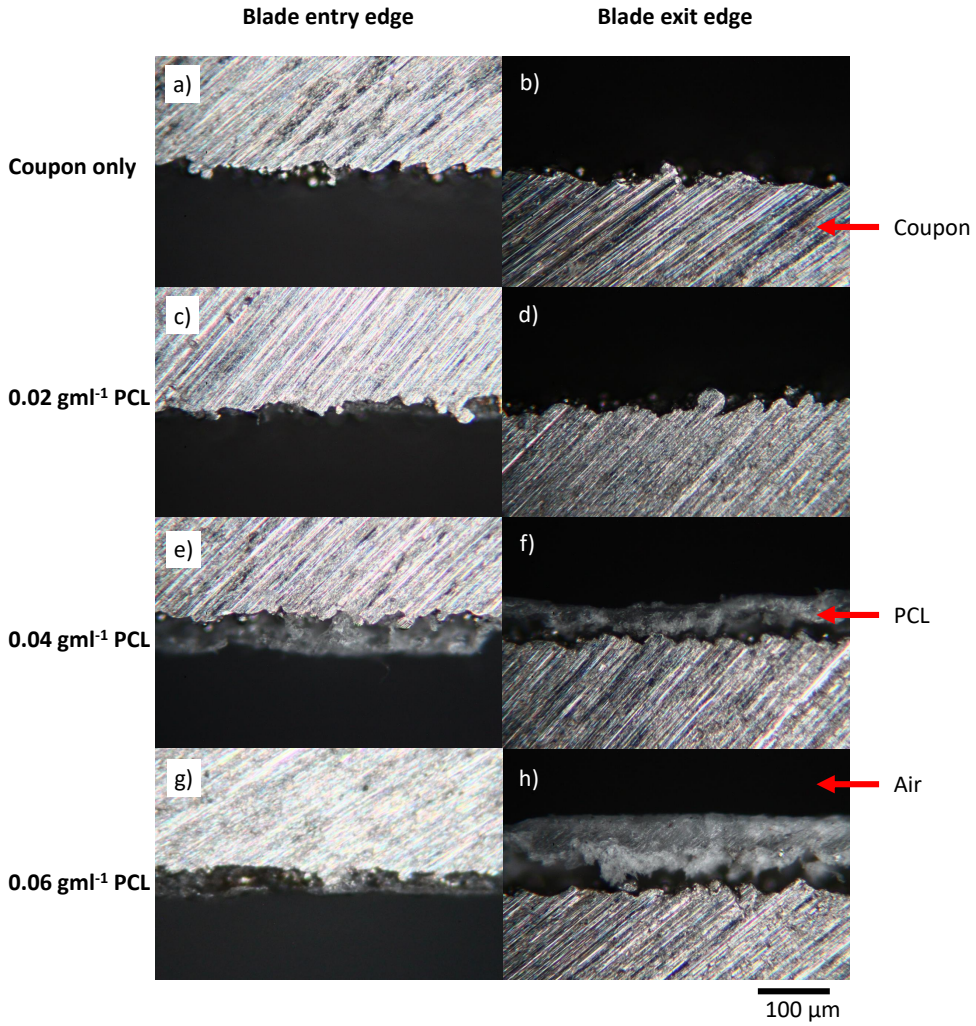

Figure 4.5: Optical microscopy images of the cut face of the coupons coated in PCL. The left hand column shows the edge of the face where the saw blade entered the coupon so the PCL is close to the coupon, while the left hand column shows where the saw blade exited the coupon so the PCL has come away from the coupon. The PCL concentration in chloroform for dip coating were as follows: a&b) 0 gml^{-1}, c&d) 0.02 gml^{-1}, e&f) 0.04 gml^{-1}, g&h) 0.06 gml^{-1}

fluorescence values for the coupons with covalently attached albumin are spread across the fluorescence range. The adsorbed albumin with wash step coupons (figure 4.8c) have a larger fluorescence range than that of only PCL but lower than the other two coupon sets.

When the mean fluorescence values of the coupons are compared (figure 4.9), the covalently attached albumin coupons have the highest fluorescence at 19200 ± 2670, while the PCL only coupons have the lowest at 3680 ± 1150. However there is no statistical

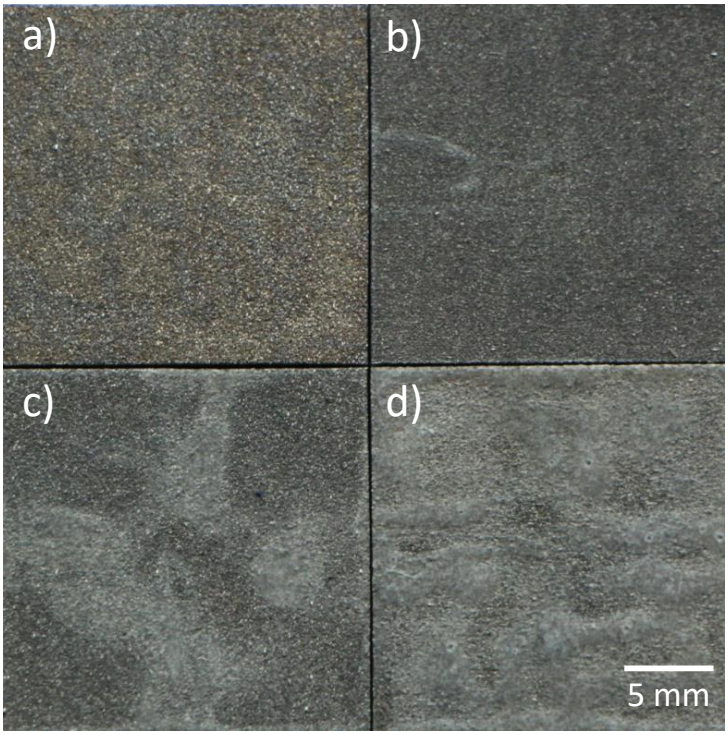

Figure 4.6: Image of the coupons with PCL attached. The PCL concentration in chloroform for dip coating were as follows: a) 0 gml^{-1}, b) 0.02 gml^{-1}, c) 0.04 gml^{-1}, d) 0.06 gml^{-1}

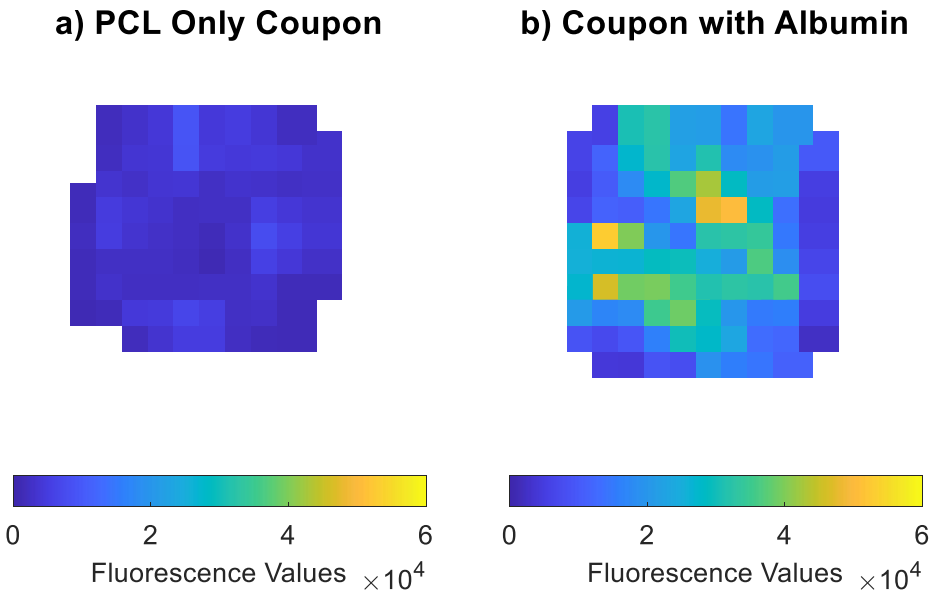

Figure 4.7: Heat map of coupons showing natural fluorescence measurements with colour-bar underneath, a) PCL only, b) PCL and albumin

difference (ANOVA and post hoc testing) between the coupons with only PCL and those with adsorbed albumin and a 10 minute wash which have a fluorescence of 5760 ± 848.

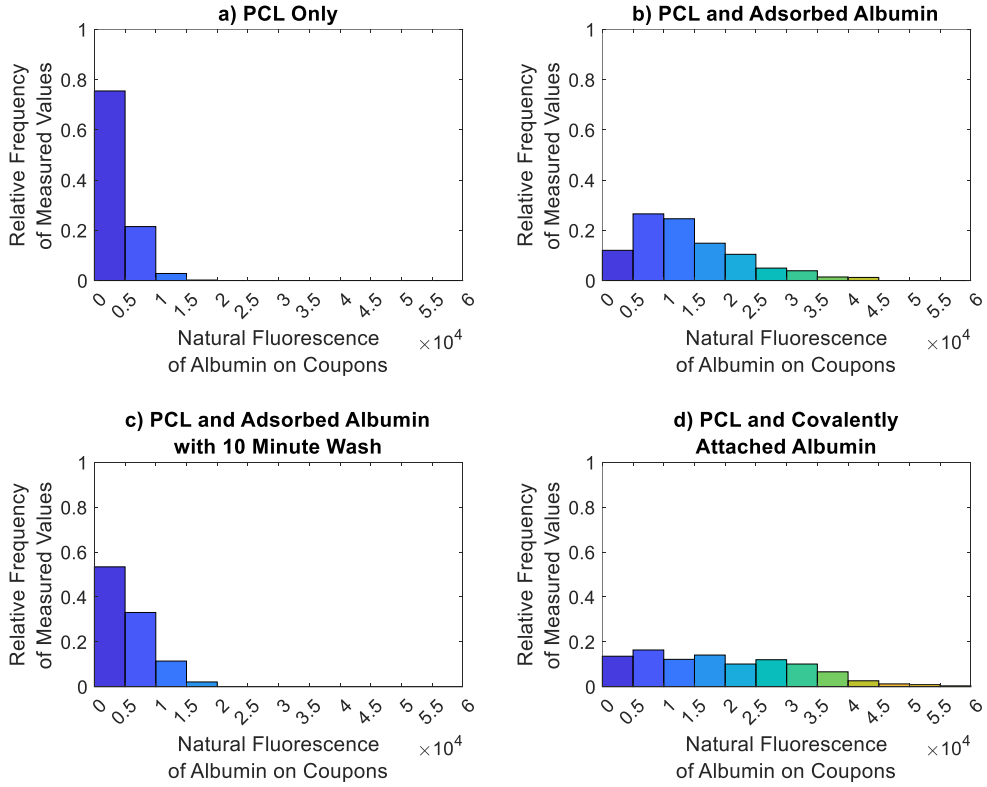

Figure 4.8: Relative frequency of the natural fluorescence measurement of coupon scans, a) PCL only, b) PCL and adsorbed albumin, c) PCL and adsorbed albumin followed by a 10 minute wash step in deionised water, d) PCL and covalently attached albumin

While the adsorbed (no wash) coupons are not statistically different from the covalent samples with a fluorescence of 14000 ± 4990.

Quantification of Albumin in Solution

In order to calibrate to fluorescence of the albumin on the coupons with the mass of albumin, forcing the albumin into solution was proposed. This enables the albumin to be measured in solution and compared with known concentrations of albumin in solution. Sodium hydroxide and a citrate buffer were explored as potential reagents for this process. While natural fluorescence, absorbance, and fluorescence with a fluorogenic agent were all investigated as methods of quantifying the albumin in solution.

Excitation and emission wavelength spectra of albumin dissolved in PBS enabled the appropriate wavelengths to be chosen. The initial absorbance scan performed at

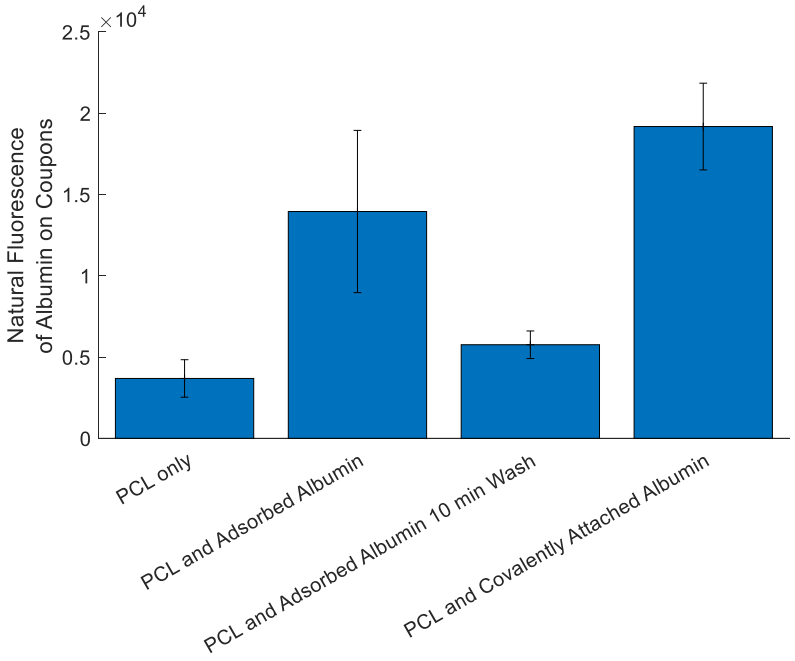

Figure 4.9: Mean fluorescence values of coupons coated in PCL, a) without albumin, b) with adsorbed albumin, c) with adsorbed albumin followed by a 10 minute water wash, d) with covalently attached albumin. Error bars are one standard deviation, n=3

20 mgml^{-1} had an absorbance around three, so the solution was diluted to 5 mgml^{-1} in order to have absorbance values below two in accordance with Beer-Lambert's Law [418, 419]. The maximum absorbance value of 5 mgml^{-1} albumin was 0.820 at 280 nm. The highest fluorescence value of 20 mgml^{-1} albumin was 349000, with an excitation wavelength of 290 nm and an emission wavelength of 335 nm.

Calibration curves of albumin in sodium hydroxide and citrate buffer were generated for absorbance and natural fluorescence without the solution being neutralised (figure 4.11a,b,d&e), and with OPA as a fluorogen where sodium hydroxide was neutralised with hydrochloric acid, and citrate buffer was neutralised with sodium hydroxide (figure 4.11c&f). Both the calibration curves for absorbance readings had points which fit a linear model well with R^2 values of 1.00, while exponential curves were fit to the fluorescence measurements with R^2 values of 1.00 for each data set.

Prior to release there was no statistical difference between the fluorescence readings of the coupons with adsorbed albumin at 17200 $\pm$ 2720 and 19000 $\pm$ 20500. There

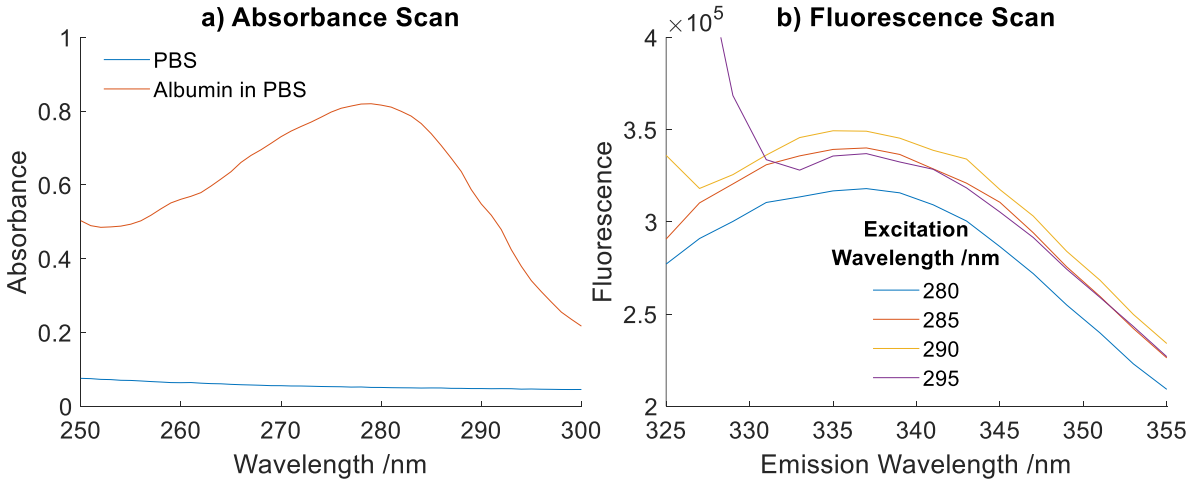

Figure 4.10: Wavelength scans to find the excitation and emission wavelengths that give the highest values of absorbance and fluorescence. a) Absorbance spectra for PBS, and 5 mgml^{-1} albumin dissolved in PBS, b) fluorescence spectra for 20 mgml^{-1} albumin dissolved in PBS, with different excitation wavelengths shown on different curves and emission wavelengths along the x axis

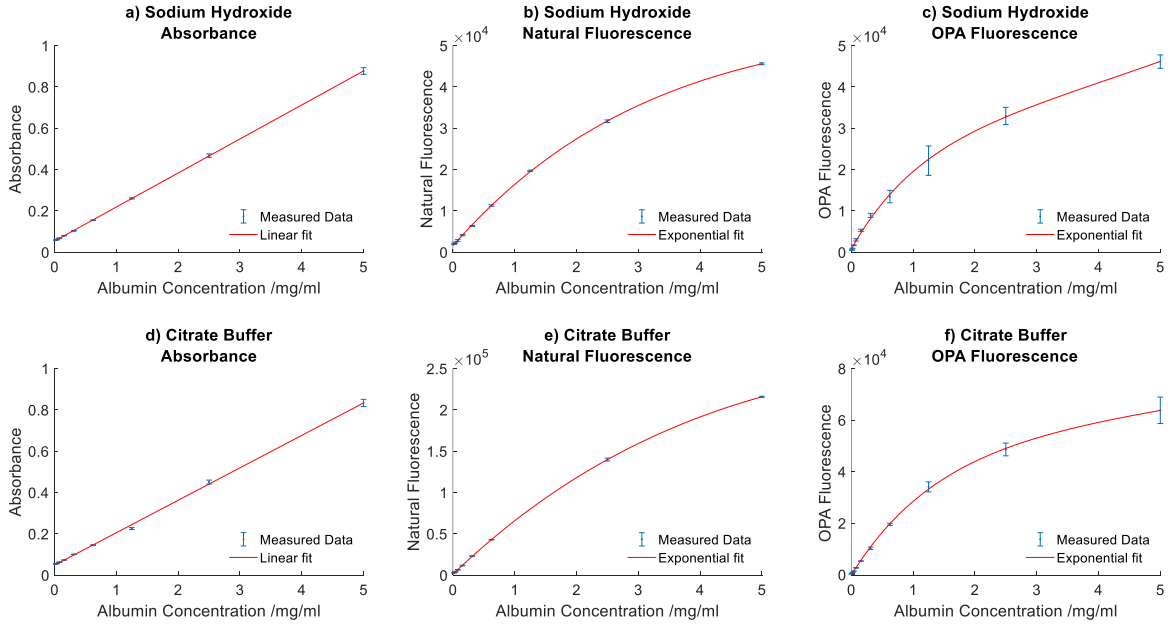

Figure 4.11: Calibration curves for albumin in sodium hydroxide and citrate buffer. a) absorbance of albumin in sodium hydroxide (not neutralised), b) natural fluorescence of albumin in sodium hydroxide (not neutralised), c) fluorescence of albumin in sodium hydroxide neutralised with hydrochloric acid, using OPA as a fluorogen. d) absorbance readings of albumin in citrate buffer (not neutralised), b) natural fluorescence of albumin in citrate buffer (not neutralised), c) fluorescence of albumin in citrate buffer neutralised with sodium hydroxide, using OPA as a fluorogen. Error bars are one standard deviation, n=3

was also no statistical difference between the covalent coupons despite the differences in mean fluorescence values of 128000 ± 1370 and 9940 ± 1840. However the adsorbed samples had statistically higher fluorescence values than the covalent ones. After the forced release of the albumin the coupons which were placed in sodium hydroxide had coupon fluorescence values of 4660 ± 838 and 4590 ± 476. This is in the range of values of coupons with just PCL on (figure 4.9), with no statistical differences between the three sets of coupons (adsorbed and covalent in sodium hydroxide, and PCL only coupons). While the coupons which had been placed in citrate buffer had values above that, with coupons with adsorbed albumin giving a higher fluorescence reading of 7590 ± 615 while the coupons with covalently attached albumin had a fluorescence of 6130 ± 821. All of the fluorescence values after release were statistically lower than those before release, however they were not statistically different from each other.

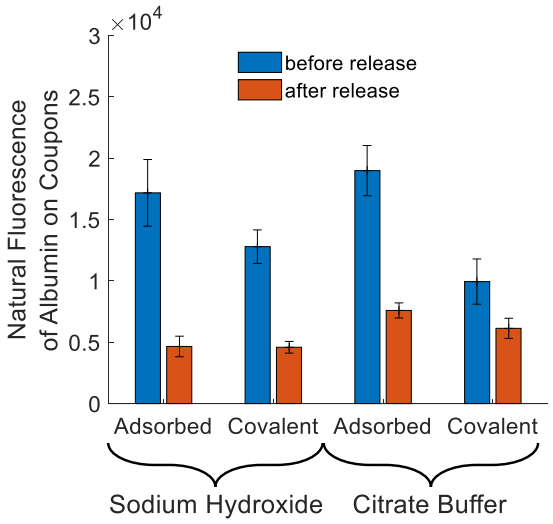

Figure 4.12: Fluorescence scans of the coupons before and after forced release with sodium hydroxide and citrate buffer for 54 hours. Albumin was attached by adsorption or covalent bonding. Error bars are one standard deviation, n=3

The absorbance, natural fluorescence, and fluorogenic fluorescence of the solutions were measured and the calibration curves (figure 4.11) were used to convert these values into concentrations of albumin in solution (figure 4.13). The highest concentration estimates were from the absorbance readings, with the adsorbed albumin released by sodium

hydroxide giving an estimate of 0.351 $\pm$ 0.026 mgml^{-1} at 54 hours, while adsorbed albumin release by citrate buffer had an estimated concentration of 0.106 $\pm$ 0.035 mgml^{-1} at 54 hours, both higher than their respective covalently attached samples.

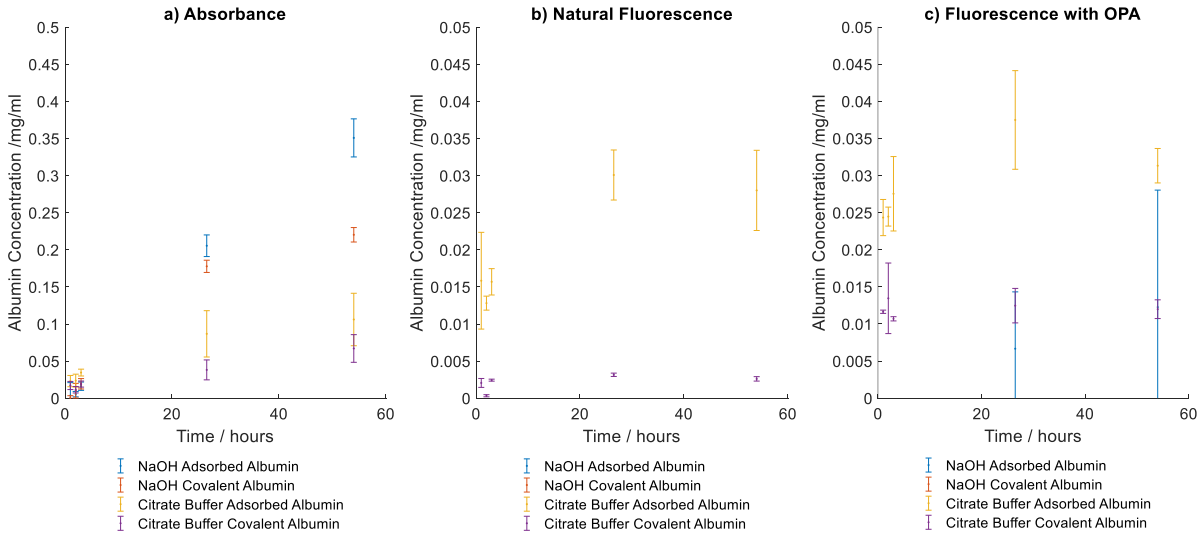

Figure 4.13: Concentration of albumin in solution in mgml^{-1} during forced release with sodium hydroxide and citrate buffer. Albumin was attached by adsorption or covalent bonding. Error bars are one standard deviation, n=3

When the absorbance measurements were used to estimate the albumin concentration in solution the concentration increased with time for all coupon sets. For natural fluorescence and fluorogenic fluorescence the concentration estimate peaked at 26.5 hours for the citrate buffer released adsorbed albumin at 0.030 $\pm$ 0.003 mgml^{-1} for natural fluorescence, and 0.037 $\pm$ 0.007 mgml^{-1} for OPA fluorescence. These are less than half of the value estimated with absorbance of 0.087 $\pm$ 0.031 mgml^{-1}. The covalently attached albumin also peaked at 26.5 hours for citrate buffer release by fluorescence measurements, but at lower concentrations of 0.003 $\pm$ 0.000 mgml^{-1} for natural fluorescence and 0.012 $\pm$ 0.002 mgml^{-1} for OPA fluorescence. Absorbance gave the highest estimate of albumin concentration in solution while natural fluorescence gave the lowest. For citrate buffer, the difference between concentration estimates of adsorbed and covalently attached albumin was different between the methods. For absorbance methods the concentration of adsorbed albumin was 1.3 to 2.3 times more than covalently attached albumin, while for

natural fluorescence estimates this range was 6.4 to 38.5 times, fluorogenic fluorescence multipliers were closer to absorbance at 1.8 to 3.0 times.

The values for the natural fluorescence of the solutions containing sodium hydroxide were so low that they could not be distinguished from solution without albumin so no concentration values are shown on the graph. This was similarly true for fluorogenic fluorescence, with only two time points (26.5 and 54 hours) having measurable values for adsorbed albumin in sodium hydroxide.

4.3.4 Albumin Attachment Process Optimisation

Influence of Reaction Buffers

Buffers were used to maintain the pH during the coupling process. PBS (pH of 7.4) and MES (pH of 5.5) were used for the EDC/NHS step while PBS and sodium phosphate buffer (pH of 4) were used for the albumin step. There was no statistical difference between the fluorescence readings taken of the coupons using any of the combinations of buffers with values of around 15000 for all coupons (figure 4.14).

Influence of Sodium Hydroxide Hydrolysis Time on Albumin Attachment

Comparison was made between the fluorescence of albumin on coupons with covalently attached albumin, which had different lengths of time in sodium hydroxide for the initial hydrolysis of the PCL. The highest fluorescence value was seen for a hydrolysis time of 60 minutes, this was 12000 $\pm$ 1680. Coupons which had been in sodium hydroxide overnight during the albumin attachment process gave the lowest fluorescence values of 6540 $\pm$ 1270. The overall trend was an increase from 10 minutes to 60 minutes before falling with more time (figure 4.15a).

Influence of Time in Buffer Containing EDC and NHS on Albumin Attachmen

When the time in EDC and NHS is varied the highest fluorescence measured is at 30 minutes with a value of 12000 $\pm$ 1680, which is statistically higher than fluorescence

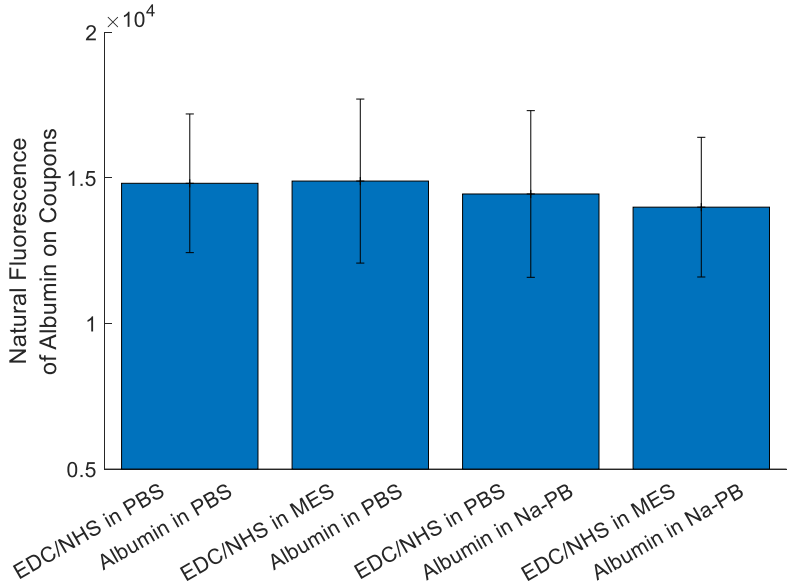

Figure 4.14: Fluorescence scans of coupons with covalently attached albumin using different buffers during the coupling process. With PBS or MES used for the EDC/NHS step, and PBS or sodium phosphate buffer used during the albumin step. Error bars are one standard deviation, n=3

values at 60 and 120 minutes, which are not statistically different from each other (figure 4.15b).

Understanding the Influence of Time Spent in Albumin on Attachment

Coupons placed in albumin for longer periods of time gave higher fluorescence values than those at shorter times (figure 4.15c). With the highest fluorescence value of 12000 $\pm$ 1680 for coupons left in albumin overnight, these are statistically different from all the other time points. While the lowest fluorescence value was seen at 10 minutes with a reading of 5660 $\pm$ 993.

Investigating Whether a One Step Method for Activation and Attachment Improves Albumin Attachment

As an alternative to EDC/NHS and albumin being two separate steps, they were combined into one step with all three reagents in the same solution. Three reaction times were explored for this combination (figure 4.15d) with 60 minutes giving the highest flu-

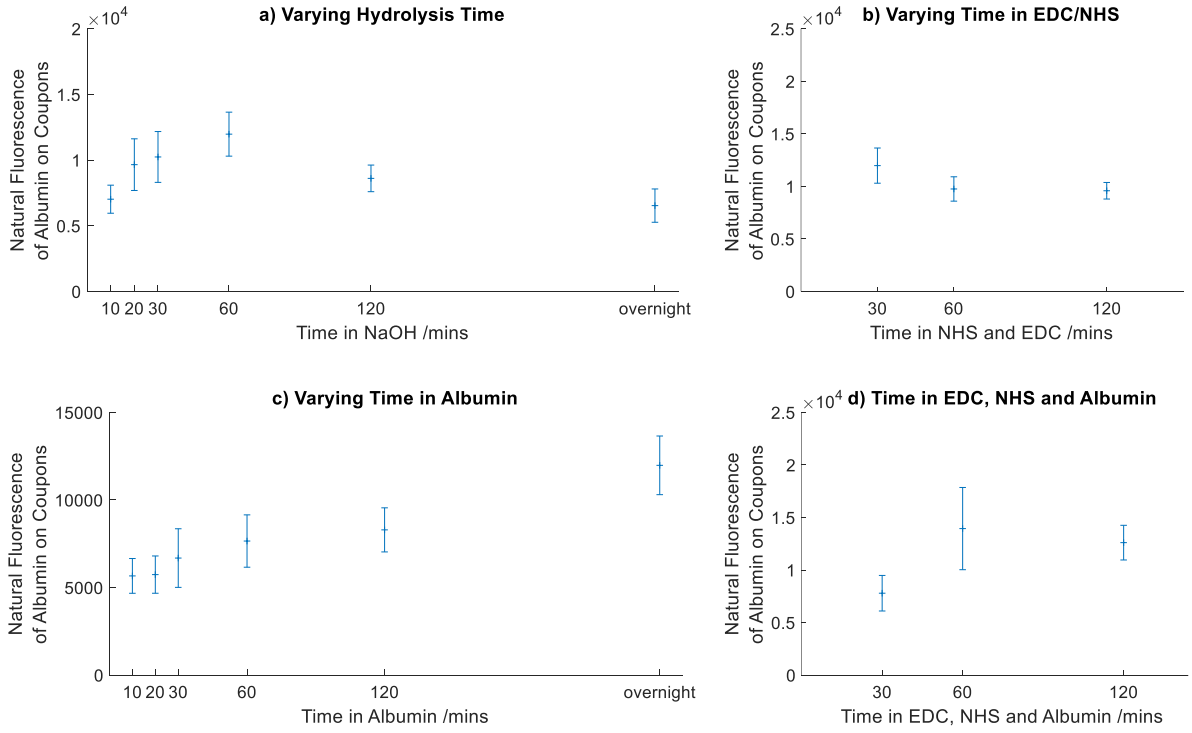

Figure 4.15: Comparison of the fluorescence values of albumin on coupons when varying the time of various steps in the covalent attachment of albumin to PCL. a) varying hydrolysis time, b) varying time in EDC and NHS, c) varying time in albumin, d) varying time in EDC, NHS and albumin all in one solution. Error bars are one standard deviation, n=3

orescence value of 13900 $\pm$ 3910, although this was not statistically different from the fluorescence of 12600 $\pm$ 1650 at 120 minutes. Both of these were statistically higher than the fluorescence at 30 minutes of 7800 $\pm$ 1690.

Understanding the Temporal Effects of Soaking in Deionised Water to Remove Adsorbed Albumin

It is clear from the albumin attachment study that washing in water removes some of the adsorbed albumin (figure 4.9), however the time required to remove all the additionally adsorbed albumin from the covalent samples in unknown so a wash time study was used. Samples with adsorbed albumin were used as the base, since the quantity of covalently attached albumin would not be known. Therefore when the fluorescence of the coupons reaches approximately 5000 it is known there is no more albumin adsorbed onto the

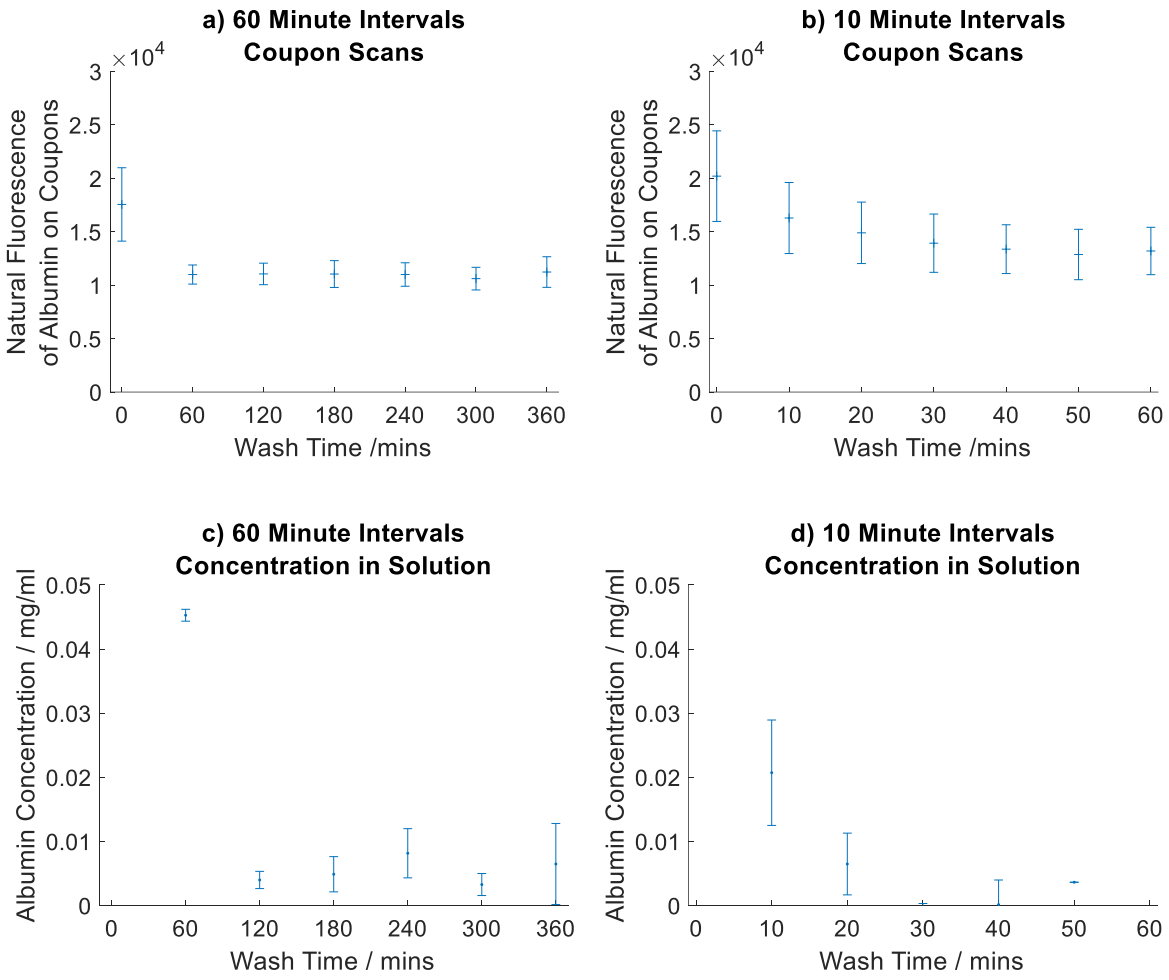

Figure 4.16: Graphs of albumin after different amounts of time soaking in water. a) fluorescence of albumin on the coupons after each step at 60 minute intervals, b) after 10 minute intervals, c) concentration of albumin in solution after 60 minute intervals with fresh water each step at 60 minute intervals, and d) 10 minute intervals calculated from absorbance measurements of the solution. Error bars are one standard deviation, n=3

coupon. When the wash time steps were 60 minutes the fluorescence of the albumin on the coupons falls from 17600 ± 3430 prior to washing to 11000 ± 894 after 60 minutes, the values after this point were not statistically different. This was mirrored by the albumin concentration in solution where the initial concentration of albumin in the solution used for the first 60 minute wash step was 0.0453 ± 0.0009 mgml^{-1}. The solutions for the remaining time points had concentrations below 0.01 mgml^{-1}, the highest of which was at 180-240 minutes with a concentration of 0.0082 ± 0.0038 mgml^{-1}.

For the 10 minute wash time intervals there was less of a step change in the fluorescence

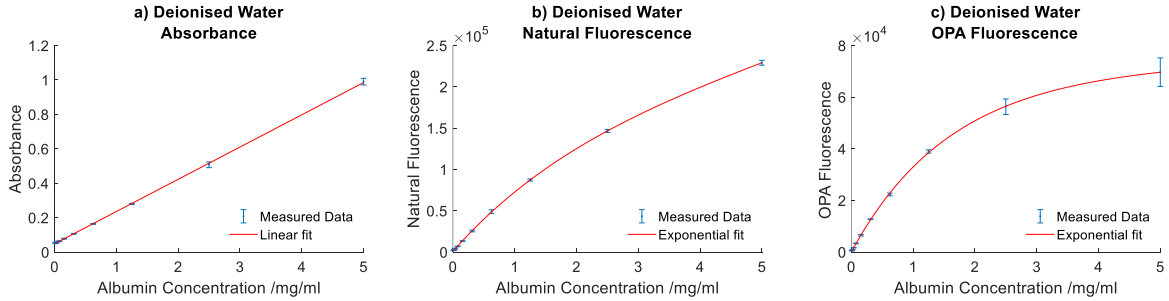

Figure 4.17: Calibration curves for albumin in deionised water, a) absorbance, b) natural fluorescence, c) fluorescence with OPA. Error bars are one standard deviation, n=3

of the albumin on the coupons, although the only time point statistically different from others was the one prior to washing as in the 60 minute interval series. This series started with coupons with a higher fluorescence of 20200 $\pm$ 4240, after 10 minutes this was 16300 $\pm$ 3320. The lowest fluorescence after 50 minutes was 12900 $\pm$ 2360, this was a larger but similar fluorescence change to than that seen in the 60 minute interval series. The albumin concentration in solution during the first interval was less than half of that in the 60 minute series at 0.0207 $\pm$ 0.0082 mgml^{-1}, while the further intervals had concentrations below 0.01 mgml^{-1}, mirroring the 60 minute interval series. The largest concentration of these was at 10-20 minutes, with a concentration of 0.0065 $\pm$ 0.0048 mgml^{-1}.

The fluorescence of the albumin on the coupons in neither series reaches the range of coupons without albumin ($\sim$ 5000).

4.3.5 Investigating the Release of Albumin under Physiological Conditions

Coupon scans were taken of the samples before and after the release period (figure 4.18). Prior to release the coupons with adsorbed albumin which were not washed had the highest fluorescence of 19400 $\pm$ 2310, whereas the coupons with covalently attached albumin had the lowest at 12000 $\pm$ 1670. After 128 days the fluorescence on the coupons with adsorbed albumin without a wash had dropped by 30% to 13300 $\pm$ 1150. While the values for the coupons with covalently attached albumin and adsorbed albumin with

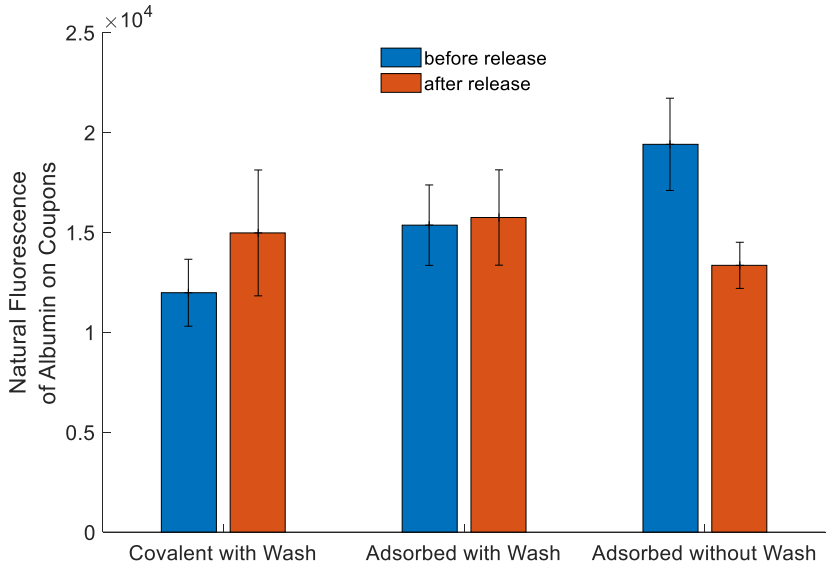

Figure 4.18: Fluorescence of coupons with albumin attached covalently and adsorbed, before and after release in PBS for 128 days. Error bars are one standard deviation, n=3

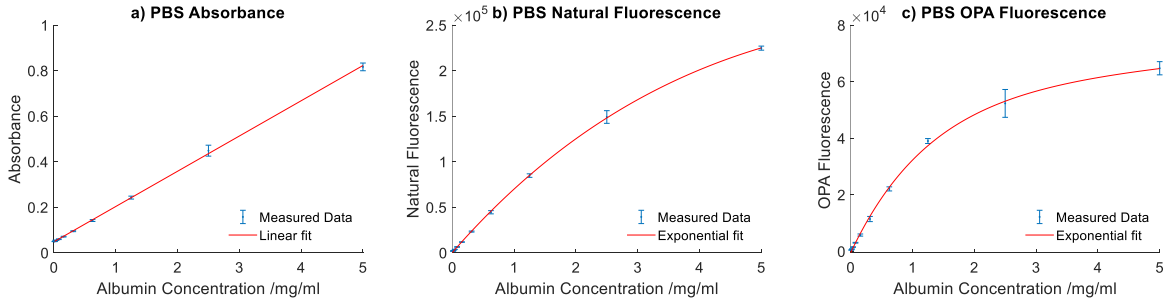

Figure 4.19: Calibration curves for albumin in PBS, a) absorbance, b) natural fluorescence, c) fluorescence with OPA. Error bars are one standard deviation, n=3

a wash step were not statistically different from their respective values prior to release.

The absorbance, natural fluorescence, and fluorescence of the solution with the fluorogen OPA were also measured at 16 and 128 days (table 4.1), and converted to concentrations using calibration curves of albumin in PBS (figure 4.19). The highest recorded concentration was for the solution from the coupons with covalently attached albumin at 128 days, with a concentration of 0.710 ± 0.741. For all three albumin attachment methods, absorbance readings gave higher concentration estimates at 128 days than 16 days. However for fluorescence readings, the concentration estimates were lower at 128 days than 16 days for all except covalent measured by natural fluorescence. These values

Table 4.1: Calculated concentrations of albumin in solution (in $mgml^{-1}$) from simulated physiological release by absorbance, natural fluorescence and fluorogenic release approaches

Measurement Method	Time / days	Calculated Concentration of Albumin / $mgml^{-1}$ Covalent with Wash	Adsorbed with Wash	Adsorbed without Wash
Absorbance	16	0.414 ± 0.313	0.111 ± 0.055	0.137 ± 0.028
	128	0.710 ± 0.741	0.168 ± 0.004	0.199 ± 0.037
Natural Fluorescence	16	0.039 ± 0.040	0.020 ± 0.006	0.037 ± 0.004
	128	0.064 ± 0.046	0.015 ± 0.005	0.030 ± 0.002
OPA Fluorescence	16	0.047 ± 0.046	0.024 ± 0.003	0.038 ± 0.004
	128	0.023 ± 0.006	0.021 ± 0.000	0.021 ± 0.000

were also only 10% of those estimated by absorbance for covalent coupons, and between 10 and 30% for adsorbed coupons.

4.4 Discussion

Characterisation of Coupons

SEM micrographs of the coupon surfaces show the large faces, which were vertical during building, have a higher roughness with increased particle adhesion compared to the top and bottom faces which were horizontal during building. This increased roughness and particle adhesion is likely to be caused by powder next to the part adhering to the part while it is still hot after lasing [182]. In contrast there is minimal powder adhered to the top surface as the coupons were the tallest samples built on the build plate, so no additional powder layer was placed on top of the parts. Additionally the thermal energy from the last lasing will be able to dissipate into the previous layers reducing the likelihood of energy radiating into the surrounding powder melting it (figure 2.23e).

The bottom view is not an as manufactured surface, but instead where the coupon was removed from the build plate by EDM. This allows the effects of EDM on the surface to be seen. Evidence of pitting and cracking can be seen, but these features are at a smaller

size scale than the adhered particles seen on the vertical faces. EDM is a non contact machining process that uses an electrical field to locally heat the part sufficiently to cause evaporation and therefore cut the part. This is done in a pulsed way creating a crater at each pulse [420, 421]. Although most of the molten and evaporated material is removed by dielectric fluid some is recast onto the surface where it is prone to cracks [422]. This results in the pitting and cracked surface displayed.

The rough surface seen on the vertical faces has some advantages in that it provides mechanical stability for the PCL layer on top. This is not the case for the smoother top and bottom surfaces where evidence of PCL peeling off was seen. Additionally surface roughness enables cell attachment, which can be beneficial in the form of human cells such as proteoblasts, or detrimental due to the attachment of bacteria [113].

Characterisation of PCL Attachment

Various parameters can be used to control polymer thickness during the dip coating process, including the number of dips, the concentration of polymer in the solvent, and the withdrawal speed [423]. In this study the desire was for a coat with an even thickness, beyond the protrusions from the surface roughness of the Ti-6Al-4V coupon, with the purpose of reducing the risk of bacterial attachment. Although it is common to dip coat with just a single layer of polymer [424, 425], multiple coating layers have been used to create a thicker polymer layer [423, 426, 427, 428].

Yusoff et al found that the thickness of a PCL/hydroxyapatite coating increased with the number of dips in a parabolic way [423], which was not seen here. This could be to do with the different coating material, or the trend could have been obscured in this work by the large measurement variability. Additionally the two studies had substrates with very different surface roughness. The surface of the Ti-6Al-4V substrate that Yusoff et coated the PCL/hydroxyapatite composite coating onto in their study was not additively manufactured. Although the roughness was not reported there are no visible signs of particle adhesion and the roughness was less than 10 μm in the figure. In contrast in this

work the particles are in the 100 μm size range. Thus in the study performed by Yusoff et al the coatings layers were predominantly only attaching to previous layers which could lead to a reduction in coating attachment with subsequent layers, while in this study there was a combination of PCL and Ti-6Al-4V to attach to for a large number of the layers, which could explain the more linear trend in mass with number of dips. In both cases the coating mass increased with the number of dips.

Increasing the PCL concentration led to increased mass of PCL on the coupons but also greater variability in mass. Increase in mass deposited with PCL concentration has previously been reported and attributed to increased viscosity of the suspension [423, 429]. This variability in mass was previously seen by Peñas et al when the concentration was too high [430]. The increased viscosity led to high concentrations of polymer in certain regions of the coupon, which can also be seen in the photographs of the coupons used in this study (figure 4.6).

By cutting the coupons the polymer thickness can be compared against the desired outcome of polymer extending beyond the Ti-6Al-4V protrusions, which was achieved for the 0.04 and 0.06 gml^{-1} samples. An additional observation is that an indication of the mechanical adhesion of the PCL to the coupon can also be inferred from the blade exit images. As the blade exits the coupon, the PCL is partially melted due to the heat of the blade, resulting in partial adhesion of the PCL onto the blade, combined with friction between the PCL and the blade. So as the blade exits it exerts some force on the PCL, pulling it away from the coupon. For the 0.02 gml^{-1} coupon the mechanical adhesion of the PCL to the coupon is less than the force pulling it away so the PCL is not visible in figure 4.5d. While for 0.04 and 0.06 gml^{-1} the PCL is visible but with some gaps between the PCL and the coupon, which appears larger for the 0.06 gml^{-1} coupon. The PCL is thicker in this region of the 0.06 gml^{-1} coupon than the region of the 0.04 gml^{-1} coupon so the contact area with the blade would be larger, enabling the blade to exert a greater force on the PCL which could explain the larger gap seen here. These images also show the variability in the 0.06 gml^{-1} coupons discussed above between figure 4.5g and 4.5h.

Albumin Attachment

PCL is hydrophobic and albumin is hydrophilic and thus they display different solubility profiles. Their respective solvents are either not miscible or negligibly miscible, such that they cannot be simultaneously dip coated onto the coupons and an alternative method for attaching the albumin was required. Amide bond coupling using EDC/NHS has previously been used to attach proteins to polymers and is a favourable conjugation method due to its diversity [263, 266, 329]. Thus it was used as the coupling method here, while immersion in albumin without surface functionalisation was used as a control. In this work basic hydrolysis using sodium hydroxide was used to create carboxylic acid groups on the PCL, while in other works ion irradiation has been used instead [266, 431]. Both methods are comparable in outcome but hydrolysis requires less equipment.

Fluorescence scans of the coupons showed higher fluorescence values on coupons with albumin than without as expected. Variations in fluorescence values were also seen across the coupons indicating an uneven albumin coating, this was previously seen by Choi et al for SYBR Green I labelled T4 bacteriophage EDC/NHS coupled to PCL [329]. Albumin is a protein with 385 amino acid residues [432], only two of which are tryptophan [433] which provides the fluorescence signal [434] for albumin. This may cause variation in signal even if an even coating was present, although this is unlikely due to the nanometer scale size of albumin compared to the millimeter scale distance between measurement points on the coupons.

Covalent attachment of albumin gave the highest fluorescence values of this experiment while adsorbed albumin had a lower fluorescence reading, but higher than without albumin. This was again in agreement with results seen by Choi et al [329]. Additionally the adsorbed samples which underwent a ten minute wash step had a significantly lower fluorescence reading, suggesting only weak interactions between the albumin and the PCL were present, such as hydrogen bonding or van der waals forces. Choi et al found a 45 minute sonication step reduced antibacterial activity of T4 bacteriophages. They attributed this to detachment of the T4 phages due to the initial binding only being

weak van der Waals interactions [329].

Quantifying Albumin on Coupons

Acid and base hydrolysis were investigated as methods to cleave albumin from the coupons, in order to quantify the albumin previously on the coupons by measuring it in solution. The natural fluorescence of the albumin on the coupons was measured prior to immersion, the fluorescence values were higher for the adsorbed albumin than the covalent albumin (figure 4.13), in contrast to the coupons used to check the albumin attachment (figure 4.9). This difference may be explained by differences in the experimental protocol between the experiments, specifically the covalent samples were not soaked in the earlier experiment while they were soaked in deionised water for 60 minutes in the latter experiment. The samples that were soaked had lower fluorescence values than those that were not, indicating that there is albumin present on the covalent samples which is not covalently attached, given it was removed by soaking in water. The adsorbed samples were washed in both experiments and had similar fluorescence values.

After 54 hours of immersion the fluorescence of the albumin on the coupons was measured again. The fluorescence of the coupons which had been in sodium hydroxide was not statistically different from coupons without albumin, this could be because all the albumin had been removed from the coupons. However it could also be because the albumin had denatured, resulting in quenching of the fluorescence signal [435, 436]. Albumin is known to conform (undergo structural changes) at pH values above 8.0, while above pH 10.0 it exists in its "A" aged conformational state [437, 438]. These denatured states have reduced emission intensity due to quenching of the tryptophan amino acid residues (which are responsible for the majority of the fluorescence signal [434, 435, 439]) by electron transfer from the ring or proton transfer to the ring. This results in the ring energy ending up at a ground state, so there is no return to ground state to release the energy that is the fluorescence [434].

The coupons which were in citrate buffer also exhibit a reduction in fluorescence values

after immersion, however the adsorbed coupons' fluorescence is above that of coupons without albumin, indicating some albumin remains on the coupons. This result could be due to some chemisorption of the albumin to the PCL which the citrate buffer is not able to overcome during this time frame and conditions. Alternatively this could be a stronger physisorption mechanism than those which were washed off in ten minutes in water during the soak step of the albumin attachment experiment (figure 4.9). One mechanism which has previously been shown to be stable over this time frame is hydrogen bonding between the carbonyl group of PCL and amine groups of albumin [440], this is one of the strongest forms of physisorption [441].

In addition to measuring the fluorescence changes on the coupons, the albumin in solution was also measured and calibration curves used to convert the measured values into albumin concentrations. Absorbance, intrinsic fluorescence and fluorogenic fluorescence with OPA were all used as measurement methods, and all gave different values for albumin concentration. Although this does not allow corroboration of the results it enables additional information about the samples to be explored.

The absorbance measurements gave the highest estimates of albumin concentration. The estimated value was highest for adsorbed sodium hydroxide samples at 0.351 ± 0.026 mgml^{-1} for 54 hours. This correlated with the coupon scans, where these samples had the greatest drop in fluorescence of around 12500. While covalent citrate buffer had the lowest concentration at 54 hours of 0.067 ± 0.019 mgml^{-1}, it also corresponds to the lowest drop in coupon fluorescence of approximately 3800. This gives weight to the theory that the coupon scan values after release are statistically similar to those of only PCL for sodium hydroxide due to full release of the albumin.

Despite sodium hydroxide giving the highest estimates for concentration using absorbance, the intrinsic fluorescence readings were so low that they could not be distinguished from solution without albumin. It can therefore be assumed that the sodium hydroxide is causing a denaturing of the albumin sufficient to cause complete quenching of the fluorescence emission as describe above. So despite the correlation between

absorbance estimates of concentration and the drops in fluorescence of albumin on the coupons, the lack of intrinsic fluorescence signal of albumin in sodium hydroxide solution gives weight to the theory that the low values of fluorescence on the coupons in sodium hydroxide is due to denaturing of the albumin rather than complete removal of albumin from the coupons.

Additionally the concentration estimates for citrate buffer coupons by natural fluorescence are lower than those from absorbance, this would indicate some quenching of the fluorescence signal. This result is in contrast to previous work which has found albumin at pH 5.18 to be in its "N" native form [437, 438]. An alternative explanation for these finding is the presence of PCL attached to the albumin molecules causing the quenching. PCL is known to undergo random hydrolytic ester scission (chain breakdown), which is accelerated by acidic pH [442]. This enables the release of the albumin molecule from the coupon but with a section of PCL chain attached. This PCL chain may cause the quenching effect seen here. The covalent coupons were washed so the assumption is that all the albumin molecules are covalently attached to the PCL, while the adsorbed coupons were not washed so a mixture of physisorbed and chemisorbed albumin molecules may be present. Some albumin molecules may be in solution without PCL attached and some with, leading to some quenching but less than in the covalent coupons. This could explain the larger differences between concentration estimates of adsorbed and covalent by natural fluorescence measurements compared to absorbance measurements where they are quite similar.

For the absorbance estimates of albumin concentration there was a positive correlation between time and concentration, however this was not the case for the intrinsic and fluorogenic fluorescence measurements where the concentrations of adsorbed citrate buffer rose to a maximum at 26.5 hours and then fell. Whereas for covalent citrate buffer there was no clear trend in concentration with time. These relationships may be partly explained by aggregation of albumin molecules over time [443, 444]. This aggregation is unlikely to change the primary structure of the albumin molecules so the absorbance

readings would be unaffected, but the close proximity of albumin molecules will increase the probability of proton or electron transfer to and from the ring in tryptophan (which causes the fluorescence emission), resulting in this signal being quenched for the natural fluorescence measurement [380, 445]. This dense cluster of albumin molecules will also restrict the ability of OPA molecules to reach the amine groups of the albumin in order to covalently bond enabling fluorescence. So over time as the albumin aggregates the intrinsic fluorescence and fluorogenic fluorescence decrease while the absorbance is not affected by aggregation.

Estimated albumin concentrations from fluorescence with OPA for citrate buffer show similar trends to with intrinsic fluorescence. While for sodium hydroxide non zero concentrations for adsorbed albumin are found at 26.5 and 54 hours where as none are present under natural fluorescence. This suggests that although the albumin is sufficiently denatured to result in complete quenching, some amine groups are still available for OPA attachment.

Unfortunately although estimates of albumin in solution can be made from this experiment they cannot be used to calibrate the albumin on the coupons as it is unknown whether all the albumin was successfully removed from the coupons during the experiment. Although it appears all the albumin has been removed based on the fluorescence scans of the coupons after sodium hydroxide immersion, the fluorescence of the albumin in sodium hydroxide solution indicates that quenching of the albumin fluorescence is occurring at this pH.

Buffers

Phosphate buffered saline (PBS), 2-(N-morpholino)ethanesulfonic acid buffer (MES) and sodium phosphate buffer (Na-PB) were investigated as buffers for the EDC/NHS coupling reaction and albumin attachment process. Activation with EDC is most efficient between pH 4.5 and 7.2, because below this pH hydrolysis occurs, and if the pH become too high it is no longer electrophilic so it does not react [446]. Thus MES with a pH of between 5 and

6.5 have previously been used for the EDC/NHS step [329, 447], it was used here at pH 5.5 and compared with PBS buffer at pH 7.4. However the reaction of the amine reactive NHS ester with proteins is most efficient in the pH range of 7 to 9 [448]. Sometimes a subisoelectric pH is used instead [449], causing the protein to become positively charged. The isoelectric point for egg albumin is pH 4.5 [414], so sodium phosphate buffer with a pH of 4 was compared with PBS (pH 7.4) for the albumin attachment step.

Despite using combinations of pH values which included values outside of the optimal pH ranges no statistical difference was seen between the fluorescence values of the coupons manufactured by the different methods. This suggests that the activation and attachment steps can be performed at different pHs due to the contrasting benefits of these pHs.

Hydrolysis Time

Sodium hydroxide was used for alkali hydrolysis of the PCL to create carboxylic acid groups for cross linking. Different time frames for hydrolysis were compared to find an optimum, with 60 minutes giving the highest fluorescence value. Sun and Onneby undertook similar experiments and found a curve fitted to their data gave an optimum value at 40 minutes although they did not take a reading at that time point [263]. Shorter time points result in fewer carboxyl groups and consequently less albumin attachment and fluorescence signal [329]. While longer hydrolysis time leads to a loss of PCL due to break down of the polymer chain by random chain scission of the ester groups [450].

Varying Time in EDC and NHS

The highest fluorescence reading came from coupons which had been in EDC and NHS for 30 minutes suggesting that this was sufficient time for all the caboxyl groups to form NHS-esters prior to albumin attachment. For the longer time frames the fluorescence was lower than at 30 minutes, suggesting less albumin was attached. This reduction in protein fluorescence with increased EDC/NHS time has previously been seen and attributed to the half life of the NHS ester, which is in the order of an hour at this pH [451].

A by product of EDC coupling with carboxyl groups is isourea which contains amine groups. Given NHS-ester reacts with amine groups on proteins it is likely to react with amine groups on isourea, so the longer the functionalised PCL is in solution with isourea the greater chance of the NHS-esters being unavailable for albumin attachment in the next step [446]. Additionally, the NHS ester can hydrolyse resulting in regeneration of the carboxyl groups so EDC/NHS coupling to albumin can no longer occur [451, 452].

Varying Time in Albumin

There was a positive correlation between time in albumin and fluorescence of the albumin on the coupons. This result was in agreement with previous literature which found protein surface reaction occurred rapidly in the first hour before slowing but continuing to increase up to the 48 hours investigated [328]. This initial phase was attributed to covalent attachment while subsequent attachment was ascribed to physisorption. This explanation may not be sufficient to describe the work here as the citrate buffer wash step was likely to have removed physisorbed albumin. Another study found protein attachment plateaued with time when physisorbed protein was removed [261], suggesting that the peak reached in albumin fluorescence overnight is just from covalently attached albumin.

Varying Time in EDC, NHS and Albumin Together

Rather than the two step coupling process previously explored here, a one step process can also be used where the protein is in the same solution as the EDC and NHS. This method is often avoided for proteins with carboxylic acid groups and amine groups as protein cross linking can occur between these groups due to EDC/NHS activation of the carboxyl groups on the proteins [453]. However this crosslinking can be advantageous as it enables more protein to attach as it is not limited by the carboxylic acid groups originally created on the PCL. The two step process has the advantage that different buffers can be used for the EDC/NHS step and the protein attachment step in order for each to be

at their optimum pH [454]. Additionally, in the one step process proteins can directly bond to the carboxylic acid groups of the hydrolysed PCL by forming hydrogen bonds, however these are not as strong as covalent bonds and so may not enable the long term attachment desired in this work [455].

By comparing the fluorescence value of the coupons in the one step process with those from the albumin time study and the EDC/NHS time study a comparison can be made between the one step and two step process. At 30 minutes the one step fluorescence was 7790 $\pm$ 1690, which is higher but not statistically different from the 30 minute albumin fluorescence at 6680 $\pm$ 1670. The one step fluorescence at 60 minutes of 13900 $\pm$ 3910 was higher than both the 60 minute albumin fluorescence of 7650 $\pm$ 1490 and the 60 minute EDC/NHS fluorescence of 9760 $\pm$ 1160. At 120 minutes the trend continued with fluorescence for the one step process at 12600 $\pm$ 1650, higher than 8290 $\pm$ 1260 for albumin and 9590 $\pm$ 788 for EDC/NHS time. The highest fluorescence value for the one step process of 13900 $\pm$ 3910 is higher than the highest fluorescence using the two step process (and the same citrate buffer wash conditions) of 12000 $\pm$ 1680, which was in albumin overnight. This suggests that crosslinking between albumin molecules is occurring, enabling a higher quantity of albumin to attach to the PCL.

Wash Time

In order to establish whether washing in water is sufficient to remove all the adsorbed albumin and the time frame required, coupons with adsorbed albumin were placed in deionised water. Adsorbed rather than covalently attached albumin was chosen for this experiment because the fluorescence of the coupon without albumin is known, whereas the fluorescence of only covalent albumin is unknown so it would not be possible to tell when the baseline had been reached. Absorbance measurements of albumin in solution were used to calculate the concentration in solution due to the challenges with fluorescence measurements of albumin discussed above.

Ten and 60 minute time intervals were investigated with similar drops in fluorescence

on the coupon scans seen after 60 minutes in both cases despite the repetitive drying of the coupons in the 10 minute interval case. However neither study resulted in coupon scan values similar to coupons without albumin, indicating some albumin remained on the coupons even after the curves plateaued. Physisorption has previously been shown to enable attachment of albumin onto PCL with minimal loss of protein after two days in PBS, suggesting that even if only physisorption is holding the albumin onto the PCL washing in water may be insufficient to remove all the adsorbed albumin [456]. So although this method cannot fully remove the adsorbed albumin it is likely to have removed the loosely attached albumin that would give a burst release if placed in the body.

The absorbance of the albumin in solution was used to determine the concentration of albumin in solution, for both the 10 and 60 minute intervals the concentration value peaked for the first time interval and then fell below 0.01 mgml^{-1} for all other time intervals. This was in contrast to the coupon fluorescence where the 60 minute interval experiment saw a step change between the initial fluorescence drop at 60 minutes and then no further changes, while the 10 minute intervals had a incremental drop in fluorescence with time. The albumin concentration in solution was 0.0453 ± 0.0009 mgml^{-1} for the first 60 minute interval, while it was only 0.0207 ± 0.0082 mgml^{-1} for the first 10 minute interval. After these initial time points the absorbance values are close to the values for water so further information about the trend of albumin in solution cannot be established.

Although all the albumin was not removed from the coupons, a comparison between the fluorescence scans before and after washing combined with the solution measurements could be used to calibrate the coupon scan fluorescence values. However the solution concentration for all time intervals except the first was not statistically higher than that of water, such that only the first time interval could be used for the calibration. This means that new coupons would have to be generated for each data point on the calibration curve, producing coupons with different albumin amounts on each for this method would be a challenge.

Release Study

Coupons with covalent and adsorbed albumin were placed in PBS buffer for 128 days to investigate whether the albumin was released. Prior to release, the fluorescence of the albumin on the coupons were measured, with non washed adsorbed coupons having the highest fluorescence in line with results seen before (figure 4.12). While washed covalent and washed adsorbed were not statistically different, suggesting similar albumin loading from the two methods. After release the coupons were scanned again and there was a statistically significant drop in fluorescence value for the non washed adsorbed samples. This follows from the wash time study where it was seen that non washed albumin released some albumin over a short time frame (60 minutes). The washed samples did not change significantly. These mean value increases after release are probably due to variation of albumin coating on the coupons as seen previously (figure 4.7b). When combined with the inconsistent placement of coupons within the well plate, which causes different points on the coupons to be scanned, would lead to the changes in values seen.

The albumin levels were also measured in solution, where the covalent samples had the highest mean concentration. However the standard deviation was in the same range due to outliers so these values must be discounted. When the adsorbed samples are compared, the washed and unwashed values have the same order of magnitude despite the differences seen in the coupon scans. There are also differences between the absorbance and fluorescence estimates for concentration as previously seen in the experiments to quantify the albumin on the coupons. The concentration estimates by absorbance increase with time, while the fluorescence measurements decrease suggesting some changes to the albumin with time. Previous works have shown that heat and shear forces in solution generally lead to denaturation [457]. Denaturation could lead to quenching, which would explain the drop with time for natural fluorescence but not fluorogenic fluorescence. However it has also been shown that heat can lead to aggregation [443, 444], which can cause quenching [380, 445], and could also reduce the ability of OPA molecules to covalently bond to amine groups on the albumin.

Despite the appearance of albumin in solution the levels on the coupons remain high even after 128 days, which raises the possibility of using EDC/NHS coupling as a method to attach proteins and therapeutics to the surface of lattices to promote bone adhesion or prevent infection in the future.

4.5 Conclusions

The aim of this research was to develop a method to attach therapeutics to the surface of lattices to promote bone adhesion or prevent infection. It was shown that albumin (used as a model molecule) could be covalently attached to PCL coated on a Ti-6Al-4V coupon, and continued to intrinsically fluoresce after four months in phosphate buffered saline at 37°C.

When the coupons were characterised by SEM it was found that the faces which were vertical during building had a higher roughness than the top and bottom faces due to the printing process in agreement with the literature. The bottom surface where the coupons were removed from the build plate by EDM exhibited pitting and cracking due to the EDM process.

The coupons were dip coated in PCL ten times with the mass measured after each dip. It was found that the mass increased with the number of dips without reaching a plateau. Three different concentrations of PCL in chloroform were compared with 0.06 gml^{-1} having a high viscocity which led to an uneven coating seen on both the photographs of the coupons and microscope images of the cut coupons. In contrast the dip coating with 0.02 gml^{-1} PCL resulted in a PCL layer that did not extend beyond the protruding particles and rough surface of the coupon which could lead to bacterial colonisation. So the 0.04 gml^{-1} concentration was chosen for the dip coating as it was sufficient to encase the coupons while providing a more even coating than the 0.06 gml^{-1} solution.

Fluorescence scans were used to quantify the albumin on the coupons. It was found than PCL gave a weak fluorescence reading while albumin gave a larger reading. However

in neither case was the reading uniform across the coupon, although the coupons with albumin on had a larger spread of fluorescence values than those with just PCL.

When covalent and adsorption methods of attaching albumin to PCL were compared it was found that there was no statistical difference between the fluorescence readings of the two methods. However, when the coupon with adsorbed albumin was soaked in water for ten minutes the fluorescence reading decreased such that it was not statistically different from a coupon which had not had albumin attached. This means the albumin was not immobilised and therefore does not meet the aim of this work.

In order to quantify the amount of albumin on the coupons and calibrate the fluoresce reading the albumin was placed into sodium hydroxide or citrate buffer in an attempt to force the albumin off the coupons by hydrolysis. The citrate buffer was unable to remove all the albumin from the coupons, while the sodium hydroxide quenched the fluorescence signal so neither could be used to calibrate the fluorescence values of the coupons. However, the coupon fluorescence scans can still be used to compare the different coupons produced during the optimisation process as there is a positive correlation between the fluorescence values and the mass of albumin on the coupons.

The first part of the amide bond coupling process which was investigated was the use of reaction buffers. It was found that there was no statistical difference between the natural fluorescence of samples when EDC and NHS were in PBS at pH 7.4 or MES at pH 5.5, nor when albumin was in PBS (pH 7.4) or sodium phosphate buffer at pH 4.

Optimisation of the amide bond coupling process found a hydrolysis time of 60 minutes, 30 minutes in EDC and NHS, and leaving the samples overnight in albumin led to the highest natural fluorescence of albumin on the coupons from the two step attachment process. While the one step attachment process with the coupons in EDC, NHS and albumin for 60 minutes gave the highest fluorescence overall. Soaking the coupons in water for 60 minutes removed some of the adsorbed albumin, increasing the time beyond this did not result in additional release.

The immobilisation of the albumin was tested by leaving coupons in PBS for 128 days

at 37°C. It was found that there was no statistical difference in the fluorescence values of the coupons with covalently attached albumin before and after the release study suggesting that amide bond coupling would be an appropriate method to attach therapeutics to the implant surfaces to prevent infection or promote bone growth.

CHAPTER 5

OVERALL CONCLUSIONS AND FUTURE WORK

5.1 Compression Testing of Lattices

The aim of this research was to identify lattice designs that were stronger than bone and with sufficient void volume for a secondary drug eluting phase to be incorporated. This was to enable their use in hip implants to treat infection where the lattice would provide weight bearing support while the secondary phase would clear the infection. It was found that four lattice designs had strength of at least 200 MPa and volume fractions below 0.6, so met this aim. These were BCC 350, BCCZ 350, Diamond 350 and Fluorite 250. Additionally two lattice designs were found that were strong enough to support weight bearing and with a stiffness in the range of cortical bone that could be used to reduce stress shielding but the volume fractions were too high to be used for bulk drug delivery, these were Fluorite 350 and Gyroid 250.

Continued exploration of the fundamentals of lattice failure will enable optimal lattice designs to be created in the future. For example by comparing the effects of unit cell size with a fixed porosity rather than fixed strut thickness. As well as using alternative methods to determine the strut thickness or profile, for example using CT scans or setting the lattices in resin and then bisecting struts. SEM micrographs could also be taken at different angles to further understand the strut profiles.

The lattice rotations explored here showed the need for build and loading orientations

to be considered separately. More configurations could be explored, for example rotating lattices through different planes including those which incorporate struts. Build and load orientations could be combined but in an additive way rather than in opposing ways as performed here. It was shown that lattices could be built with struts at any angles, so additional build and load angles could be explored. Finite element analysis to further understand the failure modes of lattices loaded in different orientations would further the understanding of the lattice mechanical properties.

Further types of mechanical testing such as tension, bending and fatigue testing are necessary to validate lattices for implant applications. These tests need to include whole implants, not just cylindrical samples. Strain energy density analysis would enable further understanding of the failure mechanisms. Post processing, including the use of heat treatment for stress relief, surface treatment to reduce the roughness and semi sintered particles, and cleaning and sterilisation prior to implantation should all remain areas of research in order to create the implants of the future.

5.2 Bulk Loading of Lattices

It was shown in chapter 3 that lattice geometry could be used to control the release of gentamicin sulphate from brushite cement. Gentamicin sulphate was released in accordance with the Korsmeyer-Peppas model. Although geometry could be used to influence the release this did not lead to predictable inhibition of *Staphylococcus aureus* and *Pseudomonas aeruginosa*. This work shows the importance of implant geometry on release kinetics, but more worked is needed to understand how this influences the *in vivo* environment.

The samples used in this chapter were cylinders 20 mm in height and 20 mm in diameter and were filled with cement by casting. However if this technology is going to be scaled up to entire implants then injection may offer a better method of filling. Phase separation is a challenge with the current formulation and alternative formulations doped with magnesium or silicon would need to be explored. The release profile followed the

Korsmeyer-Peppas model rather than fickian diffusion. This is possibly due to apatite formation. X-ray diffraction techniques could be used to establish whether this was the case. Doping with pyrophosphate could be explored to reduce apatite formation. The presence of gentamicin sulphate during the setting reaction is thought to influence the crystal structure, so loading with the therapeutic after the cement has set could be explored. Given that brushite cement setting is not as exothermic as PMMA cement setting alternative antibiotics or antimicrobial materials such as silver could be explored as alternatives to gentamicin sulphate.

An alternative biomaterial with preferential loading, release and degradation properties could be explored. For example, a polymer which releases the drug by erosion, or a hydrogel with the antibiotic encapsulated to enable a triggered release. The use of graded lattice structures would enable the exposed surface area and volume of the cement to be altered independently. It would also provide a greater understanding of the interaction between the cement and the lattice under mechanical loading. In this work only an agar diffusion assay was used to determine the antibacterial properties of the samples. In future three dimensional techniques such as broth culture could provide greater understanding of the antibacterial properties of the lattices. It is also important to undertake cytotoxicity testing, and check the antibacterial and cytotoxicity results in *in vivo* models.

5.3 Surface Loading of Implants

Chapter 4 demonstrated a way to immobilise therapeutics onto the surface of implants. This process was optimised to give the highest fluorescence reading of the albumin on the coupons. However this was not calibrated, so could not be correlated with the quantity of albumin on the coupons. Alternative methods of detecting albumin on the coupons could be considered, as well other methods for calibrating the current method. The optimisation could only find the optimal values within the ranges investigated so alternative ranges should be considered, especially where the maximum was found at the end of the range.

In this work the EDC/NHS activation time of 30 minutes was the shortest evaluated, and the albumin attachment was highest at the longest time. Where a peak was found a narrower range could be used to get a more precise value.

The surface roughness of the coupons influenced the PCL attachment, so the roughness should be measured and potentially manipulated by considering the effects of implant location and angle in the build chamber. The polymer thickness should also be measured to establish whether it will be consistently thicker than the depth of the protrusions from the implant surface to reduce the risk of bacterial adhesion following implantation.

Cells have poor attachment to hydrophobic surfaces such as polymers but surface functionalisation changes the hydrophobicity so this could be analysed using contact angle measurements. Hydrolysis of the PCL film creates carboxyl groups which can be quantified with a radio-assay. Doing this before and after the albumin attachment step would provide an estimate of potential albumin sites and then how many of them have been used.

Steps to move towards translation include switching the coupons for lattices, switching the albumin for appropriate proteins or therapeutics, before using growth or bacteria studies to understand how the attachment of these actives would influence cell signalling. Finally these devices would need to be tested in animal models. If the orientations of the proteins is not ideal for cell signalling then alternative coupling techniques would need to be considered. Alternatively, attachment with cleavable linkages could be used so that the actives would be released into the surrounding tissues.

5.4 Overall Conclusions

The exploitation of additively manufactured lattices to control drug release shows promise as a way to improve metal bone implants.

First, the mechanical properties of some additively manufactured lattices were compared. It was found that four lattice designs provided sufficient compressive strength

to support weight bearing while having a sufficient void volume for drug loading. Lattice designs were found to have different failure mechanisms, and respond differently to changes in building and loading angle, as well as changes in lattice geometry such as strut thickness and unit cell size.

Second, brushite cement was loaded into lattices to understand whether varying geometry could be used to control the release of gentamicin sulphate. The release of gentamicin sulphate fitted the Korsmeyer-Peppas model with R^2 values of at least 0.98. Varying the lattice volume fractions altered both the release of the antibiotic and the size of the inhibition zones of *Staphylococcus aureus*. The compressive strength of the cement lattice composites was sufficient to enable their use in bone implants.

Finally, amide bond coupling was used to attach albumin to PCL as a model for the attachment of therapeutics on implant surfaces. The process was optimised, to find the reaction conditions which led to the maximum immobilisation of albumin. Albumin continued to intrinsically fluoresce on the surface after immersion for four months in phosphate buffered saline at 37°C.

This work contributes to the understanding of the use of additive manufacturing to improve bone implants through the use of lattices for improved mechanical performance and drug delivery.

BIBLIOGRAPHY

[1] Rahul Davis et al. "A comprehensive review on metallic implant biomaterials and their subtractive manufacturing". In: *International Journal of Advanced Manufacturing Technology* 120 (3-4 2022), pp. 1473–1530. ISSN: 14333015. DOI: 10.1007/s00170-022-08770-8.

[2] *2019 National Joint Registry 16th Annual Report*. 2019.

[3] Ben Wilcox et al. "Systematic review of 3D printing in spinal surgery: the current state of play." In: *Journal of spine surgery (Hong Kong)* 3 (3 2017), pp. 433–443. ISSN: 2414-469X. DOI: 10.21037/jss.2017.09.01.

[4] Paulo Bartolo et al. "Biomedical production of implants by additive electro-chemical and physical processes". In: *CIRP Annals - Manufacturing Technology* 61 (2 2012), pp. 635–655. ISSN: 00078506. DOI: 10.1016/j.cirp.2012.05.005.

[5] E Langford and C A Griffiths. "The mechanical strength of additive manufactured intraosseous transcutaneous amputation prosthesis, known as the ITAP". In: *AIMS Bioengineering* 5 (3 2012), pp. 133–150. DOI: 10.3934/bioeng.2018.3.133.

[6] JPM Frölke, RA Leijendekkers, and H Van de Meent. "Osseointegrated prosthesis for patients with an amputation". In: *Unfallchirurg* 120 (2017), pp. 293–299. DOI: 10.1007/s00113-016-0302-1.

[7] Tinkara Mastnak, Uroš Maver, and Matjaž Finšgar. "Addressing the Needs of the Rapidly Aging Society through the Development of Multifunctional Bioactive Coatings for Orthopedic Applications". In: *International Journal of Molecular Sciences* 23 (5 2022), p. 2786. ISSN: 14220067. DOI: 10.3390/ijms23052786.

[8] T. Jennison and M. Brinsden. "Fracture admission trends in England over a ten-year period". In: *Annals of the Royal College of Surgeons of England* 101 (3 2019), pp. 208–214. ISSN: 00358843. DOI: 10.1308/rcsann.2019.0002.

[9] *National Joint Registry 19th Annual Report*. 2022.

[10] Kathryn R Fingar et al. "Most Frequent Operating Room Procedures Performed in U.S. Hospitals, 2003–2012: Statistical Brief 186". In: *Healthcare Cost and Utilization Project (HCUP) Statistical Briefs* (2015), pp. 1–15.

[11] T. E.F. Abbott et al. “Frequency of surgical treatment and related hospital procedures in the UK: A national ecological study using hospital episode statistics”. In: *British Journal of Anaesthesia* 119 (2 2017), pp. 249–257. ISSN: 14716771. DOI: 10.1093/bja/aex137.

[12] Amirhossein Goharian and Mohamed R. Abdullah. “Bioinert Metals (Stainless Steel, Titanium, Cobalt Chromium)”. In: *Trauma Plating Systems: Biomechanical, Material, Biological, and Clinical Aspects*. Elsevier Inc., 2017. ISBN: 9780128047583. DOI: 10.1016/B978-0-12-804634-0.00007-0.

[13] Kristina Haase and Gholamreza Rouhi. “Prediction of stress shielding around an orthopedic screw: Using stress and strain energy density as mechanical stimuli”. In: *Computers in Biology and Medicine* 43 (2013), pp. 1748–1757. DOI: 10.1016/j.compbiomed.2013.07.032.

[14] Erica Liverani et al. “Mechanical interaction between additive-manufactured metal lattice structures and bone in compression: implications for stress shielding of orthopaedic implants”. In: *Journal of the Mechanical Behavior of Biomedical Materials* 121 (March 2021), p. 104608. ISSN: 18780180. DOI: 10.1016/j.jmbbm.2021.104608.

[15] Tiffany Kim et al. “Orthopedic implants and devices for bone fractures and defects: Past, present and perspective”. In: *Engineered Regeneration* 1 (April 2020), pp. 6–18. ISSN: 26661381. DOI: 10.1016/j.engreg.2020.05.003.

[16] Richard Van Noort. “The future of dental devices is digital”. In: *Dental Materials* 28 (1 2012), pp. 3–12. ISSN: 01095641. DOI: 10.1016/j.dental.2011.10.014.

[17] Amit Bandyopadhyay et al. “Influence of porosity on mechanical properties and in vivo response of Ti6Al4V implants”. In: *Acta Biomaterialia* 6 (2009), pp. 1640–1648. ISSN: 1742-7061. DOI: 10.1016/j.actbio.2009.11.011.

[18] Edward Ebramzadeh et al. “Failure Modes of 433 Metal-on-Metal Hip Implants: How, Why, and Wear”. In: *Orthopedic Clinics of NA* 42 (2011), pp. 241–250. DOI: 10.1016/j.ocl.2011.01.001.

[19] Sushil Kandel et al. “An automated system for polymer wear debris analysis in total disc arthroplasty using convolution neural network”. In: *Frontiers in Bioengineering and Biotechnology* 11 (June 2023), pp. 1–9. ISSN: 22964185. DOI: 10.3389/fbioe.2023.1108021.

[20] Public Health England. *Surveillance of surgical site infections in NHS hospitals in England: 2016 to 2017*. 2016.

[21] S. Klouche, E. Sariali, and P. Mamoudy. "Total hip arthroplasty revision due to infection: A cost analysis approach". In: *Orthopaedics Traumatology: Surgery Research* 96 (2 2010), pp. 124–132. ISSN: 1877-0568. DOI: 10.1016/J.OTSR.2009.11.004.

[22] B Jansen and G Peters. "Foreign body associated infection". In: *Journal of Antimicrobial Chemotherapy* 32.suppl_A (1993), pp. 69–75.

[23] Werner Zimmerli et al. "Pathogenesis of foreign body infection: Description and characteristics of an animal model". In: *Journal of Infectious Diseases* 146 (4 1982), pp. 487–497. ISSN: 15376613. DOI: 10.1093/infdis/146.4.487.

[24] Hamid Reza Seyyed Hosseinzadeh et al. "Arthroplasty". In: *Orthopedics, Physical Medicine and Rehabilitation, Edited by Plamen Kinov*. IntechOpen, 2013. Chap. The Acrylic Bone Cement in Arthroplasty, pp. 101–130. DOI: 10.5772/53252.

[25] Mukta Kulkarni et al. "Biomaterial surface modification of titanium and titanium alloys for medical applications". In: *Nanomedicine* (2014), pp. 111–136. DOI: 10.1016/j.jcms.2017.09.020.

[26] Martin B. Bezuidenhout et al. "Delivery of Antibiotics from Cementless Titanium-Alloy Cubes May Be a Novel Way to Control Postoperative Infections". In: *BioMed Research International* 2015 (2015), pp. 1–7. ISSN: 2314-6133. DOI: 10.1155/2015/856859.

[27] National Institutes of Health USA. "Total hip replacement". In: *NIH consensus statement* 12 (5 1994), pp. 1–31. ISSN: 10801707.

[28] Jeppe Lange et al. "Chronic infections in hip arthroplasties: comparing risk of reinfection following one-stage and two-stage revision: a systematic review and meta-analysis." In: *Clinical epidemiology* 4 (1 2012), pp. 57–73. ISSN: 1179-1349. DOI: 10.2147/CLEP.S29025.

[29] Christopher W Jones et al. "The Influence of Spacer Design on the Rate of Complications in Two-Stage Revision Hip Arthroplasty". In: *The Journal of Arthroplasty* 34.6 (2019), pp. 1201–1206. ISSN: 0883-5403. DOI: 10.1016/j.arth.2019.02.012.

[30] Carlo L Romanò et al. "Two-stage revision surgery with preformed spacers and cementless implants for septic hip arthritis: a prospective, non-randomized cohort study". In: *BMC Infectious Diseases* 11 (1 2011), p. 129. ISSN: 1471-2334. DOI: 10.1186/1471-2334-11-129.

[31] C. J. Della Valle H. J. Cooper. "The two-stage standard in revision total hip replacement". In: *The Bone & Joint Journal* 95-B (11 2013), pp. 84–87. DOI: 10.1302/0301-620X.95B11.32906.

[32] R S J Burnett, J C Clohisy, and R L Barrack. "Antibiotic Cement Spacers in Total Hip and Total Knee Arthroplasty: Problems, Pitfalls, and Avoiding Complications". In: *Infection and Local Treatment in Orthopedic Surgery* (2007), pp. 92–111. DOI: 10.1007/978-3-540-47999-4_12.

[33] Owen J. Diamond and Bassam A. Masri. "Articulating antibiotic impregnated spacers in prosthetic joint infections: Where do we stand?" In: *International Journal of Surgery* 54 (2018), pp. 345–350. ISSN: 17439159. DOI: 10.1016/j.ijsu.2017.07.044.

[34] Scott D. Boden. "Overview of the biology of lumbar spine fusion and principles for selecting a bone graft substitute". In: *Spine* 27 (16 SUPPL. 2002), pp. 26–31. ISSN: 03622436. DOI: 10.1097/00007632-200208151-00007.

[35] Suzanne L. De Kunder et al. "Lumbar interbody fusion". In: *Spine* 43 (16 2018), pp. 1161–1168. ISSN: 15281159. DOI: 10.1097/BRS.0000000000002534.

[36] Eric H. Ledet et al. "Direct real-time measurement of in vivo forces in the lumbar spine". In: *Spine Journal* 5 (1 2005), pp. 85–94. ISSN: 15299430. DOI: 10.1016/j.spinee.2004.06.017.

[37] Hans-Joachim Wilke et al. "New In Vivo Measurements of Pressures in the Intervertebral Disc in Daily Life". In: *Spine* 24 (8 1999), pp. 755–762.

[38] Marissa D'Souza et al. "Graft materials and biologics for spinal interbody fusion". In: *Biomedicines* 7 (4 2019), pp. 1–15. ISSN: 22279059. DOI: 10.3390/biomedicines7040075.

[39] Markus Laubach, Philipp Kobbe, and Dietmar W. Hutmacher. "Biodegradable interbody cages for lumbar spine fusion: Current concepts and future directions". In: *Biomaterials* 288 (August 2022), p. 121699. ISSN: 18785905. DOI: 10.1016/j.biomaterials.2022.121699.

[40] Michael H. McCarthy, Joseph A. Weiner, and Alpesh A. Patel. "Strategies to Achieve Spinal Fusion in Multilevel Anterior Cervical Spine Surgery: An Overview". In: *Hospital for Special Surgery Journal* 16 (2 2020), pp. 155–161. ISSN: 15563324. DOI: 10.1007/s11420-019-09738-3.

[41] Amir H. Fayazi et al. “Preliminary results of staged anterior debridement and reconstruction using titanium mesh cages in the treatment of thoracolumbar vertebral osteomyelitis”. In: *Spine Journal* 4 (4 2004), pp. 388–395. ISSN: 15299430. DOI: 10.1016/j.spinee.2004.01.004.

[42] Yigal Mirovsky et al. “Management of deep wound infection after posterior lumbar interbody fusion with cages”. In: *Journal of Spinal Disorders and Techniques* 20 (2 2007), pp. 127–131. ISSN: 15360652. DOI: 10.1097/01.bsd.0000211266.66615.e5.

[43] W G Stuart Mackenzie et al. “Surgical site infection following spinal instrumentation for scoliosis: a multicenter analysis of rates, risk factors, and pathogens”. In: *Journal of Bone and Joint Surgery, American Volume* 95 (9 2013), pp. 800–806. ISSN: 1535-1386. DOI: 10.2106/JBJS.L.00010.

[44] Richard F. Frisch et al. “Clinical and radiographic analysis of expandable versus static lateral lumbar interbody fusion devices with two-year follow-up”. In: *Journal of Spine Surgery* 4 (1 2018), pp. 62–71. ISSN: 2414469X. DOI: 10.21037/jss.2018.03.16.

[45] Kun Wang et al. “Titanium dioxide nanotubes as drug carriers for infection control and osteogenesis of bone implants”. In: *Drug Delivery and Translational Research* 11 (4 2021), pp. 1456–1474. ISSN: 21903948. DOI: 10.1007/s13346-021-00980-z.

[46] Gerhard Schmidmaier et al. “Prophylaxis and treatment of implant-related infections by antibiotic-coated implants: a review”. In: *Injury* 37 (2 SUPPL. 2006), S105–S112. ISSN: 00201383. DOI: 10.1016/j.injury.2006.04.016.

[47] Andrew Fang et al. “Risk factors for infection after spinal surgery”. In: *Spine* 30 (12 2005), pp. 1460–1465. ISSN: 03622436. DOI: 10.1097/01.brs.0000166532.58227.4f.

[48] Ana I. Hijas-Gómez et al. “Surgical Wound Infection Rates and Risk Factors in Spinal Fusion in a University Teaching Hospital in Madrid, Spain”. In: *Spine* 42 (10 2017), pp. 748–754. ISSN: 15281159. DOI: 10.1097/BRS.0000000000001916.

[49] Justin S. Smith et al. “Rates of infection after spine surgery based on 108,419 procedures: A report from the Scoliosis Research Society morbidity and mortality committee”. In: *Spine* 36 (7 2011), pp. 556–563. ISSN: 03622436. DOI: 10.1097/BRS.0b013e3181eadd41.

[50] Claire D Eliasberg et al. “Complications and Rates of Subsequent Lumbar Surgery Following Lumbar Total Disc Arthroplasty and Lumbar Fusion”. In: *Spine* 41.2 (2016), p. 173. DOI: 10.1097/BRS.0000000000001180.

[51] Hao Xu et al. “Early cranioplasty vs. late cranioplasty for the treatment of cranial defect: A systematic review”. In: *Clinical Neurology and Neurosurgery* 136 (2015), pp. 33–40. ISSN: 18726968. DOI: 10.1016/j.clineuro.2015.05.031.

[52] H. Wafa et al. “Retrospective evaluation of the incidence of early periprosthetic infection with silver-treated endoprostheses in high-risk patients: Case-control study”. In: *Bone and Joint Journal* 97-B (2 2015), pp. 252–257. ISSN: 20494408. DOI: 10.1302/0301-620X.97B2.34554.

[53] Jendrik Hardes et al. “Reduction of periprosthetic infection with silver-coated megaprostheses in patients with bone sarcoma”. In: *Journal of Surgical Oncology* 101 (5 2010), pp. 389–395. ISSN: 00224790. DOI: 10.1002/jso.21498.

[54] S Ridgeway et al. “Infection of the surgical site after arthroplasty of the hip.” In: *The Journal of Bone and Joint Surgery. British Volume* 87 (6 2005), pp. 844–50. ISSN: 0301-620X. DOI: 10.1302/0301-620X.87B6.15121.

[55] Carla Renata Arciola et al. “Etiology of implant orthopedic infections: A survey on 1027 clinical isolates”. In: *International Journal of Artificial Organs* 28 (11 2005), pp. 1091–1100. ISSN: 03913988. DOI: 10.1177/039139880502801106.

[56] Anna Stefánsdóttir et al. “Microbiology of the infected knee arthroplasty: Report from the Swedish Knee Arthroplasty Register on 426 surgically revised cases”. In: *Scandinavian Journal of Infectious Diseases* 41.11-12 (2009), pp. 831–840. ISSN: 0036-5548. DOI: 10.3109/00365540903186207.

[57] Jason A. Inzana et al. “Biomaterials approaches to treating implant-associated osteomyelitis”. In: *Biomaterials* 81 (2016), pp. 58–71. ISSN: 0142-9612. DOI: 10.1016/j.biomaterials.2015.12.012.

[58] Andrej Trampuz and Andreas F Widmer. “Infections associated with orthopedic implants”. In: *Current Opinion in Infectious Diseases* 19 (0951-7375 (Print) 2006), pp. 349–356. ISSN: 0951-7375. DOI: 10.1097/01.qco.0000235161.85925.e8.

[59] J. M. Schierholz and J. Beuth. “Implant infections: A haven for opportunistic bacteria”. In: *Journal of Hospital Infection* 49 (2 2001), pp. 87–93. ISSN: 01956701. DOI: 10.1053/jhin.2001.1052.

[60] Suganthan Veerachamy et al. “Bacterial adherence and biofilm formation on medical implants: A review”. In: *Proceedings of the Institution of Mechanical Engineers, Part H: Journal of Engineering in Medicine* 228 (10 2014), pp. 1083–1099. ISSN: 20413033. DOI: 10.1177/0954411914556137.

[61] John G. Bartlett. “Treatment of infections associated with surgical implants”. In: *Infectious Diseases in Clinical Practice* 12 (4 2004), pp. 258–259. ISSN: 15369943. DOI: 10.1097/01.idc.0000130890.12611.f3.

[62] Marta Ribeiro, Fernando J. Monteiro, and Maria P. Ferraz. “Infection of orthopedic implants with emphasis on bacterial adhesion process and techniques used in studying bacterial-material interactions.” In: *Biomatter* 2 (4 2012), pp. 176–194. ISSN: 21592535. DOI: 10.4161/biom.22905.

[63] M Katsikogianni and Y F Missirlis. “Mechanisms of Bacterial Adhesion To Biomaterials and of Techniques Used in Estimating Bacteria-Material Interactions”. In: *European Cells and Materials* 8 (2004), pp. 37–57. ISSN: 14732262.

[64] Elisa J.M. Raineri, Dania Altulea, and Jan Maarten Van Dijl. “Staphylococcal trafficking and infection - From ‘nose to gut’ and back”. In: *FEMS Microbiology Reviews* 46 (1 2022), pp. 1–22. ISSN: 15746976. DOI: 10.1093/femsre/fuab041.

[65] Niels Frimodt-Møller. “How predictive is PK/PD for antibacterial agents?” In: *International Journal of Antimicrobial Agents* 19 (4 2002), pp. 333–339. ISSN: 0924-8579. DOI: 10.1016/S0924-8579(02)00029-8.

[66] Eduardo Asín-Prieto, Alicia Rodríguez-Gascón, and Arantxazu Isla. “Applications of the pharmacokinetic/pharmacodynamic (PK/PD) analysis of antimicrobial agents”. In: *Journal of Infection and Chemotherapy* 21 (5 2015), pp. 319–329. ISSN: 1341-321X. DOI: 10.1016/J.JIAC.2015.02.001.

[67] B. W. Gunderson et al. “What do we really know about antibiotic pharmacodynamics?” In: *Pharmacotherapy* 21 (11 II 2001), pp. 392–406. ISSN: 02770008. DOI: 10.1592/phco.21.18.302s.33905.

[68] William A Craig. “Choosing an Antibiotic on the basis of Pharmacodynamics”. In: *Ear, Nose & Throat Journal* 77 (6 1998), p. 7.

[69] K. A. Rodvold. “Pharmacodynamics of antiinfective therapy: Taking what we know to the patient’s bedside”. In: *Pharmacotherapy* 21 (11 II 2001), 319S–330S. ISSN: 02770008. DOI: 10.1592/phco.21.18.319s.33904.

[70] David P. Nicolau. “Optimizing outcomes with antimicrobial therapy through pharmacodynamic profiling”. In: *Journal of Infection and Chemotherapy* 9 (4 2003), pp. 292–296. ISSN: 1341321X. DOI: 10.1007/s10156-003-0279-x.

[71] Kah Wei Chin et al. “An overview of antibiotic and antibiotic resistance”. In: *Environmental Advances* 11 (November 2022 2023), p. 100331. ISSN: 26667657. DOI: 10.1016/j.envadv.2022.100331.

[72] Jose M. Munita and Cesar A. Arias. "Mechanisms of antibiotic resistance". In: *Virulence Mechanisms of Bacterial Pathogens* (6 2016), pp. 481–511. DOI: 10.1128/9781555819286.ch17.

[73] Steven L. Barriere. "Clinical, economic and societal impact of antibiotic resistance". In: *Expert Opinion on Pharmacotherapy* 16 (2 2015), pp. 151–153. ISSN: 17447666. DOI: 10.1517/14656566.2015.983077.

[74] Petra Izakovicova, Olivier Borens, and Andrej Trampuz. "Periprosthetic joint infection: current concepts and outlook". In: *EFORT Open Reviews* 4 (7 2019), pp. 482–494. ISSN: 20585241. DOI: 10.1302/2058-5241.4.180092.

[75] Schreurs W Koot H. *Arthroplasty in the Picture Annual Report of the Dutch Arthroplasty Register (Landelijke Registratie Orthopedische Implantaten) 2014*. 2014.

[76] Konstantinos Anagnostakos and Bernd Fink. "Antibiotic-loaded cement spacers–lessons learned from the past 20 years". In: *Expert Review of Medical Devices* 15 (3 2018), pp. 231–245. ISSN: 17452422. DOI: 10.1080/17434440.2018.1435270.

[77] Paulo Almeida and Pedro Simas. *Portuguese Arthroplasty Register 2013 Annual Report*.

[78] L. Nečas et al. "Slovakian arthroplasty register: Survival analysis of total hip and knee replacement in Slovakia 2003-2011". In: *Acta Chirurgiae Orthopaedicae et Traumatologiae Cechoslovaca* 80 (SUPPL. 2013), pp. 1–85. ISSN: 00015415.

[79] Matthew E. Levison and Julie H. Levison. "Pharmacokinetics and Pharmacodynamics of Antibacterial Agents". In: *Infectious Disease Clinics of North America* 23 (4 2009), pp. 791–815. ISSN: 08915520. DOI: 10.1016/j.idc.2009.06.008.

[80] Mustafa Citak et al. "Spacers". In: *Journal of Arthroplasty* 29 (2 SUPPL. 2014), pp. 93–99. ISSN: 08835403. DOI: 10.1016/j.arth.2013.09.042.

[81] G. B. Appel and H. C. Neu. "Gentamicin in 1978". In: *Annals of Internal Medicine* 89 (4 1978), pp. 528–538. ISSN: 00034819. DOI: 10.7326/0003-4819-89-4-528.

[82] Luis S. Gonzalez and Jeanne P. Spencer. "Aminoglycosides: A practical review". In: *American Family Physician* 58 (8 1998), pp. 1811–1820. ISSN: 0002838X.

[83] Kevin M Krause et al. "Aminoglycosides : An Overview". In: *Cold Spring Harbor perspectives in medicine* 6.6 (2016).

[84] A. F. Mavrogenis et al. "Biology of implant osseointegration". In: *Journal of Musculoskeletal Neuronal Interactions* 9 (2 2009), pp. 61–71. ISSN: 11087161. DOI: 10.1016/j.joms.2007.05.013.

[85] Cassidy E. Gillman and Ambalangodage C. Jayasuriya. "FDA-approved bone grafts and bone graft substitute devices in bone regeneration". In: *Materials Science and Engineering C* 130 (November 2021), p. 112466. ISSN: 18730191. DOI: 10.1016/j.msec.2021.112466.

[86] L. Di Silvio and P. Jayakumar. "Cellular response to osteoinductive materials in orthopaedic surgery". In: *Cellular Response to Biomaterials*. Woodhead Publishing, 2008, pp. 313–343. ISBN: 9781845693589. DOI: 10.1533/9781845695477.2.313.

[87] Ashim Gupta et al. "Bone graft substitutes for spine fusion: A brief review." In: *World journal of orthopedics* 6 (6 2015), pp. 449–56. ISSN: 2218-5836. DOI: 10.5312/wjo.v6.i6.449.

[88] Abhijeet Kadam et al. "Bone substitutes and expanders in spine surgery: A review of their fusion efficacies". In: *International Journal of Spine Surgery* 10 (2016 2016). ISSN: 22114599. DOI: 10.14444/3033.

[89] Tonye Briggs and Treena Livingston Arinzeh. "Examining the formulation of emulsion electrospinning for improving the release of bioactive proteins from electrospun fibers". In: *Journal of Biomedical Materials Research - Part A* 102 (3 2014), pp. 674–684. ISSN: 15493296. DOI: 10.1002/jbm.a.34730.

[90] Jamie Ferguson, Michael Diefenbeck, and Martin Mcnally. "Ceramic Biocomposites as Biodegradable Antibiotic Carriers in the Treatment of Bone Infections". In: *Journal of Bone and Joint Infection* 2 (1 2017), pp. 38–51. DOI: 10.7150/jbji.17234.

[91] Kristyn S. Masters. "Covalent Growth Factor Immobilization Strategies for Tissue Repair and Regeneration". In: *Macromolecular Bioscience* 11 (9 2011), pp. 1149–1163. ISSN: 16165187. DOI: 10.1002/mabi.201000505.

[92] U. Edlund, T. Sauter, and A. C. Albertsson. "Covalent VEGF protein immobilization on resorbable polymeric surfaces". In: *Polymers for Advanced Technologies* 22 (1 2011), pp. 166–171. ISSN: 10427147. DOI: 10.1002/pat.1811.

[93] Liang Chun Wu et al. "Photo-reactive polymers for the immobilisation of epidermal growth factors". In: *Journal of Materials Chemistry B* (2022), pp. 5514–5522. ISSN: 20507518. DOI: 10.1039/d2tb02040h.

[94] Cyril Boucher et al. "Epidermal growth factor tethered through coiled-coil interactions induces cell surface receptor phosphorylation". In: *Bioconjugate Chemistry* 20 (8 2009), pp. 1569–1577. ISSN: 10431802. DOI: 10.1021/bc9001147.

[95] Loraine L.Y. Chiu and Milica Radisic. "Scaffolds with covalently immobilized VEGF and Angiopoietin-1 for vascularization of engineered tissues". In: *Biomaterials* 31 (2 2010), pp. 226–241. ISSN: 01429612. DOI: 10.1016/j.biomaterials.2009.09.039.

[96] Mary Kathryn Thompson et al. "Design for Additive Manufacturing: Trends, opportunities, considerations, and constraints". In: *CIRP Annals - Manufacturing Technology* 65 (2 2016), pp. 737–760. ISSN: 17260604. DOI: 10.1016/j.cirp.2016.05.004.

[97] Swee Leong Sing et al. "Laser and electron-beam powder-bed additive manufacturing of metallic implants: A review on processes, materials and designs". In: *Journal of Orthopaedic Research* 34 (3 2016), pp. 369–385. ISSN: 1554527X. DOI: 10.1002/jor.23075.

[98] Wei Gao et al. "The status, challenges, and future of additive manufacturing in engineering". In: *CAD Computer Aided Design* 69 (2015), pp. 65–89. ISSN: 00104485. DOI: 10.1016/j.cad.2015.04.001.

[99] Kaufui V. Wong and Aldo Hernandez. "A Review of Additive Manufacturing". In: *ISRN Mechanical Engineering* 2012 (2012), pp. 1–10. ISSN: 2090-5130. DOI: 10.5402/2012/208760.

[100] Francesco Trevisan et al. "Additive manufacturing of titanium alloys in the biomedical field: processes, properties and applications". In: *Journal of Applied Biomaterials Functional Materials* 16 (2 2018), pp. 57–67. ISSN: 2280-8000. DOI: 10.5301/jabfm.5000371.

[101] Morgan Lowther. "Delivery of antimicrobial biomaterials through additive manufacturing". PhD thesis. University of Birmingham, 2021.

[102] Gitanjali Shanbhag et al. "Effect of specimen geometry and orientation on tensile properties of Ti-6Al-4V manufactured by electron beam powder bed fusion". In: *Additive Manufacturing* 48 (PA 2021), p. 102366. ISSN: 22148604. DOI: 10.1016/j.addma.2021.102366.

[103] Nesma T. Aboulkhair et al. "3D printing of Aluminium alloys: Additive Manufacturing of Aluminium alloys using selective laser melting". In: *Progress in Materials Science* 106 (May 2019), p. 100578. ISSN: 00796425. DOI: 10.1016/j.pmatsci.2019.100578.

[104] Morgan Lowther et al. "Clinical, industrial, and research perspectives on powder bed fusion additively manufactured metal implants". In: *Additive Manufacturing* 28 (2019), pp. 565–584. ISSN: 22148604. DOI: 10.1016/J.ADDMA.2019.05.033.

[105] Maria Averyanova, Philippe Bertrand, and Benoît Verquin. "Manufacture of Co-Cr dental crowns and bridges by selective laser Melting technology". In: *Virtual and Physical Prototyping* 6 (3 2011), pp. 179–185. ISSN: 1745-2759. DOI: 10.1080/17452759.2011.619083.

[106] Danmei Luo, Qiguo Rong, and Quan Chen. "Finite-element design and optimization of a three-dimensional tetrahedral porous titanium scaffold for the reconstruction of mandibular defects". In: *Medical Engineering Physics* 47 (2017), pp. 176–183. ISSN: 13504533. DOI: 10.1016/j.medengphy.2017.06.015.

[107] J. P. Kruth et al. "Consolidation phenomena in laser and powder-bed based layered manufacturing". In: *CIRP Annals - Manufacturing Technology* 56 (2 2007), pp. 730–759. ISSN: 00078506. DOI: 10.1016/j.cirp.2007.10.004.

[108] H Attar et al. "Manufacture by selective laser melting and mechanical behavior of commercially pure titanium". In: *Materials Science and Engineering A* 593 (2014), pp. 170–177. ISSN: 09215093. DOI: 10.1016/j.msea.2013.11.038.

[109] X P Tan et al. "Metallic powder-bed based 3D printing of cellular scaffolds for orthopaedic implants: A state-of-the-art review on manufacturing, topological design, mechanical properties and biocompatibility". In: *Materials Science Engineering C* 76 (2017), pp. 1328–1343. ISSN: 0928-4931. DOI: 10.1016/j.msec.2017.02.094.

[110] J. P. Kruth et al. "Consolidation phenomena in laser and powder-bed based layered manufacturing". In: *CIRP Annals - Manufacturing Technology* 56.2 (2007), pp. 730–759. ISSN: 00078506. DOI: 10.1016/j.cirp.2007.10.004.

[111] Bi Zhang, Yongtao Li, and Qian Bai. "Defect Formation Mechanisms in Selective Laser Melting: A Review". In: *Chinese Journal of Mechanical Engineering (English Edition)* 30 (3 2017), pp. 515–527. ISSN: 21928258. DOI: 10.1007/s10033-017-0121-5.

[112] Shaaz Ghouse et al. "The influence of laser parameters, scanning strategies and material on the fatigue strength of a stochastic porous structure". In: *Additive Manufacturing* 22 (March 2018), pp. 290–301. ISSN: 22148604. DOI: 10.1016/j.addma.2018.05.024.

[113] Victor M. Villapún et al. "A design approach to facilitate selective attachment of bacteria and mammalian cells to additively manufactured implants". In: *Additive Manufacturing* 36 (December 2020), p. 101528. ISSN: 22148604. DOI: 10.1016/j.addma.2020.101528.

[114] Andrey Koptioug et al. “Additive manufacturing for medical and biomedical applications: Advances and challenges”. In: *Materials Science Forum* 783 (2014), pp. 1286–1291. ISSN: 1662-9752. DOI: 10.4028/www.scientific.net/MSF.783-786.1286.

[115] Emmanouil Bouzakis et al. “Comparison of Additively Manufactured vs. Conventional Maraging Steel in Corrosion-Fatigue Performance after various surface treatments”. In: *Procedia CIRP* 87 (March 2020), pp. 469–473. ISSN: 22128271. DOI: 10.1016/j.procir.2020.03.003.

[116] C. V. Haden et al. “Wire and arc additive manufactured steel: Tensile and wear properties”. In: *Additive Manufacturing* 16 (2017), pp. 115–123. ISSN: 22148604. DOI: 10.1016/j.addma.2017.05.010.

[117] Yong Huang et al. “Additive manufacturing: Current state, future potential, gaps and needs, and recommendations”. In: *Journal of Manufacturing Science and Engineering, Transactions of the ASME* 137 (1 2015), pp. 1–10. ISSN: 15288935. DOI: 10.1115/1.4028725.

[118] Shaaz Ghouse et al. “The influence of laser parameters and scanning strategies on the mechanical properties of a stochastic porous material”. In: *Materials and Design* 131 (2017), pp. 498–508. ISSN: 18734197. DOI: 10.1016/j.matdes.2017.06.041.

[119] Renishaw PLC. *Design for metal AM - a beginner’s guide*.

[120] Grzegorz Pyka et al. “Surface Roughness and Morphology Customization of Additive Manufactured Open Porous Ti6Al4V Structures”. In: *Materials* 6 (10 2013), pp. 4737–4757. ISSN: 1996-1944. DOI: 10.3390/MA6104737.

[121] Xue Cao et al. “Optimisation of single contour strategy in selective laser melting of Ti-6Al-4V lattices”. In: *Rapid Prototyping Journal* 28 (5 2022), pp. 907–915. ISSN: 13552546. DOI: 10.1108/RPJ-04-2021-0103.

[122] Lei Zhang et al. “Energy absorption characteristics of metallic triply periodic minimal surface sheet structures under compressive loading”. In: *Additive Manufacturing* 23 (October 2018), pp. 505–515. ISSN: 22148604. DOI: 10.1016/j.addma.2018.08.007.

[123] Irene Buj-Corral, Aitor Tejo-Otero, and Felip Fenollosa-Artés. “Development of am technologies for metals in the sector of medical implants”. In: *Metals* 10 (5 2020), pp. 1–30. ISSN: 20754701. DOI: 10.3390/met10050686.

[124] Khalid H. Hashmi et al. "Optimization of process parameters for high speed machining of Ti-6Al-4V using response surface methodology". In: *International Journal of Advanced Manufacturing Technology* 85 (5-8 2016), pp. 1847–1856. ISSN: 14333015. DOI: 10.1007/s00170-015-8057-3.

[125] *U.S. Food and Drug Administration.*

[126] *European Medicines Agency.*

[127] *Medicines and Healthcare products Regulatory Agency.*

[128] *National Medical Product Administration.*

[129] *The Medical Devices Regulations 2002 No. 618*. 2002.

[130] Krzysztof Pałka and Rafał Pokrowiecki. "Porous Titanium Implants: A Review". In: *Advanced Engineering Materials* (2018), p. 1700648. DOI: 10.1002/adem.201700648.

[131] Jonàs Martínez et al. "Polyhedral voronoi diagrams for additive manufacturing". In: *ACM Transactions on Graphics* 37 (4 2018), pp. 1–15. ISSN: 15577368. DOI: 10.1145/3197517.3201343.

[132] Lorna J. Gibson and Michael F. Ashby. *Cellular Solids: Structure and Properties*. Cambridge University Press, 1988, p. 510. ISBN: 0521499119.

[133] L E Murr et al. "Characterization of Ti6Al4V open cellular foams fabricated by additive manufacturing using electron beam melting". In: *Materials Science Engineering A* 527 (2010), pp. 1861–1868. ISSN: 09215093. DOI: 10.1016/j.msea.2009.11.015.

[134] M. Alkhader and M. Vural. "Mechanical response of cellular solids: Role of cellular topology and microstructural irregularity". In: *International Journal of Engineering Science* 46 (10 2008), pp. 1035–1051. ISSN: 0020-7225. DOI: 10.1016/j.ijengsci.2008.03.012.

[135] Mehmet Erdi Korkmaz et al. "Development of lattice structure with selective laser melting process: A state of the art on properties, future trends and challenges". In: *Journal of Manufacturing Processes* 81 (2022), pp. 1040–1063. ISSN: 1526-6125. DOI: 10.1016/J.JMAPRO.2022.07.051.

[136] M. Benedetti et al. "Architected cellular materials: A review on their mechanical properties towards fatigue-tolerant design and fabrication". In: *Materials Science and Engineering R: Reports* 144 (2021), p. 100606. ISSN: 0927796X. DOI: 10.1016/j.mser.2021.100606.

[137] M.F. Ashby. "The properties of foams and lattices." In: *Philosophical transactions. Series A, Mathematical, physical, and engineering sciences* 364 (1838 2006), pp. 15–30. ISSN: 1364-503X. DOI: 10.1098/rsta.2005.1678.

[138] I. Maskery et al. "Effective design and simulation of surface-based lattice structures featuring volume fraction and cell type grading". In: *Materials Design* 155 (2018), pp. 220–232. ISSN: 0264-1275. DOI: 10.1016/J.MATDES.2018.05.058.

[139] Meng He et al. "Compressive performance and fracture mechanism of bio-inspired heterogeneous glass sponge lattice structures manufactured by selective laser melting". In: *Materials and Design* 214 (2022), p. 110396. ISSN: 18734197. DOI: 10.1016/j.matdes.2022.110396.

[140] Zaki Alomar and Franco Concli. "Compressive behavior assessment of a newly developed circular cell-based lattice structure". In: *Materials and Design* 205 (2021), p. 109716. ISSN: 18734197. DOI: 10.1016/j.matdes.2021.109716.

[141] Jiaxi Zhao et al. "Effect of relative density on the compressive properties of Ti6Al4V diamond lattice structures with shells". In: *Mechanics of Advanced Materials and Structures* 29 (22 2022), pp. 3301–3315. ISSN: 15376532. DOI: 10.1080/15376494.2021.1893418.

[142] Fei Liu et al. "Mechanical properties of optimized diamond lattice structure for bone scaffolds fabricated via selective laser melting". In: *Materials* 11 (3 2018), p. 374. ISSN: 19961944. DOI: 10.3390/ma11030374.

[143] Niyou Wang et al. "A biomechanical evaluation on Cubic, Octet, and TPMS gyroid Ti6Al4V lattice structures fabricated by selective laser melting and the effects of their debris on human osteoblast-like cells". In: *Biomaterials Advances* 137 (June 2022), p. 212829. ISSN: 27729508. DOI: 10.1016/j.bioadv.2022.212829.

[144] Vincenzo Crupi et al. "Static behavior of lattice structures produced via direct metal laser sintering technology". In: *Materials and Design* 135 (2017), pp. 246–256. ISSN: 18734197. DOI: 10.1016/j.matdes.2017.09.003.

[145] Volker Weißmann et al. "Specific Yielding of Selective Laser-Melted Ti6Al4V Open-Porous Scaffolds as a Function of Unit Cell Design and Dimensions". In: *Metals* 6 (7 2016), p. 166. ISSN: 2075-4701. DOI: 10.3390/met6070166.

[146] Chunze Yan et al. "Evaluations of cellular lattice structures manufactured using selective laser melting". In: *International Journal of Machine Tools and Manufacture* 62 (2012), pp. 32–38. ISSN: 08906955. DOI: 10.1016/j.ijmachtools.2012.06.002.

[147] Yangli Xu et al. “Mechanical properties tailoring of topology optimized and selective laser melting fabricated Ti6Al4V lattice structure”. In: *Journal of the Mechanical Behavior of Biomedical Materials* 99 (November 2019), pp. 225–239. ISSN: 18780180. DOI: 10.1016/j.jmbbm.2019.06.021.

[148] Ifeanyichukwu Echeta et al. “Review of defects in lattice structures manufactured by powder bed fusion”. In: *The International Journal of Advanced Manufacturing Technology* 106 (5 2019), pp. 2649–2668. ISSN: 1433-3015. DOI: 10.1007/S00170-019-04753-4.

[149] Tobias Maconachie et al. “SLM lattice structures: Properties, performance, applications and challenges”. In: *Materials and Design* 183 (2019), p. 108137. ISSN: 18734197. DOI: 10.1016/j.matdes.2019.108137.

[150] Alan H Schoen. *Infinite Periodic Minimal Surfaces without Self-Intersections*. Tech. rep. 1970. DOI: 10.1057/9781137465160.0020.

[151] Dalia Mahmoud et al. “Enhancement of heat exchanger performance using additive manufacturing of gyroid lattice structures”. In: *International Journal of Advanced Manufacturing Technology* 126.9-10 (2023), pp. 4021–4036. ISSN: 14333015. DOI: 10.1007/s00170-023-11362-9.

[152] S. Bakhshandeh et al. “Simultaneous Delivery of Multiple Antibacterial Agents from Additively Manufactured Porous Biomaterials to Fully Eradicate Planktonic and Adherent Staphylococcus aureus”. In: *ACS Applied Materials Interfaces* 9 (31 2017), pp. 25691–25699. ISSN: 1944-8244. DOI: 10.1021/acsami.7b04950.

[153] Karolina Dydak et al. “Development and biological evaluation of Ti6Al7Nb scaffold implants coated with gentamycin-saturated bacterial cellulose biomaterial”. In: *PLoS ONE* 13 (10 2018). ISSN: 19326203. DOI: 10.1371/journal.pone.0205205.

[154] Aranka Ilea et al. “Osseointegration of titanium scaffolds manufactured by selective laser melting in rabbit femur defect model”. In: *Research Institute for Analytical Instrumentation* 4 (2000). DOI: 10.1007/s10856-019-6227-9.

[155] Haotian Bai et al. “3D printed porous biomimetic composition sustained release zoledronate to promote osteointegration of osteoporotic defects”. In: *Materials and Design* 189 (2020), p. 108513. ISSN: 18734197. DOI: 10.1016/j.matdes.2020.108513.

[156] Zhong hua Li et al. “Mechanical properties of AlSi10Mg lattice structures fabricated by selective laser melting”. In: *Materials Design* 192 (2020), p. 108709. ISSN: 0264-1275. DOI: 10.1016/J.MATDES.2020.108709.

[157] Brian Allen. "High-strength, 3D-printed Antibiotic-eluting Spacer to treat Periprosthetic Joint Infection". PhD thesis. Duke University, 2020.

[158] Meng Wu et al. "Metal artifact correction for x-ray computed tomography using kV and selective MV imaging". In: *Medical Physics* 41 (12 2014), pp. 1–15. ISSN: 24734209. DOI: 10.1118/1.4901551.

[159] Luke N. Carter et al. "Reducing MRI susceptibility artefacts in implants using additively manufactured porous Ti-6Al-4V structures". In: *Acta Biomaterialia* 107 (2020), pp. 338–348. ISSN: 18787568. DOI: 10.1016/j.actbio.2020.02.038.

[160] Sajad Arabnejad et al. "Fully porous 3D printed titanium femoral stem to reduce stress-shielding following total hip arthroplasty". In: *Journal of Orthopaedic Research* 35 (8 2017), pp. 1774–1783. ISSN: 1554527X. DOI: 10.1002/jor.23445.

[161] Yusef Jordan et al. "Outcomes and cost-minimization analysis of cement spacers versus expandable cages for posterior-only reconstruction of metastatic spine corpectomies". In: *Annals of Translational Medicine* 7 (10 2019), pp. 212–212. ISSN: 23055839. DOI: 10.21037/atm.2019.05.07.

[162] Man Kyu Park et al. "Risk factors for cage migration and cage retropulsion following transforaminal lumbar interbody fusion". In: *Spine Journal* 19 (3 2019), pp. 437–447. ISSN: 18781632. DOI: 10.1016/j.spinee.2018.08.007.

[163] S. Van Bael et al. "The effect of pore geometry on the in vitro biological behavior of human periosteum-derived cells seeded on selective laser-melted Ti6Al4V bone scaffolds". In: *Acta Biomaterialia* 8 (7 2012), pp. 2824–2834. ISSN: 1742-7061. DOI: 10.1016/j.actbio.2012.04.001.

[164] Patrick H Warnke et al. "Rapid prototyping: porous titanium alloy scaffolds produced by selective laser melting for bone tissue engineering". In: *Tissue Engineering: Part C* 15 (2 2009), pp. 115–125. ISSN: 1937-3384. DOI: 10.1089/ten.tec.2008.0288.

[165] Weichang Xue et al. "Processing and biocompatibility evaluation of laser processed porous titanium". In: *Acta Biomaterialia* 3 (6 2007), pp. 1007–1018. ISSN: 1742-7061. DOI: 10.1016/j.actbio.2007.05.009.

[166] Jia Ping Li et al. "Bone ingrowth in porous titanium implants produced by 3D fiber deposition". In: *Biomaterials* 28 (18 2007), pp. 2810–2820. ISSN: 01429612. DOI: 10.1016/j.biomaterials.2007.02.020.

[167] E. Baril, L. P. Lefebvre, and S. A. Hacking. "Direct visualization and quantification of bone growth into porous titanium implants using micro computed tomography". In: *Journal of Materials Science: Materials in Medicine* 22 (5 2011), pp. 1321–1332. ISSN: 0957-4530. DOI: 10.1007/s10856-011-4309-4.

[168] Bungo Otsuki et al. "Pore throat size and connectivity determine bone and tissue ingrowth into porous implants: Three-dimensional micro-CT based structural analyses of porous bioactive titanium implants". In: *Biomaterials* 27 (2006), pp. 5892–5900. ISSN: 01429612. DOI: 10.1016/j.biomaterials.2006.08.013.

[169] Ferry PW Melchels et al. "Effects of the architecture of tissue engineering scaffolds on cell seeding and culture". In: *Acta biomaterialia* 6 (11 2010), pp. 4208–4217. ISSN: 17427061. DOI: 10.1016/j.actbio.2010.06.012.

[170] T M Turner et al. "A comparative study of porous coatings in a weight-bearing total hip-arthroplasty model." In: *The Journal of bone and joint surgery. American volume* 68 (9 1986), pp. 1396–409. ISSN: 0021-9355.

[171] Sabine Ponader et al. "Effects of topographical surface modifications of electron beam melted Ti-6Al-4V titanium on human fetal osteoblasts". In: *Journal of Biomedical Materials Research* 84 (2008), pp. 1111–1119. DOI: 10.1002/jbm.a.31540.

[172] J D Bobyn et al. "Osteogenic phenomena across endosteal bone-implant spaces with porous surfaced intramedullary implants". In: *Acta Orthopaedica* 52 (2 1981), pp. 145–153. ISSN: 17453674. DOI: 10.3109/17453678108991775.

[173] J E Dalton et al. "The effect of operative fit and hydroxyapatite coating on the mechanical and biological response to porous implants." In: *The Journal of bone and joint surgery. American volume* 77 (1 1995), pp. 97–110. ISSN: 0021-9355.

[174] Patricia M. Sandborn et al. "Tissue response to porous-coated implants lacking initial bone apposition". In: *Journal of Arthroplasty* 3 (4 1988), pp. 337–346. ISSN: 0883-5403. DOI: 10.1016/S0883-5403(88)80034-2.

[175] R. M. Pilliar, J. M. Lee, and C. Maniatopoulos. "Observations on the effect of movement on bone ingrowth into porous-surfaced implants". In: *Clinical Orthopaedics and Related Research* NO. 208 (208 1986), pp. 108–113. ISSN: 0009921X. DOI: 10.1097/00003086-198607000-00023.

[176] John B Brunski. "The influence of force, motion and related quantities on the response of bone to implant". In: *Non - cemented total hip arthroplasty*. Raven Press, 1988, pp. 7–22.

[177] S. Van Bael et al. "Micro-CT-based improvement of geometrical and mechanical controllability of selective laser melted Ti6Al4V porous structures". In: *Materials Science and Engineering A* 528 (24 2011), pp. 7423–7431. ISSN: 09215093. DOI: 10.1016/j.msea.2011.06.045.

[178] M. Simonelli, Y. Y. Tse, and C. Tuck. "Effect of the build orientation on the mechanical properties and fracture modes of SLM Ti-6Al-4V". In: *Materials Science and Engineering A* 616 (2014), pp. 1–11. ISSN: 09215093. DOI: 10.1016/j.msea.2014.07.086.

[179] D Melancon et al. "Mechanical characterization of structurally porous biomaterials built via additive manufacturing: experiments, predictive models, and design maps for load-bearing bone replacement implants". In: *Acta Biomaterialia* 63 (2017), pp. 350–368. ISSN: 1742-7061. DOI: 10.1016/j.actbio.2017.09.013.

[180] Sajad Arabnejad et al. "High-strength porous biomaterials for bone replacement: A strategy to assess the interplay between cell morphology, mechanical properties, bone ingrowth and manufacturing constraints". In: *Acta Biomaterialia* 30 (2016), pp. 345–356. ISSN: 1742-7061. DOI: 10.1016/j.actbio.2015.10.048.

[181] C Emmelmann et al. "Laser Additive Manufacturing of Modified Implant Surfaces with Osseointegrative Characteristics". In: *Physics Procedia* 12 (2011), pp. 375–384. ISSN: 1875-3892. DOI: 10.1016/j.phpro.2011.03.048.

[182] S. L. Sing et al. "Characterization of Titanium Lattice Structures Fabricated by Selective Laser Melting Using an Adapted Compressive Test Method". In: *Experimental Mechanics* 56 (5 2016), pp. 735–748. ISSN: 17412765. DOI: 10.1007/s11340-015-0117-y.

[183] Lu Liu et al. "Elastic and failure response of imperfect three-dimensional metallic lattices: the role of geometric defects induced by Selective Laser Melting". In: *Journal of the Mechanics and Physics of Solids* 107 (2017), pp. 160–184. ISSN: 00225096. DOI: 10.1016/j.jmps.2017.07.003.

[184] S. Murchio et al. "Additively manufactured Ti–6Al–4V thin struts via laser powder bed fusion: Effect of building orientation on geometrical accuracy and mechanical properties". In: *Journal of the Mechanical Behavior of Biomedical Materials* 119 (March 2021), p. 104495. ISSN: 18780180. DOI: 10.1016/j.jmbbm.2021.104495.

[185] M. Dallago et al. "On the effect of geometrical imperfections and defects on the fatigue strength of cellular lattice structures additively manufactured via Selective Laser Melting". In: *International Journal of Fatigue* 124 (February 2019), pp. 348–360. ISSN: 01421123. DOI: 10.1016/j.ijfatigue.2019.03.019.

[186] Bill Lozanovski et al. "Computational modelling of strut defects in SLM manufactured lattice structures". In: *Materials Design* 171 (2019), p. 107671. ISSN: 0264-1275. DOI: 10.1016/j.matdes.2019.107671.

[187] Hongshuai Lei et al. "Evaluation of compressive properties of SLM-fabricated multi-layer lattice structures by experimental test and -CT-based finite element analysis". In: *Materials and Design* 169 (2019), p. 107685. ISSN: 18734197. DOI: 10.1016/j.matdes.2019.107685.

[188] Dalia Mahmoud and M. A. Elbestawi. "Selective laser melting of porosity graded lattice structures for bone implants". In: *International Journal of Advanced Manufacturing Technology* 100 (9-12 2019), pp. 2915–2927. ISSN: 14333015. DOI: 10.1007/s00170-018-2886-9.

[189] Alexander Großmann, Julian Gosmann, and Christian Mittelstedt. "Lightweight lattice structures in selective laser melting: Design, fabrication and mechanical properties". In: *Materials Science Engineering: A* 766 (June 2019), p. 138356. ISSN: 0921-5093. DOI: 10.1016/j.msea.2019.138356.

[190] Chia-Ying Ying Lin et al. "Structural and mechanical evaluations of a topology optimized titanium interbody fusion cage fabricated by selective laser melting process". In: *Journal of Biomedical Materials Research Part A* (2 2007), pp. 272–279. ISSN: 15493296. DOI: 10.1002/jbm.a.31231.

[191] Dirk A Hollander et al. "Structural, mechanical and in vitro characterization of individually structured Ti-6Al-4V produced by direct laser forming". In: *Biomaterials* 27 (7 2006), pp. 955–963. ISSN: 01429612. DOI: 10.1016/j.biomaterials.2005.07.041.

[192] Sebastian Rott et al. "Surface roughness in laser powder bed fusion – Interdependency of surface orientation and laser incidence". In: *Additive Manufacturing* 36 (December 2020), p. 101437. ISSN: 22148604. DOI: 10.1016/j.addma.2020.101437.

[193] S Kleszczynskia et al. "Position Dependency of Surface Roughness in Parts From Laser Beam". In: *Proceedings of the 26th Internation Solid Free Form Fabrication (SFF) Symposium* (2015), pp. 360–370.

[194] Zhuoer Chen et al. "Surface roughness of Selective Laser Melted Ti-6Al-4V alloy components". In: *Additive Manufacturing* 21 (February 2018), pp. 91–103. ISSN: 22148604. DOI: 10.1016/j.addma.2018.02.009.

[195] Reza Esmaeilizadeh et al. “On the effect of spatter particles distribution on the quality of Hastelloy X parts made by laser powder-bed fusion additive manufacturing”. In: *Journal of Manufacturing Processes* 37 (April 2018 2019), pp. 11–20. ISSN: 15266125. DOI: 10.1016/j.jmapro.2018.11.012.

[196] Leonhard Hitzler et al. “Non-destructive evaluation of AlSi10Mg prismatic samples generated by selective laser melting: Influence of manufacturing conditions”. In: *Materialwissenschaft und Werkstofftechnik* 47 (5-6 2016), pp. 564–581. ISSN: 15214052. DOI: 10.1002/mawe.201600532.

[197] Alexander Ladewig et al. “Influence of the shielding gas flow on the removal of process by-products in the selective laser melting process”. In: *Additive Manufacturing* 10 (2016), pp. 1–9. ISSN: 22148604. DOI: 10.1016/j.addma.2016.01.004.

[198] J. Kranz, D. Herzog, and C. Emmelmann. “Design guidelines for laser additive manufacturing of lightweight structures in TiAl6V4”. In: *Journal of Laser Applications* 27 (S1 2015), S14001. ISSN: 1042-346X. DOI: 10.2351/1.4885235.

[199] J. Fu et al. “Multi-scale defects in powder-based additively manufactured metals and alloys”. In: *Journal of Materials Science and Technology* 122 (2022), pp. 165–199. ISSN: 10050302. DOI: 10.1016/j.jmst.2022.02.015.

[200] Martin Leary et al. “Feasible Build Orientations for Self-Supporting Fused Deposition Manufacture: A Novel Approach to Space-Filling Tesselated Geometries”. In: *Advanced Materials Research* 633 (2013), pp. 148–168. ISSN: 1662-8985. DOI: 10.4028/www.scientific.net/AMR.633.148.

[201] Ahmad Alghamdi et al. “Experimental and numerical assessment of surface roughness for Ti6Al4V lattice elements in selective laser melting”. In: *International Journal of Advanced Manufacturing Technology* 105 (1-4 2019), pp. 1275–1293. ISSN: 14333015. DOI: 10.1007/s00170-019-04092-4.

[202] Authors Yan et al. “Ti-6Al-4V triply periodic minimal surface structures for bone implants fabricated via selective laser melting”. In: *Journal of the Mechanical Behavior of Biomedical Materials* 51 (2015), pp. 61–73. ISSN: 18780180. DOI: 10.1016/j.jmbbm.2015.06.024.

[203] Luke W Hunter et al. “Assessment of trapped powder removal and inspection strategies for powder bed fusion techniques”. In: *The International Journal of Advanced Manufacturing Technology* 106 (2020), pp. 4521–4532. ISSN: 14333015. DOI: 10.1007/s00170-020-04930-w.

[204] ASTM. *ASTM F3335 - 20: Standard Guide for Assessing the Removal of Additive Manufacturing Residues in Medical Devices Fabricated by Powder Bed Fusion.* 2020. DOI: 10.1520/F3335-20.1.7.

[205] Rama Krishna Alla et al. "Surface Roughness of Implants: A Review". In: *Trends in Biomaterials Artificial Organs* 25 (3 2011), pp. 112–118.

[206] Subhashini Govindaraj and Meenakshi Sundaram Muthuraman. "Systematic review on sterilization methods of implants and medical devices". In: *International Journal of ChemTech Research* 8.2 (2015), pp. 897–911. ISSN: 09744290.

[207] ASTM. *ASTM F3127 22: Standard Guide for Validating Cleaning Processes Used During the Manufacture of Medical Devices 1.* 2022. DOI: 10.1520/F3127-22.Development.

[208] Anton Du Plessis et al. "X-ray microcomputed tomography in additive manufacturing: a review of the current technology and applications". In: *3D Printing and Additive Manufacturing* 5.3 (2018), pp. 227–247. ISSN: 23297670. DOI: 10.1089/3dp.2018.0060.

[209] Amir Malakizadi et al. "Post-processing of additively manufactured metallic alloys – A review". In: *International Journal of Machine Tools and Manufacture* 179.February (2022), p. 103908. ISSN: 08906955. DOI: 10.1016/j.ijmachtools.2022.103908.

[210] Xing Peng et al. "A review of post-processing technologies in additive manufacturing". In: *Journal of Manufacturing and Materials Processing* 5.2 (2021). ISSN: 25044494. DOI: 10.3390/jmmp5020038.

[211] Solomon O. Obadimu and Kyriakos I. Kourousis. "Compressive Behaviour of Additively Manufactured Lattice Structures: A Review". In: *Aerospace* 8 (8 2021), p. 207. ISSN: 2226-4310. DOI: 10.3390/AEROSPACE8080207.

[212] Gladius Lewis. "Properties of open-cell porous metals and alloys for orthopaedic applications". In: *Journal of Materials Science: Materials in Medicine* 24 (10 2013), pp. 2293–2325. ISSN: 0957-4530. DOI: 10.1007/s10856-013-4998-y.

[213] Donald T. Reilly, Albert H. Burstein, and Victor H. Frankel. "The elastic modulus for bone". In: *Journal of Biomechanics* 7 (3 1974), pp. 271–275. ISSN: 0021-9290. DOI: 10.1016/0021-9290(74)90018-9.

[214] A H Burstein, D T Reilly, and M Martens. "Aging of bone tissue: mechanical properties". In: *The Journal of Bone and Joint Surgery. American Volume* 58 (1 1976), pp. 82–86. ISSN: 0021-9355. DOI: 1249116.

[215] H. Cezayirlioglu et al. “Anisotropic yield behavior of bone under combined axial force and torque”. In: *Journal of Biomechanics* 18 (1 1985), pp. 61–69. ISSN: 0021-9290. DOI: 10.1016/0021-9290(85)90045-4.

[216] Guisheng Yu et al. “The select of internal architecture for porous Ti alloy scaffold: A compromise between mechanical properties and permeability”. In: *Materials and Design* 192 (2020), p. 108754. ISSN: 18734197. DOI: 10.1016/j.matdes.2020.108754.

[217] S. Amin Yavari et al. “Relationship between unit cell type and porosity and the fatigue behavior of selective laser melted meta-biomaterials”. In: *Journal of the Mechanical Behavior of Biomedical Materials* 43 (2015), pp. 91–100. ISSN: 1751-6161. DOI: 10.1016/j.jmbbm.2014.12.015.

[218] Pei Yao Li et al. “Mechanical behaviors and failure modes of additive manufactured Ti6Al4V lattice structures under compressive load”. In: *Thin-Walled Structures* 180 (November 2022 2022), p. 109778. ISSN: 02638231. DOI: 10.1016/j.tws.2022.109778.

[219] J. Clerk Maxwell. “On the calculation of the equilibrium and stiffness of frames”. In: *The London, Edinburgh, and Dublin Philosophical Magazine and Journal of Science* 27 (182 1864), pp. 294–299. ISSN: 1941-5982. DOI: 10.1080/14786446408643668.

[220] M. Leary. “Design of titanium implants for additive manufacturing”. In: *Titanium in Medical and Dental Applications* (2018), pp. 203–224. DOI: 10.1016/B978-0-12-812456-7.00009-3.

[221] S. N. Khaderi, V. S. Deshpande, and N. A. Fleck. “The stiffness and strength of the gyroid lattice”. In: *International Journal of Solids and Structures* 51 (23-24 2014), pp. 3866–3877. ISSN: 00207683. DOI: 10.1016/j.ijsolstr.2014.06.024.

[222] Recep Gümrük, R.A.W. Mines, and Sami Karadeniz. “Static mechanical behaviours of stainless steel micro-lattice structures under different loading conditions”. In: *Materials Science and Engineering A* 586 (2013), pp. 392–406. ISSN: 09215093. DOI: https://doi.org/10.1016/j.msea.2013.07.070.

[223] S.M. M Ahmadi et al. “Mechanical behavior of regular open-cell porous biomaterials made of diamond lattice unit cells”. In: *Journal of the Mechanical Behavior of Biomedical Materials* 34 (2014), pp. 106–115. ISSN: 17516161. DOI: 10.1016/j.jmbbm.2014.02.003.

[224] Johan Van Der Stok et al. “Selective laser melting-produced porous titanium scaffolds regenerate bone in critical size cortical bone defects”. In: *Journal of Orthopaedic Research* 31 (5 2013), pp. 792–799. ISSN: 07360266. DOI: 10.1002/jor.22293.

[225] S. Amin Yavari et al. “Fatigue behavior of porous biomaterials manufactured using selective laser melting”. In: *Materials Science and Engineering: C* 33 (8 2013), pp. 4849–4858. ISSN: 0928-4931. DOI: 10.1016/J.MSEC.2013.08.006.

[226] Y. Shen et al. “The mechanical properties of sandwich structures based on metal lattice architectures”. In: *Journal of Sandwich Structures and Materials* 12 (2 2010), pp. 159–180. ISSN: 10996362. DOI: 10.1177/1099636209104536.

[227] S. Tsopanos et al. “The Influence of Processing Parameters on the Mechanical Properties of Selectively Laser Melted Stainless Steel Microlattice Structures”. In: *Journal of Manufacturing Science and Engineering* 132 (4 2010), p. 041011. ISSN: 15288935. DOI: 10.1115/1.4001743.

[228] Jan Bültmann et al. “Scalability of the mechanical properties of selective laser melting produced micro-struts”. In: *Journal of Laser Applications* 27 (S2 2015), S29206. ISSN: 1042-346X. DOI: 10.2351/1.4906392.

[229] Jan Bültmann et al. “Scalability of the mechanical properties of selective laser melting produced micro-struts”. In: *Journal of Laser Applications* 27.S2 (2015), S29206. ISSN: 1042-346X. DOI: 10.2351/1.4906392.

[230] Nikhil Kabbur. “Design and Manufacturing Guidelines for Additive Manufacturing of High Porosity Cellular structures”. PhD thesis. University of Cincinnati, 2017.

[231] Volker Weißmann et al. “Comparison of single Ti6Al4V struts made using selective laser melting and electron beam melting subject to part orientation”. In: *Metals* 7 (3 2017). ISSN: 20754701. DOI: 10.3390/met7030091.

[232] Ruben Wauthle et al. “Effects of build orientation and heat treatment on the microstructure and mechanical properties of selective laser melted Ti6Al4V lattice structures”. In: *Additive Manufacturing* 5 (2015), pp. 77–84. ISSN: 2214-8604. DOI: 10.1016/J.ADDMA.2014.12.008.

[233] Umar Hossain. “Design and testing of additively manufactured lattice structures for musculoskeletal applications”. PhD thesis. Imperial College London, 2021.

[234] Chunze Yan et al. “Advanced lightweight 316L stainless steel cellular lattice structures fabricated via selective laser melting”. In: *Materials and Design* 55 (2014), pp. 533–541. ISSN: 18734197. DOI: 10.1016/j.matdes.2013.10.027.

[235] Sing Ying Choy et al. “Compressive properties of functionally graded lattice structures manufactured by selective laser melting”. In: *Materials Design* 131 (2017), pp. 112–120. ISSN: 02641275. DOI: 10.1016/j.matdes.2017.06.006.

[236] Volker Weißmann et al. “Influence of the structural orientation on the mechanical properties of selective laser melted Ti6Al4V open-porous scaffolds”. In: *Materials and Design* 95 (2016), pp. 188–197. ISSN: 18734197. DOI: 10.1016/j.matdes.2016.01.095.

[237] S McKown et al. “The quasi-static and blast loading response of lattice structures”. In: *International Journal of Impact Engineering* 35 (2008), pp. 795–810. ISSN: 0734743X. DOI: 10.1016/j.ijimpeng.2007.10.005.

[238] Maciej Mazur et al. “SLM additive manufacture of H13 tool steel with conformal cooling and structural lattices”. In: *Rapid Prototyping Journal* (October 2017 2016), pp. 504–518. DOI: 10.1108/RPJ-06-2014-0075.

[239] G. Campoli et al. “Mechanical properties of open-cell metallic biomaterials manufactured using additive manufacturing”. In: *Materials Design* 49 (2013), pp. 957–965. ISSN: 0261-3069. DOI: 10.1016/J.MATDES.2013.01.071.

[240] Sonu Singh et al. “Cellular studies and sustained drug delivery via nanostructures fabricated on 3D printed porous Neovius lattices of Ti6Al4V ELI”. In: *Biomedical Materials (Bristol)* 17 (4 2022), p. 045004. ISSN: 1748605X. DOI: 10.1088/1748-605X/ac6922.

[241] Maninder Singh, Amoljit Singh Gill, and Mukhtiar Singh. “Titanium Implants for Localized Drug Delivery: A Drug-Eluting Approach”. In: *European Chemical Bulletin* 1 (10 2023), pp. 8540–8562.

[242] Stuart B. Goodman et al. “The future of biologic coatings for orthopaedic implants”. In: *Biomaterials* 34 (13 2013), pp. 3174–3183. ISSN: 0142-9612. DOI: 10.1016/J.BIOMATERIALS.2013.01.074.

[243] S. Amin Yavari et al. “Layer by layer coating for bio-functionalization of additively manufactured meta-biomaterials”. In: *Additive Manufacturing* 32 (2020), p. 100991. ISSN: 22148604. DOI: 10.1016/j.addma.2019.100991.

[244] F. Jahanmard et al. “Bactericidal coating to prevent early and delayed implant-related infections”. In: *Journal of Controlled Release* 326 (2020), pp. 38–52. ISSN: 18734995. DOI: 10.1016/J.JCONREL.2020.06.014.

[245] Chiara Micheletti et al. “Drug release from polymer-coated TiO2 nanotubes on additively manufactured Ti-6Al-4V bone implants: a feasibility study”. In: *Nano Express* 2 (1 2021), p. 010018. ISSN: 2632959X. DOI: 10.1088/2632-959X/abe278.

[246] Ingmar A.J. van Hengel et al. "Selective laser melting porous metallic implants with immobilized silver nanoparticles kill and prevent biofilm formation by methicillin-resistant Staphylococcus aureus". In: *Biomaterials* 140 (2017), pp. 1–15. ISSN: 01429612. DOI: 10.1016/j.biomaterials.2017.02.030.

[247] Regina MacBarb et al. "Fortifying the Bone-Implant Interface Part 2: An In Vivo Evaluation of 3D-Printed and TPS-Coated Triangular Implants". In: *International Journal of Spine Surgery* 11 (3 2017), pp. 116–128. ISSN: 22114599. DOI: 10.14444/4016.

[248] Elia Vidal et al. "Multifunctional homogeneous calcium phosphate coatings: Toward antibacterial and cell adhesive titanium scaffolds". In: *Surface and Coatings Technology* 405 (2021), p. 405. ISSN: 02578972. DOI: 10.1016/j.surfcoat.2020.126557.

[249] K. C. Nune et al. "Interplay between self-assembled structure of bone morphogenetic protein-2 (BMP-2) and osteoblast functions in three-dimensional titanium alloy scaffolds: Stimulation of osteogenic activity". In: *Journal of Biomedical Materials Research - Part A* 104 (2 2016), pp. 517–532. ISSN: 15524965. DOI: 10.1002/JBM.A.35592.

[250] S. Amin Yavari et al. "Antibacterial Behavior of Additively Manufactured Porous Titanium with Nanotubular Surfaces Releasing Silver Ions". In: *ACS Applied Materials Interfaces* 8 (27 2016), pp. 17080–17089. ISSN: 1944-8244. DOI: 10.1021/acsami.6b03152.

[251] Shaheer Maher et al. "Engineering of Micro- to Nanostructured 3D-Printed Drug-Releasing Titanium Implants for Enhanced Osseointegration and Localized Delivery of Anticancer Drugs". In: *ACS Applied Materials Interfaces* 9 (35 2017), pp. 29562–29570. ISSN: 1944-8244. DOI: 10.1021/acsami.7b09916.

[252] Mohammed Mehdi Benmassaoud et al. "Efficacy of eluted antibiotics through 3D printed femoral implants". In: *Biomedical Microdevices* 21 (3 2019), pp. 1–10. ISSN: 15728781. DOI: 10.1007/s10544-019-0395-8.

[253] Martin B. Bezuidenhout et al. "Selective Laser Melting of Integrated Ti6Al4V ELI Permeable Walls for Controlled Drug Delivery of Vancomycin". In: *ACS Biomaterials Science Engineering* 4 (12 2018), pp. 4412–4424. ISSN: 2373-9878. DOI: 10.1021/acsbiomaterials.8b00676.

[254] Miao Guo and Xiang Li. "Development of porous Ti6Al4V/chitosan sponge composite scaffold for orthopedic applications". In: *Materials Science and Engineering C* 58 (2016), pp. 1177–1181. ISSN: 09284931. DOI: 10.1016/j.msec.2015.09.061.

[255] Zehao Jing et al. “Practical strategy to construct anti-osteosarcoma bone substitutes by loading cisplatin into 3D-printed titanium alloy implants using a thermosensitive hydrogel”. In: *Bioactive Materials* 6 (12 2021), pp. 4542–4557. ISSN: 2452199X. DOI: 10.1016/j.bioactmat.2021.05.007.

[256] Brian Allen et al. “Modulating antibiotic release from reservoirs in 3D-printed orthopedic devices to treat periprosthetic joint infection”. In: *Journal of Orthopaedic Research* 38 (10 2020), pp. 2239–2249. ISSN: 1554527X. DOI: 10.1002/jor.24640.

[257] Sophie C. Cox et al. “Adding functionality with additive manufacturing: Fabrication of titanium-based antibiotic eluting implants”. In: *Materials Science and Engineering: C* 64 (2016), pp. 407–415. ISSN: 0928-4931. DOI: 10.1016/J.MSEC.2016.04.006.

[258] Tae Won B. Kim et al. “3D printed liner for treatment of periprosthetic joint infections”. In: *Medical Hypotheses* 102 (2017), pp. 65–68. ISSN: 15322777. DOI: 10.1016/J.MEHY.2017.03.014.

[259] K Man et al. “Development of a Bone-Mimetic 3D Printed Ti6Al4V Scaffold to Enhance Osteoblast-Derived Extracellular Vesicles’ Therapeutic Efficacy for Bone Regeneration”. In: *Frontiers in Bioengineering and Biotechnology* 9 (2021), p. 757220. DOI: 10.3389/fbioe.2021.757220.

[260] Maria Daniela Vlad et al. “Novel titanium-apatite hybrid scaffolds with spongy bone-like micro architecture intended for spinal application: In vitro and in vivo study”. In: *Materials Science and Engineering C* 110 (2020), p. 110658. ISSN: 18730191. DOI: 10.1016/J.MSEC.2020.110658.

[261] Eric Y. Liu, Sukwon Jung, and Hyunmin Yi. “Improved Protein Conjugation with Uniform, Macroporous Poly(acrylamide-co-acrylic acid) Hydrogel Microspheres via EDC/NHS Chemistry”. In: *Langmuir* 32 (42 2016), pp. 11043–11054. ISSN: 15205827. DOI: 10.1021/acs.langmuir.6b02591.

[262] Raquel De Castro. “Development of Biomaterials for Drug Delivery”. PhD thesis. University of Arkansas, 2021.

[263] Hui Sun and Sara Önneby. “Facile polyester surface functionalization via hydrolysis and cell-recognizing peptide attachment”. In: *Polymer International* 55 (11 2006), pp. 1336–1340. ISSN: 09598103. DOI: 10.1002/pi.2090.

[264] Maria Pau Ginebra and Edgar B. Montufar. *Cements as bone repair materials*. Woodhead Publishing Limited, 2018, pp. 233–271. ISBN: 9780081024515. DOI: 10.1016/B978-0-08-102451-5.00009-3.

[265] Stalin Kondaveeti et al. “Microbicidal gentamicin-alginate hydrogels”. In: *Carbohydrate Polymers* 186 (2018), pp. 159–167. ISSN: 0144-8617. DOI: 10.1016/J.CARBPOL.2018.01.044.

[266] In Tae Hwang et al. “Patterning of biomolecules on a poly(ϵ-caprolactone) film surface functionalized by ion implantation”. In: *Colloids and Surfaces B: Biointerfaces* 74.1 (2009), pp. 375–379. ISSN: 09277765. DOI: 10.1016/j.colsurfb.2009.08.007.

[267] Sedigheh Borandeh et al. “Polymeric drug delivery systems by additive manufacturing”. In: *Advanced Drug Delivery Reviews* 173 (2021), pp. 349–373. ISSN: 0169-409X. DOI: 10.1016/J.ADDR.2021.03.022.

[268] Owen S. Fenton et al. “Advances in Biomaterials for Drug Delivery”. In: *Advanced Materials* 30 (29 2018), pp. 1–29. ISSN: 15214095. DOI: 10.1002/adma.201705328.

[269] Zhidao Xia et al. “In vitro biodegradation of three brushite calcium phosphate cements by a macrophage cell-line”. In: *Biomaterials* 27 (26 2006), pp. 4557–4565. ISSN: 01429612. DOI: 10.1016/j.biomaterials.2006.04.030.

[270] David King and Sean McGinty. “Assessing the potential of mathematical modelling in designing drug-releasing orthopaedic implants”. In: *Journal of Controlled Release* 239 (2016), pp. 49–61. ISSN: 0168-3659. DOI: 10.1016/J.JCONREL.2016.08.009.

[271] Richard W. Korsmeyer et al. “Mechanisms of solute release from porous hydrophilic polymers”. In: *International Journal of Pharmaceutics* 15 (1 1983), pp. 25–35. ISSN: 03785173. DOI: 10.1016/0378-5173(83)90064-9.

[272] Takeru Higuchi. “Rate of Release of Medicaments from Ointment Bases Containing Drugs in Suspension”. In: *Journal of pharmaceutical sciences.* 50.10 (1961), pp. 874–875. ISSN: 0022-3549. DOI: 10.1002/jps.2600501018.

[273] Juergen Siepmann and Florence Siepmann. “Modeling of diffusion controlled drug delivery”. In: *Journal of Controlled Release* 161 (2 2012), pp. 351–362. ISSN: 01683659. DOI: 10.1016/j.jconrel.2011.10.006.

[274] Philip L. Ritger and Nikolaos A. Peppas. “A simple equation for description of solute release I. Fickian and non-fickian release from non-swellable devices in the form of slabs, spheres, cylinders or discs”. In: *Journal of Controlled Release* 5 (1 1987), pp. 23–36. ISSN: 01683659. DOI: 10.1016/0168-3659(87)90034-4.

[275] J. Siepmann and F. Siepmann. “Mathematical modeling of drug delivery”. In: *International Journal of Pharmaceutics* 364 (2 2008), pp. 328–343. ISSN: 03785173. DOI: 10.1016/j.ijpharm.2008.09.004.

[276] Uwe Gbureck, Elke Vorndran, and Jake E. Barralet. “Modeling vancomycin release kinetics from microporous calcium phosphate ceramics comparing static and dynamic immersion conditions”. In: *Acta Biomaterialia* 4 (5 2008), pp. 1480–1486. DOI: https://doi.org/10.1016/j.actbio.2008.02.027.

[277] Rajesh Kumar Ranjan et al. “Bone cement”. In:
79
International Journal of Orthopaedics Sciences 3.4 (2017), pp. 79–82. DOI: 10.22271/ortho.2017.v3.i4b.12.

[278] Richard Milner. “The development of theoretical relationships between some handling parameters (setting time and setting temperature), composition (relative amounts of initiator and activator) and ambient temperature for acrylic bone cement”. In: *Journal of Biomedical Materials Research* 68B (2 2004), pp. 180–185. ISSN: 0021-9304. DOI: 10.1002/jbm.b.20019.

[279] Wayne Nishio Ayre et al. “A novel liposomal drug delivery system for PMMA bone cements”. In: *Journal of Biomedical Materials Research - Part B Applied Biomaterials* 104 (8 2016), pp. 1510–1524. ISSN: 15524981. DOI: 10.1002/jbm.b.33488.

[280] Wayne Nishio Ayre, Stephen P. Denyer, and Samuel L. Evans. “Ageing and moisture uptake in polymethyl methacrylate (PMMA) bone cements”. In: *Journal of the Mechanical Behavior of Biomedical Materials* 32 (2014), pp. 76–88. ISSN: 1751-6161. DOI: 10.1016/J.JMBBM.2013.12.010.

[281] Tom A. G. van Vugt, Jacobus J. Arts, and Jan A. P. Geurts. “Antibiotic-Loaded Polymethylmethacrylate Beads and Spacers in Treatment of Orthopedic Infections and the Role of Biofilm Formation”. In: *Frontiers in Microbiology* 10 (2019), p. 1626. ISSN: 1664-302X. DOI: 10.3389/fmicb.2019.01626.

[282] Pang Hsin Hsieh et al. “Liquid Gentamicin and Vancomycin in Bone Cement. A Potentially More Cost-Effective Regimen”. In: *Journal of Arthroplasty* 24 (1 2009), pp. 125–130. ISSN: 08835403. DOI: 10.1016/j.arth.2008.01.131.

[283] Sandra Downes and Peter A Maughan. “Mechanism of Antibiotic Release from Poly methyl methacrylate) Bone Cement”. In: *Clinical Materials* 4 (1989), pp. 109–122. DOI: 10.1016/0267-6605(89)90002-4.

[284] L Bunetel, E Percheron, and F Langlais. “Release of Gentamicin from Acrylic Bone Cement”. In: *Clinical Pharmacokinetics* 17 (4 1989), pp. 291–297. DOI: 10.2165/00003088-198917040-00006.

[285] Hilbrand Van De Belt et al. “Infection of orthopedic implants and the use of antibiotic-loaded bone cements: A review”. In: *Acta Orthopaedica Scandinavica* (2009), pp. 557–571. ISSN: 0001-6470. DOI: 10.1080/000164701317268978.

[286] H. Van De Belt et al. “Surface roughness, porosity and wettability of gentamicin-loaded bone cements and their antibiotic release”. In: *Biomaterials* 21 (19 2000), pp. 1981–1987. ISSN: 01429612. DOI: 10.1016/S0142-9612(00)00082-X.

[287] Ekkehard W. Fritsch. “Static and fatigue properties of two new low-viscosity PMMA bone cements improved by vacuum mixing”. In: *Journal of Biomedical Materials Research* 31 (4 1996), pp. 451–456. ISSN: 00219304. DOI: 10.1002/(SICI)1097-4636(199608)31:4<451::AID-JBM3>3.0.CO;2-K.

[288] Julie M Hasenwinkel et al. “A novel high-viscosity, two-solution acrylic bone cement: Effect of chemical composition on properties”. In: *Journal of Biomedical Materials Research* 47 (1 1999), pp. 36–45. ISSN: 00219304. DOI: 10.1002/(SICI)1097-4636(199910)47:1%3C36::AID-JBM5%3E3.0.CO;2-R.

[289] Ryan C.R. Gergely et al. “Towards the optimization of the preparation procedures of PMMA bone cement”. In: *Journal of Orthopaedic Research* 34 (6 2016), pp. 915–923. ISSN: 1554527X. DOI: 10.1002/jor.23100.

[290] Maria-Pau Pau Ginebra et al. “Calcium phosphate cements as drug delivery materials”. In: *Advanced Drug Delivery Reviews* 64 (12 2012), pp. 1090–1110. ISSN: 0169409X. DOI: 10.1016/j.addr.2012.01.008.

[291] Lena Schröter et al. “Biological and mechanical performance and degradation characteristics of calcium phosphate cements in large animals and humans”. In: *Acta Biomaterialia* 117 (2020), pp. 1–20. ISSN: 18787568. DOI: 10.1016/J.ACTBIO.2020.09.031.

[292] F. C. M. Driessens et al. “In vivo behaviour of three calcium phosphate cements and a magnesium phosphate cement”. In: *Journal of Materials Science: Materials in Medicine* 6 (5 1995), pp. 272–278. ISSN: 09574530. DOI: 10.1007/BF00120270.

[293] Alberto J. Ambard and Leonard Mueninghoff. “Calcium phosphate cement: Review of mechanical and biological properties”. In: *Journal of Prosthodontics* 15 (5 2006), pp. 321–328. ISSN: 1059941X. DOI: 10.1111/j.1532-849X.2006.00129.x.

[294] E. Munting, A. A. Mirtchi, and J. Lemaitre. “Bone repair of defects filled with a phosphocalcic hydraulic cement: an in vivo study”. In: *Journal of Materials Science: Materials in Medicine* 4 (3 1993), pp. 337–344. ISSN: 09574530. DOI: 10.1007/BF00122290.

[295] Kouichito Ohura et al. “Resorption of, and bone formation from, new -tricalcium phosphate-monocalcium phosphate cements: An in vivo study”. In: *Journal of Biomedical Materials Research* 30 (2 1996), pp. 193–200. ISSN: 00219304. DOI: 10.1002/(SICI)1097-4636(199602)30:2%3C193::AID-JBM9%3E3.0.CO;2-M.

[296] Ingrid Ajaxon and Cecilia Persson. “Mechanical properties of brushite calcium phosphate cements”. In: *Frontiers in Nanobiomedical Research* 9 (2017), pp. 285–300. ISSN: 22513965. DOI: 10.1142/9789813205573_0008.

[297] Marc Bohner, Jacques Lemaitre, and Terry A Ring. “Effects of sulfate, pyrophosphate, and citrate ions on the physicochemical properties of cements made of β-tricalcium phosphate-phosphoric acid-water mixtures”. In: *Journal of the American Ceramic Society* 79.6 (1996), pp. 1427–1434. ISSN: 0002-7820. DOI: 10.1111/j.1151-2916.1996.tb08746.x.

[298] Faleh Tamimi, Zeeshan Sheikh, and Jake Barralet. “Dicalcium phosphate cements: Brushite and monetite”. In: *Acta Biomaterialia* 8 (2 2012), pp. 474–487. ISSN: 17427061. DOI: 10.1016/j.actbio.2011.08.005.

[299] M. Bohner and U. Gbureck. “Thermal reactions of brushite cements”. In: *Journal of Biomedical Materials Research - Part B Applied Biomaterials* 84 (2 2007), pp. 375–385. ISSN: 15524973. DOI: 10.1002/jbm.b.30881.

[300] Marc Bohner et al. “Gentamicin-Loaded Hydraulic Calcium Phosphate Bone Cement as Antibiotic Delivery System”. In: *Journal of Pharmaceutical Sciences* 86 (5 1997), pp. 565–572. ISSN: 00223549. DOI: 10.1021/js960405a.

[301] K. Hurle et al. “Ion-doped Brushite Cements for Bone Regeneration”. In: *Acta Biomaterialia* 123 (2021), pp. 51–71. ISSN: 18787568. DOI: 10.1016/j.actbio.2021.01.004.

[302] Aleksandra Laskus and Joanna Kolmas. “Ionic substitutions in non-apatitic calcium phosphates”. In: *International Journal of Molecular Sciences* 18 (12 2017), pp. 1–22. ISSN: 14220067. DOI: 10.3390/ijms18122542.

[303] M Bohner et al. “Effects of sulphate ions on the in vitro properties of beta-TCP-MCPM-water mixtures. Preliminary in vivo results”. In: *Ceramic Transactions* 48 (1994), pp. 245–259.

[304] Hein P. Stallmann et al. “In vitro gentamicin release from commercially available calcium-phosphate bone substitutes influence of carrier type on duration of the release profile”. In: *BMC Musculoskeletal Disorders* 7 (1 2006), pp. 1–8. ISSN: 14712474. DOI: 10.1186/1471-2474-7-18.

[305] J. E. Barralet, L. M. Grover, and U. Gbureck. "Ionic modification of calcium phosphate cement viscosity. Part II: Hypodermic injection and strength improvement of brushite cement". In: *Biomaterials* 25 (11 2004), pp. 2197–2203. ISSN: 01429612. DOI: 10.1016/j.biomaterials.2003.09.085.

[306] M. Hamdan Alkhraisat et al. "Beta-tricalcium phosphate release from brushite cement surface". In: *Journal of Biomedical Materials Research Part A* 84A (3 2008), pp. 710–717. ISSN: 15493296. DOI: 10.1002/jbm.a.31381.

[307] Jennifer L. Giocondi et al. "Molecular mechanisms of crystallization impacting calcium phosphate cements". In: *Philosophical Transactions of the Royal Society A: Mathematical, Physical and Engineering Sciences* 368 (1917 2010), pp. 1937–1961. ISSN: 1364503X. DOI: 10.1098/rsta.2010.0006.

[308] Uwe Gbureck et al. "Factors influencing calcium phosphate cement shelf-life". In: *Biomaterials* 26 (17 2005), pp. 3691–3697. ISSN: 01429612. DOI: 10.1016/j.biomaterials.2004.09.036.

[309] Mohamed Habib et al. "Mechanisms underlying the limited injectability of hydraulic calcium phosphate paste". In: *Acta Biomaterialia* 4 (5 2008), pp. 1465–1471. ISSN: 17427061. DOI: 10.1016/j.actbio.2008.03.004.

[310] Patrick Frayssinet et al. "Short-term implantation effects of a DCPD-based calcium phosphate cement". In: *Biomaterials* 19 (11-12 1998), pp. 971–977. ISSN: 01429612. DOI: 10.1016/S0142-9612(97)00163-4.

[311] B. Flautre et al. "Volume effect on biological properties of a calcium phosphate hydraulic cement: Experimental study in sheep". In: *Bone* 25 (2 SUPPL. 1 1999), 35S–39S. ISSN: 87563282. DOI: 10.1016/S8756-3282(99)00147-7.

[312] Minoru Ikenaga et al. "Biomechanical characterization of a biodegradable calcium phosphate hydraulic cement: A comparison with porous biphasic calcium phosphate ceramics". In: *Journal of Biomedical Materials Research* 40 (1 1998), pp. 139–144. ISSN: 00219304. DOI: 10.1002/(SICI)1097-4636(199804)40:1%3C139::AID-JBM16%3E3.0.CO;2-J.

[313] Liam M Grover et al. "Biologically mediated resorption of brushite cement in vitro". In: *Biomaterials* 27 (10 2006), pp. 2178–2185. ISSN: 01429612. DOI: 10.1016/J.BIOMATERIALS.2005.11.012.

[314] K. J. Lilley et al. "Cement from magnesium substituted hydroxyapatite". In: *Journal of Materials Science: Materials in Medicine* 16 (5 2005), pp. 455–460. ISSN: 09574530. DOI: 10.1007/s10856-005-6986-3.

[315] Liam M Grover et al. “The effect of amorphous pyrophosphate on calcium phosphate cement resorption and bone generation”. In: *Biomaterials* 34 (28 2013), pp. 6631–6637. ISSN: 01429612. DOI: 10.1016/j.biomaterials.2013.05.001.

[316] J. T. Zhang, F. Tancret, and J. M. Bouler. “Fabrication and mechanical properties of calcium phosphate cements (CPC) for bone substitution”. In: *Materials Science and Engineering C* 31 (4 2011), pp. 740–747. ISSN: 09284931. DOI: 10.1016/j.msec.2010.10.014.

[317] Jingtao Zhang et al. “Calcium phosphate cements for bone substitution: Chemistry, handling and mechanical properties”. In: *Acta Biomaterialia* 10 (3 2014), pp. 1035–1049. ISSN: 18787568. DOI: 10.1016/j.actbio.2013.11.001.

[318] M. P. Hofmann et al. “High-strength resorbable brushite bone cement with controlled drug-releasing capabilities”. In: *Acta Biomaterialia* 5 (1 2009), pp. 43–49. ISSN: 17427061. DOI: 10.1016/j.actbio.2008.08.005.

[319] Liam M Grover et al. “Frozen delivery of brushite calcium phosphate cements”. In: *Acta Biomaterialia* 4 (6 2008), pp. 1916–1923. ISSN: 17427061. DOI: 10.1016/j.actbio.2008.06.003.

[320] Amir A. Mirtchi, Jacques Lemaître, and E. Hunting. “Calcium phosphate cements: action of setting regulators on the properties of the -tricalcium phosphate-monocalcium phosphate cements”. In: *Biomaterials* 10 (9 1989), pp. 634–638. ISSN: 01429612. DOI: 10.1016/0142-9612(89)90120-8.

[321] Maria Pau Ginebra. *Cements as bone repair materials*. Woodhead Publishing Limited, 2009, pp. 271–308. ISBN: 9781845693855. DOI: 10.1533/9781845696610.2.271.

[322] Michal Bartnikowski et al. “Degradation mechanisms of polycaprolactone in the context of chemistry, geometry and environment”. In: *Progress in Polymer Science* 96 (2019), pp. 1–20. ISSN: 00796700. DOI: 10.1016/j.progpolymsci.2019.05.004.

[323] K Deshmukh et al. “Biopolymer composites with high dielectric performance: interface engineering”. In: *Biopolymer composites in electronics*. Elsevier, 2017, pp. 27–128. ISBN: 9780128092613. DOI: 10.1016/B978-0-12-809261-3.00003-6.

[324] NR Nair et al. “Biodegradation of biopolymers”. In: *Current developments in biotechnology and bioengineering*. Elsevier, 2017, pp. 739–755. ISBN: 9780444636621. DOI: 10.1016/B978-0-444-63662-1.00032-4.

[325] Laurence McKeen. "The effect of heat aging on the properties of sustainable polymers". In: *The Effect of Long Term Thermal Exposure on Plastics and Elastomers*. 2021, pp. 313–332. DOI: 10.1016/b978-0-323-85436-8.00001-1.

[326] Friederike von Burkersroda, Luise Schedl, and Achim Göpferich. "Why degradable polymers undergo surface erosion or bulk erosion". In: *Biomaterials* 23 (21 2002), pp. 4221–4231. ISSN: 01429612. DOI: 10.1016/S0142-9612(02)00170-9.

[327] Amaia Cipitria et al. "Design, fabrication and characterization of PCL electrospun scaffolds—a review". In: *Journal of Materials Chemistry* 21.26 (2011), pp. 9419–9453. ISSN: 09599428. DOI: 10.1039/c0jm04502k.

[328] Nicole E. Zander et al. "Quantification of protein incorporated into electrospun polycaprolactone tissue engineering scaffolds". In: *ACS Applied Materials and Interfaces* 4 (4 2012), pp. 2074–2081. ISSN: 19448244. DOI: 10.1021/am300045y.

[329] Inyoung Choi et al. "Polycaprolactone film functionalized with bacteriophage T4 promotes antibacterial activity of food packaging toward Escherichia coli". In: *Food Chemistry* 346 (September 2020 2021), p. 128883. ISSN: 18737072. DOI: 10.1016/j.foodchem.2020.128883.

[330] Vivek A.S. Ramakrishna et al. "Smart orthopaedic implants: A targeted approach for continuous postoperative evaluation in the spine". In: *Journal of Biomechanics* 104 (2020), p. 109690. ISSN: 18732380. DOI: 10.1016/j.jbiomech.2020.109690.

[331] A. Schultz et al. "Loads on the lumbar spine. Validation of a biomechanical analysis by measurements of intradiscal pressures and myoelectric signals". In: *Journal of Bone and Joint Surgery - Series A* 64.5 (1982), pp. 713–720. ISSN: 00219355. DOI: 10.2106/00004623-198264050-00008.

[332] Ichiro Takahashi et al. "Mechanical load of the lumbar spine during forward bending motion of the trunk-A biomechanical study". In: *Spine* 31.1 (2006), pp. 18–23. ISSN: 03622436. DOI: 10.1097/01.brs.0000192636.69129.fb.

[333] Antonius Rohlmann, Georg Bergmann, and Friedmar Graichen. "Loads on an internal spinal fixation device during walking". In: *Journal of Biomechanics* 30.1 (1997), pp. 41–47. ISSN: 00219290. DOI: 10.1016/S0021-9290(96)00103-0.

[334] F. Graichen, G. Bergmann, and A. Rohlmann. "Patient monitoring system for load measurement with spinal fixation devices". In: *Medical Engineering and Physics* 18.2 (1996), pp. 167–174. ISSN: 13504533. DOI: 10.1016/1350-4533(95)00030-5.

[335] A. Rohlmann et al. "Monitoring the load on a telemeterised vertebral body replacement for a period of up to 65 months". In: *European Spine Journal* 22.11 (2013), pp. 2575–2581. ISSN: 14320932. DOI: 10.1007/s00586-013-3057-1.

[336] ISO. *ISO 12189:2008*. 2008.

[337] *ISO 7206-6:2013*. 2013.

[338] G Bergmann et al. "Realistic loads for testing hip implants". In: *Bio-medical materials and engineering* 20.2 (2010), pp. 65–75. ISSN: 0959-2989.

[339] Z. Gorgin Karaji et al. "Additively Manufactured and Surface Biofunctionalized Porous Nitinol". In: *ACS Applied Materials Interfaces* 9 (2 2016), pp. 1293–1304. ISSN: 1944-8244. DOI: 10.1021/acsami.6b14026.

[340] E. Vanderleyden et al. "Gelatin functionalised porous titanium alloy implants for orthopaedic applications". In: *Materials Science and Engineering: C* 42 (2014), pp. 396–404. ISSN: 09284931. DOI: 10.1016/j.msec.2014.05.048.

[341] Michiel Croes et al. "A multifaceted biomimetic interface to improve the longevity of orthopedic implants". In: *Acta Biomaterialia* 110 (2020), pp. 266–279. ISSN: 18787568. DOI: 10.1016/J.ACTBIO.2020.04.020.

[342] B Gorny et al. "In situ characterization of the deformation and failure behavior of non-stochastic porous structures processed by selective laser melting". In: *Materials Science Engineering A* 528 (2011), pp. 7962–7967. DOI: 10.1016/j.msea.2011.07.026.

[343] Pei Yao Li et al. "Fracture and failure behavior of additive manufactured Ti6Al4V lattice structures under compressive load". In: *Engineering Fracture Mechanics* 244 (August 2020 2021). ISSN: 00137944. DOI: 10.1016/j.engfracmech.2021.107537.

[344] Seyed Ahmadi et al. "Additively Manufactured Open-Cell Porous Biomaterials Made from Six Different Space-Filling Unit Cells: The Mechanical and Morphological Properties". In: *Materials* 8 (4 2015), pp. 1871–1896. ISSN: 1996-1944. DOI: 10.3390/ma8041871.

[345] Sing Ying Choy et al. "Compressive properties of Ti-6Al-4V lattice structures fabricated by selective laser melting: Design, orientation and density". In: *Additive Manufacturing* 16 (2017), pp. 213–224. ISSN: 2214-8604. DOI: 10.1016/J.ADDMA.2017.06.012.

[346] Jinguo Ge et al. "Microstructural features and compressive properties of SLM Ti6Al4V lattice structures". In: *Surface and Coatings Technology* 403 (August 2020), p. 126419. ISSN: 02578972. DOI: 10.1016/j.surfcoat.2020.126419.

[347] L.J. Gibson. "The mechanical behaviour of cancellous bone". In: *Journal of Biomechanics* 18 (5 1985), pp. 317–328. ISSN: 00219290. DOI: 10.1016/0021-9290(85)90287-8.

[348] Ruben Wauthle et al. “Revival of pure titanium for dynamically loaded porous implants using additive manufacturing”. In: *Materials Science and Engineering: C* 54 (2015), pp. 94–100. ISSN: 0928-4931. DOI: 10.1016/J.MSEC.2015.05.001.

[349] Hanna E. Burton, Sean Peel, and Dominic Eggbeer. “Reporting fidelity in the literature for computer aided design and additive manufacture of implants and guides”. In: *Additive Manufacturing* 23 (2018), pp. 362–373. ISSN: 2214-8604. DOI: 10.1016/J.ADDMA.2018.08.027.

[350] Oraib Al-Ketan, Reza Rowshan, and Rashid K. Abu Al-Rub. “Topology-mechanical property relationship of 3D printed strut, skeletal, and sheet based periodic metallic cellular materials”. In: *Additive Manufacturing* 19 (2018), pp. 167–183. ISSN: 22148604. DOI: 10.1016/j.addma.2017.12.006.

[351] Jan Wieding, Anika Jonitz, and Rainer Bader. “The effect of structural design on mechanical properties and cellular response of additive manufactured titanium scaffolds”. In: *Materials* 5 (8 2012), pp. 1336–1347. ISSN: 19961944. DOI: 10.3390/ma5081336.

[352] Joep de Krijger et al. “Effects of applied stress ratio on the fatigue behavior of additively manufactured porous biomaterials under compressive loading”. In: *Journal of the Mechanical Behavior of Biomedical Materials* 70 (2017), pp. 7–16. ISSN: 18780180. DOI: 10.1016/j.jmbbm.2016.11.022.

[353] Sabina Campanelli et al. “Manufacturing and Characterization of Ti6Al4V Lattice Components Manufactured by Selective Laser Melting”. In: *Materials* 7 (6 2014), pp. 4803–4822. ISSN: 1996-1944. DOI: 10.3390/ma7064803.

[354] Ahmad Alghamdi et al. “Buckling phenomena in AM lattice strut elements: A design tool applied to Ti-6Al-4V LB-PBF”. In: *Materials Design* 208 (2021), p. 109892. ISSN: 0264-1275. DOI: 10.1016/J.MATDES.2021.109892.

[355] Xin Shi et al. “Comparison of Compression Performance and Energy Absorption of Lattice Structures Fabricated by Selective Laser Melting”. In: *Advanced Engineering Materials* 22 (11 2020), pp. 1–9. ISSN: 15272648. DOI: 10.1002/adem.202000453.

[356] Kenichi Nakanishi et al. “Mechanical properties of the hollow-wall graphene gyroid lattice”. In: *Acta Materialia* 201 (2020), pp. 254–265. ISSN: 13596454. DOI: 10.1016/j.actamat.2020.09.077.

[357] Lucas R. Meza et al. “Reexamining the mechanical property space of three-dimensional lattice architectures”. In: *Acta Materialia* 140 (2017), pp. 424–432. ISSN: 13596454. DOI: 10.1016/j.actamat.2017.08.052.

[358] M. Smith, Z. Guan, and W.J. Cantwell. "Finite element modelling of the compressive response of lattice structures manufactured using the selective laser melting technique". In: *International Journal of Mechanical Sciences* 67 (2013), pp. 28–41. ISSN: 0020-7403. DOI: 10.1016/j.ijmecsci.2012.12.004.

[359] Tianyu Yu et al. "Structure-property relationship in high strength and lightweight AlSi10Mg microlattices fabricated by selective laser melting". In: *Materials Design* 182 (2019), p. 108062. ISSN: 0264-1275. DOI: 10.1016/J.MATDES.2019.108062.

[360] Holden Hyer et al. "High strength WE43 microlattice structures additively manufactured by laser powder bed fusion". In: *Materialia* 16 (2021), p. 101067. ISSN: 2589-1529. DOI: 10.1016/j.mtla.2021.101067.

[361] Akshay Namdeo et al. "Tetrahedral and strut-reinforced tetrahedral microlattices: Selectively laser melted high-strength and high-stiffness cellular metamaterials". In: *Materials Science and Engineering: A* (2022), p. 143878. ISSN: 09215093. DOI: 10.1016/J.MSEA.2022.143878.

[362] Jin Li, Guoqiang Jiang, and Fuxin Ding. "Effects of Polymer Degradation on Drug Release from PLGA-mPEG Microparticles: A Dynamic Study of Microparticle Morphological and Physicochemical Properties". In: *Journal of Applied Polymer Science* 108 (2008), pp. 2458–2466. ISSN: 00218995. DOI: 10.1002/app.27823.

[363] S.J. J. Li et al. "Influence of cell shape on mechanical properties of Ti6Al4V meshes fabricated by electron beam melting method". In: *Acta Biomaterialia* 10 (10 2014), pp. 4537–4547. ISSN: 1742-7061. DOI: 10.1016/J.ACTBIO.2014.06.010.

[364] Shuai Ma et al. "Mechanical behaviours and mass transport properties of bone-mimicking scaffolds consisted of gyroid structures manufactured using selective laser melting". In: *Journal of the Mechanical Behavior of Biomedical Materials* 93 (August 2018 2019), pp. 158–169. ISSN: 18780180. DOI: 10.1016/j.jmbbm.2019.01.023.

[365] I Maskery et al. "Compressive failure modes and energy absorption in additively manufactured double gyroid lattices". In: *Additive Manufacturing* 16 (2017), pp. 24–29. ISSN: 22148604. DOI: 10.1016/j.addma.2017.04.003.

[366] A. B. Sturm, P. Visintin, and D. J. Oehlers. "Design-Oriented Solutions for the Shear Capacity of Reinforced Concrete Beams with and without Fibers". In: *Journal of Structural Engineering* 147 (6 2021), p. 04021066. ISSN: 0733-9445. DOI: 10.1061/(asce)st.1943-541x.0003023.

[367] Lima Corporate. *Delta TT Cup*.

[368] M. Dallago et al. “The role of node fillet, unit-cell size and strut orientation on the fatigue strength of Ti-6Al-4V lattice materials additively manufactured via laser powder bed fusion”. In: *International Journal of Fatigue* 142 (June 2020 2021), p. 105946. ISSN: 01421123. DOI: 10.1016/j.ijfatigue.2020.105946.

[369] L Lindberg et al. “The release of gentamicin after total hip replacement using low or high viscosity bone cement A prospective, randomized study”. In: *International Orthopaedics (SICOT)* 15 (1991), pp. 305–309. ISSN: 14325195. DOI: 10.1007/BF00186866.

[370] H. Wahlig et al. “Pharmacokinetic study of gentamicin-loaded cement in total hip replacements. Comparative effects of varying dosage”. In: *Journal of Bone and Joint Surgery - Series B* 66 (2 1984), pp. 175–179. ISSN: 0301620X. DOI: 10.1302/0301-620x.66b2.6707051.

[371] C. Torholm et al. “Total hip joint arthroplasty with gentamicin-impregnated cement. A clinical study of gentamicin excretion kinetics”. In: *Clinical Orthopaedics and Related Research* NO. 181 (181 1983), pp. 99–106. ISSN: 0009921X. DOI: 10.1097/00003086-198312000-00014.

[372] Jia Lv et al. “Enhanced angiogenesis and osteogenesis in critical bone defects by the controlled release of BMP-2 and VEGF: Implantation of electron beam melting-fabricated porous Ti 6 Al 4 V scaffolds incorporating growth factor-doped fibrin glue”. In: *Biomedical Materials (Bristol)* 10 (3 2015). ISSN: 1748605X. DOI: 10.1088/1748-6041/10/3/035013.

[373] J. Van Der Stok et al. “Full regeneration of segmental bone defects using porous titanium implants loaded with BMP-2 containing fibrin gels”. In: *European Cells and Materials* 29 (2015), pp. 141–154. ISSN: 14732262. DOI: 10.22203/eCM.v029a11.

[374] Maria Rosa Virto et al. “Improvement of gentamicin poly(d,l-lactic-co-glycolic acid) microspheres for treatment of osteomyelitis induced by orthopedic procedures”. In: *Biomaterials* 28 (5 2007), pp. 877–885. ISSN: 01429612. DOI: 10.1016/j.biomaterials.2006.09.045.

[375] Marc Roth. “Fluorescence Reaction for Amino Acids”. In: *Analytical Chemistry* 43 (7 1971), pp. 880–882. ISSN: 15206882. DOI: 10.1021/ac60302a020.

[376] Wayne Nishio Ayre. “Novel approaches to the development of PMMA bone cement”. PhD thesis. Cardiff, 2013.

[377] European Medicines Agency EMA. *ICH Topic Q 2 (R1) Validation of Analytical Procedures: Text and Methodology*. 1995.

[378] Shih Ming Liu et al. “In vitro evaluation of calcium phosphate bone cement composite hydrogel beads of cross-linked gelatin-alginate with gentamicin-impregnated porous scaffold”. In: *Pharmaceuticals* 14 (10 2021), p. 1000. ISSN: 14248247. DOI: 10.3390/ph14101000.

[379] Suchitra S. Sampath and Dennis H. Robinson. “Comparison of new and existing spectrophotometric methods for the analysis of tobramycin and other aminoglycosides”. In: *Journal of Pharmaceutical Sciences* 79 (5 1990), pp. 428–431. ISSN: 15206017. DOI: 10.1002/jps.2600790514.

[380] Lei Long et al. “Effects of Human Serum Albumin on the Fluorescence Intensity and Tumor Imaging Properties of IR-780 Dye”. In: *Photochemistry and Photobiology* 98 (4 2022), pp. 935–944. ISSN: 17511097. DOI: 10.1111/php.13547.

[381] Knauer. *Determination of Amino acids by UHPLC with automated OPA- Derivatization by the Autosampler*. 2012.

[382] Jonathan Ernest Lacy. “Analytical and chromatographic studies on aminoglycoside antibiotics”. PhD thesis. University of Bath, 1984.

[383] Ali Taha Saleh, Lee Siew Ling, and Rafaqat Hussain. “Injectable magnesium-doped brushite cement for controlled drug release application”. In: *Journal of Materials Science* 51 (16 2016), pp. 7427–7439. ISSN: 15734803. DOI: 10.1007/s10853-016-0017-2.

[384] Marc Bohner et al. “Control of gentamicin release from a calcium phosphate cement by admixed poly(acrylic acid)”. In: *Journal of Pharmaceutical Sciences* 89 (10 2000), pp. 1262–1270. ISSN: 00223549. DOI: 10.1002/1520-6017(200010)89:10<1262::AID-JPS4>3.0.CO;2-7.

[385] M. R. Virto et al. “Gentamicin release from modified acrylic bone cements with lactose and hydroxypropylmethylcellulose”. In: *Biomaterials* 24 (1 2003), pp. 79–87. ISSN: 01429612. DOI: 10.1016/S0142-9612(02)00254-5.

[386] Susana Torrado, Paloma Frutos, and Gloria Frutos. “Gentamicin bone cements: characterisation and release (in vitro and in vivo assays)”. In: *International Journal of Pharmaceutics* 217 (1-2 2001), pp. 57–69. ISSN: 0378-5173. DOI: 10.1016/S0378-5173(01)00587-7.

[387] AS Baker and LW Greenham. “Release of gentamicin from acrylic bone cement. Elution and diffusion studies”. In: *Journal of Bone and Joint Surgery* 70.10 (1988), pp. 1551–1557.

[388] M. Bohner et al. “Effect of several additives and their admixtures on the physicochemical properties of a calcium phosphate cement”. In: *Journal of Materials Science: Materials in Medicine* 11 (2 2000), pp. 111–116. ISSN: 09574530. DOI: 10.1023/A:1008997118576.

[389] R O’Neill et al. “Critical review: Injectability of calcium phosphate pastes and cements”. In: *Acta biomaterialia* 50 (2017), pp. 1–19. ISSN: 0793-0283. DOI: 10.1515/hc.2006.12.5.300.

[390] Elisa Boanini et al. “Synthesis and Hydrolysis of Brushite (DCPD): The Role of Ionic Substitution”. In: *Crystal Growth & Design* 21 (2021), pp. 1689–1697. DOI: 10.1021/acs.cgd.0c01569.

[391] LM Grover et al. “In vitro ageing of brushite calcium phosphate cement”. In: *Biomaterials* 24 (23 2003), pp. 4133–4141. ISSN: 01429612. DOI: 10.1016/S0142-9612(03)00293-X.

[392] Y. N. Tan et al. “Controlling degradation in calcium phosphate cements”. In: *Advances in Applied Ceramics* 110 (8 2011), pp. 457–463. ISSN: 17436753. DOI: 10.1179/1743676111Y.0000000034.

[393] E. Vorndran et al. “Ready-to-use injectable calcium phosphate bone cement paste as drug carrier”. In: *Acta Biomaterialia* 9 (12 2013), pp. 9558–9567. DOI: 10.1016/j.actbio.2013.08.009.

[394] Ruth Meißner et al. “Bioprinted 3D calcium phosphate scaffolds with gentamicin releasing capability”. In: *Ceramics International* 45 (6 2019), pp. 7090–7094. ISSN: 02728842. DOI: 10.1016/j.ceramint.2018.12.212.

[395] JACKSON GG RUBENIS M KOZIJ VM. “LABORATORY STUDIES ON GENTAMICIN.” In: *Antimicrobial Agents and Chemotherapy* 161 (1963), pp. 153–156.

[396] U. Joosten et al. “Evaluation of an in situ setting injectable calcium phosphate as a new carrier material for gentamicin in the treatment of chronic osteomyelitis: Studies in vitro and in vivo”. In: *Biomaterials* 25 (18 2004), pp. 4287–4295. ISSN: 01429612. DOI: 10.1016/j.biomaterials.2003.10.083.

[397] Carl W. Norden and Elizabeth Kennedy. “Experimental osteomyelitis. I. A description of the model”. In: *Journal of Infectious Diseases* 122 (5 1970), pp. 410–418. ISSN: 15376613. DOI: 10.1093/infdis/122.5.410.

[398] Wenge Jiang et al. “Biomimetically triggered inorganic crystal transformation by biomolecules: A new understanding of biomineralization”. In: *Journal of Physical Chemistry B* 113 (31 2009), pp. 10838–10844. ISSN: 15206106. DOI: 10.1021/jp904633f.

[399] G. Cama et al. “Tailoring brushite for in situ setting bone cements”. In: *Materials Chemistry and Physics* 130 (3 2011), pp. 1139–1145. ISSN: 02540584. DOI: 10.1016/j.matchemphys.2011.08.047.

[400] A. Valero et al. “Modelling the growth boundaries of Staphylococcus aureus: Effect of temperature, pH and water activity”. In: *International Journal of Food Microbiology* 133 (1-2 2009), pp. 186–194. ISSN: 01681605. DOI: 10.1016/j.ijfoodmicro.2009.05.023.

[401] Haluk Beyenal, Suet Nee Chen, and Zbigniew Lewandowski. “The double substrate growth kinetics of Pseudomonas aeruginosa”. In: *Enzyme and Microbial Technology* 32 (2003), pp. 92–98. ISSN: 0141-0229. DOI: 10.1016/S0141-0229(02)00246-6.

[402] M. Seto and K. Misawa. “Growth rate, biomass production and carbon balance of Pseudomonas aeruginosa in a glucose-limited medium at temperature and osmotic pressure extremes.” In: *Japanese Journal of Ecology* 32 (3 1982), pp. 365–371. ISSN: 00215007. DOI: 10.18960/seitai.32.3_365.

[403] Masoumeh Haghbin-Nazarpak et al. “Preparation, characterization and gentamicin sulfate release investigation of biphasic injectable calcium phosphate bone cement”. In: *Ceramics - Silikaty* 54 (4 2010), pp. 334–340. ISSN: 08625468.

[404] E. P. Lautenschlager et al. “Mechanical strength of acrylic bone cements impregnated with antibiotics”. In: *Journal of Biomedical Materials Research* 10 (6 1976), pp. 837–845. ISSN: 10974636. DOI: 10.1002/jbm.820100603.

[405] E. P. Lautenschlager et al. “Mechanical properties of bone cements containing large doses of antibiotic powders”. In: *Journal of Biomedical Materials Research* 10 (6 1976), pp. 929–938. ISSN: 10974636. DOI: 10.1002/jbm.820100610.

[406] Russell C. Nelson, Richard O. Hoffman, and Thomas A. Burton. “The Effect of Antibiotic Additions on the Mechanical Properties of Acrylic Cement”. In: *Journal of Biomedical Materials Research* 12 (4 1978), pp. 473–490. ISSN: 16609336. DOI: 10.1002/jbm.820120403.

[407] Brian Salazar et al. “Polymer lattice-reinforcement for enhancing ductility of concrete”. In: *Materials and Design* 196 (2020), p. 109184. ISSN: 18734197. DOI: 10.1016/j.matdes.2020.109184.

[408] Wenfeng Hao, Junwei Liu, and Humaira Kanwal. “Compressive properties of cementitious composites reinforced by 3D printed PA 6 lattice”. In: *Polymer Testing* 117 (October 2022 2023), p. 107811. ISSN: 01429418. DOI: 10.1016/j.polymertesting.2022.107811.

[409] Jessica A. Rosewitz, Habibeh Ashouri Choshali, and Nima Rahbar. “Bioinspired design of architected cement-polymer composites”. In: *Cement and Concrete Composites* 96 (February 2019 2019), pp. 252–265. ISSN: 09589465. DOI: 10.1016/j.cemconcomp.2018.12.010.

[410] M. R. Bambach et al. “Hollow and concrete filled steel hollow sections under transverse impact loads”. In: *Engineering Structures* 30 (10 2008), pp. 2859–2870. ISSN: 01410296. DOI: 10.1016/j.engstruct.2008.04.003.

[411] Mohammad Yousuf et al. “Transverse impact resistance of hollow and concrete filled stainless steel columns”. In: *Journal of Constructional Steel Research* 82 (2013), pp. 177–189. ISSN: 0143974X. DOI: 10.1016/j.jcsr.2013.01.005.

[412] Yong Ye et al. “Experimental behaviour of concrete-filled steel tubular members under lateral shear loads”. In: *Journal of Constructional Steel Research* 122 (2016), pp. 226–237. ISSN: 0143974X. DOI: 10.1016/j.jcsr.2016.03.012.

[413] Yu Wang et al. “Experimental behavior of cement filled pipe-in-pipe composite structures under transverse impact”. In: *International Journal of Impact Engineering* 72 (2014), pp. 1–16. ISSN: 0734743X. DOI: 10.1016/j.ijimpeng.2014.05.004.

[414] Ramin Raoufinia et al. “Overview of albumin and its purification methods”. In: *Advanced Pharmaceutical Bulletin* 6 (4 2016), pp. 495–507. ISSN: 22517308. DOI: 10.15171/apb.2016.063.

[415] Sandeep J Sonawane, Rahul S Kalhapure, and Thirumala Govender. “Hydrazone linkages in pH responsive drug delivery systems”. In: *European Journal of Pharmaceutical Sciences* 99 (2017), pp. 45–65. ISSN: 18790720. DOI: 10.1016/j.ejps.2016.12.011.

[416] Michał G. Nowak, Andrzej S. Skwarecki, and Maria J. Milewska. “Amino Acid Based Antimicrobial Agents – Synthesis and Properties”. In: *ChemMedChem* 16.23 (2021), pp. 3513–3544. ISSN: 18607187. DOI: 10.1002/cmdc.202100503.

[417] Nicole K. Brogden and Kim A. Brogden. “Will new generations of modified antimicrobial peptides improve their potential as pharmaceuticals?” In: *International Journal of Antimicrobial Agents* 38 (3 2011), pp. 217–225. ISSN: 18727913. DOI: 10.1016/j.ijantimicag.2011.05.004.

[418] Beer. “Bestimmung der Absorption des rothen Lichts in farbigen Flüssigkeiten”. In: *Annalen der Physik* 162 (5 1852), pp. 78–88. ISSN: 0003-3804. DOI: 10.1002/andp.18521620505.

[419] Johann Heinrich Lambert. *Photometria sive de mensura et gradibus luminis, colorum et umbrae*. sumptibus vidvae E. Klett, typis CP Detleffsen, 1760.

[420] Amin Razeghiyadaki et al. “Modeling of material removal rate and surface roughness generated during electro-discharge machining”. In: *Machines* 7 (2 2019), pp. 1–17. ISSN: 20751702. DOI: 10.3390/machines7020047.

[421] Neeraj Ahuja, Uma Batra, and Kamal Kumar. “Experimental Investigation and Optimization of Wire Electrical Discharge Machining for Surface Characteristics and Corrosion Rate of Biodegradable Mg Alloy”. In: *Journal of Materials Engineering and Performance* 29 (6 2020), pp. 4117–4129. ISSN: 15441024. DOI: 10.1007/s11665-020-04905-8.

[422] J. W. Murray and A. T. Clare. “Repair of EDM induced surface cracks by pulsed electron beam irradiation”. In: *Journal of Materials Processing Technology* 212 (12 2012), pp. 2642–2651. ISSN: 09240136. DOI: 10.1016/j.jmatprotec.2012.07.018.

[423] Mohd Faiz Mohd Yusoff et al. “Dipcoating of poly (-caprolactone)/hydroxyapatite composite coating on Ti6Al4V for enhanced corrosion protection”. In: *Surface and Coatings Technology* 245 (2014), pp. 102–107. ISSN: 02578972. DOI: 10.1016/j.surfcoat.2014.02.048.

[424] Carolina Cruz Ferreira et al. “Improvement of titanium corrosion resistance by coating with poly-caprolactone and poly-caprolactone/titanium dioxide: Potential application in heart valves”. In: *Materials Research* 20 (2017), pp. 126–133. ISSN: 15161439. DOI: 10.1590/1980-5373-MR-2017-0425.

[425] Anita Ioana Visan et al. “Long-term evaluation of dip-coated PCL-blend-PEG coatings in simulated conditions”. In: *Polymers* 12 (3 2020), p. 717. ISSN: 20734360. DOI: 10.3390/polym12030717.

[426] Zhihui Zhang et al. “Adhesion and corrosion resistance of polycaprolactone coating on NiTi alloy surface after alkali heat pretreatment”. In: *Biosurface and Biotribology* 8 (4 2022), pp. 307–314. ISSN: 24054518. DOI: 10.1049/bsb2.12051.

[427] Julia Matena et al. “Comparison of selective laser melted titanium and magnesium implants coated with PCL”. In: *International Journal of Molecular Sciences* 16 (6 2015), pp. 13287–13301. ISSN: 14220067. DOI: 10.3390/ijms160613287.

[428] Michael Grau et al. “In vitro evaluation of PCL and P(3HB) as coating materials for selective laser melted porous titanium implants”. In: *Materials* 10 (12 2017), p. 1344. ISSN: 19961944. DOI: 10.3390/ma10121344.

[429] Ding Fwu Lii et al. “Formation of BN films on carbon fibers by dip-coating”. In: *Surface and Coatings Technology* 150 (2-3 2002), pp. 269–276. ISSN: 02578972. DOI: 10.1016/S0257-8972(01)01539-0.

[430] Mario Iván Peñas et al. “Nanostructural organization of thin films prepared by sequential dip-coating deposition of poly(butylene succinate), poly(-caprolactone) and their copolyesters (PBS-ran-PCL)”. In: *Polymer* 226 (January 2021). ISSN: 00323861. DOI: 10.1016/j.polymer.2021.123812.

[431] In-Tae Hwang et al. “Efficient immobilization and patterning of biomolecules on Poly(ethylene terephthalate) films functionalized by ion irradiation for biosensor applications”. In: *ACS Applied Materials and Interfaces* 3 (7 2011), pp. 2235–2239. ISSN: 19448244. DOI: 10.1021/am200630p.

[432] Andrew D. Nisbet et al. “The Complete Amino-Acid Sequence of Hen Ovalbumin”. In: *European Journal of Biochemistry* 115 (2 1981), pp. 335–345. ISSN: 14321033. DOI: 10.1111/j.1432-1033.1981.tb05243.x.

[433] Anna Sułkowska. “Interaction of drugs with bovine and human serum albumin”. In: *Journal of Molecular Structure* 614 (1-3 2002), pp. 227–232. ISSN: 0022-2860. DOI: 10.1016/S0022-2860(02)00256-9.

[434] Patrik R. Callis. “Binding phenomena and fluorescence quenching. II: Photophysics of aromatic residues and dependence of fluorescence spectra on protein conformation”. In: *Journal of Molecular Structure* 1077 (2014), pp. 22–29. ISSN: 00222860. DOI: 10.1016/j.molstruc.2014.04.051.

[435] Laura H. Lucas et al. “Probing protein structure and dynamics by second-derivative ultraviolet absorption analysis of cation- interactions”. In: *Protein Science* 15 (10 2006), pp. 2228–2243. ISSN: 09618368. DOI: 10.1110/ps.062133706.

[436] Rahul Chib et al. “Effect of quencher, denaturants, temperature and pH on the fluorescent properties of BSA protected gold nanoclusters”. In: *Journal of luminescence* 168 (2015), pp. 62–68. DOI: 10.1016/j.jlumin.2015.07.030.

[437] Xue Ling Cao et al. “PH-Induced conformational changes of BSA in fluorescent AuNCs@BSA and its effects on NCs emission”. In: *Vibrational Spectroscopy* 65 (2013), pp. 186–192. ISSN: 09242031. DOI: 10.1016/j.vibspec.2013.01.004.

[438] K. Baler et al. “Electrostatic Unfolding and Interactions of Albumin Driven by pH Changes: A Molecular Dynamics Study”. In: *The Journal of Physical Chemistry. B* 118 (4 2014), p. 921. DOI: 10.1021/JP409936V.

[439] J. C. Lewis et al. “Amino acid composition of egg proteins.” In: *The Journal of biological chemistry* 186 (1 1950), pp. 23–35. ISSN: 00219258. DOI: 10.1016/s0021-9258(18)56283-9.

[440] Shahin Homaeigohar et al. “Biomimetic biohybrid nanofibers containing bovine serum albumin as a bioactive moiety for wound dressing”. In: *Materials Science and Engineering C* 123 (2021), p. 111965. ISSN: 18730191. DOI: 10.1016/j.msec.2021.111965.

[441] Omowumi D. Agboola and Nsikak U. Benson. “Physisorption and Chemisorption Mechanisms Influencing Micro (Nano) Plastics-Organic Chemical Contaminants Interactions: A Review”. In: *Frontiers in Environmental Science* 9 (May 2021), pp. 1–27. ISSN: 2296665X. DOI: 10.3389/fenvs.2021.678574.

[442] Colin G. Pitt and Gu Zhong-wei. “Modification of the rates of chain cleavage of poly(-caprolactone) and related polyesters in the solid state”. In: *Journal of Controlled Release* 4 (4 1987), pp. 283–292. ISSN: 01683659. DOI: 10.1016/0168-3659(87)90020-4.

[443] Alexis Oliva et al. “Stability Study of Human Serum Albumin Pharmaceutical Preparations”. In: *Journal of Pharmacy and Pharmacology* 51 (4 2010), pp. 385–392. ISSN: 0022-3573. DOI: 10.1211/0022357991772574.

[444] Rolf Wetzel et al. “Temperature Behaviour of Human Serum Albumin”. In: *European Journal of Biochemistry* 104 (2 1980), pp. 469–478. ISSN: 14321033. DOI: 10.1111/j.1432-1033.1980.tb04449.x.

[445] Hiroki Jozawa et al. “Amorphous protein aggregation monitored using fluorescence self-quenching”. In: *FEBS Letters* 590 (20 2016), pp. 3501–3509. ISSN: 18733468. DOI: 10.1002/1873-3468.12439.

[446] Naoki Nakajima and Yoshito Ikada. “Mechanism of Amide Formation by Carbodiimide for Bioconjugation in Aqueous Media”. In: *Bioconjugate Chemistry* 6 (1 1995), pp. 123–130. ISSN: 15204812. DOI: 10.1021/bc00031a015.

[447] Stefano Perni and Polina Prokopovich. “Continuous release of gentamicin from gold nanocarriers”. In: *Royal Society of Chemistry Advances* 4 (94 2014), pp. 51904–51910. ISSN: 20462069. DOI: 10.1039/c4ra10023a.

[448] Greg T. Hermanson. “(Strept)avidin –Biotin Systems”. In: *Bioconjugate Techniques*. Academic press, 2013, pp. 465–505. ISBN: 9780123822390. DOI: 10.1016/b978-0-12-382239-0.00011-x.

[449] Wenwei Lin and Taosheng Chen. “Using TR-FRET to Investigate Protein–Protein Interactions: A Case Study of PXR-Coregulator Interaction”. In: *Advances in Protein Chemistry and Structural Biology* 110 (January 2018), pp. 31–63. ISSN: 18761631. DOI: 10.1016/bs.apcsb.2017.06.001.

[450] Lucy A. Bosworth and Sandra Downes. "Physicochemical characterisation of degrading polycaprolactone scaffolds". In: *Polymer Degradation and Stability* 95 (12 2010), pp. 2269–2276. ISSN: 01413910. DOI: 10.1016/j.polymdegradstab.2010.09.007.

[451] Ling Sheng Jang and Hao Kai Keng. "Modified fabrication process of protein chips using a short-chain self-assembled monolayer". In: *Biomedical Microdevices* 10 (2 2008), pp. 203–211. ISSN: 13872176. DOI: 10.1007/s10544-007-9126-7.

[452] James V. Staros. "N-Hydroxysulfosuccinimide Active Esters : Bis (N-hydroxysulfosuccinimide) Esters of Two Dicarboxylic Acids Are Hydrophilic, Membrane- Impermeant, Protein Cross-Linkers". In: *Biochemistry* 21 (1981 1982), pp. 3950–3955. ISSN: 0006-2960. DOI: 10.1021/bi00260a008.

[453] Zenon Grabarek and John Gergely. "Zero-length crosslinking procedure with the use of active esters". In: *Analytical Biochemistry* 185 (1 1990), pp. 131–135. ISSN: 10960309. DOI: 10.1016/0003-2697(90)90267-D.

[454] James V Staros. "Membrane-Impermeant Cross-Linking Reagents: Probes of the Structure and Dynamics of Membrane Proteins". In: *Accounts of Chemical Research* 21 (12 1988), pp. 435–441. ISSN: 15204898. DOI: 10.1021/ar00156a001.

[455] Jeong Yeol Yoon et al. "Adsorption of BSA on highly carboxylated microspheres - Quantitative effects of surface functional groups and interaction forces". In: *Journal of Colloid and Interface Science* 177 (2 1996), pp. 613–620. ISSN: 00219797. DOI: 10.1006/jcis.1996.0075.

[456] Mohidus Samad Khan et al. "Biosurface engineering through ink jet printing". In: *Colloids and Surfaces B: Biointerfaces* 75 (2 2010), pp. 441–447. ISSN: 09277765. DOI: 10.1016/j.colsurfb.2009.09.032.

[457] Dimuthu Bogahawaththa and Todor Vasiljevic. "Shear-induced structural changes and denaturation of bovine immunoglobulin G and serum albumin at different temperatures". In: *Food Hydrocolloids* 124 (PA 2022), p. 107283. ISSN: 0268005X. DOI: 10.1016/j.foodhyd.2021.107283.

APPENDIX A

LATTICE SAMPLES

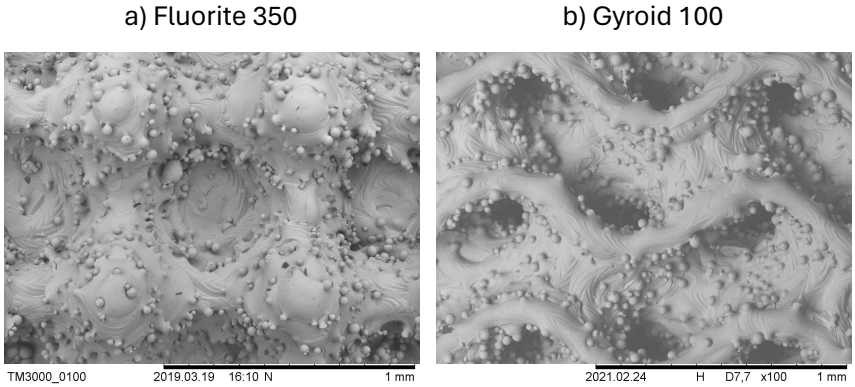

Figure A.1: SEM micrographs of a) Fluorite 350 to show that the struts are sufficiently thick to have created a closed cell structure and b) Gyroid 100 showing the uneven wall thickness making measurement challenging

Table A1: Table of sample parameters for unit cell comparison study

Sample Name	Unit Cell	Unit Cell Length / mm	Designed Strut Thickness /μm	Sample Height /mm	Sample Diameter /mm	Compression Tester	Design Volume Fraction /%
BCC 150	BCC	1	150	15	12	Universal	9.3
BCC 250	BCC	1	250	15	12	Universal	23.7
BCC 350	BCC	1	350	15	12	ESH	44.7
BCCZ 150	BCCZ	1	150	15	12	Universal	10.8
BCCZ 250	BCCZ	1	250	15	12	Universal	27.7
BCCZ 350	BCCZ	1	350	15	12	ESH	51.1
Cubic 150	Cubic	1	150	15	12	Universal	4.3
Cubic 250	Cubic	1	250	15	12	Universal	11.5
Cubic 350	Cubic	1	350	15	12	Universal	21.6
Diamond 150	Diamond	1	150	15	12	Universal	9.7
Diamond 250	Diamond	1	250	15	12	Universal	25.6
Diamond 350	Diamond	1	350	15	12	ESH	46.1
Fluorite 150	Fluorite	1	150	15	12	Universal	17.9
Fluorite 250	Fluorite	1	250	15	12	ESH	44.0
Fluorite 350	Fluorite	1	350	15	12	ESH	92.3
Gyroid 60	Gyroid	1	60	15	12	ESH	19.3
Gyroid 100	Gyroid	1	100	15	12	ESH	32.3
Gyroid 150	Gyroid	1	150	15	12	ESH	48.8
Gyroid 200	Gyroid	1	200	15	12	ESH	65.9
Gyroid 250	Gyroid	1	250	15	12	ESH	83.9

Table A2: Sample parameters for study of the influence of build rotation on compressive strength

Sample Name	Unit Cell Length / mm	Designed Strut Thickness /μm	Sample Size / mm	Compression Tester	Design Volume Fraction /%	BCCZ Z Strut Orientation During Build /°	BCCZ Z Strut Orientation During Compression /°
BCCZ 0	1	250	H 15, D 12	Universal	27.7	0	0
BCCZ 10	1	250	H 15, D 12	Universal	27.7	10	0
BCCZ 20	1	250	H 15, D 12	Universal	27.7	20	0
BCCZ 30	1	250	H 15, D 12	Universal	27.7	30	0
Diamond 0	1	250	H 15, D 12	Universal	25.6	0	0
Diamond 10	1	250	H 15, D 12	Universal	25.6	10	0
Diamond 20	1	250	H 15, D 12	Universal	25.6	20	0
Diamond 30	1	250	H 15, D 12	Universal	25.6	30	0
Gyroid 0	1	150	H 15, D 12	ESH	48.8	0	0
Gyroid 10	1	150	H 15, D 12	ESH	48.8	10	0
Gyroid 20	1	150	H 15, D 12	ESH	48.8	20	0
Gyroid 30	1	150	H 15, D 12	ESH	48.8	30	0

Table A3: Sample parameters for study of the influence of load rotation on compressive strength

Sample Name	Unit Cell Length / mm	Designed Strut Thickness /μm	Sample Size / mm	Compression Tester	Design Volume Fraction /%	BCCZ Z Strut Orientation During Build /°	BCCZ Z Strut Orientation During Compression /°
BCCZ 0	1	250	H 15, D 12	Universal	27.7	0	0
BCCZ 10	1	250	H 15, D 12	Universal	27.8	0	10
BCCZ 20	1	250	H 15, D 12	Universal	27.8	0	20
BCCZ 30	1	250	H 15, D 12	Universal	27.9	0	30
Diamond 0	1	250	H 15, D 12	Universal	25.6	0	0
Diamond 10	1	250	H 15, D 12	Universal	28.5	0	10
Diamond 20	1	250	H 15, D 12	Universal	27.5	0	20
Diamond 30	1	250	H 15, D 12	Universal	27.3	0	30
Gyroid 0	1	150	H 15, D 12	ESH	48.5	0	0
Gyroid 10	1	150	H 15, D 12	ESH	48.6	0	10
Gyroid 20	1	150	H 15, D 12	ESH	48.6	0	20
Gyroid 30	1	150	H 15, D 12	ESH	48.6	0	30

Table A4: Sample parameters for study of the influence of both build and load rotation combined on compressive strength

Sample Name	Unit Cell Length / mm	Designed Strut Thickness /μm	Sample Size / mm	Compression Tester	Design Volume Fraction /%	BCCZ Z Strut Orientation During Build /°	BCCZ Z Strut Orientation During Compression /°
BCCZ 0	1	250	H 15, D 12	Universal	27.7	0	0
BCCZ 10	1	250	H 15, D 12	Universal	27.8	10	10
BCCZ 20	1	250	H 15, D 12	Universal	27.8	20	20
BCCZ 30	1	250	H 15, D 12	Universal	27.9	30	30
BCCZ 45	1	250	H 15, D 12	Universal	28.0	45	45
BCCZ 90	1	250	H 15, D 12	Universal	27.2	90	90
Diamond 0	1	250	H 15, D 12	Universal	25.6	0	0
Diamond 10	1	250	H 15, D 12	Universal	28.5	10	10
Diamond 20	1	250	H 15, D 12	Universal	27.5	20	20
Diamond 30	1	250	H 15, D 12	Universal	27.3	30	30
Diamond 45	1	250	H 15, D 12	Universal	28.9	45	45
Diamond 90	1	250	H 15, D 12	Universal	28.4	90	90
Gyroid 0	1	150	H 15, D 12	ESH	48.5	0	0
Gyroid 10	1	150	H 15, D 12	ESH	48.6	10	10
Gyroid 20	1	150	H 15, D 12	ESH	48.6	20	20
Gyroid 30	1	150	H 15, D 12	ESH	48.6	30	30
Gyroid 45	1	150	H 15, D 12	ESH	48.6	45	45
Gyroid 90	1	150	H 15, D 12	ESH	48.5	90	90

Table A5: Sample parameters for study of the influence of unit cell size on compressive strength

Sample Name	Unit Cell Length /mm	Designed Strut Thickness /μm	Sample Size /mm	Compression Tester	Design Volume Fraction /%
BCCZ 1.0	1.0	250	H 20, D 20	ESH	27.4
BCCZ 1.5	1.5	250	H 20, D 20	Universal	13.1
BCCZ 2.0	2.0	250	H 20, D 20	Universal	7.5
Diamond 1.0	1.0	250	H 20, D 20	Universal	7.9
Diamond 1.5	1.5	250	H 20, D 20	Universal	3.6
Diamond 2.0	2.0	250	H 20, D 20	Universal	2.1
Gyroid 1.0	1.0	150	H 20, D 20	ESH	48.4
Gyroid 1.5	1.5	200	H 20, D 20	ESH	48.6
Gyroid 2.0	2.0	250	H 20, D 20	ESH	48.6

Table A6: Measured volume fraction and strut thickness

Sample Name	Design Volume Fraction /%	Measured Volume Fraction by Mass /%	Measured Volume Fraction by Archimedes /%	Designed Strut Thickness /μm	Measured Top View Strut Thickness /μm
BCC 150	9.3	17.0 $\pm$ 0.1	17.2 $\pm$ 0.2	150	183 $\pm$ 20
BCC 250	23.7	35.4 $\pm$ 0.2	35.7 $\pm$ 0.3	250	253 $\pm$ 28
BCC 350	44.7	56.6 $\pm$ 0.2	57.1 $\pm$ 0.2	350	362 $\pm$ 33
BCCZ 150	10.8	18.3 $\pm$ 0.1	18.6 $\pm$ 0.1	150	176 $\pm$ 27
BCCZ 250	27.7	37.8 $\pm$ 0.1	38.1 $\pm$ 0.4	250	250 $\pm$ 29
BCCZ 350	51.1	58.3 $\pm$ 0.1	58.8 $\pm$ 0.4	350	350 $\pm$ 46
Cubic 150	4.3	8.0 $\pm$ 0.0	8.3 $\pm$ 0.1	150	157 $\pm$ 25
Cubic 250	11.5	17.1 $\pm$ 0.2	17.3 $\pm$ 0.2	250	230 $\pm$ 27
Cubic 350	21.6	27.1 $\pm$ 0.1	27.3 $\pm$ 0.2	350	324 $\pm$ 47
Diamond 150	9.7	17.0 $\pm$ 0.1	17.3 $\pm$ 0.2	150	168 $\pm$ 25
Diamond 250	25.6	35.1 $\pm$ 0.1	35.6 $\pm$ 0.4	250	230 $\pm$ 29
Diamond 350	46.1	55.3 $\pm$ 0.1	55.9 $\pm$ 0.3	350	350 $\pm$ 45
Fluorite 150	17.9	31.6 $\pm$ 0.4	32.2 $\pm$ 0.9	150	165 $\pm$ 32
Fluorite 250	44.0	58.6 $\pm$ 0.5	69.8 $\pm$ 2.4	250	235 $\pm$ 52
Fluorite 350	92.3	89.8 $\pm$ 0.2	92.2 $\pm$ 0.2	350	
Gyroid 60	19.3	34.2 $\pm$ 0.1	34.2 $\pm$ 0.2	60	
Gyroid 100	32.3	47.5 $\pm$ 0.3	48.1 $\pm$ 0.3	100	
Gyroid 150	48.8	64.2 $\pm$ 0.3	65.4 $\pm$ 0.5	150	
Gyroid 200	65.9	80.1 $\pm$ 0.3	85.4 $\pm$ 1.4	200	
Gyroid 250	83.9	92.1 $\pm$ 0.3	95.5 $\pm$ 0.4	250	

Table A7: Measured strut thickness of struts at different angles from the top view

Strut Miller Index	Angle to vertical /°	Mean / μm
<111>	35.3	235 ± 26
<111>	37.9	240 ± 45
<111>	42.3	240 ± 40
<111>	48.0	253 ± 44
<111>	54.7	255 ± 34
<111>	62.1	242 ± 39
<111>	69.8	252 ± 43
<111>	77.8	258 ± 45
[001]	90.0	213 ± 43

Table A8: Measured strut thickness of struts at different angles from the right view

Strut Miller Index	Angle to vertical /°	Angle to vertical in plane /°	Mean / μm
[001]	0.0	0.0	330 ± 77
[001]	10.0	0.0	260 ± 36
[001]	20.0	0.0	233 ± 42
[001]	30.0	0.0	265 ± 47
<111>	37.9	36.2	332 ± 114
<111>	42.3	38.0	330 ± 65
[001]	45.0	0.0	255 ± 46
<111>	48.0	40.8	352 ± 66
<111>	54.7	45.0	333 ± 59
<111>	62.1	51.0	347 ± 66
<111>	69.8	59.1	338 ± 63
<111>	77.8	69.9	372 ± 81
<111>	90.0	90.0	254 ± 52

Table A9: Measured strut thickness of struts at different angles from the back view

Strut Miller Index	Angle to vertical /°	Angle to vertical in plane /°	Mean / μm
[001]	0.0	0	281 ± 69
[001]	10.0	10	218 ± 31
[001]	20.0	20	224 ± 43
[001]	30.0	30	176 ± 45
<111>	35.3	0	265 ± 40
<111>	37.9	15	247 ± 41
<111>	42.3	25	265 ± 50
<111>	48.0	35	296 ± 51
<111>	54.7	45	335 ± 65
<111>	62.1	55	384 ± 50
<111>	69.8	65	395 ± 58
<111>	77.8	75	416 ± 58
[001]	90.0	90	398 ± 31
<111>	90.0	90	387 ± 60

Table A10: 0.2% offset stress and Young's Modulus values for compression testing of unit cell comparison samples

Sample Name	Offset stress / MPa	Young's Modulus / GPa
BCC 150	9.5 ± 7.3	0.36 ± 0.01
BCC 250	103.3 ± 1.0	2.35 ± 0.03
BCC 350	257.0 ± 10.6	8.10 ± 0.69
BCCZ 150	15.6 ± 13.0	0.78 ± 0.06
BCCZ 250	154.3 ± 3.2	3.02 ± 0.07
BCCZ 350	364.8 ± 6.6	9.62 ± 0.46
Cubic 150	2.5 ± 0.1	0.09 ± 0.00
Cubic 250	20.9 ± 1.4	0.70 ± 0.05
Cubic 350	59.4 ± 1.4	1.83 ± 0.06
Diamond 150	26.8 ± 0.7	0.85 ± 0.04
Diamond 250	110.6 ± 1.8	2.63 ± 0.08
Diamond 350	269.9 ± 13.9	7.31 ± 0.93
Fluorite 150	68.7 ± 4.0	2.00 ± 0.14
Fluorite 250	305.5 ± 11.7	8.93 ± 1.76
Fluorite 350	934.4 ± 20.4	17.18 ± 0.11
Gyroid 60	109.5 ± 5.0	3.36 ± 0.18
Gyroid 100	183.3 ± 9.4	3.12 ± 0.11
Gyroid 150	358.8 ± 9.5	9.14 ± 0.86
Gyroid 200	563.4 ± 10.2	13.39 ± 0.45
Gyroid 250	994.9 ± 18.2	18.97 ± 0.35

Table A11: 0.2% offset stress and Young's Modulus values for compression testing of lattice at different rotations

Unit Cell	Angle /°	Build Rotate Offset Stress / MPa	Build Rotate Yield Stress / GPa	Load Rotate Offset Stress / MPa	Load Rotate Yield Stress / GPa	Combined Rotate Offset Stress / MPa	Combined Rotate Yield Stress / GPa
BCCZ	0	154.3 ± 3.2	3.02 ± 0.07	154.3 ± 3.2	3.02 ± 0.07	154.3 ± 3.2	3.02 ± 0.07
BCCZ	10	115.2 ± 3.7	2.86 ± 0.14	145.2 ± 7.6	3.25 ± 0.17	132.6 ± 2.6	2.98 ± 0.39
BCCZ	20	116.0 ± 5.9	3.13 ± 0.11	141.4 ± 1.7	3.19 ± 0.05	136.5 ± 2.9	3.18 ± 0.30
BCCZ	30	120.5 ± 2.7	3.01 ± 0.03	138.1 ± 1.8	3.45 ± 0.03	127.4 ± 2.8	3.12 ± 0.18
BCCZ	45					116.1 ± 3.9	2.81 ± 0.12
BCCZ	90					110.4 ± 1.7	2.59 ± 0.10
Diamond	0	110.6 ± 1.8	2.63 ± 0.08	110.6 ± 1.8	2.63 ± 0.08	110.6 ± 1.8	2.63 ± 0.08
Diamond	10	101.5 ± 1.7	2.86 ± 0.05	126.0 ± 1.9	3.14 ± 0.07	101.3 ± 6.8	2.56 ± 0.14
Diamond	20	99.1 ± 1.4	2.78 ± 0.02	118.7 ± 1.8	2.85 ± 0.01	105.5 ± 4.0	2.58 ± 0.21
Diamond	30	97.0 ± 0.6	2.71 ± 0.01	117.4 ± 3.8	3.08 ± 0.04	103.1 ± 2.6	2.65 ± 0.19
Diamond	45					109.9 ± 2.8	2.40 ± 0.19
Diamond	90					127.8 ± 3.7	2.82 ± 0.14
Gyroid	0	358.8 ± 9.5	9.14 ± 0.86	358.8 ± 9.5	9.14 ± 0.86	358.8 ± 9.5	9.14 ± 0.86
Gyroid	10	337.0 ± 3.4	9.64 ± 0.31	354.8 ± 9.9	9.83 ± 0.24	361.9 ± 5.7	8.86 ± 0.26
Gyroid	20	338.2 ± 5.6	9.31 ± 0.19	374.6 ± 3.9	9.43 ± 0.35	357.9 ± 4.8	8.67 ± 0.38
Gyroid	30	336.7 ± 3.7	9.51 ± 0.07	393.1 ± 12.3	10.30 ± 0.15	364.0 ± 13.6	8.87 ± 0.35
Gyroid	45					363.3 ± 4.3	9.26 ± 0.28
Gyroid	90					352.4 ± 6.7	8.72 ± 0.38

Table A12: 0.2% offset stress and Young's Modulus values for compression testing of unit cell size samples

Sample Name	Offset stress / MPa	Young's Modulus / GPa
BCCZ 1.0	148.5 ± 2.5	4.83 ± 0.50
BCCZ 1.5	31.9 ± 0.4	1.16 ± 0.06
BCCZ 2.0	11.0 ± 0.2	0.56 ± 0.04
Diamond 1.0	16.3 ± 0.3	0.52 ± 0.00
Diamond 1.5	3.6 ± 0.1	0.11 ± 0.00
Diamond 2.0	1.4 ± 0.0	0.03 ± 0.00
Gyroid 1.0	326.5 ± 10.4	8.00 ± 0.40
Gyroid 1.5	317.3 ± 6.3	7.97 ± 0.35
Gyroid 2.0	303.4 ± 12.5	8.31 ± 0.17

APPENDIX B

STATISTICAL ANALYSIS OF LATTICE ELUTION

Table B1: Significance values for ANOVA and Tukey post hoc testing to understand which **Peppas a** values were significantly different for the lattice elution studies. Significantly different values are shown in bold, GS - gentamicin sulphate

	Brushite with GS	PMMA with GS	BCCZ20	BCCZ40	BCCZ60	Gyroid20	Gyroid40
PMMA with GS	**0.00**						
BCCZ20	**0.00**	**0.00**					
BCCZ40	**0.00**	**0.00**	**0.00**				
BCCZ60	**0.00**	**0.00**	**0.00**	**0.00**			
Gyroid20	**0.00**	**0.00**	0.55	**0.01**	**0.00**		
Gyroid40	**0.00**	**0.00**	**0.00**	0.06	**0.01**	**0.00**	
Gyroid60	**0.00**	**0.01**	**0.00**	**0.00**	1.00	**0.00**	**0.01**

Table B2: Significance values for ANOVA and Tukey post hoc testing to understand which **Peppas b** values were significantly different for the lattice elution studies. Significantly different values are shown in bold, GS - gentamicin sulphate

	Brushite with GS	PMMA with GS	BCCZ20	BCCZ40	BCCZ60	Gyroid20	Gyroid40
PMMA with GS	**0.00**						
BCCZ20	0.93	**0.00**					
BCCZ40	0.80	**0.00**	0.21				
BCCZ60	0.76	**0.00**	1.00	0.10			
Gyroid20	0.42	**0.00**	0.97	**0.04**	1.00		
Gyroid40	0.79	**0.00**	1.00	0.12	1.00	1.00	
Gyroid60	0.76	**0.00**	1.00	0.10	1.00	1.00	1.00

Table B3: Significance values for ANOVA and Tukey post hoc testing to understand which plateau **mass of gentamicin sulphate** values were significantly different for the lattice elution studies. Significantly different values are shown in bold, GS - gentamicin sulphate

	Brushite with GS	Brushite no GS	PMMA with GS	PMMA no GS	BCCZ20	BCCZ40	BCCZ60	Gyroid20	Gyroid40
Brushite no GS	**0.00**								
PMMA with GS	**0.00**	1.00							
PMMA no GS	**0.00**	1.00	1.00						
BCCZ20	**0.02**	**0.00**	**0.00**	**0.00**					
BCCZ40	**0.00**	**0.00**	**0.00**	**0.00**	**0.00**				
BCCZ60	**0.00**	**0.00**	**0.00**	**0.00**	**0.00**	**0.00**			
Gyroid20	**0.00**	**0.00**	**0.00**	**0.00**	0.33	**0.01**	**0.00**		
Gyroid40	**0.00**	**0.00**	**0.00**	**0.00**	**0.00**	0.46	**0.00**	**0.00**	
Gyroid60	**0.00**	**0.00**	**0.00**	**0.00**	**0.00**	**0.00**	1.00	**0.00**	**0.00**

Table B4: Significance values for ANOVA and Tukey post hoc testing to understand which zone of inhibition value for ***Staphylococcus aureus*** were significantly different for the lattice elution studies. Significantly different values are shown in bold, GS - gentamicin sulphate

	Brushite with GS	Brushite no GS	PMMA with GS	PMMA no GS	BCCZ20	BCCZ40	BCCZ60	Gyroid20	Gyroid40
Brushite no GS	**0.00**								
PMMA with GS	0.16	**0.00**							
PMMA no GS	**0.00**	**0.00**	**0.00**						
BCCZ20	**0.00**	0.97	0.01	**0.00**					
BCCZ40	**0.00**	0.10	0.29	**0.00**	0.62				
BCCZ60	**0.00**	1.00	**0.00**	**0.00**	0.82	**0.04**			
Gyroid20	**0.00**	**0.02**	0.74	**0.00**	0.21	1.00	**0.01**		
Gyroid40	**0.00**	1.00	**0.00**	**0.00**	0.98	0.13	1.00	**0.03**	
Gyroid60	**0.00**	0.74	**0.00**	**0.00**	0.15	**0.00**	0.93	**0.00**	0.67

Table B5: Significance values for ANOVA and Tukey post hoc testing to understand which zone of inhibition value for ***Pseudomonas aeruginosa*** were significantly different for the lattice elution studies. Significantly different values are shown in bold, GS - gentamicin sulphate

	Brushite with GS	Brushite no GS	PMMA with GS	PMMA no GS	BCCZ20	BCCZ40	BCCZ60	Gyroid20	Gyroid40
Brushite no GS	**0.00**								
PMMA with GS	0.96	**0.02**							
PMMA no GS	**0.00**	**0.00**	**0.00**						
BCCZ20	0.98	**0.02**	1.00	**0.00**					
BCCZ40	0.75	0.07	1.00	**0.00**	1.00				
BCCZ60	**0.02**	0.97	0.23	**0.00**	0.19	0.50			
Gyroid20	0.64	0.10	1.00	**0.00**	1.00	1.00	0.61		
Gyroid40	1.00	**0.00**	1.00	**0.00**	1.00	0.92	**0.05**	0.85	
Gyroid60	0.76	0.07	1.00	**0.00**	1.00	1.00	0.48	1.00	0.93